WHEN THE SHAPE DOES MATTER: THREE-DIMENSIONAL IN VITRO MODELS OF EPITHELIAL BARRIERS

EDITED BY: Elena Martinez, Vanesa Fernández-Majada, María García-Díaz, Núria Torras and Michael Raghunath

PUBLISHED IN: Frontiers in Bioengineering and Biotechnology

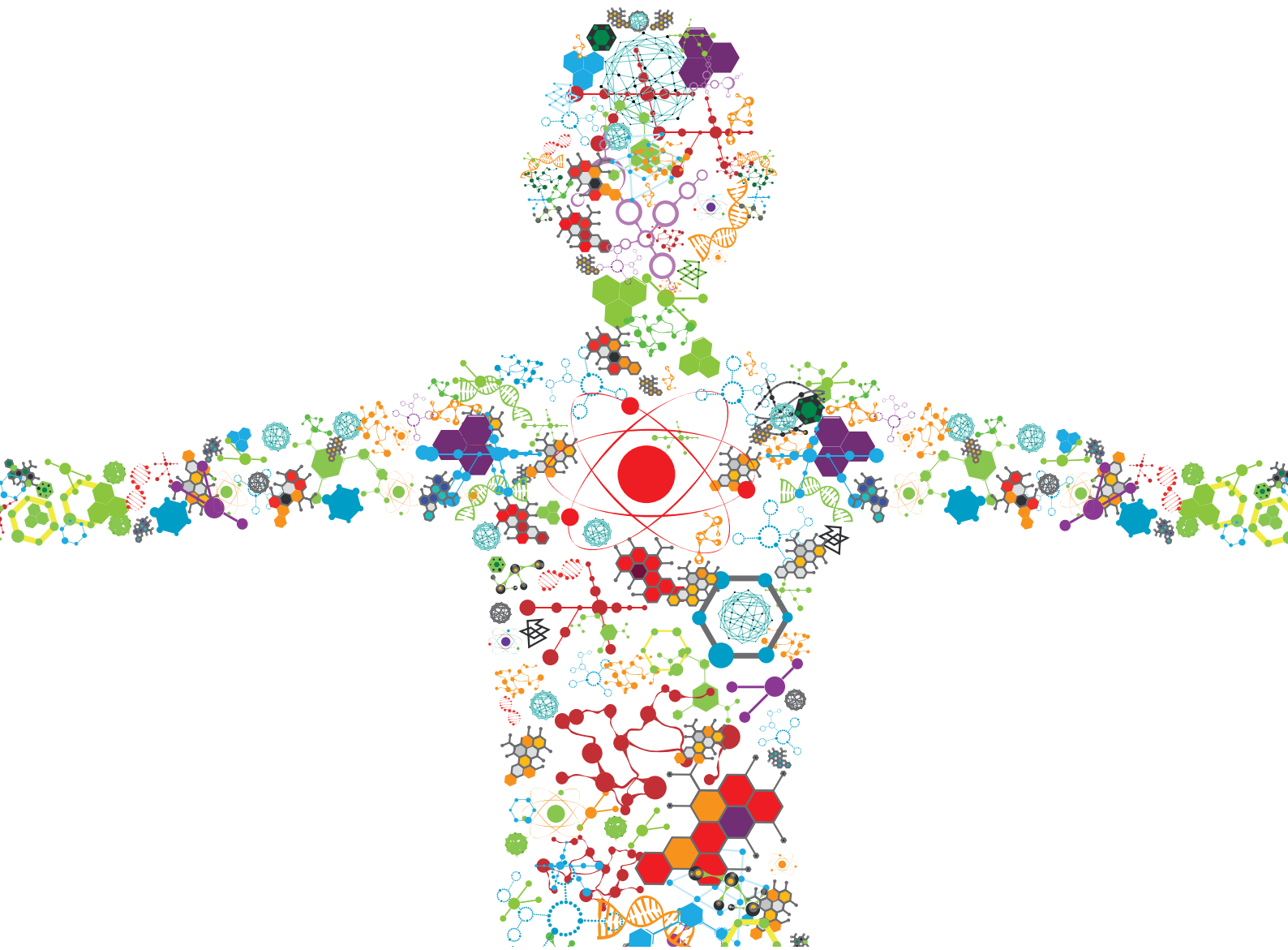

frontiers Research Topics

ISSN 1664-8714
ISBN 978-2-88966-394-1
DOI 10.3389/978-2-88966-394-1

About Frontiers

Frontiers is more than just an open-access publisher of scholarly articles: it is a pioneering approach to the world of academia, radically improving the way scholarly research is managed. The grand vision of Frontiers is a world where all people have an equal opportunity to seek, share and generate knowledge. Frontiers provides immediate and permanent online open access to all its publications, but this alone is not enough to realize our grand goals.

Frontiers Journal Series

The Frontiers Journal Series is a multi-tier and interdisciplinary set of open-access, online journals, promising a paradigm shift from the current review, selection and dissemination processes in academic publishing. All Frontiers journals are driven by researchers for researchers; therefore, they constitute a service to the scholarly community. At the same time, the Frontiers Journal Series operates on a revolutionary invention, the tiered publishing system, initially addressing specific communities of scholars, and gradually climbing up to broader public understanding, thus serving the interests of the lay society, too.

Dedication to Quality

Each Frontiers article is a landmark of the highest quality, thanks to genuinely collaborative interactions between authors and review editors, who include some of the world's best academicians. Research must be certified by peers before entering a stream of knowledge that may eventually reach the public - and shape society; therefore, Frontiers only applies the most rigorous and unbiased reviews.
Frontiers revolutionizes research publishing by freely delivering the most outstanding research, evaluated with no bias from both the academic and social point of view. By applying the most advanced information technologies, Frontiers is catapulting scholarly publishing into a new generation.

What are Frontiers Research Topics?

Frontiers Research Topics are very popular trademarks of the Frontiers Journals Series: they are collections of at least ten articles, all centered on a particular subject. With their unique mix of varied contributions from Original Research to Review Articles, Frontiers Research Topics unify the most influential researchers, the latest key findings and historical advances in a hot research area! Find out more on how to host your own Frontiers Research Topic or contribute to one as an author by contacting the Frontiers Editorial Office: researchtopics@frontiersin.org

WHEN THE SHAPE DOES MATTER: THREE-DIMENSIONAL IN VITRO MODELS OF EPITHELIAL BARRIERS

Topic Editors:
Elena Martinez, Institute for Bioengineering of Catalonia (IBEC), Spain
Vanesa Fernández-Majada, Institute for Bioengineering of Catalonia (IBEC), Spain
María García-Díaz, Institute for Bioengineering of Catalonia (IBEC), Spain
Núria Torras, Institute for Bioengineering of Catalonia (IBEC), Spain
Michael Raghunath, Zurich University of Applied Sciences, Switzerland

Citation: Martinez, E., Fernández-Majada, V., García-Díaz, M., Torras, N., Raghunath, M., eds. (2021). When the Shape Does Matter: Three-Dimensional In Vitro Models of Epithelial Barriers. Lausanne: Frontiers Media SA.
doi: 10.3389/978-2-88966-394-1

Table of Contents

frontiers in Bioengineering and Biotechnology

EDITORIAL
published: 01 December 2020
doi: 10.3389/fbioe.2020.617361

Editorial: When the Shape Does Matter: Three-Dimensional *In Vitro* Models of Epithelial Barriers

Vanesa Fernández-Majada[1]*, *María García-Díaz*[1], *Núria Torras*[1], *Michael Raghunath*[2] and *Elena Martínez*[1,3,4]*

[1] Biomimetic Systems for Cell Engineering, Institute for Bioengineering of Catalonia, The Barcelona Institute of Science and Technology, Barcelona, Spain, [2] Center for Cell Biology and Tissue Engineering, Institute for Chemistry and Biotechnology, Zurich University of Applied Sciences, Wädenswil, Switzerland, [3] Centro de Investigación Biomédica en Red en Bioingeniería, Biomateriales y Nanomedicina, Madrid, Spain, [4] Department of Electronics and Biomedical Engineering, University of Barcelona, Barcelona, Spain

Keywords: 3D cell culture models, organ-on-a chip, microengineered tissues, epithelial barriers, computer modeling

Editorial on the Research Topic

When the Shape Does Matter: Three-Dimensional *In Vitro* Models of Epithelial Barriers

The Research Topic presented here includes a collection of selected pre-reviewed manuscripts that describe relevant recent advances in the fields of bioengineering and biophysics with a focus on the generation and analysis of novel three-dimensional (3D) *in vitro* models of epithelial barriers.

Recapitulating the 3D *in vivo* tissue environment at the biochemical, mechanical, and cellular level to obtain more physiologically relevant *in vitro* organotypic models is currently a very active line of research due to its direct impact on basic biology, drug testing, and disease modeling studies. Recent advances in cell biology and bioengineering techniques have opened new landscapes in the field. For example, it has been shown that the use of both artificial and natural matrices favors cellular self-organization in *in vivo*-like 3D tissue structures through cell-to-matrix signaling. This is the case for many engineered tissues, the liver among them. Although the was previously great success in reproducing the hepatic function *in vitro*, a method to include the biliary tree that is capable of removing toxic metabolites has not yet been developed yet. Funfak et al. demonstrate that normal rat cholangiocytes grown in 3D matrices based on artificial polymers (PEG) can form polarized and functional cysts comparable to those generated in natural polymers (Matrigel). In addition, the authors discovered that the elastic modulus of the substrate and the integrin ligand density directly affects cholangiocytes cyst formation frequency, size, and polarization. This work proves the suitability of artificial polymers for cholangiocytes organotypic models and decouples the biochemical and biophysical effects derived from the substrate on hepatic organoid formation.

The manuscripts of Macedo et al. and Darling et al. highlight the importance of upgrading standard 2D monocultures to more physiologically relevant *in vitro* models which represent not only the cell-to-matrix interface but also the interactions between the different cell types present in the *in vivo* organ. Both works focus on generating intestinal epithelial models. Macedo et al. engineered a 3D mucosal intestinal model comprising a collagen layer with embedded human intestinal fibroblasts, mimicking the cellular components and physico-chemical properties of the intestinal lamina propria and, on top, an epithelial monolayer composed of enterocyte-like (Caco-2) and mucus secretory-like (HT29-MTX) cells. They demonstrate that this advanced intestinal model better reproduces the cellular and physiological characteristics of the *in vivo* organ as proved by a more physiological absorption than that observed with standard 2D Caco-2 monocultures. Employing a similar experimental set up, Darling et al. investigated the effect of either the paracrine

OPEN ACCESS

Edited and reviewed by:
Ranieri Cancedda, Independent Researcher, Genova, Italy

***Correspondence:**
Vanesa Fernández-Majada
vfernandez@ibecbarcelona.eu
Elena Martínez
emartinez@ibecbarcelona.eu

Specialty section:
This article was submitted to Tissue Engineering and Regenerative Medicine, a section of the journal Frontiers in Bioengineering and Biotechnology

Received: *14 October 2020*
Accepted: *09 November 2020*
Published: *01 December 2020*

Citation:
Fernández-Majada V, García-Díaz M, Torras N, Raghunath M and Martínez E (2020) Editorial: When the Shape Does Matter: Three-Dimensional In Vitro Models of Epithelial Barriers. Front. Bioeng. Biotechnol. 8:617361. doi: 10.3389/fbioe.2020.617361

signals or the physical presence of fibroblast on the above growing epithelium. They show that when co-cultured in 3D and close to fibroblasts, Caco-2 monolayers display morphological characteristics such as enhanced columnar shape polarization and altered lateral membrane morphology like the *in vivo* intestinal epithelial monolayer. This improved cellular architecture translated into more physiological TEER and permeability values than those achieved with standard monocultures or with only the fibroblast-derived condition medium.

In addition to fibroblasts, basic intestinal epithelial cultures have been upgraded by incorporating the other cell types present in the *in vivo* tissue including endothelial, immune, and neuronal cells, their interface with the microbiome, as well as physical cues such as peristaltic movements. Steinway et al. extensively review recent progress in developing advanced micro-physiological intestinal systems and their use in evaluating normal intestinal physiology such as nutrient absorption, digestion, and secretion as well as metabolism, intestinal infection, inflammation, and cancer.

One of the most relevant applications of advanced *in vitro* organotypic models is the replacement of animal testing in the safety evaluation for consumer products and drugs. For instance, assessing the skin irritation potential of topical drugs and cosmetics by employing advanced *in vitro* cultures is already mandatory by law in the European Union since 2013. Wei et al. established an integrated organotypic skin model in a high throughput screening platform that enables large-scale dermal toxicology testing based on tissue viability, barrier integrity, and cytokine secretion. They employed bioprinting technology to produce organotypic skin constructs with controlled spatial cell layering, consistent cellular composition and distribution, and extracellular matrix (ECM) organization. With the aim of predicting oral drug administration-induced toxicity, De Gregorio et al. designed a microfluidic intestine-liver-on-chip (InLiver-OC). In contrast to single-organ systems, multiple organ-on-chip models recapitulate the complex *in vivo* intercellular and interorgan interfaces and therefore are excellent *in vitro* platforms to reliably model the enterohepatic circulation and first-pass metabolism, which are critical for assessing drug and xenobiotic metabolism. These authors employed a bottom-up tissue engineering strategy to build-up a physiologically functional 3D intestinal model with independent access to the apical and basolateral site of the tissue. This intestinal chamber is interconnected via microfluidic channels with a 3D Liver microtissue (HepG2-μTPs). With this advanced InLiver-OC, the authors thoroughly evaluated the intestine-liver metabolic and absorptive crosstalk of harmful model substances, such as ethanol. They propose their device as a tool to reduce the number of drug candidates and accelerate the pre-clinical screening process reducing animal testing.

Impedance spectroscopy (IS) is a promising technology, compatible with high throughput screening, that carries out a wide range of measurements in real time. It is been widely used as an analytical method of various physiological parameters, employing 3D tissue models and organ-on-a-chip devices. The applications, advantages, and limitations of IS as an analytical tool for advance culture systems are thoroughly discussed and reviewed by Gerasimenko et al..

Mimicking *in vitro* the complex 3D architecture of native tissues is important since it has been shown that it can better recapitulate the cellular and physiological functional properties of the *in vivo* organs. These complex 3D shapes of epithelial tissues require new analytical methods, both *in silico* and *in vitro*. Ioannou et al. present a 3D hybrid computer model that permits them to model epithelial movements that do not occur as planar deformations but which are, rather, characterized by out-of-plane mechanics and 3D effects such as tissue bending, invagination, and extrusion. The developed model simulates differential contractilities at the apical, basal, and lateral sides of the monolayer. On the practical side, Altay et al. introduce a new technology that allows for the histological processing of microstructured 3D intestinal models, preserving the fragile intestinal villi-like topology of the scaffolds. The high-resolution imaging of these 3D constructs enables a thorough study of cellular behavior on physiologically relevant matrix shapes. The authors reveal the positive effect of the substrate curvature on the cell shape and orientation along the villus axis and advocate for this as the cause of the more physiologically relevant barrier properties of the engineered intestinal tissues when compared with regular 2D monolayers.

This collection of original articles and reviews provides insights into the relevance of generating and properly analyzing micro-physiological *in vitro* epithelial tissues that aim to bridge the gap between traditional *in vitro* tools and costly animal studies.

AUTHOR CONTRIBUTIONS

EM and MR coordinated the research topic. VF-M coordinated the editorial and together with EM, MG-D, and NT wrote the manuscript. All authors contributed to the article and approved the submitted version.

FUNDING

Funding for this project was provided by the European Union's Horizon 2020 ERC Grant Agreement No. 647863 (COMIET), and the Spanish Ministry of Economy and Competitiveness (TEC2017-83716-C2-1-R).

Conflict of Interest: The authors declare that the research was conducted in the absence of any commercial or financial relationships that could be construed as a potential conflict of interest.

frontiers in Bioengineering and Biotechnology

ORIGINAL RESEARCH
published: 13 December 2019
doi: 10.3389/fbioe.2019.00417

Biophysical Control of Bile Duct Epithelial Morphogenesis in Natural and Synthetic Scaffolds

Anette Funfak[1], Latifa Bouzhir[2], Emilie Gontran[2], Nicolas Minier[1,3], Pascale Dupuis-Williams[2,4†] and Samy Gobaa[1*†]*

[1] Institut Pasteur, Biomaterials and Microfluidics Core Facility, Paris, France, [2] Université Paris-Saclay, UMR-S1174 INSERM, Orsay, France, [3] Université de Technologie de Compiègne, Alliance Sorbonne Université, Compiègne, France, [4] ESPCI, PSL University, Paris, France

OPEN ACCESS

Edited by:
Elena Martinez, Institute for Bioengineering of Catalonia (IBEC), Spain

Reviewed by:
Sharon DeMorrow, University of Texas at Austin, United States
Romina Mancinelli, Sapienza University of Rome, Italy

***Correspondence:**
Pascale Dupuis-Williams
pascale.dupuis-williams@u-psud.fr
Samy Gobaa
samy.gobaa@pasteur.fr

† These authors have contributed equally to this work

Specialty section:
This article was submitted to Tissue Engineering and Regenerative Medicine, a section of the journal Frontiers in Bioengineering and Biotechnology

Received: *02 October 2019*
Accepted: *29 November 2019*
Published: *13 December 2019*

Citation:
Funfak A, Bouzhir L, Gontran E, Minier N, Dupuis-Williams P and Gobaa S (2019) Biophysical Control of Bile Duct Epithelial Morphogenesis in Natural and Synthetic Scaffolds. Front. Bioeng. Biotechnol. 7:417. doi: 10.3389/fbioe.2019.00417

The integration of bile duct epithelial cells (cholangiocytes) in artificial liver culture systems is important in order to generate more physiologically relevant liver models. Understanding the role of the cellular microenvironment on differentiation, physiology, and organogenesis of cholangiocytes into functional biliary tubes is essential for the development of new liver therapies, notably in the field of cholangiophaties. In this study, we investigated the role of natural or synthetic scaffolds on cholangiocytes cyst growth, lumen formation and polarization. We demonstrated that cholangiocyte cyst formation efficiency can be similar between natural and synthetic matrices provided that the mechanical properties of the hydrogels are matched. When using synthetic matrices, we also tried to understand the impact of elasticity, matrix metalloprotease-mediated degradation and integrin ligand density on cyst morphogenesis. We demonstrated that hydrogel stiffness regulates cyst formation. We found that controlling integrin ligand density was key in the establishment of large polarized cysts of cholangiocytes. The mechanism of lumen formation was found to rely on cell self-organization and proliferation. The formed cholangiocyte organoids showed a good MDR1 (multi drug resistance protein) transport activity. Our study highlights the advantages of fully synthetic scaffold as a tool to develop bile duct models.

Keywords: bile duct, microenvironment, organoids, hydrogels, 3D cell culture

INTRODUCTION

Cellular microenvironment cues, including surface topography, substrate rigidity and biochemical signals determine to a large extent the outcome of many biological processes (Tan et al., 2003; Gobaa et al., 2011; Unadkat et al., 2011). Strikingly, the exposure of stem cells to mechanical cues allows steering the differentiation process (Engler et al., 2006). Gaining control over the mechanical stress landscape of the cell was cornerstone in the development of successful organ-on-chip and strategies (Huh et al., 2013; Benam et al., 2016) and of advanced 3D culture systems (Gjorevski et al., 2016).

Recapitulating a physiological hepatic function *in vitro* is currently a very active line of research. Approaches, based on the use of primary adult hepatic cells (Broutier et al., 2016) or on the controlled differentiation of induced Pluripotent Stem Cells (iPSC) (Takebe et al., 2014) have led to the derivation of new organotypic models. These advanced cell culture systems were developed in order to improve on the physiological relevance of standard 2D culture hepatic cell lines.

Despite great successes (Broutier et al., 2016) in recapitulating the hepatic function *in vitro*, the inclusion of a biliary tree capable of removing the toxic metabolite is yet to be developed. The biliary tree is composed of intra and extra hepatic ducts organized in a complex network of interconnected tubes with luminal diameters ranging from $<15\,\mu m$ to a few mm capable of carrying the bile from the liver to the intestine (Roskams et al., 2004; Boyer, 2013). The bile ducts are lined with the epithelial cholangiocytes which regulate, through secretion and adsorption, the composition and flow of the bile (Bogert and LaRusso, 2007).

The biliary system is itself the target of a vast array of liver pathologies called cholangiopathies (Cheung et al., 2018) that account for a large proportion of liver transplants (Murray et al., 2005). Today's treatments of cholangiopathies consist mostly in either largely ineffective pharmacotherapies or in surgeries that are restricted to the extrahepatic large duct. Living donors of liver grafts often suffer from biliary complications like stricture formation, bile leaks and infection (De Assuncao et al., 2017).

The field of bile duct engineering, previously hindered by the lack of available cells, has recently benefited from progress in the understanding of biliary physiopathology and the availability of cholangiocytes cell lines or methods recapitulating differentiation of hepatic precursor cells, stem cells or iPSCs, using various mixtures of growth factors known to direct bile duct embryogenesis (Dianat et al., 2014; De Assuncao et al., 2015; Ogawa et al., 2015; Sampaziotis et al., 2015; Takayama et al., 2016). What remains to be explored when considering developing innovative liver therapies is to understand how the microenvironment guides the self-organization of cholangiocytes into functional biliary tubes (Shiojiri and Sugiyama, 2004; Raynaud et al., 2011).

Cell culture in 3D has shown that cholangiocytes possess *in vitro* morphogenetic capabilities in natural hydrogels like collagen or Matrigel (Ishida et al., 2001; Tanimizu et al., 2007; Hashimoto et al., 2008; Kido et al., 2015). The scaffolding properties of Matrigel help supporting the 3D reorganization of adult cells. The production of "cholangioids" in Matrigel from healthy cholangiocytes versus issued from patients with primary sclerosing cholangitis (PSC) (Soroka et al., 2019) has recently exemplified their interest for the study of pathogenicity of biliary diseases and their putative use in the identification of therapeutic targets (Loarca et al., 2017). Matrigel embedding is also used as a final step in most cholangiocytes differentiation protocols, to assess their capacity to organize in biliary cysts (Dianat et al., 2014; De Assuncao et al., 2015; Ogawa et al., 2015; Sampaziotis et al., 2015; Takayama et al., 2016). However, relaying on hydrogels based on natural extracellular matrix (ECM) clearly hinders the mechanistic understanding of organogenesis or cysts formation as these scaffolds prohibits the decoupling of the biophysical and biochemical signaling. Similarly, liver stiffness is a key marker of liver pathology (Wells, 2008; Mueller and Sandrin, 2010) and marks the development of chronic fibrotic diseases (Saneyasu et al., 2016). In this context using liver organoids to study disease progression begs for the development of hydrogel systems with tunable mechanical properties. Interestingly, the stiffness-dependent differentiation of cholangiocytes seems to be modulated by the biochemical nature of the used matrix (Kourouklis et al., 2016). This indicates the high level of intricacy of both the biochemical and biophysical cues for these finely regulated biological processes.

This complex, and sometime undefined, nature of ECM-based hydrogels including Matrigel (MT) hinders the mechanistic understanding of organogenesis in a dish. On the other hand, synthetic hydrogels technology, such as systems based on the polymerization of polyethylene glycol (PEG), underwent many developments in the last decades placing them at the top of the list of the most physiologically relevant yet fully defined substrates for cell culture (Gjorevski et al., 2016). Today, synthetic hydrogel systems gained key functionalities including physiological elastic moduli (Ranga et al., 2014), easy tethering of biochemical ligands (Mosiewicz et al., 2013) and matrix metalloprotease (MMP) mediated proteolytic degradation allowing cell migration (Lutolf and Hubbell, 2003). These engineered functionalities opened the door for the establishment of advanced and physiologically relevant assays in fully synthetic scaffolds including the production of intestinal organoids (Gjorevski et al., 2016), the differentiation of embryoid bodies into neural tubes (Ranga et al., 2016) and the production of epithelial cysts (Enemchukwu et al., 2016). Therefore, the side-by-side comparison of organotypic development in both synthetic (PEG) and natural (MT) hydrogels could help with defining the set of microenvironment features that are essential to the proper self-organization of the seeded cells.

Cholangiocytes, like most other epithelial cells are able, when embedded in natural ECM like Matrigel or collagen, to self-organize into polarized monolayers enclosing a central lumen termed cyst. These structures are good models for studying duct morphogenesis since they share with the tubes the same topology and the same organization of the epithelium, where the polarized cells are connected by adherens and tight junctions, thus ensuring secretion, cohesiveness, and coordinated growth of the monolayer. Here we report on the quantitative impacts of biochemical and biophysical cues on the development of cholangiocyte cysts *in vitro*. We demonstrate that cholangiocytes can organize and produce polarized cysts in both natural and synthetic scaffolds. We also show that the biophysical and biochemical parameters of the extracellular milieu are key for cyst morphogenesis. We also report on the dynamics of lumen formation and how this process is influenced by the extracellular milieu.

MATERIALS AND METHODS

Cell Culture

Normal Rat Cholangiocytes (NRC) cell line was obtained from N. LaRusso's laboratory (Vroman and LaRusso, 1996). The cells were cultured on collagen coated T25 flasks and maintained in DMEM F12 medium supplemented with 5% fetal bovine serum (Life Technologies), 1× Antibiotic-Antimycotic (Life Technologies) and growth active factors including Insulin (Life Technologies), Dexomethosane (Sigma), 3,3,5-Triiodo-L-thyroninen sodium salt (Sigma), Bovine Pituitary Extract (BPE, Life Technologies) were added as described in de Groen et al. (1998).

Hydrogel Formation

Synthetic hydrogels were formed by Michael-type addition of bicystein-bearing peptides onto star-shaped, vinylsulfone-functionalized, polyethylene glycol macromeres. Lyophilized peptides were ordered from Pepmic (China). Peptide sequences 16A (Ac-GCRD-GPQG↓I**A**GQ-DRCG-NH2) and 16R (Ac-GCRD-VPMS↓M**R**GG-DRCG-NH2) were chosen in order to ensure varying MMP sensitivity as established elsewhere (Lutolf and Hubbell, 2003; Patterson and Hubbell, 2010). An RGD peptide (Ac-GCGYG**RGD**SPG-NH2) was used at various concentrations in order to promote the integrin mediated adhesion of encapsulated cells. Briefly, peptides were resuspended in Milli-Q water to obtain a 12% (w/v) working solution. Before using these peptides to form hydrogel, we controlled their integrity and purity on a Bruker UltrafeXtreme MALDI-TOF/TOF instrumentation (Bruker-Daltonics, Germany). One microliter of peptide at 0.1 mg/ml was deposited on a MTP 384 ground steel target plate with 1 μl of 2,5-Dihydroxybenzoic acid (2,5-DHB) in 50% acetonitrile, 0.1% trifluoroacetic acid as matrix solution. Data were acquired using Flexcontrol software (Bruker-Daltonics, Germany) and shots were recorded in positive ion reflectron mode. Mass spectra were externally calibrated in the m/z range of 700–3,500 Da with a peptide calibration standard (Bruker-Daltonics, Germany) and analyzed with the Flexanalysis software (Bruker). Next, we performed an Ellman assay as per the manufacturer instructions in order to quantify free thiol concentration in each peptide working solution. The difference between theoretical and measured thiol concentration was taken in consideration in order to produce hydrogels with the desired Thiol (Th)/Vinyl Sulfone (VS) stoichiometry. Finally, we measured the peptide net content by hydrolyzing the samples in 1% phenol 6 N HCL for 20 and 48 h at 110°C in presence of known amount of NorLeucine as internal standard. After HCL evaporation the samples are analyzed on a L-8800 Hitachi amino acids analyzer (post-column derivatization with ninhydrin after ion-exchange chromatography separation).

Eight-arm polyethylene glycol-vinyl sulfone or PEG-VS 40 kDa macromeres were ordered as a custom synthesis from NOF (Japan). Lyophilized powder was dissolved in a 0.3 M, pH 7.5, HEPES buffer (Dominique Dutscher, France) at 12% (w/v). Hydrogel sterility was ensured by filtering both peptide and PEG-VS working solutions on a 0.22 μm syringe filter (Millex-GS, Merck). Polyethylene glycol (PEG) hydrogels were produced as described in Lutolf and Hubbell (2003). Rapidly, 4.5% (w/v) containing 100 μM RGD gels were formed by mixing 63 μl PEG-VS macromere (12% w/v) with 103 μl HEPES buffer, 2 μl RGD peptide (10 mM) and 40 μl NRC cells resuspended in HEPES buffer with a cell concentration of 1.5×10^6 cells/ml. In a second step we added 12 μl of 16R or 16A peptide working solutions (12% w/v). Before gelation, the mixture was pipetted up and down gently. Fifty microliters drops of gel mixture were sandwiched between two mirror-polished PTFE pieces separated with a 1 mm spacer in order to produce 50 μl hydrogel disks. The assemblage was then placed in a Heracell 150i incubator (ThermoFisher Scientific, Waltham, MA USA) at 37°C, 100% relative humidity for 30 min. Upon crosslinking, gel disks were demolded and transferred to a 12 well plate (Falcon® multiwell plate, Corning) loaded with the adequate cell culture medium.

For Matrigel experiments, NRC cells were first mixed with a 7 mg/ml growth factor reduced Matrigel (Corning) solution and then diluted to 3.5 mg/ml with pre-cooled NRC complete medium on ice with a cell concentration of 3×10^5 cells/ml. Before the filling of 8-well μ-slides with the Matrigel-cell mixture, the pre-cooled slides were coated with 50 μl 3.5 mg/ml Matrigel solution and polymerized for 15 min at 37°C and 5% CO_2. Subsequently 300 μl of Matrigel-cell mixture was pipetted in each well and polymerized for 15 min at 37°C and 5% CO_2 before adding cell culture medium.

For both hydrogel systems NRC cells were pre-dissociated by up and down pipetting of the cell suspension followed by a post-dissociation step using a 40 μm cell strainer (Merck). The dissociated cell suspension was then diluted to the aimed cell concentration and mixed with the hydrogel solutions. It is to mention, that the natural and synthetic hydrogel system required a different state of cell dissociation (low for PEG hydrogel and high for Matrigel) due to the system requirements and the inhibition of NRC cell migration in PEG hydrogels. This was achieved by the adjustment of the pre-dissociation step.

Rheology

The hydrogel shear modulus was obtained by rheometric measurement with a Kinexus Ultra Plus Rheometer (Malvern Panalytical, UK). Briefly, gels of different concentration were casted as cylinders of 4 mm in diameter after swelling in water overnight. The rheometer was fitted with a 4 mm geometry. Each gel disk was compressed to 80% of its nominal height in order to avoid slippage during the measurements. An amplitude sweep was performed to determine the linear viscoelasticity region (LVER) of the measured material. Shear moduli were extracted from a frequency sweep analysis performed with a constant 1% strain. The reported G′ values were obtained at 0.5 Hz.

The hydrogel shear modulus for Matrigel was obtained by a direct polymerization of the polymer solution on the working stage of the rheometer. Therefore, samples of 314 μl were added to the center of the pre-cooled (4°C) lower working plate. The geometry of 20 mm was then immediately lowered before the gel started to form, to a working gap of 1 mm. For the polymerization of the polymer suspension, the temperature was increased stepwise with a rate of 5°C/min from 4 to 37°C and kept at 37°C during measurement. A solvent trap cover was used to prevent evaporation effects around the working stage. Rheometric measurements were performed at 0.5 Hz and a constant 0.1% strain.

Viability/Cytotoxicity Assay

PEG and Matrigel hydrogels were washed with PBS and then incubated for 30 min at 37°C, 5% CO_2 with 4 μM Ethidium homodimer-1 and 2 μM Calcein, AM (ThermoFisher scientific) in growth medium. After a second washing step, the gels were imaged as described below. In average 12 images were acquired per condition. Fluorescence intensity was measured after background correction and normalized for the variations in

cyst surface using ImageJ, an image analysis software available on the NCBI website (https://imagej.nih.gov/ij/).

Functionality Assays

To demonstrate the multidrug resistance protein 1 (MDR1) transporter activity of single or multi-lumen cysts, polyethylene glycol (PEG) and Matrigel hydrogels were treated with 50 μM rhodamine 123 (Rh123, Sigma) in serum free medium for 1 h at 37°C. After a washing step (3× in serum free medium) the hydrogels were incubated for 2 h at 37°C, 5% CO_2 in fresh complete medium. To inhibit the MDR1 transporter activity the cysts containing hydrogels were incubated with 50 μM verapamil (Sigma-Aldrich) at 37°C for 30 min before adding Rh123. The rhodamine assay was then repeated as described above. For the quantification of the Rh123 assay the number of cysts containing Rh 123 in the luminal space and the number of cysts showing Rh 123 signal only at the level of the epithelium (blocked cysts) were counted with ImageJ.

Immunostaining of the Cysts

Immunostaining were performed without extracting the NRC cysts from PEG hydrogel or Matrigel. The PEG hydrogels were washed with PBS and then fixed with 4% paraformaldehyde (PFA) overnight at 4°C. Cysts were permeabilized with 0.5% Triton X-100 in PBS for 1–2 h at 4°C and then blocked with 2% BSA, 0.1% Tween-20 in PBS for 3 h. The primary polyclonal anti-E-cadherin antibody (Thermo Fisher Scientific PA5-32178, 1: 400) was diluted in blocking solution and incubated for 2–4 days at 4°C. Unbound primary antibodies were washed by incubating the gels in blocking buffer (3 times, 10 min each). The secondary antibody Goat anti-Rabbit IgG (H+L), Alexa Fluor Plus 647 (Thermo Fisher Scientific A32733, 1:400) was diluted in blocking solution and incubated for 2–4 days at 4°C. Nuclei and f-actin filaments were stained by adding 10 μM Hoechst and 16.5 nM Phalloidin 488 (Thermo Fisher Scientific) in PBS containing 1% BSA. Gels were incubated for 2 days at 4°C. Stained gels were then washed intensively in PBS.

Matrigel hydrogels were washed with PBS and fixed with 4% paraformaldehyde and 5% sucrose in PBS. Cyst were permeabilized with 0.5% Triton X-100 in PBS for 30 min and then blocked with 0.1% BSA and 1% goat serum for 30 min at RT. The primary polyclonal anti-E-cadherin antibody (Thermo Fisher Scientific PA5-32178, 1: 400) and 16.5 nM Phalloidin 488 (Thermo Fisher Scientific) were diluted in blocking solution and incubated overnight at 4°C. The Matrigel gels were washed by incubation in PBS containing 0.05% Tween (3 times, 10 min each). The secondary antibody Goat anti-Rabbit IgG (H+L), Alexa Fluor Plus 647 (Thermo Fisher Scientific A32733, 1:400) was diluted in blocking solution and incubated for 1 h at RT. After washing, the gels were mounted with Prolong Gold antifade reagent (Invitrogen Molecular probes) containing DAPI for nuclei staining.

Imaging

Wide field microscopy was performed on an inverted axio Observer Z1 inverted microscope from Zeiss (Carl Zeiss Microscopy GmbH, Jena, Germany) equipped with an OrcaFlash 4 V2.0 camera (Hamamatsu, Hamamatsu city, Japan) and Plan-Apochromat phase 1 10× (NA, 0.45) or Plan-Apochromat phase 2 20× (NA, 0.5) objectives. In case of live imaging (cyst growth in PEG hydrogel) temperature and CO_2 were ensured with a PeCon incubator equipped with the corresponding CO_2 and temperature modules.

Confocal imaging was performed on an SP8 inverted microscope (Leica Microsystems, Germany) equipped with HC FLUOTAR L 25×/0.95 W 0.17 VISIR objective and a white laser system. Confocal imaging of cyst polarization in Matrigel was acquired with a confocal microscope Nikon Eclipse TE-2000-E equipped with a X20/0.45 Plan Fluor ELWD Ph1 DM objective (∞/0–2 WD 7.4).

Quantification of Cysts Growth and Morphology

For the quantification of cyst growth, cyst and lumen formation in PEG and Matrigel hydrogels up to 15 z-stacks per condition and time point were acquired. Between 2 and 3 z-stacks were taken from non-overlapping regions within a hydrogel. Z-stacks were performed from the bottom to the top of the hydrogel with fixed height and image sampling number for all condition. Cyst size, number of cysts and number of single- or multi-lumen formed per imaged z-stack was then analyzed using Matlab Image processing toolbox. The cyst formation frequency was determined by relating the cyst number per z-stack to the corresponding initial cell number per z-stack. Lumen formation was also characterized by staining for actin, E-cadherin, and DNA as described above.

Statistical Analysis

All values are expressed as mean±SEM except for the rheological and viability measurements (mean±SD). Statistical significance was determined using Kruskal-Wallis *t*-test. The dynamics of cyst formation and single lumen production were analyzed in R (3.6.0) or the R project for statistical computing downloadable from https://www.r-project.org/. The fitted curves were generated with the GLM function fed with the models: Cyst frequency ∼ scaffold * log(Day) and single lumen ∼ scaffold * exp(Day). The obtained *p*-values were corrected for multiple comparisons with the Benjamini and Yekutieli method (BY) (Benjamini and Yekutieli, 2001).

RESULTS

Normal Rat Cholangiocytes Form Cysts Upon Culture in 3D Scaffolds

Triggering morphogenetic processes and achieving high levels cell-self organization is best recapitulated when initiated in the presence of a three-dimensional support or scaffold. The initial objective of this study was to identify 3D microenvironments supportive of cholangiocytes self-organization. Based on observations made with other epithelial cell lines we first seeded Normal Rat Cholangiocytes (NRC) in both synthetic, fully defined polyethylene glycol (PEG) hydrogels and in natural extracellular matrix-based Matrigel (MT) (**Figure 1A**). We quickly confirmed that NRCs can survive and proliferate in both

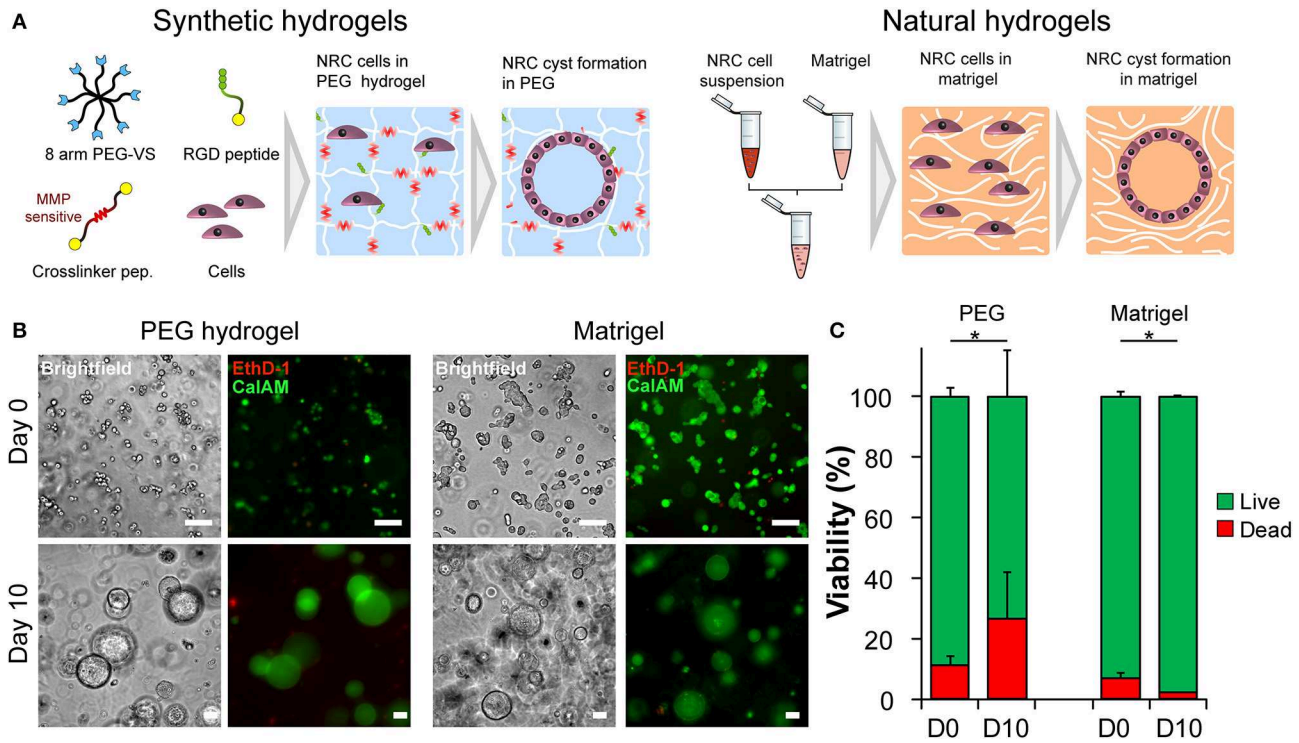

FIGURE 1 | Normal Rat Cholangiocyte (NRC) encapsulation and viability assessment. **(A)** Schematic representation of the used encapsulation procedure showing the differences between PEG (synthetic) and Matrigel (natural) hydrogels in terms of composition. In order to assess the self-organization capabilities of NRCs in synthetic and natural matrices, harvested cells were seeded into PEG hydrogels and Matrigel. Eight-arm PEG macromers bearing a vinyl sulfone function at the end of each arm were crosslinked with different peptides sensitive to matrix metalloprotease degradation in order to produce synthetic hydrogels. These synthetic PEG scaffolds were further functionalized with integrin ligands and proteolytic degradation capabilities in order to ensure NRC survival whereas in Matrigel encapsulated NRCs naturally formed cysts. **(B)** Brightfield and fluorescent images of live/dead staining of NRCs cultured in PEG and MT for 3 h or 10 days. The NRC cells when maintained for 10 days in culture formed hollow 3D structures, termed cysts. **(C)** When viability was assessed we found that the obtained structures were viable with PEG hydrogel causing slightly higher cell mortality. Represented PEG hydrogels condition corresponds to 4.5% (w/v) functionalized with 1,200 μM RGD ligand. $n = 3$. *Significant at $p < 0.05$ in a Kruskal-Wallis test. Error bars represent SD. Scale bar equal 100 μm.

conditions. Over a culture period of 10 days, cultured NRCs self-organized into hollow spheres or cysts where a very thin layer of epithelial cells marked the boundary between an inner lumen and the extracellular milieu (**Video S1**). We also observed that unlike in MT, NRCs cannot migrate in PEG and that cyst formation was mostly due to the seeding of small cell aggregates rather than single cells. When assessing cell viability, we found that encapsulated NRC showed globally a good viability in PEG and in MT. At day 10 a modest decrease in viability was observed in PEG, most probably due to the death of the cells that could not form cysts (**Figures 1B,C**). Overall, the growth kinetics (**Video S2**) in both materials allowed for the formation of cysts with sizes ranging from 40 to 800 μm. At this stage, we could not observe obvious differences between cysts cultured in either synthetic or natural scaffolds.

Matrix Stiffness and Integrin Ligand Density Modulate Cyst Formation

After confirming that NRC could self-organize into 3D structures reminiscent of polarized cysts. Unlike unpolarized cell aggregates, the obtained structure clearly showed a large lumen, cells organized as a monolayer that are staining positive for actin on the apical side and for E-cadherin on the basolateral side. First, we sought to investigate the determinants of cyst formation dynamics across gel composition (natural vs. synthetic matrices), matrix stiffness (or elastic modulus noted G') regime and integrin ligand density. Initially, we varied both the PEG concentration and the integrin ligand density (**Figure 2A**) of the synthetic hydrogel system while documenting the impact of PEG concentration of the elastic modulus (**Figure 2B**). Unlike ECM-based scaffolds, PEG hydrogels can be produced at varying elastic moduli while maintaining a constant molarity of integrin ligand (Gobaa et al., 2011). In this scenario the impact of increased RGD concentration on elastic modulus remains important and often overlooked (Enemchukwu et al., 2016). In order to quantify the impact of RGD peptides on the mechanical properties of the gel we measured the shear modulus of gels of different concentration while also varying RGD molarity. This showed that the incorporation of 100 μM RGD peptides to the hydrogel network had a very limited impact on the gel stiffness. Increasing the RGD dose up to 1,200 μM led to a 32% decrease of elastic modulus in the stiffest gels (**Figure 2B**). This RGD-mediated

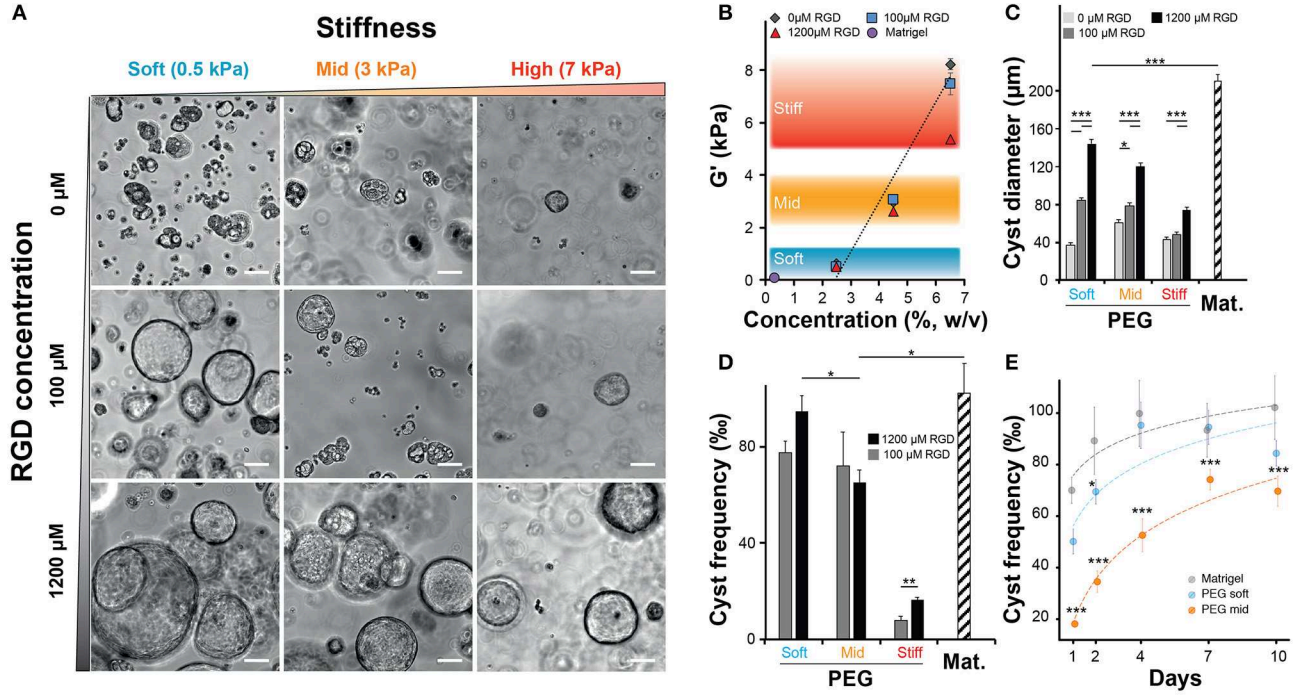

FIGURE 2 | Impact of matrix stiffness and integrin ligand density on Normal Rat Cholangiocytes (NRC) cyst formation. **(A)** Brightfield images of NRC cysts cultured for 10 days. NRCs were encapsulated in PEG hydrogels crosslinked with an MMP sensitive peptide (16R) and varying for concentration (w/v) and integrin ligand density. **(B)** Quantification of the impact of varying PEG and RGD concentration on the elastic modulus or G′ indicating the stiffness of produced PEG hydrogels. There we defined three stiffness domains including soft (2.5% PEG w/v, around 0.5 kPa), intermediate (4.5% PEG w/v, around 3 kPa) and stiff gels (6.5% PEG w/v, >5.5 kPa). The addition of up to 1,200 µM RGD had an overall moderate impact on the elasticity regime. **(C,D)** Quantification of cyst size and cyst frequency, respectively, at day 10 across soft, intermediate, and stiff polyethylene glycol gels and in Matrigel. **(E)** Dynamic study showing the evolution of the frequency of cyst production across the studied conditions. *, **, and *** Significant at $p < 0.05$, $p < 0.01$, and $p < 0.001$, respectively. $n = 4$. Error bars represent SEM. Scale bar equal 100 µm.

decrease in stiffness is relatively modest when compared to the impact of varying PEG concentration. Altogether, the measured rheological data showed that varying PEG concentration allowed the production of soft (around 0.5 kPa), intermediate (2–4 kPa) and stiff (around 7 kPa) gels while the measured stiffness of the Matrigel scaffolds was several orders of magnitude lower. Furthermore, we also investigated the impact of gel proteolytic degradation by tuning the matrix metalloproteases sensitivity of PEG hydrogels according to Patterson and Hubbell (2010). There we found that cell survival was independent of the proteolytic degradation of the substrate (**Figure S3**). We also demonstrated that the most sensitive gels crosslinked with the 16R peptide allowed systematically for a higher efficiency of cyst formation across the entire range of gel stiffness and RGD concentrations (**Figure S4**).

When we quantified the average cyst size, we found that softer gels favored the formation of larger cysts with the largest cysts being systematically produced in Matrigel (approximatively 20% larger than in the best PEG condition). In addition, this experiment also showed that the presence of RGD, in a dose dependent manner, was critical for the formation of large cysts (**Figure 2C**). Interestingly, the measurement of cyst sizes across the nine RGD/Stiffness conditions showed that while increasing RGD concentration in soft gels dramatically increased cyst size, it only had a much lower (but still significant $p < 0.001$) effect in stiff gels. This indicates that stiffness seems to be the parameter that determines the possible maximum cyst size while the addition of RGD allows for the realization of that potential. Conversely, high stiffness clearly overrides the effect of integrin engagement and prohibits the formation of larger NRC cysts. This trend was further confirmed when we looked at the frequency of cyst formation (**Figures 2D,E**). There we found that increasing the elastic modulus of the hydrogels significantly reduced the frequency of cyst formation. When looking at maximal cyst formation efficiency we found that Matrigel and soft synthetic gels (1,200 µM RGD) had reached comparable levels. We also found that removing RGD from soft PEG drastically limited cyst formation (**Figure S5**). Finally, when quantifying cyst formation efficiency over 10 days we confirmed that both soft PEG and Matrigel imposed a similar logarithmic increase. Increasing the matrix stiffness was sufficient to significantly ($p < 0.001$) reduce this efficiency while the logarithmic trend was maintained (**Figure 2E**). Taken together these data clearly show that both, cholangiocytes cyst formation frequency and size are determined to a large extent by variation in the elastic modulus of the substrate. The presence of RGD ligand in high concentration further improved this trend.

Establishment of Cyst Polarity

When cultured in 3D, epithelial cells such as the kidney cell line (MDCK) self-assemble in hollow spheres and recapitulate the morphogenetic program leading to the production of rudimentary epithelial organoids (McAteer et al., 1986). Detailed analysis showed that interactions between key integrins and the extracellular matrix (ECM) regulate the establishment of cell polarity and morphogenesis (Manninen, 2015). In both cases whether NRC cysts can become polarized upon cultured in a synthetic 3D scaffold was investigated first by immunochemistry and rhodamine transport assay. There we found that large NRC cysts stain positive for basolateral E-Cadherin and apical F-actin (**Figure 3A**; **Figure S6**). Canonical epithelial polarity was observed in cysts of different dimensions across the tested 3D culture conditions. NRC cysts with inverted polarity could also be observed as described elsewhere (Enemchukwu et al., 2016). However, these observations were very seldom and did appear to correlate with either stiffness or RGD concentration. When looking at the shape of the nuclei of the cholangiocytes lining the cyst wall, we found that in Matrigel these structures seemed to be more elongated and placed tangentially to the formed circle whereas in PEG the nuclei seemed rounder, organized into a mixed mono- and/or double-layer structure (**Figure 3A**). *In vivo*, the morphology of the nuclei in the lining of the bile duct seems to vary from round to oval with preferentially a basal localization in the cell. On the functional level we found that, in MT or in PEG hydrogels, formed cysts could accumulate rhodamine 123 in their lumen and that this accumulation was blocked by the addition of verapamil in the culture medium. This clearly indicates that the accumulation of rhodamine is resulting from transmembrane channel protein-multidrug resistance protein-1 (MDR1) activity and not passive diffusion (**Figure 3B**). Furthermore, we could show that the frequency of rhodamine accumulating cysts was reduced when matrix stiffness was increased (**Figure 3C**). These data suggest that NRC cysts cultured in either PEG or MT are showing apicobasal polarity and functioning as mature epithelial cysts.

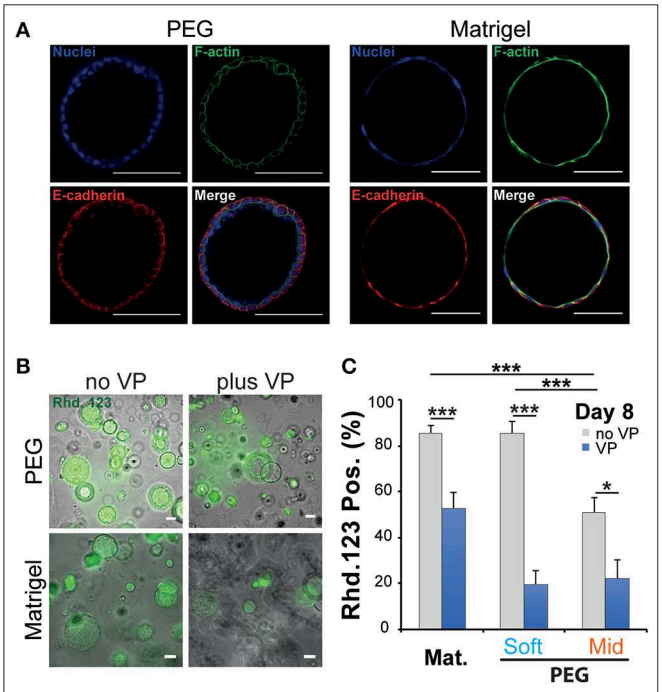

FIGURE 3 | Phenotypic and functional assessment of Normal Rat Cholangiocytes (NRC) cysts produced in both polyethylene glycol and Matrigel hydrogels. **(A)** Scanning confocal microphotographs of immunostained NRC cysts after 10 days of culture. Both structures stain positive for actin (apically) and E-cadherin (basolaterally). **(B,C)** Widefield microphotographs and subsequent quantification showing the accumulation of rhodamine 123 (Rhd. 123) in the lumen of NRC cysts. Adding the channel blocking agent verapamil (VP) reduced this accumulation. * and *** Significant at $p < 0.05$ and $p < 0.001$ respectively. $n = 4$. Error bars represent SEM. Scale bar equal 100 μm.

Morphogenesis and Lumen Formation

When imaging the different structures obtained after culturing NRC in PEG and MT hydrogels, we have identified different cell organizations including large cysts including a unique lumen bordered by a thin layer of cells (SL) (**Figure 3A**; **Video S1**), spherical cell structures containing multiple gaps (ML) (**Figure 4A**; **Figure S7**) and small and compact cell aggregates. We found that the hydrogel recipe was determining to a certain extent the frequency of each structure. Quantifications preformed on different scaffolding conditions showed that decreasing the hydrogel stiffness and increasing the RGD concentration increased the frequency of SL structures (**Figures 4B–D**). More interestingly the effect of stiffness seemed to plateau for gels between 2.5 and 4.5% (w/v) PEG. We observed that NRCs cultured in 2.5% PEG hydrogel ($G' \approx 0.5$ kPa) showed a SL frequency of 73 and 56% for high and low RGD concentrations respectively. The formation of SL was decreased by 20% when using stiffer gels. An even further decrease was observed when using low RGD in the stiffest gels. This indicates that above a certain elasticity threshold (between 0.5 and 2.5 kPa) the luminal organization seems to be rather independent of the hydrogel stiffness whereas RGD density remains an important determinant for the formation of single lumen with normal polarity. Although comparable at day 10, the frequency of SL cyst formation did not appear to follow identical trajectories in PEG vs. MT. Observing the dynamics of SL cyst formation over the course of 10 days revealed that the formation of SL cysts seemed to follow an exponential law in PEG whereas cyst formation dynamics was found more linear in MT. These dynamics reveal that the gap in percent of SL cyst formation is strongly decreasing over time when comparing MT and PEG (**Figure 4C**). When investigating cyst organization in relation to size we found that ML cysts are significantly smaller than SL cysts. This observation remained true for longer observations (2 weeks plus) (**Figure S7**). We also found that limiting the dose of RGD clearly restricted the growth of the produced ML cysts (**Figure 4D**). This experiment also showed that cyst size and organization are not fully correlated and that the two parameters could respond to different microenvironment cues.

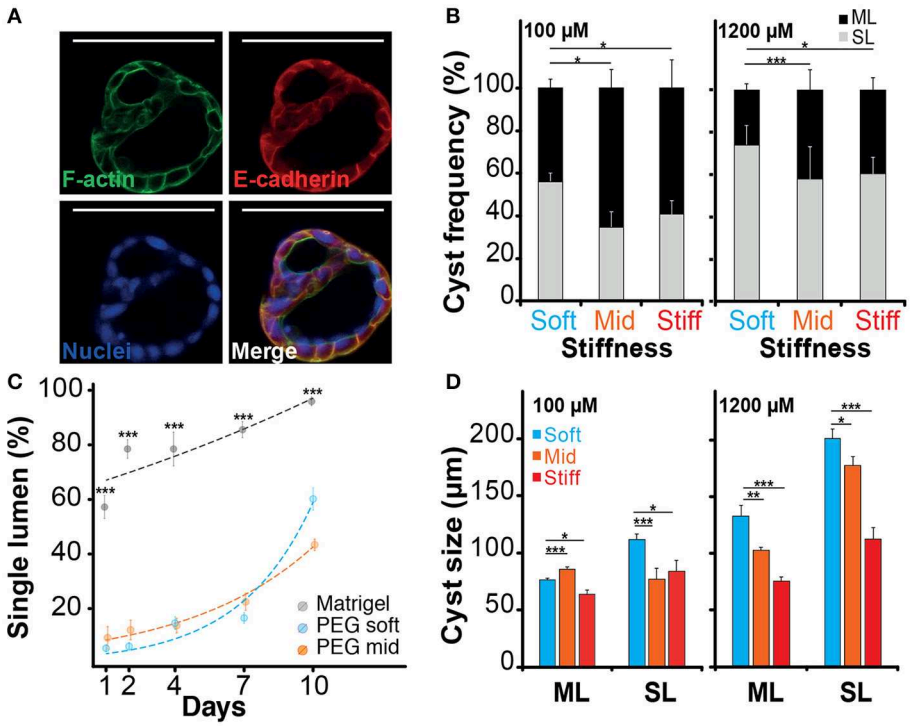

FIGURE 4 | Impact of the microenvironment on lumen formation. **(A)** Immunostaining of f-actin and E-cadherin localization in normal rat cholangiocyte (NRC) cyst with multi-lumen phenotype. The observation of Normal Rat Cholangiocytes (NRC) cysts formation in different matrices showed that some NRC cysts could comprise multiple lumens. **(B)** Quantification of single lumen formation of NRC cysts during 10 day. The quantifications showed that this phenomenon was prevalent in PEG hydrogel and marginal in Matrigel. We also found that the fraction of single lumen cysts in PEG tended to exponentially increase over time. **(C)** The analysis of the "multi-lumen" and "single-lumen" phenotype frequency indicated that a soft microenvironment containing 1,200 µM RGD caused the lowest rates of multi-lumen formation. **(D)** Finally, cyst size analysis showed that variation in RGD concentration seemed to alter the multi-lumen/single-lumen ratio. SL and ML is for single-lumen and multi-lumen, respectively. *, **, and *** Significant at $p < 0.05$, $p < 0.01$, and $p < 0.001$, respectively. $n = 4$. Error bars represent SEM. Scale bar equal 100 µm.

DISCUSSION

The ECM-cholangiocyte interaction is essential for the formation of the biliary tree. *In vitro,* the ECM is classically mimicked by natural hydrogels known to promote well-cholangiocyte differentiation and morphogenesis (Tanimizu et al., 2007). Understanding the role of the microenvironment cues on bile duct formation is clearly limited by the type of assays that can recapitulate this process *in vitro*. On one hand, hydrogels based on naturel ECM allow to faithfully recapitulate key morphogenetic processes (Tanimizu et al., 2007). However, mechanistic studies in these systems are difficult because of the intertwined biochemical and biophysical signaling. On the other hand, synthetic hydrogels are more amenable to experiment design and systematic variation (Ranga et al., 2014) but less efficient in the support of biological processes. In this work we clearly benefitted from these developments in order to produce synthetic, and fully defined scaffolds capable of efficiently supporting cholangiocyte cyst formation.

Structure wise, epithelial organoids are organized as a monolayer of polarized epithelial cells surrounding a central lumen. Two typical structures can emerge from this basic concept: cysts or tubes. Nevertheless, the precise underlying morphogenetic mechanism remains elusive and the contribution of the microenvironment is yet to be quantified (Yu et al., 2007; Martin-Belmonte et al., 2008). Other studies have shown that primary biliary mouse epithelial cells (BECs) do form cysts from a single cell when cultured in Matrigel and that the resulting cyst formation efficiency is determined by the initial cell number in the aggregates (Rizki-Safitri et al., 2018). Similarly, the encapsulation of single MDCK cells was found sufficient to trigger cyst formation in synthetic and natural hydrogels (Martin-Belmonte et al., 2008; Enemchukwu et al., 2016). Interestingly, the cell aggregation route for the formation of MDCK cysts was also shown pertinent when these cells were encapsulated at high density. Unlike NRCs or MDCKs, other cell types showing very limited proliferation capabilities such as epithelial lung cells (AT II) still produce cysts with sizes directly linked to initial cell density (Yu et al., 2007). Our experiments showed that the encapsulation of aggregates of multiple NRC resulted in cyst formation by cellular rearrangement whereas single cells systematically failed to proliferate and organize. Similar findings were made for NRC cyst formation in MT with the difference that single cells could migrate and aggregate before proliferating and forming cysts.

When stiffness was considered, we demonstrated that matrix elasticity variation modulates cyst formation (**Figure 2D**). Strikingly, cyst formation was found to be very comparable in soft PEG gels and in MT despite the order of magnitude difference in elastic moduli. This is probably due to the fact that both MT and soft PEG conditions are still below the elastic modulus of a healthy liver (∼1 kPa) (Yeh et al., 2002). Globally, the cyst formation process was found to tolerate departure from the healthy liver condition. Even recapitulating fibrotic liver conditions (∼5 kPa, Stiff PEG) did not fully block the process. Very interestingly this observation is consistent with the fact that an abnormal increase in intrahepatic biliary mass is taking place during the earliest stages of liver fibrogenesis (Schuppan et al., 2018). In comparison, when encapsulating MDCK cells cyst formation is completely blocked at 7 kPa (Enemchukwu et al., 2016). Matrix elasticity was found to play a key role in other systems including intestinal organoids and lung adenocarcinoma spheres (Gill et al., 2012; Raza et al., 2013; Gjorevski et al., 2016; Broguiere et al., 2018). In these systems, relatively high initial stiffness was needed to drive cell compaction. A quick softening over time was also important in order to help with the 3D rearrangement of cells.

When considering the biochemical cues, we first tried to recapitulate physiologically relevant integrin ligand densities by adjusting the RGD peptide concentration in the PEG hydrogels. However, as the *in vivo* density of RGD motifs accessible to intrahepatic cholangiocytes is hard to assess we employed 100 μM as the best approximation based on the fibrin structure (Raeber et al., 2005) and 1,200 μM as the most efficient concentration for cysts derivation in an equivalent MDCK model (Enemchukwu et al., 2016). In these conditions NRC cyst formation frequency was found independent of the level of integrin engagement. This is in good agreement with the work performed on MDCK cells in synthetic hydrogels (Enemchukwu et al., 2016). This way we found that cyst size (growth of cysts) and thus lumen formation relied on integrin engagement (**Figures 2C**, **4B**). The growth in diameter of NRC cysts is known to be fueled by fluid secretion into the cyst lumen and cell proliferation (Neufeld et al., 1992; Doctor et al., 2007). Our results suggest that hydrogel elasticity and cell adhesion can synergistically determine the growth of NRC cysts. When comparing Matrigel and PEG-based systems, Matrigel systematically produced larger cysts. This might be due to the different mechanisms of lumen formation, where NRC cysts cultured in MT achieved cyst polarization at an early time point of cyst formation followed by rapid cyst expansion. The formation of a central lumen is a key feature of epithelial morphogenesis. The mechanism of lumen formation in MDCK cysts grown in natural hydrogels depends on the used ECM composition. MDCK cells cultured in collagen I showed later cell polarization during cyst formation and formed lumen by center cell apoptosis passing through a multi lumen state, whereas MDCK cysts grown in laminin rich Matrigel induced early cell polarization and formed lumen through cell proliferation with almost negligible center cell apoptosis (Martin-Belmonte et al., 2008). This was further confirmed when MDCK cysts were found to form luminal space even when apoptosis was suppressed, hinting to the involvement of multiple lumen forming mechanisms (O'Brien et al., 2002). In comparison, cysts derived from lung epithelial cells cultured in natural hydrogels formed lumen through cell rearrangement without cell proliferation and cell apoptosis (Yu et al., 2007).

In general, epithelial cysts grown in natural hydrogels clearly show single lumen phenotype predominantly. In synthetic hydrogels different phenotypes were observed for NRC and MDCK cells (Enemchukwu et al., 2016). We demonstrated that NRC cyst grown in PEG hydrogels or in MT both formed lumen with a typical apical-basolateral polarity (**Figure 3A**). The accumulation of Rhodamine 123 in the produced cysts hints to a proper and functional organization of the cells. Staining for primary cilia and quantifying the response to farnesoid X receptor could help further confirm this aspect. The mechanisms of lumen formation for cysts cultured in PEG hydrogels was found to be based on cell rearrangement, rather than on early cell polarization as shown in MT. Hydrogel stiffness and RGD concentrations were found to be linked to polarization and to the frequency of single lumen formation. A high integrin engagement was shown to enhance the single lumen phenotype over multi-lumen phenotype in NRC cysts for Soft and Stiff PEG hydrogels, respectively. A positive correlation between lumen formation and adhesive ligand density of a synthetic scaffold was also demonstrated in lung adenocarcinoma models (Gill et al., 2012). Not providing polarization cues in synthetic 3D culture systems systematically delays the acquisition of the cyst polarity (Martin-Belmonte et al., 2008; deLeon et al., 2012). For MDCKs a delayed polarization led to the production of multiple lumens that could fuse at later stages. The size of multi-lumen MDCK cysts cultured in natural and synthetic hydrogels was reported to be similar to cysts containing a single lumen (Martin-Belmonte et al., 2008; Enemchukwu et al., 2016). In our hands a majority of NRC cysts with a single lumen derive from multi-lumen structures. In some cases, these multi-lumen cysts persist. In the MDCK system, the multi-lumen cysts phenotype was found associated with the mislocalization of basal components leading to the accumulation of ECM in the luminal space (Torkko et al., 2008). Unlike MDCKs, the NRC multi-lumen cysts were found to be systematically smaller when compared to single-lumen cysts. The suppression of outer layer coat complex II in human intestinal epithelial cells (Caco-2) cultured in 3D resulted in cysts with defective lumen expansion attributed to a faulty ECM signaling when spatially directing cell division. Similar to multi-lumen NRCs, these cysts show a reduced cell number, multi-lumen formation, and smaller sizes (Townley et al., 2012). We speculate that providing NRCs cultured in PEG with a stronger polarization cues by replacing RGD with laminin or laminin derived peptides could significantly stimulate single-lumen formation and expansion of NRC cysts.

In summary, we have established a tunable PEG-based hydrogel system that can be used for cholangiocyte cyst formation and morphogenesis studies. We demonstrated that making these gel cell responsive by adding MMP sensitivity and integrin ligand contributed to meet the cyst

production capacity of NRCs encapsulated in MT. We expect that in the future, this system will be employed to study pathogenicity of biliary diseases and to identify therapeutic targets.

DATA AVAILABILITY STATEMENT

The datasets generated for this study are available on request to the corresponding author.

AUTHOR CONTRIBUTIONS

AF carried out the experiments performed in PEG hydrogel including cell culture, hydrogel casting, and cell encapsulation, helped with the main figures, and arranged the supplementary figures. NM Performed the rheology tests on PEG gels. LB and EG carried out the experiments in natural hydrogels, including cell culture, cell encapsulation, microscopy, and rheology tests on Matrigel. SG, PD-W, and AF produced together a first outline of the manuscript. PD-W wrote part of the introduction. SG arranged the four main figures, wrote the abstract, part of the introduction, the results, and the discussion. All the authors reviewed the manuscript.

FUNDING

This work received the financial support of both the iLite RHU program (grant ANR ANR-16-RHUS-0005) and the Institut Carnot Pasteur. France-BioImaging infrastructure was supported by the French National Research Agency (ANR 10-INSB-04, Investments for the Future).

ACKNOWLEDGMENTS

The authors would like thank Sébastien Brûlé from the protein quality control service of the molecular biophysics facility in Institut Pasteur for technical assistance with MALDI experiments. We also would like to extend our thanks to Françoise Baleux for her help with measuring the net peptide. Finally, we acknowledged the support of UTechS PBI (Imagopole) a France-BioImaging infrastructure.

SUPPLEMENTARY MATERIAL

The Supplementary Material for this article can be found online at: https://www.frontiersin.org/articles/10.3389/fbioe.2019.00417/full#supplementary-material

REFERENCES

Benam, K. H., Villenave, R., Lucchesi, C., Varone, A., Hubeau, C., Lee, H. H., et al. (2016). Small airway-on-a-chip enables analysis of human lung inflammation and drug responses *in vitro*. *Nat. Methods* 13, 151–157. doi: 10.1038/nmeth.3697

Benjamini, Y., and Yekutieli, D. (2001). The control of the false discovery rate in multiple testing under dependency. *Ann. Stat.* 29, 1165–1188. doi: 10.1214/aos/1013699998

Bogert, P. T., and LaRusso, N. F. (2007). Cholangiocyte biology. *Curr. Opin. Gastroenterol.* 23, 299–305. doi: 10.1097/MOG.0b013e3280b079fb

Boyer, J. L. (2013). Bile formation and secretion. *Compr. Physiol.* 3, 1035–1078. doi: 10.1002/cphy.c120027

Broguiere, N., Isenmann, L., Hirt, C., Ringel, T., Placzek, S., Cavalli, E., et al. (2018). Growth of epithelial organoids in a defined hydrogel. *Adv. Mater.* 30:e1801621. doi: 10.1002/adma.201801621

Broutier, L., Andersson-Rolf, A., Hindley, C. J., Boj, S. F., Clevers, H., Koo, B. K., et al. (2016). Culture and establishment of self-renewing human and mouse adult liver and pancreas 3D organoids and their genetic manipulation. *Nat. Protoc.* 11, 1724–1743. doi: 10.1038/nprot.2016.097

Cheung, A. C., Lorenzo Pisarello, M. J., and LaRusso, N., F. (2018). Pathobiology of biliary epithelia. *Biochim. Biophys. Acta Mol. Basis Dis.* 1864(4 Pt B), 1220–1231. doi: 10.1016/j.bbadis.2017.06.024

De Assuncao, T. M., Jalan-Sakrikar, N., and Huebert, R. C. (2017). Regenerative medicine and the biliary tree. *Semin. Liver Dis.* 37, 17–27. doi: 10.1055/s-0036-1597818

De Assuncao, T. M., Sun, Y., Jalan-Sakrikar, N., Drinane, M. C., Huang, B. Q., Li, Y., et al. (2015). Development and characterization of human-induced pluripotent stem cell-derived cholangiocytes. *Lab. Invest.* 95, 684–696. doi: 10.1038/labinvest.2015.51

de Groen, P. C., Vroman, B., Laakso, K., and LaRusso, N. F. (1998). Characterization and growth regulation of a rat intrahepatic bile duct epithelial cell line under hormonally defined, serum-free conditions. *In Vitro Cell Dev. Biol. Anim.* 34, 704–710. doi: 10.1007/s11626-998-0066-1

deLeon, O., Puglise, J. M., Liu, F., Smits, J., ter Beest, M. B., and Zegers, M. M. (2012). Pak1 regulates the orientation of apical polarization and lumen formation by distinct pathways. *PLoS ONE* 7:e41039. doi: 10.1371/journal.pone.0041039

Dianat, N. H., Dubois-Pot-Schneider, Steichen, C., Desterke, C., Leclerc, P., Raveux, A., et al. (2014). Generation of functional cholangiocyte-like cells from human pluripotent stem cells and HepaRG cells. *Hepatology* 60, 700–714. doi: 10.1002/hep.27165

Doctor, R. B., Johnson, S., Brodsky, K. S., Amura, C. R., Gattone, V., Fitz, J., et al. (2007). Regulated ion transport in mouse liver cyst epithelial cells. *Biochim. Biophys. Acta* 1772, 345–354. doi: 10.1016/j.bbadis.2006.11.006

Enemchukwu, N. O., Cruz-Acuna, R., Bongiorno, T., Johnson, C. T., Garcia, J. R., Sulchek, T., et al. (2016). Synthetic matrices reveal contributions of ECM biophysical and biochemical properties to epithelial morphogenesis. *J. Cell Biol.* 212, 113–124. doi: 10.1083/jcb.201506055

Engler, A. J., Sen, S., Sweeney, H. L., and Discher, D., E. (2006). Matrix elasticity directs stem cell lineage specification. *Cell* 126, 677–689. doi: 10.1016/j.cell.2006.06.044

Gill, B. J., Gibbons, D. L., Roudsari, L. C., Saik, J. E., Rizvi, Z. H., Roybal, J. D., et al. (2012). A synthetic matrix with independently tunable biochemistry and mechanical properties to study epithelial morphogenesis and EMT in a lung adenocarcinoma model. *Cancer Res.* 72, 6013–6023. doi: 10.1158/0008-5472.CAN-12-0895

Gjorevski, N., Sachs, N., Manfrin, A., Giger, S., Bragina, M. E., Ordonez-Moran, P., et al. (2016). Designer matrices for intestinal stem cell and organoid culture. *Nature* 539, 560–564. doi: 10.1038/nature20168

Gobaa, S., Hoehnel, S., Roccio, M., Negro, A., Kobel, S., Lutolf, M., et al. (2011). Artificial niche microarrays for probing single stem cell fate in high throughput. *Nat. Methods* 8, 949–955. doi: 10.1038/nmeth.1732

Hashimoto, W., Sudo, R., Fukasawa, K., Ikeda, M., Mitaka, T., and Tanishita, K. (2008). Ductular network formation by rat biliary epithelial cells in the dynamical culture with collagen gel and dimethylsulfoxide stimulation. *Am. J. Pathol.* 173, 494–506. doi: 10.2353/ajpath.2008.071024

Huh, D., Kim, H. J., Fraser, J. P., Shea, D. E., Khan, M., Bahinski, A., et al. (2013). Microfabrication of human organs-on-chips. *Nat. Protoc.* 8, 2135–2157. doi: 10.1038/nprot.2013.137

Ishida, Y., Smith, S., Wallace, L., Sadamoto, T., Okamoto, M., Auth, M., et al. (2001). Ductular morphogenesis and functional polarization of normal human

biliary epithelial cells in three-dimensional culture. *J. Hepatol.* 35, 2–9. doi: 10.1016/S0168-8278(01)00078-2

Kido, T., Koui, Y., Suzuki, K., Kobayashi, A., Miura, Y., Chern, E. Y., et al. (2015). CPM is a useful cell surface marker to isolate expandable bi-potential liver progenitor cells derived from human iPS cells. *Stem Cell Rep.* 5, 508–515. doi: 10.1016/j.stemcr.2015.08.008

Kourouklis, A. P., Kaylan, K. B., and Underhill, G. H. (2016). Substrate stiffness and matrix composition coordinately control the differentiation of liver progenitor cells. *Biomaterials* 99, 82–94. doi: 10.1016/j.biomaterials.2016.05.016

Loarca, L., De Assuncao, T. M., Jalan-Sakrikar, N., Bronk, S., Krishnan, A., Huang, B., et al. (2017). Development and characterization of cholangioids from normal and diseased human cholangiocytes as an *in vitro* model to study primary sclerosing cholangitis. *Lab. Invest.* 97, 1385–1396. doi: 10.1038/labinvest.2017.63

Lutolf, M. P., and Hubbell, J. A. (2003). Synthesis and physicochemical characterization of end-linked poly(ethylene glycol)-co-peptide hydrogels formed by Michael-type addition. *Biomacromolecules* 4, 713–722. doi: 10.1021/bm025744e

Manninen, A. (2015). Epithelial polarity–generating and integrating signals from the ECM with integrins. *Exp. Cell Res.* 334, 337–349. doi: 10.1016/j.yexcr.2015.01.003

Martin-Belmonte, F., Yu, W., Rodriguez-Fraticelli, A. E., Ewald, A. J., Werb, Z., Alonso, M. A., et al. (2008). Cell-polarity dynamics controls the mechanism of lumen formation in epithelial morphogenesis. *Curr. Biol.* 18, 507–513. doi: 10.1016/j.cub.2008.02.076

McAteer, J. A., Dougherty, G. S., Gardner, K. D. Jr., and Evan, A. P. (1986). Scanning electron microscopy of kidney cells in culture: surface features of polarized epithelia. *Scan. Electron Microsc.* 1986(Pt 3), 1135–1150.

Mosiewicz, K. A., Kolb, L., A. J., van der Vlies, Martino, M. M., Lienemann, P. S., Hubbell, J. A., et al. (2013). *In situ* cell manipulation through enzymatic hydrogel photopatterning. *Nat. Mater.* 12, 1072–1078. doi: 10.1038/nmat3766

Mueller, S., and Sandrin, L. (2010). Liver stiffness: a novel parameter for the diagnosis of liver disease. *Hepat. Med.* 2, 49–67. doi: 10.2147/HMER.S7394

Murray, K. F., Carithers, R. L. Jr., and AASLD (2005). AASLD practice guidelines: evaluation of the patient for liver transplantation. *Hepatology* 41, 1407–1432. doi: 10.1002/hep.20704

Neufeld, T. K., Douglass, D., Grant, M., Ye, M., Silva, F., Nadasdy, T., et al. (1992). *In vitro* formation and expansion of cysts derived from human renal cortex epithelial cells. *Kidney Int.* 41, 1222–1236. doi: 10.1038/ki.1992.184

O'Brien, L. E., Zegers, M. M., and Mostov, K. E. (2002). Opinion: building epithelial architecture: insights from three-dimensional culture models. *Nat. Rev. Mol. Cell. Biol.* 3, 531–537. doi: 10.1038/nrm859

Ogawa, M., Ogawa, S., Bear, C. E., Ahmadi, S., Chin, S., Li, B., et al. (2015). Directed differentiation of cholangiocytes from human pluripotent stem cells. *Nat. Biotechnol.* 33, 853–861. doi: 10.1038/nbt.3294

Patterson, J., and Hubbell, J. A. (2010). Enhanced proteolytic degradation of molecularly engineered PEG hydrogels in response to MMP-1 and MMP-2. *Biomaterials* 31, 7836–7845. doi: 10.1016/j.biomaterials.2010.06.061

Raeber, G. P., Lutolf, M. P., and Hubbell, J. A. (2005). Molecularly engineered PEG hydrogels: a novel model system for proteolytically mediated cell migration. *Biophys. J.* 89, 1374–1388. doi: 10.1529/biophysj.104.050682

Ranga, A., Girgin, M., Meinhardt, A., Eberle, D., Caiazzo, M., Tanaka, E. M., et al. (2016). Neural tube morphogenesis in synthetic 3D microenvironments. *Proc. Natl. Acad. Sci. U.S.A.* 113, E6831–E6839. doi: 10.1073/pnas.1603529113

Ranga, A., Gobaa, S., Okawa, Y., Mosiewicz, K., Negro, A., Lutolf, M., et al. (2014). 3D niche microarrays for systems-level analyses of cell fate. *Nat. Commun.* 5:4324. doi: 10.1038/ncomms5324

Raynaud, P., Carpentier, R., Antoniou, A., and Lemaigre, F. P. (2011). Biliary differentiation and bile duct morphogenesis in development and disease. *Int. J. Biochem. Cell Biol.* 43, 245–256. doi: 10.1016/j.biocel.2009.07.020

Raza, A., Ki, C. S., and Lin, C. C. (2013). The influence of matrix properties on growth and morphogenesis of human pancreatic ductal epithelial cells in 3D. *Biomaterials* 34, 5117–5127. doi: 10.1016/j.biomaterials.2013.03.086

Rizki-Safitri, A., Shinohara, M., Miura, Y., Danoy, M., Tanaka, M., Miyajima, A., et al. (2018). Efficient functional cyst formation of biliary epithelial cells using microwells for potential bile duct organisation *in vitro*. *Sci Rep* 8:11086. doi: 10.1038/s41598-018-29464-w

Roskams, T. A., Theise, N. D., Balabaud, C., Bhagat, G., Bhathal, P. S., Bioulac-Sage, P., et al. (2004). Nomenclature of the finer branches of the biliary tree: canals, ductules, and ductular reactions in human livers. *Hepatology* 39, 1739–1745. doi: 10.1002/hep.20130

Sampaziotis, F., de Brito, M. C., Madrigal, P., Bertero, A., Saeb-Parsy, K., Soares, F. A. C., et al. (2015). Cholangiocytes derived from human induced pluripotent stem cells for disease modeling and drug validation. *Nat. Biotechnol.* 33, 845–852. doi: 10.1038/nbt.3275

Saneyasu, T., Akhtar, R., and Sakai, T. (2016). Molecular cues guiding matrix stiffness in liver fibrosis. *Biomed. Res. Int.* 2016:2646212. doi: 10.1155/2016/2646212

Schuppan, D., Surabattula, R., and Wang, X. Y. (2018). Determinants of fibrosis progression and regression in NASH. *J. Hepatol.* 68, 238–250. doi: 10.1016/j.jhep.2017.11.012

Shiojiri, N., and Sugiyama, Y. (2004). Immunolocalization of extracellular matrix components and integrins during mouse liver development. *Hepatology* 40, 346–355. doi: 10.1002/hep.20303

Soroka, C. J., Assis, D. N., and Boyer, J. L. (2019). Patient-derived organoids from human bile: an *in vitro* method to study cholangiopathies. *Methods Mol. Biol.* 1981, 363–372. doi: 10.1007/978-1-4939-9420-5_24

Takayama, K., Mitani, S., Nagamoto, Y., Sakurai, F., Tachibana, M., Taniguchi, Y., et al. (2016). Laminin 411 and 511 promote the cholangiocyte differentiation of human induced pluripotent stem cells. *Biochem. Biophys. Res. Commun.* 474, 91–96. doi: 10.1016/j.bbrc.2016.04.075

Takebe, T., Zhang, R. R., Koike, H., Kimura, M., Yoshizawa, E., Enomura, M., et al. (2014). Generation of a vascularized and functional human liver from an iPSC-derived organ bud transplant. *Nat. Protoc.* 9, 396–409. doi: 10.1038/nprot.2014.020

Tan, J. L., Tien, J., Pirone, D. M., Gray, D. S., Bhadriraju, K., Chen, C., et al. (2003). Cells lying on a bed of microneedles: an approach to isolate mechanical force. *Proc. Natl. Acad. Sci. U.S.A.* 100, 1484–1489. doi: 10.1073/pnas.0235407100

Tanimizu, N., Miyajima, A., and Mostov, K. E. (2007). Liver progenitor cells develop cholangiocyte-type epithelial polarity in three-dimensional culture. *Mol. Biol. Cell* 18, 1472–1479. doi: 10.1091/mbc.e06-09-0848

Torkko, J. M., Manninen, A., Schuck, S., and Simons, K. (2008). Depletion of apical transport proteins perturbs epithelial cyst formation and ciliogenesis. *J. Cell. Sci.* 121(Pt 8), 1193–1203. doi: 10.1242/jcs.015495

Townley, A. K., Schmidt, K., Hodgson, L., and Stephens, D., J. (2012). Epithelial organization and cyst lumen expansion require efficient Sec13-Sec31-driven secretion. *J. Cell. Sci.* 125(Pt 3), 673–684. doi: 10.1242/jcs.091355

Unadkat, H. V., Hulsman, M., Cornelissen, K., Papenburg, B. J., Truckenmuller, R. K., Carpenter, A. E., et al. (2011). An algorithm-based topographical biomaterials library to instruct cell fate. *Proc. Natl. Acad. Sci. U.S.A.* 108, 16565–16570. doi: 10.1073/pnas.1109861108

Vroman, B., and LaRusso, N. F. (1996). Development and characterization of polarized primary cultures of rat intrahepatic bile duct epithelial cells. *Lab. Invest.* 74, 303–313.

Wells, R. G. (2008). The role of matrix stiffness in regulating cell behavior. *Hepatology* 47, 1394–1400. doi: 10.1002/hep.22193

Yeh, W. C., Li, P. C., Jeng, Y. M., Hsu, H. C., Kuo, P. L., Li, M. L., et al. (2002). Elastic modulus measurements of human liver and correlation with pathology. *Ultrasound Med. Biol.* 28, 467–474. doi: 10.1016/S0301-5629(02)00489-1

Yu, W., Fang, X., Ewald, A., Wong, K., Hunt, C. A., Werb, Z., et al. (2007). Formation of cysts by alveolar type II cells in three-dimensional culture reveals a novel mechanism for epithelial morphogenesis. *Mol. Biol. Cell* 18, 1693–1700. doi: 10.1091/mbc.e06-11-1052

Conflict of Interest: The authors declare that the research was conducted in the absence of any commercial or financial relationships that could be construed as a potential conflict of interest.

frontiers in Bioengineering and Biotechnology

REVIEW
published: 24 January 2020
doi: 10.3389/fbioe.2019.00474

Impedance Spectroscopy as a Tool for Monitoring Performance in 3D Models of Epithelial Tissues

Tatiana Gerasimenko[1†], *Sergey Nikulin*[1,2†], *Galina Zakharova*[3], *Andrey Poloznikov*[2,4], *Vladimir Petrov*[1,5], *Ancha Baranova*[6,7,8*] *and Alexander Tonevitsky*[9,10,11]

[1] *Scientific Research Centre Bioclinicum, Moscow, Russia,* [2] *Laboratory of Microphysiological Systems, School of Biomedicine, Far Eastern Federal University, Vladivostok, Russia,* [3] *Laboratory of Molecular Oncoendocrinology, Endocrinology Research Centre, Moscow, Russia,* [4] *Department of Translational Oncology, National Medical Research Radiological Center of the Ministry of Health of the Russian Federation, Obninsk, Russia,* [5] *Department of Development and Research of Micro- and Nanosystems, Institute of Nanotechnologies of Microelectronics RAS, Moscow, Russia,* [6] *School of Systems Biology, George Mason University, Fairfax, VA, United States,* [7] *Laboratory of Molecular Genetics, Moscow Institute of Physics and Technology, Dolgoprudny, Russia,* [8] *Laboratory of Functional Genomics, "Research Centre for Medical Genetics", Moscow, Russia,* [9] *Faculty of Biology and Biotechnologies, Higher School of Economics, Moscow, Russia,* [10] *Laboratory of Microfluidic Technologies for Biomedicine, Shemyakin-Ovchinnikov Institute of Bioorganic Chemistry RAS, Moscow, Russia,* [11] *art photonics GmbH, Berlin, Germany*

OPEN ACCESS

Edited by:
Elena Martinez, Institute for Bioengineering of Catalonia (IBEC), Spain

Reviewed by:
Abhigyan Satyam, Harvard Medical School, United States
Huseyin Cumhur Tekin, Izmir Institute of Technology, Turkey

***Correspondence:**
Ancha Baranova
abaranov@gmu.edu

[†] These authors have contributed equally to this work and share first authorship

Specialty section:
This article was submitted to Tissue Engineering and Regenerative Medicine, a section of the journal Frontiers in Bioengineering and Biotechnology

Received: *08 October 2019*
Accepted: *23 December 2019*
Published: *24 January 2020*

Citation:
Gerasimenko T, Nikulin S, Zakharova G, Poloznikov A, Petrov V, Baranova A and Tonevitsky A (2020) Impedance Spectroscopy as a Tool for Monitoring Performance in 3D Models of Epithelial Tissues. Front. Bioeng. Biotechnol. 7:474. doi: 10.3389/fbioe.2019.00474

In contrast to traditional 2D cell cultures, both 3D models and organ-on-a-chip devices allow the study of the physiological responses of human cells. These models reconstruct human tissues in conditions closely resembling the body. Translation of these techniques into practice is hindered by associated labor costs, a need which may be remedied by automation. Impedance spectroscopy (IS) is a promising, automation-compatible label-free technology allowing to carry out a wide range of measurements both in real-time and as endpoints. IS has been applied to both the barrier cultures and the 3D constructs. Here we provide an overview of the impedance-based analysis in different setups and discuss its utility for organ-on-a-chip devices. Most attractive features of impedance-based assays are their compatibility with high-throughput format and supports for the measurements in real time with high temporal resolution, which allow tracing of the kinetics. As of now, IS-based techniques are not free of limitations, including imperfect understanding of the parameters that have their effects on the impedance, especially in 3D cell models, and relatively high cost of the consumables. Moreover, as the theory of IS stems from electromagnetic theory and is quite complex, work on popularization and explanation of the method for experimental biologists is required. It is expected that overcoming these limitations will lead to eventual establishing IS based systems as a standard for automated management of cell-based experiments in both academic and industry environments.

Keywords: impedance spectroscopy, TEER, epithelium, barrier tissues, 3D cell culture models, organs-on-a-chip, microfluidic devices, label-free monitoring

INTRODUCTION

In vitro cell models are indispensable as the tools of modern biology and medicine; these models are widely used in studies of molecular pathogenesis and metabolism of bioactive compounds (Astashkina et al., 2012; Caicedo-Carvajal et al., 2012; Marx et al., 2016). Nowadays, cell-based models have gained their popularity as a replacement for laboratory animals, especially in the area of drug discovery, where these models improved productivity in a cost efficient way (Doke and Dhawale, 2015; Poloznikov et al., 2018). Recently, traditional 2D cell culture models have evolved into 3D tissue-engineered scaffolds, organ-on-a-chip platforms and organoid test beds (Marx et al., 2016; Dehne et al., 2017; Maschmeyer et al., 2017; Spielmann and Marx, 2017; Torras et al., 2018). These physiologically relevant systems allow experiments with various human cells in conditions resembling the ones found in the human body. It is important to recognize that human-based 3D models and organ-on-a-chip devices provide several advantages over animal testing as human biological processes differ from those in a typical laboratory animal, the majority of which are rodents. Moreover, these models open up the possibilities for personalized testing.

Currently, monitoring of a cell's state mainly depends on assaying various endpoints require introducing one or another type of label. Endpoint assessment techniques are laborious, expensive and often disruptive, as they require a portion of biological material collected before each test. Hence, the recent advent of real-time label-free assays is not surprising (Limame et al., 2012; Single et al., 2015). Non-invasive, label-free longitudinal monitoring of cell states is a key component for the development of automated microphysiological systems slated to be eventually adopted by industry.

Impedance spectroscopy (IS) is a label-free technique suitable for quantification of cell properties in real time. One of the common applications of impedance measurement is quality control (QC) for *in vitro* models of barrier tissues. Being compatible with a variety of culture formats, IS has already found its way into organs-on-a-chip devices. Here we review applications of impedance spectroscopy with special attention to 3D cell culture formats and 3D structures formed by barrier tissues.

BASIC THEORY OF IMPEDANCE SPECTROSCOPY

Impedance is a generalization of the concept of "resistance" in the case of an alternating current. By definition, impedance is a proportionality factor between the alternating voltage V with frequency f applied to the system under investigation and the electric current I flowing through it:

$$Z(f) = \frac{V(f)}{I(f)}$$

Since the conventional description of alternating current and voltage involves complex numbers, impedance is also a complex quantity, which may be written as follows (Cartesian form):

$$Z = \mathrm{Re}[Z] + j\mathrm{Im}[Z],$$

where Re[Z] and Im[Z] are the real and imaginary parts, $\boldsymbol{j}$ is the imaginary unit ($j^2 = -1$). The equivalent polar form can also be used:

$$Z = |Z|\, e^{j\phi}$$

The absolute value $|Z|$ of impedance and phase shift between current and voltage φ are related to the real and imaginary parts of impedance as follows (**Figure 1**):

$$|Z| = \sqrt{\mathrm{Re}[Z]^2 + \mathrm{Im}[Z]^2}$$
$$\varphi = \arctan\frac{\mathrm{Im}[Z]}{\mathrm{Re}[Z]}$$

The real part of impedance is responsible for dissipation of energy in the system (active resistance). The imaginary part describes electrical capacitance and induction of the system. When the imaginary part is not equal to zero, there is a phase shift between current and voltage (**Figure 2**). The magnitude of the shift also depends on the real part of impedance.

Impedance depends on the frequency of the applied voltage; therefore, in order to obtain comprehensive information on the system, one has to scan a range of frequencies in order to generate so-called impedance spectrum. A typical example of such a spectrum of a cell monolayer growing on a semipermeable membrane is depicted in **Figure 3**. As one can see, in this case both real and imaginary parts of the impedance change with the change of frequency. Importantly, the dependency of imaginary part on frequency is not monotonous. Analysis of the obtained impedance spectra often includes construction of Nyquist plot that reflects the dependence of -Im[Z] on Re[Z]. This type of graphs facilitates interpretation of resultant data, each configurations of the studied model systems will be recognized by a characteristic shape of observed impedance spectrum.

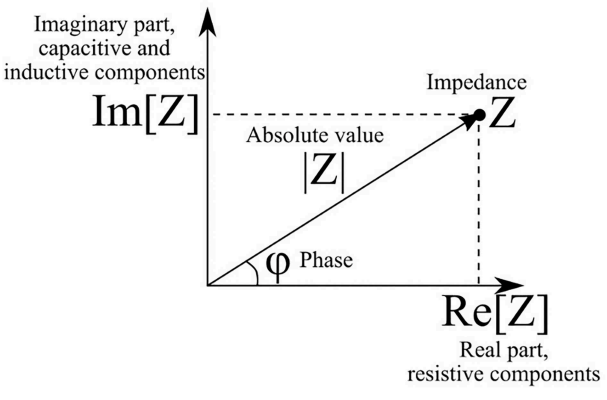

FIGURE 1 | Phasor diagram of complex impedance (illustrates the relationship between Cartesian and polar representations of complex number).

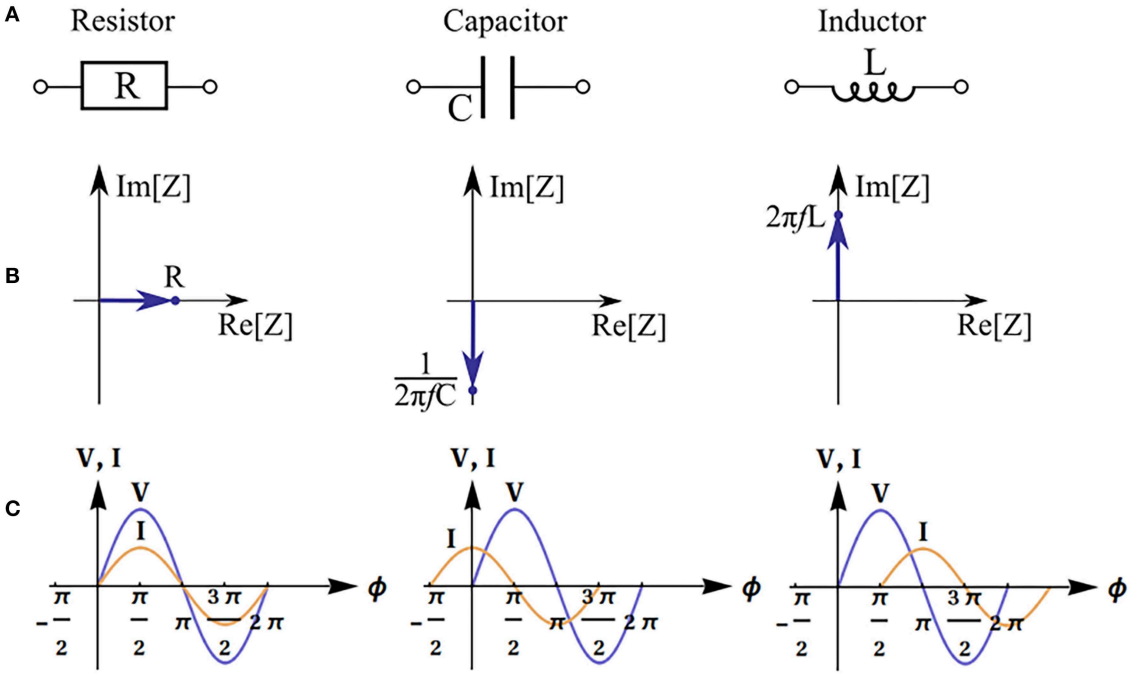

FIGURE 2 | Impedance of basic equivalent circuit components: resistor, capacitor and inductor. Electronic schematic symbols **(A)**, phasor diagrams and impedance values (f is the frequency) **(B)**, and illustration of phase shift between voltage (*V*) and current (*I*) (φ is the phase) **(C)**.

In the simplest case, a cell may be considered as a plasma membrane shell filled with cytoplasm (Morgan et al., 2007). Both the conductivity σ_{ct} and permittivity ε_{ct} of a living cell are assumed to be of the same order of magnitude as the properties of the surrounding extracellular liquid. At the same time, its membrane is considered as an insulator with permittivity $\varepsilon_m << \varepsilon_{ct}$ and conductivity $\sigma_m << \sigma_{ct}$. As the membrane of a dead cell becomes perforated, its ability to obstruct the traffic of ions would be lost. Therefore, its conductivity approaches that of the extracellular liquid (Fricke, 1924; Lvovich, 2012; Castellví, 2014).

One may examine directly the dependency of complex permittivity instead of impedance on frequency. Complex permittivity is a value that integrates permittivity and conductivity into a single value in the following manner:

$$\varepsilon(f) = \varepsilon'(f) + j\varepsilon''(f) = \varepsilon_r(f)\,\varepsilon_0 + j\frac{\sigma(f)}{2\pi f},$$

where ε_r is a relative permittivity and ε_0 is a dielectric constant. This approach, which is widely used to study electrical properties of various suspensions, relies on models that consider the dispersion of electromagnetic waves in a continuous medium (Schwan, 1994; Morgan et al., 2007; Sun et al., 2007). These models provide an insight into the physics of the system under study. A study of distributed parameters such as conductivity and permittivity requires quite complex mathematical apparatus; therefore, lumped parameter models are more attractive. As an example, one may consider conductivity as a resistance *R*:

$$\mathrm{Re}[Z] = R, \mathrm{Im}[Z] = 0$$

On the other hand, permittivity can be considered as a capacitor *C*:

$$\mathrm{Re}[Z] = 0, \mathrm{Im}[Z] = \frac{1}{j2\pi fC}$$

Here, the single-shell model (Xu et al., 2016) is used to describe each cell as an equivalent circuit (**Figure 4**), where C_m and R_m correspond to the cellular membrane, while C_{ct} and R_{ct} correspond to the cytoplasm. A typical value of membrane conductance per unit area is about 0.3 mS/cm^2, its specific capacitance is about 1 μF/cm^2, and the cytoplasm conductance σ_{ct} is about 0.005 S/cm^2 (Asami et al., 1996). The value of R_m is usually much greater than R_{ct}, while C_{ct} is much smaller than C_m. Because of that, analysis of the impedance is amenable to simplification by neglecting C_{ct} and R_m. At very high frequencies ($f > 100$ MHz), the cell membrane capacitance C_{ct} is effectively short-circuited, and the impedance is then determined by the cytoplasm resistance (Sun et al., 2008). More detailed information about single cell equivalent circuits can be found in a review (Xu et al., 2016). Yet another degree of simplification may be achieved by the replacement of the entire system under study by an equivalent circuit. In this case, the resulting impedance is expressed analytically in terms of the parameters of each separate element of the equivalent circuit, which, in turn, are estimated by fitting experimental data.

At the same time, the method of equivalent circuits implies a significant simplification of the processes that take place in real biological objects. This simplification is primarily due to

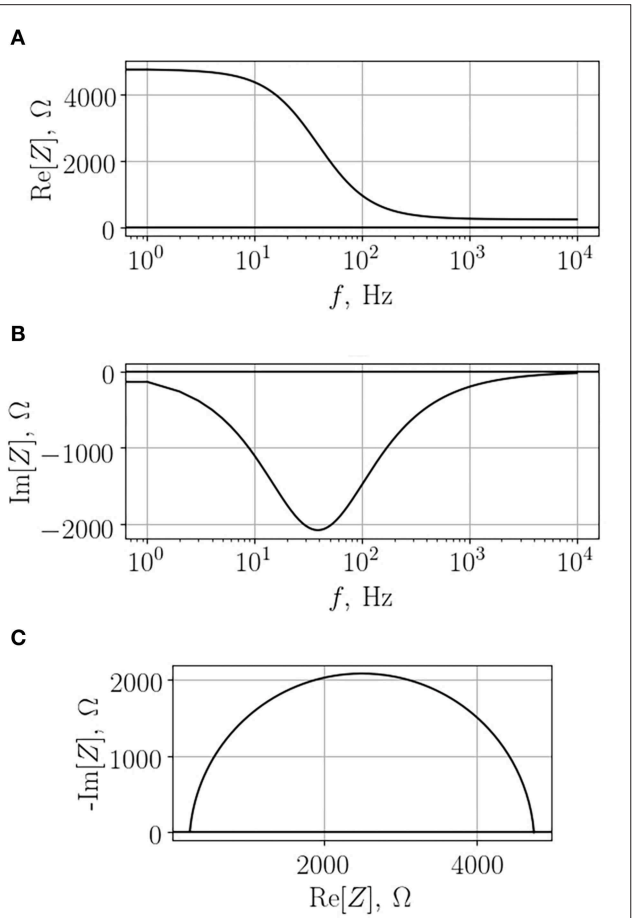

FIGURE 3 | Typical impedance spectrum of a cell monolayer grown on a semi-permeable membrane. The real part **(A)**, the imaginary part **(B)**, and the Nyquist diagram **(C)**.

the assumption of ideal electrical characteristics. The majority of impedance spectra may be described by more than one equivalent circuit. Selection of this circuit relies on initial judgment calls made by the researcher, which reflect his understanding of underlying biological processes. When the choice of the equivalent circuit is far from being optimal, the results may in fact end up incorrectly interpreted as well. Particular care is required when equivalent circuits incorporate large numbers of elements. In these cases, the relevance of a given circuit configuration is difficult to establish, even though excellent fitting of the data can be achieved (McAdams and Jossinet, 1996).

PRACTICAL ASPECTS OF IMPEDANCE MEASUREMENTS IN CELL CULTURE MODELS

The impedance measurement procedure should not significantly affect the state of the cells. This imposes certain restrictions on the characteristics of the electromagnetic fields used. In particular, transmembrane potential should remain significantly lower than the threshold value for membrane electroporation (250–350 mV). Typically, this restriction is not a problem, since such values of the membrane potential are usually achieved by external fields with a strength of the order of 1 kV/cm. It should be noted, however, that muscle and nerve cell membranes can be damaged with electrical fields as small as 60 V/cm (Lee, 2005). In addition, both relatively weak constant electric fields with field strengths about 0.1–10 V/cm and electromagnetic fields with extremely low frequency are capable of affecting cytoskeleton and cell shape, influencing migration, proliferation, and differentiation of at least some types of human cells (Funk and Monsees, 2006). Moreover, electrical fields of 1–10 V/cm applied to a cell of 10 μm in radius can change the membrane potential by as much as 1.5–15 mV, which, in turn, may alter the activity of some membrane channels (Mycielska and Djamgoz, 2004; Funk and Monsees, 2006; Taghian et al., 2015). Therefore, one has to ensure that applied voltage (or current) produces a field with the strength not exceeding specified values.

The choice of such specific values of applied voltage or current strongly depends on the spatial arrangement of electrodes and cells, resistance of culture medium and number of cells. As a rule of thumb, investigations of suspensions and *in vitro* models of barrier tissues call for relatively small currents of about tens of μA (Gitter et al., 2000; Krug et al., 2009). In the case of 3D cultures, voltages of 10–100 mV may be applicable (Thielecke et al., 2001b; Canali et al., 2015a). On the other hand, in microfluidic devices, due to a significant voltage drop observed in microchannels, the potential difference across the electrodes can reach 0.1–0.5 V (Gawad et al., 2001; van der Helm et al., 2016).

In a majority of applications of impedance spectroscopy to living matter, electrodes are placed in direct contact with culturing medium. In this case the interface between the medium and the electrode should be included into complete equivalent circuit of the system under study. The interactions between electrode and medium are usually described by an equivalent circuit shown at **Figure 5** (Grafov and Ukshe, 1973) where R_{el} is a charge transfer resistance, $Z_W = \frac{W_F}{\sqrt{2\pi f}}\ (1-j)$ is an impedance of Warburg element describing a Gouy-Chapman diffusive layer, and W_F is the Warburg constant. The Helmholtz double-layer is usually modeled by a capacitor C_{dl}. (**Figure 5A**); however, in some cases, a constant phase element (CPE) $Z_{CPE} = \frac{A}{(2\pi f)^\alpha}\left(\cos\frac{\pi\alpha}{2} - j\sin\frac{\pi\alpha}{2}\right)$ with $A > 0$ and $0 \leq \alpha \leq 1$ as constant values may be used instead (**Figure 5B**) (Moulton et al., 2004; Chang et al., 2007; Yang et al., 2008). A review of Chassagne et al. (2016) delves into a detailed theory of electrode polarization processes as well as ways to compensate them. In particular, a four-electrode scheme helps to eliminate the influence of interface between the electrode and the medium on data output (Amini et al., 2018).

Both the shape and the size of an electrode are of extreme importance. Generally speaking, each experimental setting requires electrodes of specific shape and size, with particular designs being guided by theoretical calculations (Franks et al., 2005; Abdur Rahman et al., 2007; Alexander et al., 2010; MacKay et al., 2015). In the case of rod-shaped electrodes, the results of the

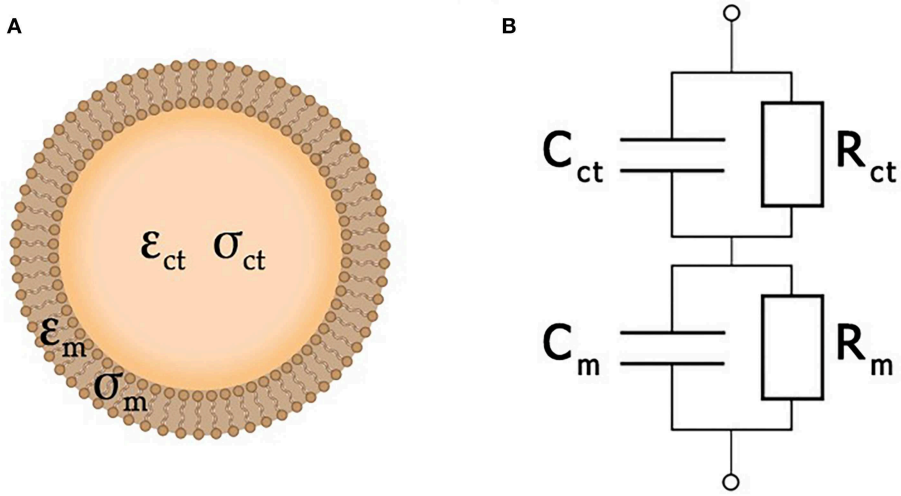

FIGURE 4 | A simplified cell structure **(A)** and its equivalent circuit **(B)**.

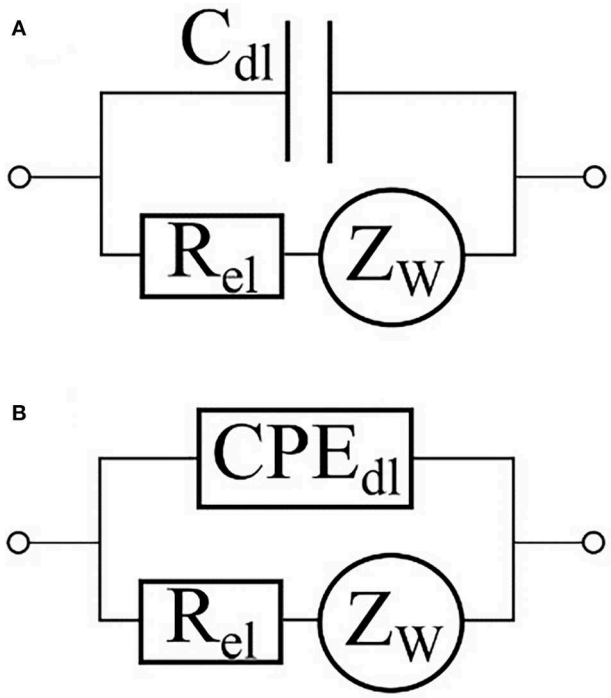

FIGURE 5 | Equivalent circuits of an electrode-electrolyte interface. The double-layer capacity is represented either by a capacitor **(A)** or by a constant phase element **(B)**.

measurements may be influenced by the relative positioning of electrodes and the distance to the studied monolayer (Srinivasan et al., 2015). Moreover, since Helmholtz double layer impedance is inversely proportional to the surface area, in the case of microelectrodes, this effect may lead to very large impedances, particularly at low frequencies (Alexander et al., 2019). One of the possibilities to overcome this problem is to add 3D micro- or nanostructures on top of the sensing electrodes as it is described in details (Decker et al., 2018).

Therefore, in order to decrease the impact of this interface, the electrode area should be as large as possible. Another important factor which decreases the accuracy of the measurement is the background noise caused by chemical processes taking place on the surface of the electrode. This noise is especially important when the magnitude of the signal is low. Increasing the surface area of the electrodes allows electrode-electrolyte interface noise to be lowered (Huigen et al., 2002).

As impedance-measuring electrodes function in close proximity to the living cells, the electrode material should not cause any toxic effect and remain chemically and physically stable across the experiment. Gold, platinum, palladium, and titanium are the materials of choice (Hoffmann et al., 2006; Riistama and Lekkala, 2006; Pliquett et al., 2010; Howlader et al., 2013), with some researchers experimenting with indium tin oxide, nickel, ultra-nanocrystalline diamond, and electrolyte solutions (Xu et al., 2016). Silver chloride electrodes have become a primary component of many electrochemical chambers due to their low cost and stable potential (Shinwari et al., 2010). However, the contact with biological media greatly enhances erosion of such electrodes, causing the loss of AgCl coating, leading to a change of electrode potential and marked cytotoxicity. Even with the development of stabilizing coatings (Kaji et al., 1995; Polk et al., 2006; Riistama and Lekkala, 2006; Shinwari et al., 2010), these electrodes are less biocompatible than the ones based on gold, platinum and titanium. However, it is still true to say that silver chloride electrodes are useful for short time measurements. For example, STX-electrodes compatible with EVOM^2 (World Precision Instruments) are made from silver/silver chloride. It is also worth noting that some powder metallurgy-produced titanium alloys containing Mo, Nb, or Si show a certain degree of cytotoxicity (Li et al., 2010).

INVESTIGATIONS OF BARRIER FUNCTIONS

A characteristic feature of epithelial and endothelial cells is their ability to form tight junctions. Monolayers of tightly connected cells create a selectively permeable interface between apical and basal compartments, thus controlling diffusion and transport of chemical substances (Benson et al., 2013). The integrity of this barrier is vital for normal physiological functionality of the tissue. In order to deliver therapeutic agents to the targeted organs, this barrier has to be penetrated, but not destroyed. In studies of the permeability of epithelial and endothelial barriers, cells are often grown on semipermeable membranes (**Figure 6**), where the integrity of the cell monolayers could be controlled non-invasively, by measuring trans-epithelial resistance (TEER) (Samatov et al., 2015; Srinivasan et al., 2015). TEER measurements are commonly utilized for monitoring of conventional 2D cultures of epithelial cell lines such as Caco-2 and HT-29 (Hilgendorf et al., 2000). Their applicability for *in vitro* models of barrier tissues derived from primary 3D organoids has been discussed as well (Moon et al., 2014).

In a typical TEER unit, cells grow on a semipermeable membrane with the electrodes placed in apical and basal compartments separated by monolayer. In a unit depicted at **Figure 6**, two electrodes provide current, and two other electrodes measure voltage. In some other designs, employing only two electrodes, one of them is placed in the basal and another one—in the apical compartment (Bragós et al., 2006; Yufera and Rueda, 2008). In theory, monolayer integrity could be probed with the direct current, but the polarization of electrodes and the monolayer itself provided by constant electric field calls for use of an alternating current at a low frequency (about 10 Hz). For example, EVOM^2 (World Precision Instruments) and Millicell ERS-2 (EMD Millipore Corporation) devices, which can be used in conjunction with a chopstick silver/silver chloride electrode, operate at a single frequency of 12.5 Hz and current 10 μA, providing information on TEER. EVOM^2 is also compatible with EndOhm chamber (World Precision Instruments) which contains a pair of concentric electrodes, including a voltage-sensing silver/silver chloride pellet in the center and an annular current electrode around it. Symmetrical arrangement allows to generate uniform current density across the membrane, and, therefore, preferable for chopstick electrodes (Srinivasan et al., 2015).

Replacement of measurements at a single frequency with impedance spectroscopy provides an opportunity to collect

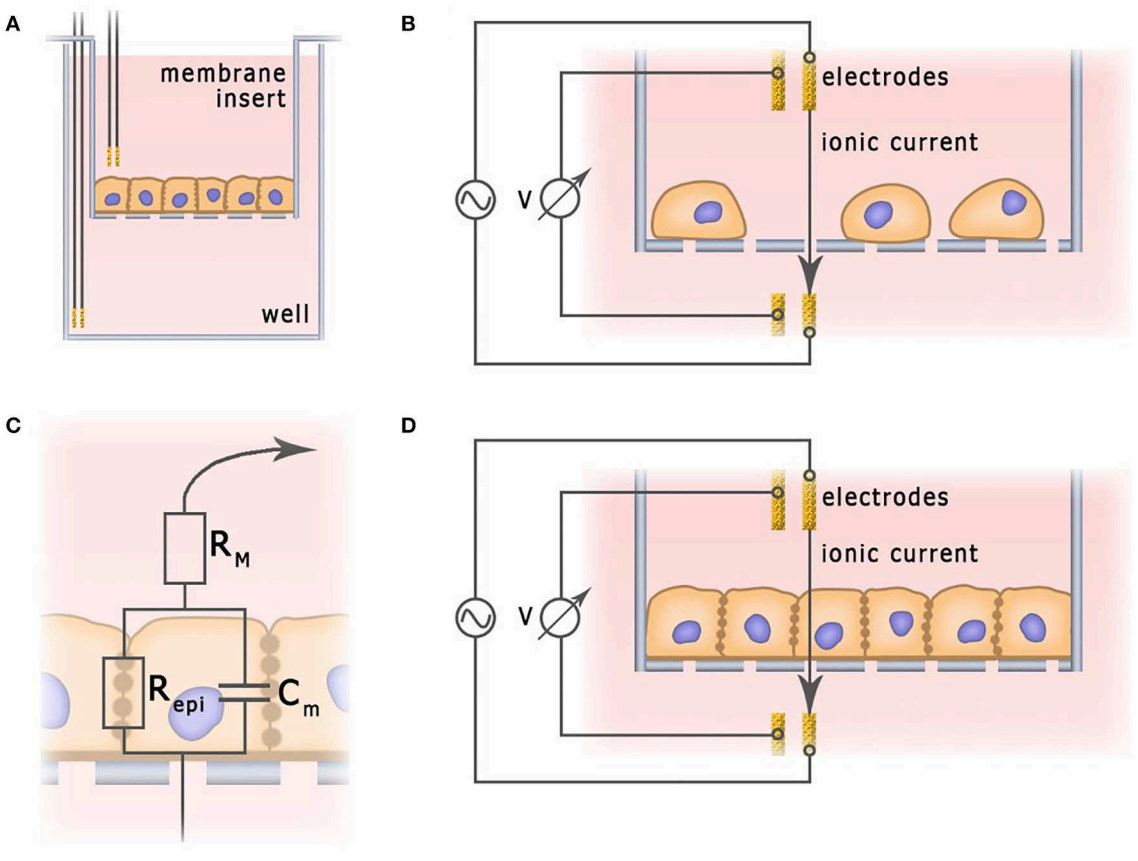

FIGURE 6 | Application of impedance spectroscopy for the measurement of barrier functions. **(A)** Typical electrochemical cell of trans-epithelial resistance measurement. **(B)** Current flow through undifferentiated low density cell culture. **(C)** Simplified equivalent circuit of cellular monolayer. **(D)** Current flow through fully differentiated cell culture.

additional information describing various properties of monolayer in question. Depending on particular equivalence circuit, one or another set of parameters may be collected. In barrier cultures, both membrane resistance and cytoplasm capacitance are negligible (**Figure 7**). In the simplest case (**Figure 7A**) the monolayer is represented as a resistor and a capacitor in parallel. The capacitor C_m corresponds to the membrane contribution whereas the resistor R_{epi} reflects the transport through the cell and tight junctions. For this circuit C_m, both R_{epi} and R_M can be determined directly from the Nyquist plot of the impedance spectrum (**Figure 7D**) (Schifferdecker and Frömter, 1978; Fromm et al., 1985). This model is especially useful when the loss of barrier function occurs simultaneously with the increase of subepithelial resistance, for instance, in course of intestinal tissue inflammation (Bürgel et al., 2002; Zeissig et al., 2007). It is worth to note that fitting of experimental impedance spectra may be improved by replacing the capacitor C_m with a constant phase element (CPE) described by parameters A and α (Cole, 1932; Grimnes and Martinsen, 2005, 2015; Lazarevi and Caji, 2015).

When equivalent circuits become more elaborate (**Figure 7B**), a direct estimation of all unknown parameters from the impedance spectrum becomes impossible, thus, requiring additional measurements. For example, in the study of paracellular transport modulated by addition of egtazic acid (EGTA), R_{trans} and R_{para} parameters were sorted out with an aid of complementary measurements of a fluorescein flux (Krug et al., 2009). The contributions of the apical and basolateral membranes (**Figure 7C**) can be dissected if their time constants ($\tau_{ap} = R_{ap}C_{ap}$ and $\tau_{bl} = R_{bl}C_{bl}$) differ substantially (Sackin and Palmer, 2013). As an example, an exposure to nystatin has selectively shown an increase in Na+, K+, and Cl– conductivity of an apical membrane by several orders of magnitude (Lewis, 1977; Wills et al., 1979), therefore decreasing its time constant. Another example of similarly designed experiment would be an activation of cAMP-dependent channels of apical membranes by forskolin (Krug et al., 2009). The influence of the latter on the impedance spectra is described in Păunescu and Helman (2001). A more complex apical/basal discrimination technique requires direct insertion of electrodes into the cells (Frömter and Diamond, 1972; Schifferdecker and Frömter, 1978; Kottra and Frömter, 1984). To collect detailed information on the local conditions within particular places of the monolayer, microscopic scanning electrodes may be placed a micrometer away from its apical surface (Cereijido et al., 1980; Gitter et al., 1997, 2000). This technique allows quantifying local variations in the current density, which reflect the state of the monolayer at each particular point while discriminating electrical properties of the cells and the tight junctions.

To date, several IS systems were designed and implemented in investigations of barrier cell cultures. For example, cellZscope systems (nanoAnalytics GmbH) relies on a single-piece stainless steel bottom electrode "pots" used both as reservoirs for culture medium, and as a support for membrane inserts (Veltman

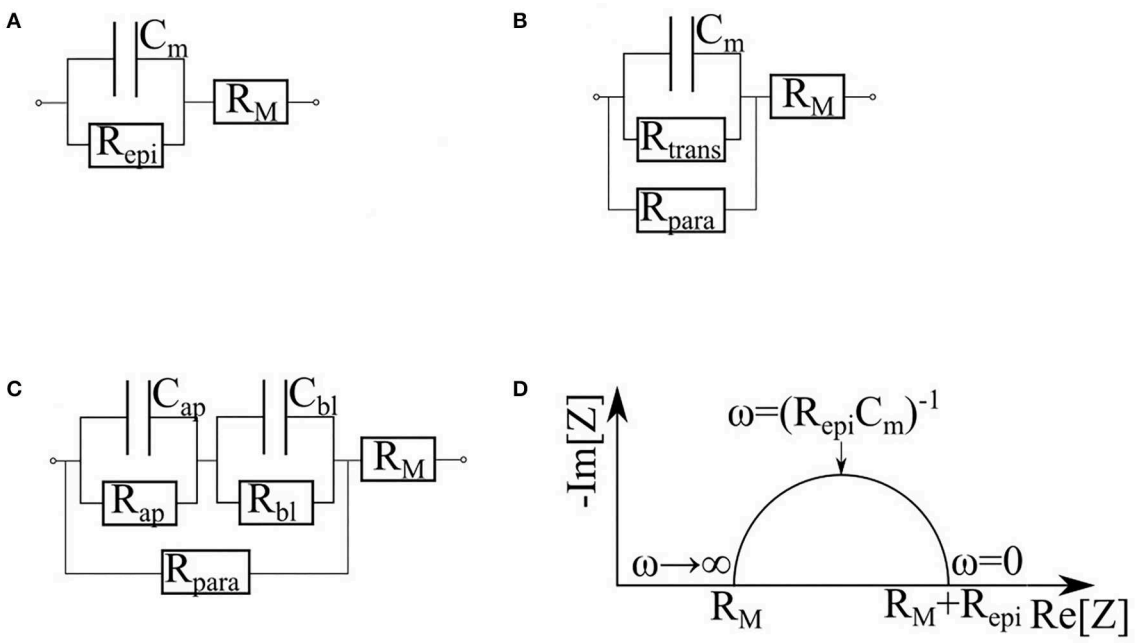

FIGURE 7 | Various equivalent circuits representing the cell, based on (Krug et al., 2009). R_M is the sum of subepithelial resistance, medium resistance and semipermeable membrane resistance. **(A)** The simplest equivalent circuit, which does not differentiate cytoplasm and tight junctions. R_{epi} is the trans-epithelial resistance. C_m is the membrane capacitance. **(B)** Circuit dividing the current flowing through the cells (R_{trans}) and through the tight junctions (R_{para}). **(C)** Circuit which represents contribution of apical and basal membranes separately (R_{ap}, C_{ap} and R_{bl}, C_{bl} correspond to the apical and basal membrane respectively). **(D)** Nyquist plot of cell monolayer.

et al., 2012; Valere et al., 2015). A lid of this "pot" serves as upper electrode, which generates uniform electric field across the membrane inserts. The device operates at frequency range between 1 Hz and 100 kHz, and provides information on TEER, medium resistance and capacitance of cell monolayer. Another IS systems, which is compatible with standard commercially available electrodes for 96-well membrane inserts, was recently developed by our team (Nikulin et al., 2019a,b).

Usually the same electrode layouts as for TEER measurements are used for impedance profiling. However, high cell resistance at low frequencies may result in low measured currents and high levels of noise. To overcome this problem, the laboratory of Dr. Owens (Jimison et al., 2012; Ramuz et al., 2014; Rivnay et al., 2015) replaced conventional electrodes with organic electrochemical transistors (OECT), and used them to measure the integrity of the barrier tissue. In the OECT, there is no direct measurement of the resistance across the cell monolayer. The drain current depends on the speed at which the transistor reaches steady state. Utilization of both the gate and drain current of an OECT allowed the authors to perform frequency-dependent impedance measurements over a broad range of frequencies while collecting high quality data at low frequencies.

When integrated into microfluidic organ-on-a-chip devices, impedance measuring electrodes allow long-term monitoring of the cultured cells in a controlled environment (Douville et al., 2010; Booth and Kim, 2012; Griep et al., 2013; Huang et al., 2014; Walter et al., 2016). The size constraint, which is common with respect to microfluidic platforms, dictates the placement of electrodes in close proximity to the cells. When the electrodes are located too close to the cell monolayer, the resultant electric field is far from being uniform. Therefore, the impact of each cell at the total TEER values depends on the position of a given cell along the electrodes, and overall cell confluence. As it has been demonstrated by Odijk et al. (2015), in microfluidic chips, TEER values obtained for the same type of cells may vary greatly, and are often different from those measured in Transwell systems.

The subsequent electrical impedance simulation method proposed by Odijk et al. (2015) was developed by the same scientific group (van der Helm et al., 2019) to normalize the cell layer resistance to TEER. The microfluidic chip was modeled, as a distributed electrical network comprised of different of elements, corresponding to culture medium, electrode, cell layer, and semipermeable membrane. The epithelial resistance derived from simulated impedance spectra was plotted against the input TEER, resulting in a calibration curve, giving the possibility of obtaining the TEER values from experimentally determined resistance. Yeste et al. (2016) suggested that TEER values should be calculated using a so-called geometric correction factor (GCF):

$$GCF = \frac{TEER_t}{TEER_s}$$

where $TEER_s$ is the $TEER$ value obtained from mathematical simulation and $TEER_t$ is used as a parameter for the electrical conductivity of the small volume in the middle of the two chambers, which represents a cell layer.

In our own studies, an organ-on-a-chip platform called "Homunculus" was recently upgraded to include an impedance spectroscopy system for real-time monitoring of the barrier function (Sakharov et al., 2017). In this device, prefabricated multi-well microfluidic chips for the co-culture of intestinal and placental barrier tissues with non-barrier cells such as hepatocytes include electrodes (Marx et al., 2016; Poloznikov et al., 2018). Utilization of this type of chip greatly reduces the time and effort of impedance measurements, providing integrative estimation of intestinal permeability while quantifying the rates of biotransformation and profiling the toxicity of tested compounds. Another organ-on-a-chip combination of the TEER impedance measurement system with microelectrode array (MEA) aimed to model the endothelialized myocardium (Maoz et al., 2017). In this system a microfluidic chip, porous PET membrane separates two microchannels. An apical chamber holds endothelial cells, while cardiomyocytes populate a basal channel. The dual sensor system (TEER-MEA) allows monitoring of the endothelial barrier function and electrical activity of the cardiomyocytes within the same device.

In contrast to conventional TEER measurements, impedance spectroscopy provides a window into overall well-being and the stage of differentiation acquired by 3D structures formed by barrier cells. For example, it has been shown that in the first few days after the seeding of cells, the TEER values peak, then decrease along with differentiation (Henry et al., 2017; Nikulin et al., 2018), possibly due to the appearance of villi and microvilli on the surface of the membrane (Geens and Niewold, 2011; van der Helm et al., 2019). On the other hand, the capacitance increases continuously during cell growth, due to the gradual increase of the area of the cell membrane (**Figure 8A**) (Henry et al., 2017; Nikulin et al., 2018; van der Helm, 2018; van der Helm et al., 2019). Thus, simultaneous measuring of TEER and electrical capacitance may adequately report about the degree of differentiation in culture.

Some cultures of epithelial barrier cells are known to form 3D multilayer structures, which may be represented by several parallel resistor-capacitor (or CPE)-circuits. Analysis of these circuits may provide information about layers' number and/or their structure. This approach was employed in a study of maturation of a reconstructed human epidermis (RHEs) (Groeber et al., 2015). Before developing any architecture, RHEs could be described as a single monolayer. In the interim phase, cells pile up, and corneous layer begin to form, building up dual layer architecture. In the late phase, the corneous layer has strengthened, and its electrical properties become dominant. At this stage, the system returns to a single monolayer architecture. Throughout RHE maturation, these measurements demonstrate an increase in transepitelial resistance and a decrease in CPE parameter A, whereas parameter α, which interpreted as so-called "ideality" of a capacitor, undergo slightly decrease (**Figure 8B**). Sensitivity of the system described above allows distinguishing effects of strong skin irritants and non-irritants. When similar methodology was employed to investigate formation of multilayers of choriocarcinoma BeWo b30 (Nikulin

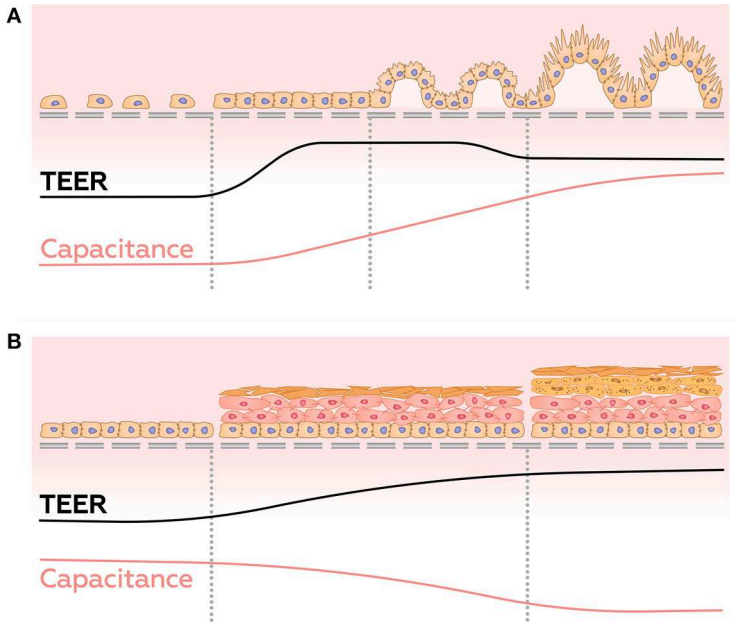

FIGURE 8 | Dynamics of TEER and capacitance changes during growth and differentiation of gut epithelial cells **(A)**, and during the development of reconstructed epidermis **(B)**.

et al., 2019b), observed shifts of the semi-circle center of Nyquist plot to the right and down allowed making conclusions about amounts of accumulated cell layers (**Figure 7D**).

The spectrum of barrier interface models amenable to TEER monitoring were recently expanded to the blood-brain barrier (BBB), which was reliably reconstituted by co-culturing human induced pluripotent stem cell (hiPSC)-derived brain microvascular endothelial cells with membrane-separated astrocyte-laden 3D hydrogel embed in a BBB-on-a-chip device that supports flow. In this model, apical addition of TGF-β1 led to the reduction of TEER and activation of astrocytes (Motallebnejad et al., 2019). There is a hope that this TEER-enabled BBB-emulating device could be used as BBB disruption model and find its use in drug screening settings.

3D CELL CULTURE

Initially, the developers of impedance spectroscopic techniques aimed at studying of cells maintained either in suspensions or in conventional 2D cultures. The growing trend of 3D culturing, which provides the cells with a physiologically relevant microenvironment (Rivnay et al., 2015), has led to a number of attempts to adapt IS to 3D. In typical laboratory settings, performing *in vitro* tests in 3D cell models is more difficult and time-consuming than in 2D. In particular, scattering effects observed in 3D constructs hampers the use of conventional optical techniques due to their thickness. Impedance spectroscopy allows relatively non-invasive, real-time glimpse into well-being of 3D cell cultures in lieu of optical microscopy or use of destructive methods.

The most widely used 3D cell culture technique produces so-called spheroids (Zanoni et al., 2016), which are formed by suspended cells either spontaneously or under the influence of various external factors. To date, several published works have employed impedance spectroscopy for the measurement of various properties of spheroids. For example, Thielecke et al. (2001a) used circular planar electrodes both to investigate the effect of bioactive substances on multicellular spheroids, and to profile the impedance produced by placing the electrodes at various distances from the spheroids. As a result, an optimal electrode/spheroid-interface for sensing the effects of drugs has been designed.

A microcavity array (MCA) biosensor chip was subsequently developed (Kloß et al., 2008a,b; Eichler et al., 2015). The chip consists of several square microcavities with rectangular gold electrodes. The impedance measured between any pair of electrodes increases if a microcavity contains a spheroid. An MCA chip can be used to assess cytotoxic effects of chemotherapeutic drugs. The data generated by impedimetric monitoring of the chemotherapeutic toxicity generally agree with the results of conventional cytotoxity end-point assays. Interestingly, some types of chemotherapeutic drugs cause an increase in the impedance, while others decrease it. Another device, capable of assessing the resistance of spheroids, was developed as a combination of a planar organic electrochemical transistor (OECT) and a microfluidic trapping device (Curto et al., 2018). In this device, the spheroids made of epithelial cells forming tight junctions demonstrated much higher resistance than the spheroids that consisted of loosely connected fibroblasts.

Bürgel et al. constructed an automated multiplexed electrical IS (AMEIS) platform for the analysis of the spheroids in a

microfluidic setting. This device, which obviated the need for pumps by utilizing a tilting stage (Bürgel et al., 2016), includes 15 separated capillaries connected to two reservoirs each, and a pair of measuring electrodes placed in the center of each capillary. When individual spheroids were manually injected into the chambers, and constant amplitude AC voltage applied between the electrodes, the passing of the spheroid between the electrodes lead to a drop in the current. The magnitude of this drop was proportional to the size of the spheroid. AMEIS devices are useful for quantifying cytotoxic effects seen in tumor cell spheroids treated with chemotherapeutic drugs, and, in slightly different settings, for the registration of action potential of the spheroids made of cardiomyocyte.

Thielecke et al. (2001b) placed the spheroids in a capillary based system for measuring their impedance with the aid of a precision pump. A comparison of spheroids made of butyrilcholinesterase knockdown cells and the controls showed that the former were smaller, contained a necrotic core, and had lower impedance in a wide range of frequencies (Thielecke et al., 2001b). Notably, simultaneous measurement of the impedance at low and high frequencies allows the determination of the volume fraction of cells comprising a spheroid. Subsequently a similar technique was successfully applied for the long term monitoring of the osteogenic differentiation of human mesenchymal stem cell cultures (Hildebrandt et al., 2010). For thorough review of impedance-based assays in stem cell cultures, we should refer to Gamal et al. (2018), who summarized achievement in this area recently.

A hanging drop platform has been IS-enabled by Schmid et al. (2016), who integrated an inlay with two pairs of platinum electrodes into the drop support structure. The distance between large electrodes placed within the drop radius was made as wide as possible (1.0×0.4 mm^2), while remaining within the geometrical margins of the inlay, confining the electrical field in the conducting liquid. As a function of the drop volume and height, the electric field lines may either compress or expand, which changes the impedance between the electrodes, thus, enabling the measurement of the size of the hanging drop. To provide optical access, relatively small electrodes (0.5×0.2 mm^2) were placed close to the presumed spheroid location, but off its center. Within the drop, the spheroids lift upwards, to the location between the electrodes. The presence of the spheroid disturbs the electric field lines and, consequently, changes the impedance. The measurements conducted in equidistant steps in the range of frequencies from 100 Hz to 40 MHz, helped to evaluate the relative sizes of the spheroid and the drop. In the case of spheroids made of cardiac cells, a set of specific frequencies was utilized to register its beating patterns.

3D cultures of cells embedded into the hydrogels or other porous scaffolds are a popular alternative to culturing cells as spheroids. Moreover, this approach is applicable for primary organoids. To date, several cases of IS application for 3D cultures of cells in gels were described. For example, Lin et al. constructed a perfusion culture system for real time monitoring of cell growth with a microelectrode array (Lin et al., 2009). In this system, cells grew within a 3D matrix synthesized from a polyethylene glycol hydrogel supplemented with poly-D-lysine *in situ*. Cell proliferation was measured by IS. Unfortunately, observed impedance kinetics of non-dividing neurons and fast proliferating fibroblasts were quite similar, thus, raising caution concerning the interpretation of the collected data.

Bagnaninchi et al. (2003, 2004; Bagnaninchi, 2010) grew the cells in microporous scaffolds and used an open-ended coaxial probe to measure their complex permittivity in the frequency range of 20 MHz−2 GHz. In these settings, the porosity of a scaffold and the cell concentrations were evaluated simultaneously (Bagnaninchi et al., 2003). Subsequently, this method was successfully used to assess variation in the morphology of the cells (Bagnaninchi et al., 2004; Bagnaninchi, 2010) and to discern normal and malignant variants of human lung cells embedded into low-conductive agarose hydrogels.

Using a pair of vertical electrodes, Lei et al. (2014) have performed rather complex IS measurements in 3D cell cultures grown in perfused agarose layers. For cell counting, the sensitivity of the technique peaked at the relatively low frequency of 500 Hz. When the same device had been employed in a real-time study of cytotoxicity, an increase rather than a decrease in impedance was observed, in sharp contrast to the data obtained in a planar electrode device constructed by the same group (Lei et al., 2012, 2015, 2017). In a colony formation assay, simultaneous quantification of cells (based on the absolute value of the impedance) and measuring colony size (based on measurements of the phase angle) was achieved. Subsequently, the same group of researchers employed impedimetric quantification of cells grown on a hydrogel-supporting paper substrate to construct a prototype for a high throughput screening of cancer cell chemosensitivity in point-of-care medical settings (Lei et al., 2016, 2018).

By inserting either three or four electrodes, Canali et al. (2015a,b) monitored spatial distribution of cells in larger 3D scaffolds. An exchange of working, counter and reference electrodes provided a variety of homogeneous electromagnetic field configurations and enabled coverage of every corner of the culturing chamber. The study revealed that cells tend to proliferate in the center of the culture chamber rather than in proximity of the chamber walls or in corners. Unfortunately, configuring electrode positions within the chamber requires multiple simulations, making the technique developed by Canali et al. far from easy to use.

More advanced application of impedance spectroscopy was developed to profile effects of various drugs on cancer cells embed in a 3D gel matrix (Pandya et al., 2017). This study was performed in a square chamber with interdigitated microelectrodes screening the frequencies ranging from 100 Hz to 1 MHz. After addition of a drug, observed magnitude of impedance of the drug-sensitive and drug-tolerant cancer cell cultures decreased over a period of 12 h. Notably, in sensitive cells, the drop in impedance was steeper than that in resistant ones, giving hope for utilization of this system for anticancer efficacy testing *in vitro*.

To date, IS has not been used for monitoring of primary 3D epithelial organoids. Existing data, however, suggest that this technique may be extremely useful for these models (**Figure 9**). Its proven ability to discriminate between different types of

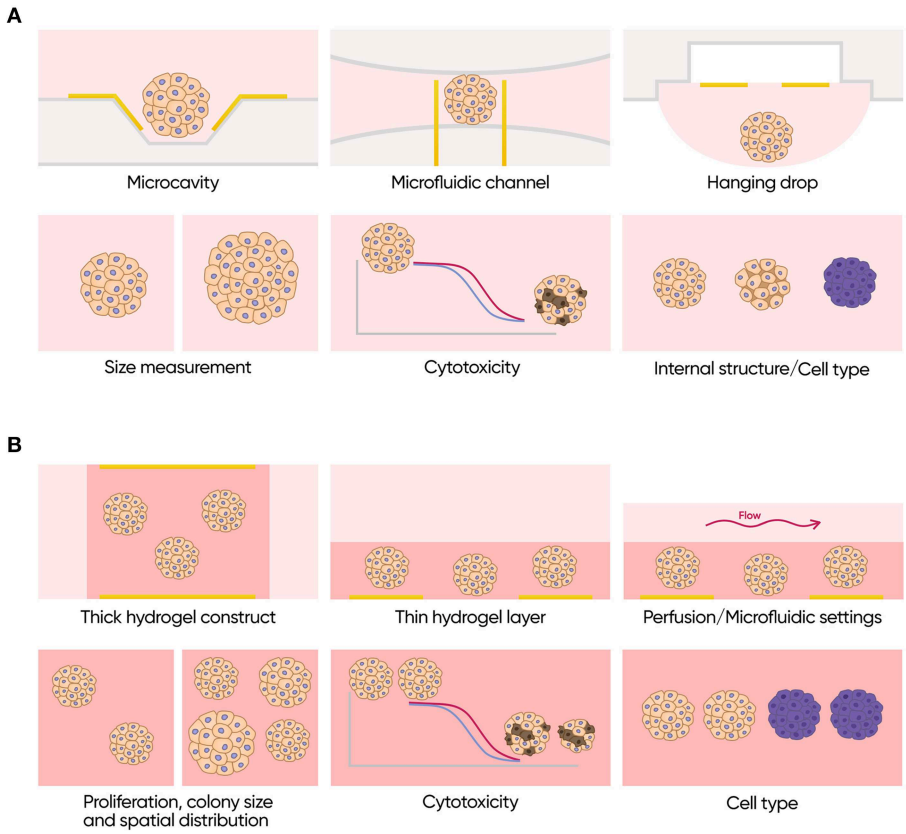

FIGURE 9 | Applications of impedance spectroscopy for 3D cell models. **(A)** Isolated scaffold-free spheroids. Possible formats (top row): microcavity array, microfluidic channel with integrated electrodes and hanging drop array with integrated electrodes. Possible applications (bottom row): size measurements, cytotoxicity assay, and investigation of internal structure and cell type composition. **(B)** Scaffold based 3D cell culture models. Possible formats (top row): thick scaffold-based constructs with the electrodes placed on the opposite sides of it, thin gel matrix layers covered with cell culture media containing electrodes only on the bottom and perfused or microfluidics formats. Possible applications (bottom row): measurements of proliferation rate colony size and spatial distribution of the cells, cytotoxicity assay and investigation of cell type composition.

cells, to measure volume fraction of cells in a spheroid and its size, and to assess effects of different compounds in real time without any labels may significantly improve penetration of such models to both research and commercial testing fields. Moreover, application of impedance in combination with engineered epithelial tissues and organ-on-a-chip devices may lead to a construction of easily automatable physiologically relevant pipelines for drug development and for personalized medicine.

CURRENT STATE-OF-THE-ART AND FUTURE DIRECTIONS

Impedance measurements are already employed by cell biologists all over the world, especially those exploring barrier tissues in various 2D culture formats. Historically, an integrity of reconstructed barriers was probed by exposing them to detectable molecules, for example, fluorescent dye lucifer yellow or enzyme horseradish peroxidase, which are capable of penetrating these barriers exclusively through paracellular route (Hidalgo et al., 1989; Hubatsch et al., 2007). Data collected in this manner are reliable enough, and have, indeed, resulted in many important insights; working with cell layer permeating dyes is, however, quite laborious and time-consuming. Impedance measurement is an attractive alternative which has almost completely replaced label-based methods in routine quality control of *in vitro* models of barrier tissues. One of the most popular commercially available devices for the measurement of barrier function in academic settings is EVOM^2 (World Precision Instruments), which allows small-scale experiments outside a cell culture incubator.

Next generation of the systems for *in vitro* models of barrier tissues was built for compatibility with the cell culture incubators. One example of that kind of systems is TEER24 (Applied Biophysics), which automatically collects impedance characteristics in real time on a single frequency of 75 Hz. Another, more advanced device cellZscope (nanoAnalytics GmbH) automatically profiles impedance over a broad range of frequencies, while also measuring electrical capacitance in real time. Recent works proved that measuring of electrical capacitance may be useful for evaluation of various 3D structures

formed in process of growth and differentiation of cells *in vitro*. For example, in intestinal model, electrical capacitance gradually increases along with formation of villi form (van der Helm et al., 2019), while in course of the development of multilayer structure of epidermis it decreases (Groeber et al., 2015). Another study showed that the impedance increases linearly with an increase in extracellular deposition of collagen and hyaluronan, but changes in a more complex manner with incorporation of bone-specific compound hydroxyapatite (Kozhevnikov et al., 2019). A simple and rapid way to assess the state of either cellular or extracellular 3D structures opens up novel avenues for both quality control and for fundamental research.

One of the main disadvantages of existing automated systems for monitoring of the barrier function is their low throughput. All of them are designed to work with up to 24 membrane inserts which is definitely not enough for large-scale screenings. Today, 96-well plates with membrane inserts are commercially available; there is hope that impedance measuring systems compatible with this format should appear soon. Even if prototypes allowing microfluidic chip compatible monitoring of barrier function with IS have been repeatedly reported, no solutions of this kind were introduced to the market yet.

On the other hand, impedance measurements have been successfully employed for monitoring of 2D cultures of adherent cells growing directly on the electrodes (Giaever and Keese, 1984, 1986, 1991; Ke et al., 2011). To date, several systems including xCELLigence (ACEA Biosciences) and ZTheta (Applied Biophysics) were made available commercially for assessing proliferation rate, cell adhesion, migration and invasion as well as cytotoxicity of various compounds. Traditionally, assaying of cytotoxicity also relied on various labeled molecules (Riss et al., 2004), including MTT, MTS and ATP, with latter being based on firefly luciferase. All these methods have proved their worth in the labs, but almost all of them are end-point, and time-consuming. A few real time cytotoxicity assays do exist, with RealTime-Glo™ MT Cell Viability Assay (Promega) being probably the most popular one. This assay allows to record luminescent signal, which is proportional to the number of viable cells, over a period of a few days. Unfortunately, real-time versions of end-point assays require use of sophisticated plate reader, equipped with gas control unit capable to reconstruct the environmental conditions in a manner similar to cell culture incubators. In contrast, impedance-based assays allow continuous monitoring of cell cultures for sufficiently longer periods, and are built to fit incubators to begin with.

Real-time imaging systems such as IncuCyte S3 (Essen BioScience) certainly may be viewed as an alternative to impedance-based analysis. In this analysis, automatic bright field microscope equipped with several fluorescent channels is placed directly inside a standard cell culture incubator to provide real-time estimates of the proliferation and migration rates, cytotoxicity and many other parameters with an aid of different fluorescent dyes. Fluorescent microscopy based monitoring allows great flexibility for continuous study of cells in culture; however, IS based techniques outperform microscopy in ease of accessing resultant data and in its compatibility with high throughput screening platforms. As data obtained by IS and fluorescent microscopy complement each other, a hybrid RTCA eSight system (ACEA Biosciences), which combines automatic microscopy with impedance analyzer, has been recently launched to the market.

One more interesting extension of impedance measuring systems introduces additional sensors for monitoring of such important parameters as pH or oxygen content (Lei, 2014; Alexander et al., 2019). These sensors themselves may also be impedance-based as the surface of the electrodes can be functionalized with various molecules selectively recognizing one or another component of culture medium (Liu et al., 2018; Seo et al., 2018). Commercially available examples of these systems include microfluidic IMOLA-IVD (Cellasys), which allows measuring both pH and dissolved oxygen along with impedance of the cells. Therefore, combination of IS with other techniques significantly expands the capabilities of the method. Another important development is recently described combination of impedance flow cytometry and electric IS within the same microfluidic device suitable for single cell measurements allowing to evaluate properties of heterogeneous populations of cancer cells by dealing with them one at a time (Feng et al., 2019). It is expected that more of the hybrid cell analysis systems of this kind should be introduced in the future.

As 3D models of human tissues are getting popular and are expected to eventually replace 2D analogs, specific challenges of these models have to be taken into account. Only a few conventional assays were designed specifically for 3D cell models, for example, a 3D modification of end-point viability assay CellTiter-Glo (Promega) features a mix of reagents that penetrates large spheroids and has increased lytic capacity. Some automatic imaging systems, like IncuCyte S3 (Essen BioScience), allow reliable real-time monitoring if all the 3D spheroids lay on the same flat surface, which is not always the case. Moreover, the size of the spheroids is not always uniform, and not directly proportional to the number of its constituent living cells, which complicates interpretation of the data. These challenges call for alternative means of non-invasive, label-free longitudinal monitoring of cell states. Impedance spectroscopy is the method to meet these challenges. A particularly attractive feature of IS monitoring is real time measurement of both the parameters of the cells and the parameters of the culture medium and the extracellular matrix, thus, allowing scaling and standardization of continuous cell-based assays. A majority of reviewed 3D cell models have not been yet adopted as an industry standard. An integration of IS technique into these models may greatly facilitate the process.

Above we discussed some 3D culture based IS-enabled devices which primarily aim at cancer research, where they are believed to be instrumental in streamlining preclinical trials due to significantly better recapitulation of the tumor microenvironment. When seeded with a particular sample of primary cells reflecting underlining genetics of a certain individual, IS-enabled devices open up new horizons for personalized medicine. In the near future, IS technologies are expected to become a critical component of organotypic models

suitable for high-throughput assaying which will eventually replace both laboratory animals and static *in vitro* cell models.

To summarize, the strongest and the most attractive features of impedance-based assays are their compatibility with high-throughput format and support for the measurements in real time with high temporal resolution. It is envisioned that most automated and the least labor-intensive assays of this and other kinds would be eventually accepted as the industry standard. So far, IS remains one of the very few techniques available for studying kinetics of a biological process rather than the resulting end points. As IS assesses biological properties based on electrical parameters of the system, an increase in sophistication of electrode layouts and experimental designs is expected, which will eventually lead to improvement of the precision and expansion of the palette of its applications. However, interpreters of IS-based data should proceed with caution, due to imperfect understanding of the parameters that have their effects on the impedance, especially in 3D cell models. Moreover, as the theory of IS stems from electromagnetic theory and is quite complex, work on popularization and explanation of the method for experimental biologists is required. Finally, we should mention one more factor preventing widespread of the impedance-based assays: the cost of consumables. Current situation should, however, improve with the rise in the popularity of IS techniques which would enable the large-scale production of the consumables.

AUTHOR CONTRIBUTIONS

TG and SN wrote the manuscript. GZ draw a part of the figures and edited the manuscript. AP, VP, AB, and AT edited the manuscript and contributed various ideas.

FUNDING

This work was supported by the Russian Science Foundation (Grant No. 16-19-10597).

ACKNOWLEDGMENTS

The authors thank Dr. Rex Palmer for proofreading the manuscript, Valeria Kuznetsova (https://www.instagram.com/lerikuz/) for her help in design of some figures and Anton Voronov for final editing the images.

REFERENCES

Abdur Rahman, A. R., Price, D. T., and Bhansali, S. (2007). Effect of electrode geometry on the impedance evaluation of tissue and cell culture. *Sensors Actuators B Chem.* 127, 89–96. doi: 10.1016/j.snb.2007.07.038

Alexander, F., Price, D. T., and Bhansali, S. (2010). Optimization of interdigitated electrode (IDE) arrays for impedance based evaluation of Hs 578T cancer cells. *J. Phys. Conf. Ser.* 224:012134. doi: 10.1088/1742-6596/224/1/012134

Alexander, F. J., Eggert, S., and Price, D. (2019). Label-free monitoring of 3D tissue models via electrical impedance spectroscopy. *Biorev.* 2, 111–134. doi: 10.1007/11663_2018_5

Amini, M., Hisdal, J., and Kalvøy, H. (2018). Applications of bioimpedance measurement techniques in tissue engineering. *J. Electr. Bioimpedance* 9, 142–158. doi: 10.2478/joeb-2018-0019

Asami, K., Yonezawa, T., Wakamatsu, H., and Koyanagi, N. (1996). Dielectric spectroscopy of biological cells. *Bioelectrochem. Bioenerg.* 40, 141–145. doi: 10.1016/0302-4598(96)05067-2

Astashkina, A., Mann, B., and Grainger, D. W. (2012). A critical evaluation of *in vitro* cell culture models for high-throughput drug screening and toxicity. *Pharmacol. Ther.* 134, 82–106. doi: 10.1016/j.pharmthera.2012.01.001

Bagnaninchi, P. O. (2010). Combined impedance spectroscopy and fourier domain optical coherence tomography to monitor cells in three-dimensional structures. *Int. J. Artif. Organs* 33, 238–243. doi: 10.1177/039139881003300408

Bagnaninchi, P. O., Dikeakos, M., Veres, T., and Tabrizian, M. (2003). Towards on-line monitoring of cell growth in microporous scaffolds: Utilization and interpretation of complex permittivity measurements. *Biotechnol. Bioeng.* 84, 343–350. doi: 10.1002/bit.10770

Bagnaninchi, P. O., Dikeakos, M., Veres, T., and Tabrizian, M. (2004). Complex permittivity measurement as a new noninvasive tool for monitoring *in vitro* tissue engineering and cell signature through the detection of cell proliferation, differentiation, and pretissue formation. *IEEE Trans. Nanobiosci.* 3, 243–250. doi: 10.1109/TNB.2004.837901

Benson, K., Cramer, S., and Galla, H.-J. (2013). Impedance-based cell monitoring: barrier properties and beyond. *Fluids Barriers CNS.* 10:5. doi: 10.1186/2045-8118-10-5

Booth, R., and Kim, H. (2012). Characterization of a microfluidic *in vitro* model of the blood-brain barrier (μBBB). *Lab Chip* 12:1784. doi: 10.1039/c2lc40094d

Bragós, R., Sarró, E., Fontova, A., Soley, A., Cairó, J., Bayés-Genís, A., et al. (2006). Four versus two-electrode measurement strategies for cell growing and differentiation monitoring using electrical impedance spectroscopy. *Annu. Int. Conf. IEEE Eng. Med. Biol. Proc.* 1, 2106–2109. doi: 10.1109/IEMBS.2006.260287

Bürgel, N., Bojarski, C., Mankertz, J., Zeitz, M., Fromm, M., and Schulzke, J.-D. (2002). Mechanisms of diarrhea in collagenous colitis. *Gastroenterology* 123, 433–443. doi: 10.1053/gast.2002.34784

Bürgel, S. C., Diener, L., Frey, O., Kim, J.-Y., and Hierlemann, A. (2016). Automated, multiplexed electrical impedance spectroscopy platform for continuous monitoring of microtissue spheroids. *Anal. Chem.* 88, 10876–10883. doi: 10.1021/acs.analchem.6b01410

Caicedo-Carvajal, C. E., Liu, Q., and Goy, A. (2012). Three-dimensional cell culture models for biomarker discoveries and cancer research. *Transl. Med.* 1, 1–8. doi: 10.4172/2161-1025.S1-005

Canali, C., Heiskanen, A., Muhammad, H. B., Høyum, P., Pettersen, F.-J., Hemmingsen, M., et al. (2015a). Bioimpedance monitoring of 3D cell culturing—complementary electrode configurations for enhanced spatial sensitivity. *Biosens. Bioelectron.* 63, 72–79. doi: 10.1016/j.bios.2014.07.020

Canali, C., Mazzoni, C., Larsen, L. B., Heiskanen, A., Martinsen, Ø. G., Wolff, A., et al. (2015b). An impedance method for spatial sensing of 3D cell constructs – towards applications in tissue engineering. *Analyst* 140, 6079–6088. doi: 10.1039/C5AN00987A

Castellví, Q. (2014). Bioimpedance measurements and the electroporation phenomenon (avail. in French as Les Mesures de Bio-impédance pour l'Electroporation). *La Revue 3EI.*

Cereijido, M., Stefani, E., and Palomo, A. M. (1980). Occluding junctions in a cultured transporting epithelium: structural and functional heterogeneity. *J. Membr. Biol.* 53, 19–32. doi: 10.1007/BF01871169

Chang, J., Park, J., Pak, Y. K., and Pak, J. J. (2007). "Fitting improvement using a new electrical circuit model for the electrode-electrolyte interface," in *2007 3rd International IEEE/EMBS Conference on Neural Engineering* (Kohala Coast, HI: IEEE), 572–574.

Chassagne, C., Dubois, E., Jiménez, M. L., van der Ploeg, J. P. M., and van Turnhout, J. (2016). Compensating for electrode polarization in dielectric spectroscopy studies of colloidal suspensions: theoretical assessment of existing methods. *Front. Chem.* 4:30. doi: 10.3389/fchem.2016.00030

Cole, K. S. (1932). Electric phase angle of cell membranes. *J. Gen. Physiol.* 15, 641–649. doi: 10.1085/jgp.15.6.641

Curto, V. F., Ferro, M. P., Mariani, F., Scavetta, E., and Owens, R. M. (2018). A planar impedance sensor for 3D spheroids. *Lab Chip* 18, 933–943. doi: 10.1039/C8LC00067K

Decker, D., Hempelmann, R., Natter, H., Pirrung, M., Rabe, H., Schäfer, K. H., et al. (2018). 3D nanostructured multielectrode arrays: fabrication, electrochemical characterization, and evaluation of cell – electrode. *Adhesion*. 1800436, 1–10. doi: 10.1002/admt.201800436

Dehne, E.-M., Hasenberg, T., and Marx, U. (2017). The ascendance of microphysiological systems to solve the drug testing dilemma. *Futur. Sci. OA* 3:FSO0185. doi: 10.4155/fsoa-2017-0002

Doke, S. K., and Dhawale, S. C. (2015). Alternatives to animal testing: a review. *Saudi Pharm. J.* 23, 223–229. doi: 10.1016/j.jsps.2013.11.002

Douville, N. J., Tung, Y.-C., Li, R., Wang, J. D., El-Sayed, M. E. H., and Takayama, S. (2010). Fabrication of two-layered channel system with embedded electrodes to measure resistance across epithelial and endothelial barriers. *Anal. Chem.* 82, 2505–2511. doi: 10.1021/ac9029345

Eichler, M., Jahnke, H.-G., Krinke, D., Müller, A., Schmidt, S., Azendorf, R., et al. (2015). A novel 96-well multielectrode array based impedimetric monitoring platform for comparative drug efficacy analysis on 2D and 3D brain tumor cultures. *Biosens. Bioelectron.* 67, 582–589. doi: 10.1016/j.bios.2014.09.049

Feng, Y., Huang,. L., Zhao, P., Liang,. F., and Wang, W. (2019). A microfluidic device integrating impedance flow cytometry and electric impedance spectroscopy for high-efficiency single-cell electrical property measurement. *Anal. Chem.* 91, 15204–15212. doi: 10.1021/acs.analchem.9b04083

Franks, W., Schenker, I., Schmutz, P., and Hierlemann, A. (2005). Impedance characterization and modeling of electrodes for biomedical applications. *IEEE Trans. Biomed. Eng.* 52, 1295–1302. doi: 10.1109/TBME.2005.847523

Fricke, H. (1924). A mathematical treatment of the electrical conductivity of colloids and cell suspensions. *J. Gen. Physiol.* 4, 375–383. doi: 10.1085/jgp.6.4.375

Fromm, M., Palant, C. E., Bentzel, C. J., and Hegel, U. (1985). Protamine reversibly decreases paracellular cation permeability inNecturus gallbladder. *J. Membr. Biol.* 87, 141–150. doi: 10.1007/BF01870660

Frömter, E., and Diamond, J. (1972). Route of passive ion permeation in epithelia. *Nat. New Biol.* 235, 9–13. doi: 10.1038/newbio235009a0

Funk, R. H. W., and Monsees, T. K. (2006). Effects of electromagnetic fields on cells: Physiological and therapeutical approaches and molecular mechanisms of interaction. A review. *Cells Tissues Organs* 182, 59–78. doi: 10.1159/000093061

Gamal, W., Wu, H., Underwood, I., Jia, J., Smith, S., and Bagnaninchi, P. O. (2018). Impedance-based cellular assays for regenerative medicine. *Philos. Trans. R. Soc. B Biol. Sci.* 373:20170226. doi: 10.1098/rstb.2017.0226

Gawad, S., Schild, L., and Renaud, P. (2001). Micromachined impedance spectroscopy flow cytometer for cell analysis and particle sizing. *Lab Chip* 1:76. doi: 10.1039/b103933b

Geens, M. M., and Niewold, T. A. (2011). Optimizing culture conditions of a porcine epithelial cell line IPEC-J2 through a histological and physiological characterization. *Cytotechnology* 63, 415–423. doi: 10.1007/s10616-011-9362-9

Giaever, I., and Keese, C. R. (1984). Monitoring fibroblast behavior in tissue culture with an applied electric field. *Proc. Natl. Acad. Sci. U.S.A.* 81, 3761–3764. doi: 10.1073/pnas.81.12.3761

Giaever, I., and Keese, C. R. (1986). Use of electric fields to monitor the dynamical aspect of cell behavior in tissue culture. *IEEE Trans. Biomed. Eng.* BME-33, 242–247. doi: 10.1109/TBME.1986.325896

Giaever, I., and Keese, C. R. (1991). Micromotion of mammalian cells measured electrically. *Proc. Natl. Acad. Sci. U.S.A.* 88, 7896–7900. doi: 10.1073/pnas.88.17.7896

Gitter, A. H., Bendfeldt, K., Schulzke, J. D., and Fromm, M. (2000). Trans/paracellular, surface/crypt, and epithelial/subepithelial resistances of mammalian colonic epithelia. *Pflügers Arch. Eur. J. Physiol.* 439, 477–482. doi: 10.1007/s004249900202

Gitter, A. H., Bertog, M., Schulzke, J.-D., and Fromm, M. (1997). Measurement of paracellular epithelial conductivity by conductance scanning. *Pflügers Arch. Eur. J. Physiol.* 434, 830–840. doi: 10.1007/s004240050472

Grafov, B. M., and Ukshe, Y. A. (1973). *Electrochemical Circuits of Alternating Current (in Russian)*. Moscow: Nauka.

Griep, L. M., Wolbers, F., De Wagenaar, B., Ter Braak, P. M., Weksler, B. B., Romero, I., et al. (2013). BBB on CHIP: Microfluidic platform to mechanically and biochemically modulate blood-brain barrier function. *Biomed. Microdevices* 15, 145–150. doi: 10.1007/s10544-012-9699-7

Grimnes, S., and Martinsen, O. G. (2005). Cole electrical impedance model–a critique and an alternative. *IEEE Trans. Biomed. Eng.* 52, 132–135. doi: 10.1109/TBME.2004.836499

Grimnes, S., and Martinsen, O. G. (2015). *Bioimpedance and Bioelectricity Basics*. Amsterdam; Boston, MA; Heidelberg; London; New York, NY; Oxford; Paris; San Diego, CA; San Francisco, CA; Singapore; Sydney; Tokyo: Academic Press.

Groeber, F., Engelhardt, L., Egger, S., Werthmann, H., Monaghan, M., Walles, H., et al. (2015). Impedance spectroscopy for the non-destructive evaluation of *in vitro* epidermal models. *Pharm. Res.* 32, 1845–1854. doi: 10.1007/s11095-014-1580-3

Henry, O. Y. F., Villenave, R., Cronce, M. J., Leineweber, W. D., Benz, M. A., and Ingber, D. E. (2017). Organs-on-chips with integrated electrodes for trans-epithelial electrical resistance (TEER) measurements of human epithelial barrier function. *Lab Chip* 17, 2264–2271. doi: 10.1039/C7LC00155J

Hidalgo, I. J., Raub, T. J., and Borchardt, R. T. (1989). Characterization of the human colon carcinoma cell line (Caco-2) as a model system for intestinal epithelial permeability. *Gastroenterology* 96, 736–749. doi: 10.1016/S0016-5085(89)80072-1

Hildebrandt, C., Büth, H., Cho, S., Impidjati, and Thielecke, H. (2010). Detection of the osteogenic differentiation of mesenchymal stem cells in 2D and 3D cultures by electrochemical impedance spectroscopy. *J. Biotechnol.* 148, 83–90. doi: 10.1016/j.jbiotec.2010.01.007

Hilgendorf, C., Spahn-Langguth, H., Regårdh, C. G., Lipka, E., Amidon, G. L., and Langguth, P. (2000). Caco-2 versus caco-2/HT29-MTX co-cultured cell lines: permeabilities via diffusion, inside- and outside-directed carrier-mediated transport. *J. Pharm. Sci.* 89, 63–75. doi: 10.1002/(SICI)1520-6017(200001)89:1<63::AID-JPS7>3.0.CO;2-6

Hoffmann, K.-P., Ruff, R., and Poppendieck, W. (2006). "Long-term characterization of electrode materials for surface electrodes in biopotential recording," in *2006 International Conference of the IEEE Engineering in Medicine and Biology Society* (New York, NY: IEEE), 2239–2242.

Howlader, M. M. R., Doyle, T. E., Mohtashami, S., and Kish, J. R. (2013). Charge transfer and stability of implantable electrodes on flexible substrate. *Sensors Actuators B Chem.* 178, 132–139. doi: 10.1016/j.snb.2012.12.051

Huang, C., Ramadan, Q., Wacker, J. B., Tekin, H. C., Ruffert, C., Vergères, G., et al. (2014). Microfluidic chip for monitoring Ca^{2+} transport through a confluent layer of intestinal cells. *RSC Adv.* 4, 52887–52891. doi: 10.1039/C4RA09370D

Hubatsch, I., Ragnarsson, E. G. E., and Artursson, P. (2007). Determination of drug permeability and prediction of drug absorption in Caco-2 monolayers. *Nat. Protoc.* 2, 2111–2119. doi: 10.1038/nprot.2007.303

Huigen, E., Peper, A., and Grimbergen, C. A. (2002). Investigation into the origin of the noise of surface electrodes. *Med. Biol. Eng. Comput.* 40, 332–338. doi: 10.1007/BF02344216

Jimison, L. H., Tria, S. A., Khodagholy, D., Gurfinkel, M., Lanzarini, E., Hama, A., et al. (2012). Measurement of barrier tissue integrity with an organic electrochemical transistor. *Adv. Mater.* 24, 5919–5923. doi: 10.1002/adma.201202612

Kaji, T., Suzuki, M., Yamamoto, C., Mishima, A., Sakamoto, M., and Kozuka, H. (1995). Severe damage of cultured vascular endothelial cell monolayer after simultaneous exposure to cadmium and lead. *Arch. Environ. Contam. Toxicol.* 28, 168–172. doi: 10.1007/BF00217612

Ke, N., Wang, X., Xu, X., and Abassi, Y. A. (2011). "The xCELLigence system for real-time and label-free monitoring of cell viability," in *Methods in Molecular Biology,* ed M. J. Stoddart (Totowa, NJ: Humana Press), 33–43.

Kloß, D., Fischer, M., Rothermel, A., Simon, J. C., and Robitzki, A. A. (2008a). Drug testing on 3D *in vitro* tissues trapped on a microcavity chip. *Lab Chip* 8:879. doi: 10.1039/b800394g

Kloß, D., Kurz, R., Jahnke, H.-G., Fischer, M., Rothermel, A., Anderegg, U., et al. (2008b). Microcavity array (MCA)-based biosensor chip for functional drug screening of 3D tissue models. *Biosens. Bioelectron.* 23, 1473–1480. doi: 10.1016/j.bios.2008.01.003

Kottra, G., and Frömter, E. (1984). Rapid determination of intraepithelial resistance barriers by alternating current spectroscopy (I.

Experimental procedures). *Pflügers Arch. Eur. J. Physiol.* 402, 409–420. doi: 10.1007/BF00583942

Kozhevnikov, E., Qiao, S., Han, F., Yan, W., Zhao, Y., Hou, X., et al. (2019). A dual-transduction-integrated biosensing system to examine the 3D cell-culture for bone regeneration. *Biosens Bioelectron.* 141:111481. doi: 10.1016/j.bios.2019.111481

Krug, S. M., Fromm, M., and Günzel, D. (2009). Two-path impedance spectroscopy for measuring paracellular and transcellular epithelial resistance. *Biophys. J.* 97, 2202–2211. doi: 10.1016/j.bpj.2009.08.003

Lazarevi, M. P., and Caji, M. S. (2015). "Biomechanical modelling and simulation of soft tissues using fractional memristive elements," in *8th GRACM International Congress on Computational Mechanics Volos*. Volos.

Lee, R. C. (2005). Cell injury by electric forces. *Ann. N.Y. Acad. Sci.* 1066, 85–91. doi: 10.1196/annals.1363.007

Lei, K. (2014). Review on impedance detection of cellular responses in micro/nano environment. *Micromachines* 5, 1–12. doi: 10.3390/mi5010001

Lei, K. F., Huang, C.-H., and Tsang, N.-M. (2016). Impedimetric quantification of cells encapsulated in hydrogel cultured in a paper-based microchamber. *Talanta* 147, 628–633. doi: 10.1016/j.talanta.2015.10.052

Lei, K. F., Kao, C.-H., and Tsang, N.-M. (2017). High throughput and automatic colony formation assay based on impedance measurement technique. *Anal. Bioanal. Chem.* 409, 3271–3277. doi: 10.1007/s00216-017-0270-5

Lei, K. F., Liu, T.-K., and Tsang, N.-M. (2018). Towards a high throughput impedimetric screening of chemosensitivity of cancer cells suspended in hydrogel and cultured in a paper substrate. *Biosens. Bioelectron.* 100, 355–360. doi: 10.1016/j.bios.2017.09.029

Lei, K. F., Wu, M.-H., Hsu, C.-W., and Chen, Y.-D. (2014). Real-time and non-invasive impedimetric monitoring of cell proliferation and chemosensitivity in a perfusion 3D cell culture microfluidic chip. *Biosens. Bioelectron.* 51, 16–21. doi: 10.1016/j.bios.2013.07.031

Lei, K. F., Wu, M.-H., Liao, P.-Y., Chen, Y.-M., and Pan, T.-M. (2012). Development of a micro-scale perfusion 3D cell culture biochip with an incorporated electrical impedance measurement scheme for the quantification of cell number in a 3D cell culture construct. *Microfluid. Nanofluidics* 12, 117–125. doi: 10.1007/s10404-011-0854-x

Lei, K. F., Wu, Z.-M., and Huang, C.-H. (2015). Impedimetric quantification of the formation process and the chemosensitivity of cancer cell colonies suspended in 3D environment. *Biosens. Bioelectron.* 74, 878–885. doi: 10.1016/j.bios.2015.07.060

Lewis, S. A. (1977). Nystatin as a probe for investigating the electrical properties of a tight epithelium. *J. Gen. Physiol.* 70, 427–440. doi: 10.1085/jgp.70.4.427

Li, Y., Wong, C., Xiong, J., Hodgson, P., and Wen, C. (2010). Cytotoxicity of titanium and titanium alloying elements. *J. Dent. Res.* 89, 493–497. doi: 10.1177/0022034510363675

Limame, R., Wouters, A., Pauwels, B., Fransen, E., Peeters, M., Lardon, F., et al. (2012). Comparative analysis of dynamic cell viability, migration and invasion assessments by novel real-time technology and classic endpoint assays. *PLoS ONE* 7:e46536. doi: 10.1371/journal.pone.0046536

Lin, S.-P., Kyriakides, T. R., and Chen, J.-J. J. (2009). On-line observation of cell growth in a three-dimensional matrix on surface-modified microelectrode arrays. *Biomaterials* 30, 3110–3117. doi: 10.1016/j.biomaterials.2009.03.017

Liu, F., Ni, L., and Zhe, J. (2018). Lab-on-a-chip electrical multiplexing techniques for cellular and molecular biomarker detection. *Biomicrofluidics.* 12:021501. doi: 10.1063/1.5022168

Lvovich, V. F. (2012). *Impedance Spectroscopy: Applications to Electrochemical and Dielectric Phenomena*. Hoboken: Wiley.

MacKay, S., Hermansen, P., Wishart, D., and Chen, J. (2015). Simulations of interdigitated electrode interactions with gold nanoparticles for impedance-based biosensing applications. *Sensors* 15, 22192–22208. doi: 10.3390/s150922192

Maoz, B. M., Herland, A., Henry, O. Y. F., Leineweber, W. D., Yadid, M., Doyle, J., et al. (2017). Organs-on-chips with combined multi-electrode array and transepithelial electrical resistance measurement capabilities. *Lab Chip* 17, 2294–2302. doi: 10.1039/C7LC00412E

Marx, U., Andersson, T. B., Bahinski, A., Beilmann, M., Beken, S., Cassee, F. R., et al. (2016). Biology-inspired microphysiological system approaches to solve the prediction dilemma of substance testing. *ALTEX* 33, 272–321. doi: 10.14573/altex.1603161

Maschmeyer, I., Lorenz, A., Bauer, S., Ramme, A., Rings, T., Kuehnl, J., et al. (2017). State-of-the-art of the assessment of ADME using multiple organs on a chip. *Toxicol. Lett.* 280:S34. doi: 10.1016/j.toxlet.2017.07.084

McAdams, E. T., and Jossinet, J. (1996). Problems in equivalent circuit modelling of the electrical properties of biological tissues. *Bioelectrochem. Bioenerg.* 40, 147–152. doi: 10.1016/0302-4598(96)05069-6

Moon, C., VanDussen, K. L., Miyoshi, H., and Stappenbeck, T. S. (2014). Development of a primary mouse intestinal epithelial cell monolayer culture system to evaluate factors that modulate IgA transcytosis. *Mucosal Immunol.* 7, 818–828. doi: 10.1038/mi.2013.98

Morgan, H., Sun, T., Holmes, D., Gawad, S., and Green, N. G. (2007). Single cell dielectric spectroscopy. *J. Phys. D. Appl. Phys.* 40, 61–70. doi: 10.1088/0022-3727/40/1/S10

Motallebnejad, P., Thomas, A., Swisher, S. L., and Azarin, S. M. (2019). An isogenic hiPSC-derived BBB-on-a-chip. *Biomicrofluidics.*13:064119. doi: 10.1063/1.5123476

Moulton, S. E., Barisci, J. N., Bath, A., Stella, R., and Wallace, G. G. (2004). Studies of double layer capacitance and electron transfer at a gold electrode exposed to protein solutions. *Electrochim. Acta.* 49, 4223–4230. doi: 10.1016/j.electacta.2004.03.034

Mycielska, M. E., and Djamgoz, M. B. A. (2004). Cellular mechanisms of direct-current electric field effects: galvanotaxis and metastatic disease. *J. Cell Sci.* 117, 1631–1639. doi: 10.1242/jcs.01125

Nikulin, S. V., Gerasimenko, T. N., Shilin, S. A., Zakharova, G. S., Gazizov, I. N., Poloznikov, A. A., et al. (2019a). Application of impedance spectroscopy for the control of the integrity of *in vitro* models of barrier tissues. *Bull. Exp. Biol. Med.* 166, 512–516. doi: 10.1007/s10517-019-04384-5

Nikulin, S. V., Knyazev, E. N., Gerasimenko, T. N., Shilin, S. A., Gazizov, I. N., Zakharova, G. S., et al. (2019b). Impedance spectroscopy and transcriptome analysis of choriocarcinoma BeWo b30 as a model of human placenta. *Mol. Biol.* 53, 411–418. doi: 10.1134/S0026893319030130

Nikulin, S. V., Knyazev, E. N., Poloznikov, A. A., Shilin, S. A., Gazizov, I. N., Zakharova, G. S., et al. (2018). Expression of SLC30A10 and SLC23A3 transporter mRNAs in Caco-2 cells correlates with an increase in the area of the apical membrane. *Mol. Biol.* 52, 577–582. doi: 10.1134/S0026893318040131

Odijk, M., van der Meer, A. D., Levner, D., Kim, H. J., van der Helm, M. W., Segerink, L. I., et al. (2015). Measuring direct current trans-epithelial electrical resistance in organ-on-a-chip microsystems. *Lab Chip* 15, 745–752. doi: 10.1039/C4LC01219D

Pandya, H. J., Dhingra, K., Prabhakar, D., Chandrasekar, V., Natarajan, S. K., Vasan, A. S., et al. (2017). A microfluidic platform for drug screening in a 3D cancer microenvironment. *Biosens. Bioelectron.* 94, 632–642. doi: 10.1016/j.bios.2017.03.054

Păunescu, T. G., and Helman, S. I. (2001). cAMP activation of apical membrane Cl – channels: theoretical considerations for impedance analysis. *Biophys. J.* 81, 838–851. doi: 10.1016/S0006-3495(01)75745-1

Pliquett, U., Frense, D., Schönfeldt, M., Frätzer, C., Zhang, Y., Cahill, B., et al. (2010). Testing miniaturized electrodes for impedance measurements within the beta-dispersion – a practical approach. *J. Electr. Bioimped.* 1:41. doi: 10.5617/jeb.111

Polk, B. J., Stelzenmuller, A., Mijares, G., MacCrehan, W., and Gaitan, M. (2006). Ag/AgCl microelectrodes with improved stability for microfluidics. *Sensors Actuators B Chem.* 114, 239–247. doi: 10.1016/j.snb.2005.03.121

Poloznikov, A., Gazaryan, I., Shkurnikov, M., Nikulin, S., Drapkina, O., Baranova, A., et al. (2018). *In vitro* and *in silico* liver models: current trends, challenges and opportunities. *ALTEX* 35, 397–412. doi: 10.14573/altex.1803221

Ramuz, M., Hama, A., Huerta, M., Rivnay, J., Leleux, P., and Owens, R. M. (2014). Combined optical and electronic sensing of epithelial cells using planar organic transistors. *Adv. Mater.* 26, 7083–7090. doi: 10.1002/adma.201401706

Riistama, J., and Lekkala, J. (2006). "Electrode-electrolyte interface properties in implantation conditions," in *2006 International Conference of the IEEE Engineering in Medicine and Biology Society* (New York, NY: IEEE), 6021–6024.

Riss, T. L., Moravec, R. A., Niles, A. L., Duellman, S., Benink, H. A., Worzella, T. J., et al. (2004). *Cell Viability Assays*. Available online at: http://www.ncbi.nlm.nih.gov/pubmed/23805433

Rivnay, J., Ramuz, M., Leleux, P., Hama, A., Huerta, M., and Owens, R. M. (2015). Organic electrochemical transistors for cell-based impedance sensing. *Appl. Phys. Lett.* 106:043301. doi: 10.1063/1.4906872

Sackin, H., and Palmer, L. G. (2013). "Electrophysiological analysis of transepithelial transport," in *Seldin and Giebisch's The Kidney, 5th Edn*, eds R. Alpern, M. Caplan, O. W. Moe (London: Elsevier), 177–216.

Sakharov, D., Shilin, S., Gazizov, I., Nikulin, S., Poloznikov, A., and Tonevitsky, A. (2017). Online TEER measurements for barrier model systems in microfluidic chips. *Toxicol. Lett.* 280, S269–S270. doi: 10.1016/j.toxlet.2017.07.953

Samatov, T. R., Shkurnikov, M. U., Tonevitskaya, S. A., and Tonevitsky, A. G. (2015). Modelling the metastatic cascade by *in vitro* microfluidic platforms. *Prog. Histochem. Cytochem.* 49, 21–29. doi: 10.1016/j.proghi.2015.01.001

Schifferdecker, E., and Frömter, E. (1978). The AC impedance of necturus gallbladder epithelium. *Pflügers Arch. Eur. J. Physiol.* 377, 125–133. doi: 10.1007/BF00582842

Schmid, Y. R. F., Bürgel, S. C., Misun, P. M., Hierlemann, A., and Frey, O. (2016). Electrical impedance spectroscopy for microtissue spheroid analysis in hanging-drop networks. *ACS Sensors* 1, 1028–1035. doi: 10.1021/acssensors.6b00272

Schwan, H. P. (1994). Electrical properties of tissues and cell suspensions: mechanisms\nand models. *Proc. 16th Annu. Int. Conf. IEEE Eng. Med. Biol. Soc.* (Baltimore, MD: IEEE), 70a–71a. doi: 10.1109/IEMBS.1994.412155

Seo, Y., Jeong, S., Lee, J., Choi, H. S., Kim, J., and Lee, H. (2018). Innovations in biomedical nanoengineering: nanowell array biosensor. *Nano Converg.* 5:9. doi: 10.1186/s40580-018-0141-6

Shinwari, M. W., Zhitomirsky, D., Deen, I. A., Selvaganapathy, P. R., Deen, M. J., and Landheer, D. (2010). Microfabricated reference electrodes and their biosensing applications. *Sensors* 10, 1679–1715. doi: 10.3390/s100301679

Single, A., Beetham, H., Telford, B. J., Guilford, P., and Chen, A. (2015). A comparison of real-time and endpoint cell viability assays for improved synthetic lethal drug validation. *J. Biomol. Screen.* 20, 1286–1293. doi: 10.1177/1087057115605765

Spielmann, H., and Marx, U. (2017). Human multi-organ-chips (MOCs) from vison to acceptance by industry and regulators. *Toxicol. Lett.* 280:S30. doi: 10.1016/j.toxlet.2017.07.073

Srinivasan, B., Kolli, A. R., Esch, M. B., Abaci, H. E., Shuler, M. L., and Hickman, J. J. (2015). TEER measurement techniques for *in vitro* barrier model systems. *J. Lab. Autom.* 20, 107–126. doi: 10.1177/2211068214561025

Sun, T., Green, N. G., Gawad, S., and Morgan, H. (2007). Analytical electric field and sensitivity analysis for two microfluidic impedance cytometer designs. *IET Nanobiotechnol.* 1, 69–79. doi: 10.1049/iet-nbt:20070019

Sun, T., Green, N. G., and Morgan, H. (2008). Analytical and numerical modeling methods for impedance analisys of single cells on-chip. *Nano* 3, 55–63. doi: 10.1142/S1793292008000800

Taghian, T., Narmoneva, D. A., and Kogan, A. B. (2015). Modulation of cell function by electric field: a high-resolution analysis. *J. R. Soc. Interface* 12, 21–25. doi: 10.1098/rsif.2015.0153

Thielecke, H., Mack, A., and Robitzki, A. (2001a). Biohybrid microarrays–impedimetric biosensors with 3D *in vitro* tissues for toxicological and biomedical screening. *Fresenius. J. Anal. Chem.* 369, 23–29. doi: 10.1007/s002160000606

Thielecke, H., Mack, A., and Robitzki, A. (2001b). A multicellular spheroid-based sensor for anti-cancer therapeutics. *Biosens. Bioelectron.* 16, 261–269. doi: 10.1016/S0956-5663(01)00140-3

Torras, N., García-Díaz, M., Fernández-Majada, V., and Martínez, E. (2018). Mimicking epithelial tissues in three-dimensional cell culture models. *Front. Bioeng. Biotechnol.* 6:197. doi: 10.3389/fbioe.2018.00197

Valere, K., Rapista, A., Eugenin, E., Lu, W., and Chang, T. L. (2015). Human alpha-defensin HNP1 increases HIV traversal of the epithelial barrier: a potential role in STI-mediated enhancement of HIV transmission. *Viral Immunol.* 28, 609–615. doi: 10.1089/vim.2014.0137

van der Helm, M. (2018). *Electrical and Microfluidic Technologies for Organs-on-chips: Mimicking Blood-Brain Barrier and Gut Tissues*. PhD thesis (Enschede: University of Twente), 210.

van der Helm, M. W., Henry, O. Y. F. F., Bein, A., Hamkins-Indik, T., Cronce, M. J., Leineweber, W. D., et al. (2019). Non-invasive sensing of transepithelial barrier function and tissue differentiation in organs-on-chips using impedance spectroscopy. *Lab Chip* 19, 452–463. doi: 10.1039/C8LC00129D

van der Helm, M. W., Odijk, M., Frimat, J.-P., van der Meer, A. D., Eijkel, J. C. T., van den Berg, A., et al. (2016). Direct quantification of transendothelial electrical resistance in organs-on-chips. *Biosens. Bioelectron.* 85, 924–929. doi: 10.1016/j.bios.2016.06.014

Veltman, K., Hummel, S., Cichon, C., Sonnenborn, U., and Schmidt, M. A. (2012). Identification of specific miRNAs targeting proteins of the apical junctional complex that simulate the probiotic effect of *E. coli* Nissle 1917 on T84 epithelial cells. *Int. J. Biochem. Cell Biol.* 44, 341–349. doi: 10.1016/j.biocel.2011.11.006

Walter, F. R., Valkai, S., Kincses, A., Petneházi, A., Czeller, T., Veszelka, S., et al. (2016). A versatile lab-on-a-chip tool for modeling biological barriers. *Sensors Actuators B Chem.* 222, 1209–1219. doi: 10.1016/j.snb.2015.07.110

Wills, N. K., Lewis, S. A., and Eaton, D. C. (1979). Active and passive properties of rabbit descending colon: a microelectrode and nystatin study. *J. Membr. Biol.* 45, 81–108. doi: 10.1007/BF01869296

Xu, Y., Xie, X., Duan, Y., Wang, L., Cheng, Z., and Cheng, J. (2016). A review of impedance measurements of whole cells. *Biosens. Bioelectron.* 77, 824–836. doi: 10.1016/j.bios.2015.10.027

Yang, G., Long, H., Tian, H., Luo, S., and Huang, H. (2008). "Bioimpedance measurement: modeling of coplanar electrodes and impedance characterization," in *2008 2nd International Conference on Bioinformatics and Biomedical Engineering* (Shanghai: IEEE), 1248–1251.

Yeste, J., Illa, X., Gutierrez, C., Sole, M., Guimera, A., and Villa, R. (2016). Geometric correction factor for transepithelial electrical resistance measurements in transwell and microfluidic cell cultures. *J. Phys. D. Appl. Phys.* 49:375401. doi: 10.1088/0022-3727/49/37/375401

Yufera, A., and Rueda, A. (2008). A method for bioimpedance measure with four- and two-electrode sensor systems. *Conf. Proc. IEEE Eng. Med. Biol. Soc.* 2008, 2318–2321. doi: 10.1109/IEMBS.2008.4649662

Zanoni, M., Piccinini, F., Arienti, C., Zamagni, A., Santi, S., Polico, R., et al. (2016). 3D tumor spheroid models for *in vitro* therapeutic screening: a systematic approach to enhance the biological relevance of data obtained. *Sci. Rep.* 6:19103. doi: 10.1038/srep19103

Zeissig, S., Burgel, N., Gunzel, D., Richter, J., Mankertz, J., Wahnschaffe, U., et al. (2007). Changes in expression and distribution of claudin 2, 5 and 8 lead to discontinuous tight junctions and barrier dysfunction in active Crohn's disease. *Gut* 56, 61–72. doi: 10.1136/gut.2006.094375

Conflict of Interest: TG, SN, and VP are affiliated with SRC Bioclinicum; AT is affiliated with art photonics GmbH.

The remaining authors declare that the research was conducted in the absence of any commercial or financial relationships that could be construed as a potential conflict of interest.

frontiers in Bioengineering and Biotechnology

ORIGINAL RESEARCH
published: 21 February 2020
doi: 10.3389/fbioe.2020.00109

Two-Dimensional Cellular and Three-Dimensional Bio-Printed Skin Models to Screen Topical-Use Compounds for Irritation Potential

Zhengxi Wei[1†], Xue Liu[1†], Masato Ooka[1], Li Zhang[1], Min Jae Song[1,2], Ruili Huang[1], Nicole C. Kleinstreuer[3], Anton Simeonov[1], Menghang Xia[1] and Marc Ferrer[1]**

[1] Division of Pre-Clinical Innovation, National Center for Advancing Translational Sciences, National Institutes of Health, Rockville, MD, United States, [2] 3D Bioprinting Core, National Eye Institute, Bethesda, MD, United States, [3] Division of the National Toxicology Program, National Institute of Environmental Health Sciences, National Institutes of Health, Research Triangle Park, NC, United States

OPEN ACCESS

Edited by:
Elena Martinez,
Institute for Bioengineering of Catalonia (IBEC), Spain

Reviewed by:
Matjaž Jeras,
University of Ljubljana, Slovenia
Pavel Makarevich,
Lomonosov Moscow State University, Russia

***Correspondence:**
Menghang Xia
mxia@mail.nih.gov
Marc Ferrer
marc.ferrer@nih.gov

[†] These authors have contributed equally to this work

Specialty section:
This article was submitted to Tissue Engineering and Regenerative Medicine, a section of the journal Frontiers in Bioengineering and Biotechnology

Received: 03 October 2019
Accepted: 03 February 2020
Published: 21 February 2020

Citation:
Wei Z, Liu X, Ooka M, Zhang L, Song MJ, Huang R, Kleinstreuer NC, Simeonov A, Xia M and Ferrer M (2020) Two-Dimensional Cellular and Three-Dimensional Bio-Printed Skin Models to Screen Topical-Use Compounds for Irritation Potential. Front. Bioeng. Biotechnol. 8:109. doi: 10.3389/fbioe.2020.00109

Assessing skin irritation potential is critical for the safety evaluation of topical drugs and other consumer products such as cosmetics. The use of advanced cellular models, as an alternative to replace animal testing in the safety evaluation for both consumer products and ingredients, is already mandated by law in the European Union (EU) and other countries. However, there has not yet been a large-scale comparison of the effects of topical-use compounds in different cellular skin models. This study assesses the irritation potential of topical-use compounds in different cellular models of the skin that are compatible with high throughput screening (HTS) platforms. A set of 451 topical-use compounds were first tested for cytotoxic effects using two-dimensional (2D) monolayer models of primary neonatal keratinocytes and immortalized human keratinocytes. Forty-six toxic compounds identified from the initial screen with the monolayer culture systems were further tested for skin irritation potential on reconstructed human epidermis (RhE) and full thickness skin (FTS) three-dimensional (3D) tissue model constructs. Skin irritation potential of the compounds was assessed by measuring tissue viability, *trans*-epithelial electrical resistance (TEER), and secretion of cytokines interleukin 1 alpha (IL-1α) and interleukin 18 (IL-18). Among known irritants, high concentrations of methyl violet and methylrosaniline decreased viability, lowered TEER, and increased IL-1α secretion in both RhE and FTS models, consistent with irritant properties. However, at low concentrations, these two compounds increased IL-18 secretion without affecting levels of secreted IL-1α, and did not reduce tissue viability and TEER, in either RhE or FTS models. This result suggests that at low concentrations, methyl violet and methylrosaniline have an allergic potential without causing irritation. Using both HTS-compatible 2D cellular and 3D tissue skin models, together with irritation relevant activity endpoints, we obtained data to help assess the irritation effects of topical-use compounds and identify potential dermal hazards.

Keywords: skin irritation, bio-printing, reconstructed human epidermis, full thickness skin tissue, skin sensitization, Toxicology in the 21st Century, high throughput screen

INTRODUCTION

Skin provides a physical barrier to protect the body from environmental insults, including chemical agents (Liu et al., 2016). In the context of regulatory hazard classification (Safety and Administration, 2012), chemicals that cause reversible local skin tissue damage upon dermal exposure are defined as skin irritants. Assessment of skin irritancy is a regulatory requirement in the safety evaluation of industrial and consumer products. Traditionally, irritation potential is evaluated by the Draize test, an acute toxicity test used by the FDA (Draize et al., 1944), which applies a patch containing the test substance directly to rabbit skin. In consideration of animal welfare, in the last decade, the cosmetics industry in the EU, Israel, India, Norway, Turkey, Australia, and New Zealand have been mandated to use RhE tissues for evaluating skin irritation and corrosion potential of cosmetics ingredients and products as an alternative to animal testing (OECD, 2004, 2015; Tornier et al., 2006; Co-operation and Development, 2013). Most RhE skin equivalents are tissues made with keratinocytes that model a stratified epidermis, but have the following drawbacks: (1) these models do not have the sample throughput needed for large scale profiling of compounds at different doses; and (2) they do not reproduce the physiological complexity found in human skin tissue, including the lack of cell-cell interactions between keratinocytes and fibroblasts in the dermis layer. These cell-cell interactions are important for the normal function of skin as a physical barrier for the body, including formation of epidermal-dermal junction, epidermal differentiation, and stratification (El Ghalbzouri et al., 2005; Wojtowicz et al., 2014). Their absence in a cellular model of the skin can result in the lack of immunological responses relevant to irritation effects caused by compounds (El-Ghalbzouri et al., 2002; Hänel et al., 2013; Sriram et al., 2015). Therefore, there is a need for a platform of cellular assays that enables the large-scale screening of compounds while producing data that are relevant to and predictive of irritation responses in humans.

In vitro cellular models for large scale drug testing currently rely on 2D cellular monolayers because of practical considerations and ease of implementation. For example, high batch-to-batch and well-to-well reproducibility and robust changes in assays are critical for HTS. However, these 2D cellular models have low physiological relevance and limited clinical predictive value. In spite of their low predictability of *in vivo* irritation responses, 2D cellular models can provide a first indication to prioritize the test substances to determine whether compounds will have toxic effects *in vivo*. In our strategy, a platform of cellular assays was developed to help predict the skin irritation potential of topical-use chemicals. We first used a cytotoxicity assay with keratinocytes grown in 2D monolayer. Compounds that were active in these assays were then further tested for irritation activity using biofabricated 3D skin tissue models. The recent advances in tissue biofabrication techniques, including the use of bioprinting technologies, enables the reproducible production of biofabricated biological tissues (Lee et al., 2013; Ng et al., 2018). It has been shown that bioprinting allows for the controlled formation of layered 3D skin tissues in a multiwell plate format (Derr et al., 2019). The bioprinting protocols are very versatile so that additional physiological complexity can be included to more closely mimic native human skin and create a more physiologically relevant assay system for compound testing.

In this study, several assay readouts were developed with both of the 3D models, RhE and FTS, including cell viability, TEER, and the secretion level of IL-1α and IL-18 which are relevant to irritation and sensitization skin responses. TEER is commonly used to measure the tight junction integrity of an epithelial monolayer and assess skin barrier function (Srinivasan et al., 2015). Damage produced by both irritants and sensitizers on keratinocytes in the epidermis is associated with release of IL-1α as a primary defense event (Galbiati et al., 2014; Worm, 2014). It has been shown that RhE models recapitulate this response when treated with irritants (Poumay et al., 2004). Keratinocytes also produce IL-18 when exposed to irritants (Companjen et al., 2000). The cleavage and release of IL-18 has been used as a biomarker to distinguish sensitizers from irritants in RhE models (Corsini et al., 2009). Thus, the IL-1α and IL-18 secretion levels in RhE and FTS models were used to assess the irritation potential of selected topical-use compounds.

The ability of the proposed assays as a screening tool to quickly and efficiently test environmental chemicals for their skin irritation potential was assessed by implementing a chemical library screen. We selected 451 topical-use compounds which included 55 OECD reference substances and 396 topical-use chemicals from the Tox21 10K chemical library. The 451 compounds were first tested by using a cell viability assay of keratinocytes grown in a 2D monolayer, enabling quick detection of potential irritants. Of the 451 compounds tested, 46 were further evaluated in the validated biofabricated RhE and FTS models developed in 96-well plate format. Measurement endpoints included tissue viability, TEER, and cytokine secretion analysis, which enabled determination of the irritation potential of compounds as well as potential sensitization effects. The workflow of this study is summarized in **Figures 1A,B**. The platform identified known irritants and also allowed us to distinguish the potential sensitizer activity of some compounds.

Abbreviations: 2D, two-dimensional; 3D, three-dimensional; ALI, air-liquid interface; ATCC, American Tissue Culture Collection; CPSCPSC, Consumer Product Safety Commission; CTG-3D, CellTiter-Glo® 3D; DMEM, Dulbecco's Modified Eagle Medium; EU, European Union; FDA, Food and Drug Administration; FDM, fully supplemented dermal medium; FTS, full thickness skin; GA-1000, Gentamicin sulfate-Amphotericin; H&E, hematoxylin and eosin; HTS, high throughput screening; IHC, immunohistochemistry; IL-1α, interleukin 1 alpha; IL-18, interleukin 18; KGM, keratinocyte growth media; KRT 10, keratin-10; MSD, Meso Scale Discovery; NCATS, National Center for Advancing Translational Sciences; NDF, neonatal human dermal fibroblast; NHEK, normal human epidermal keratinocytes NHEK/SVTERT3-5; NKTC, human primary neonatal keratinocytes; OECD, Organization for Economic Co-operation and Development; PBS, phosphate buffered saline; PBST, phosphate buffered saline with 0.05% Tween 20®; RhE, reconstructed human epidermis; SB, stratum basale; SC, stratum corneum; SD, standard deviation; SG, stratum granulosum; SP, stratum spinosum; TEER, transepithelial electrical resistance; Tox21, Toxicology in the 21st Century.

MATERIALS AND METHODS

Compound Library

The Tox21 10K chemical library consists of approximately 10,000 (~8300 unique) small molecules including pesticides, drugs, industrial chemicals, and food additives, commercially sourced by the NTP, NCATS, and EPA (Attene-Ramos et al., 2013; Tice et al., 2013). Skin related chemicals such as topical-use drugs, cosmetic ingredients, and pesticides with dermal exposure risk were selected as a subset library for this study. Also, references chemicals in OECD's test guidelines: 404, 430, 431, 435, and 439 (Griesinger et al., 2009) were included.

Cell Line and Culture Conditions

Human primary neonatal keratinocytes and KGM were purchased from Sciencell (Catalog number of the cell: 2100, catalog number of the media: 2101, Carlsbad, CA, United States). hTERT and SV40 early region immortalized NHEK were purchased from Evercyte (Vienna, Austria). The cells were cultured in KGM-2 Bullet Kit (Lonza, Walkersville, MD, United States) without adding GA-1000. Neonatal human dermal fibroblast (NDF) were purchased from the ATCC (Catalog number: PCS-201-010, Manassas, VA, United States). Fibroblasts were maintained in minimal essential medium (MEM) supplemented with 5% FBS (Thermo Fisher Scientific,

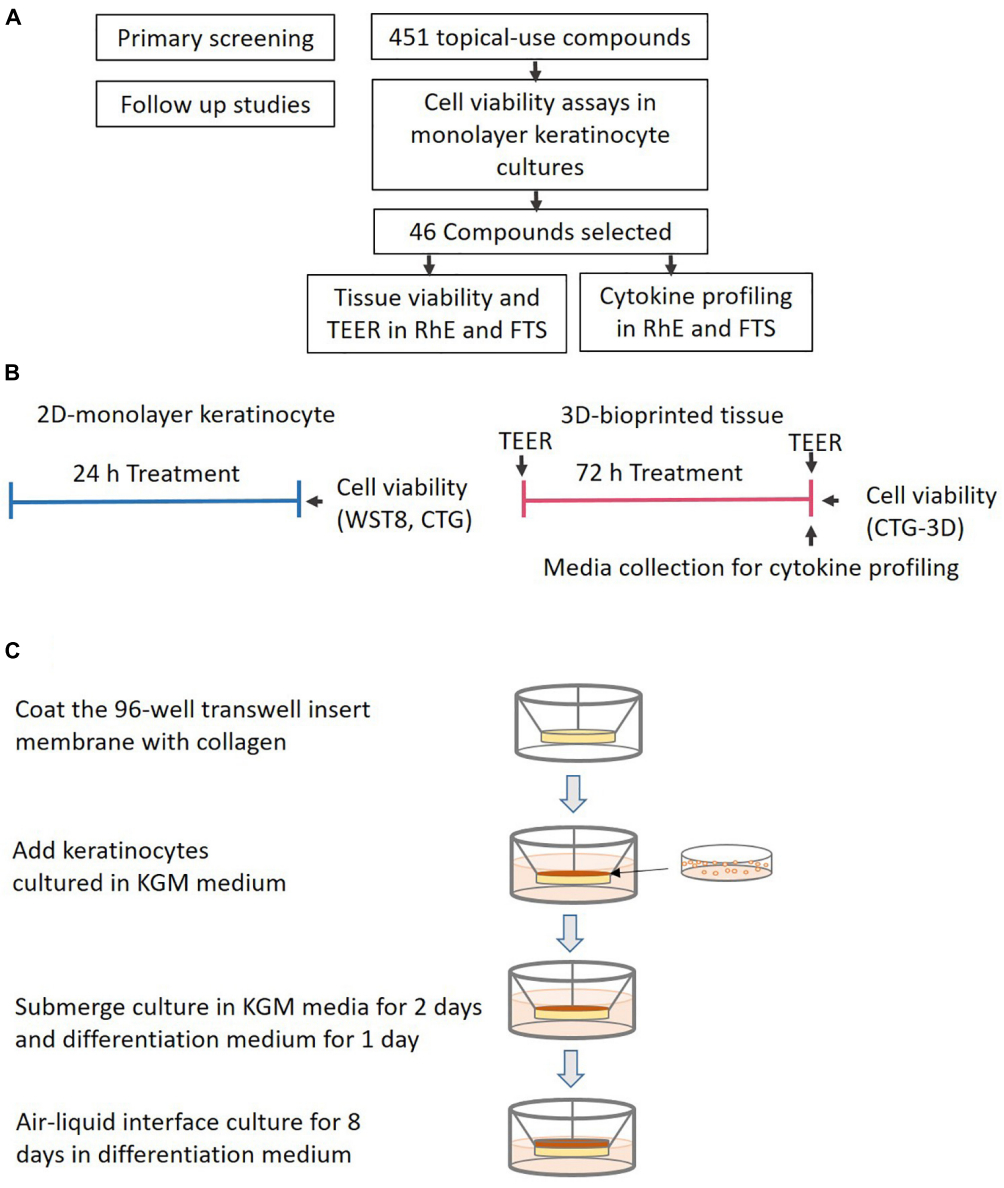

FIGURE 1 | Continued

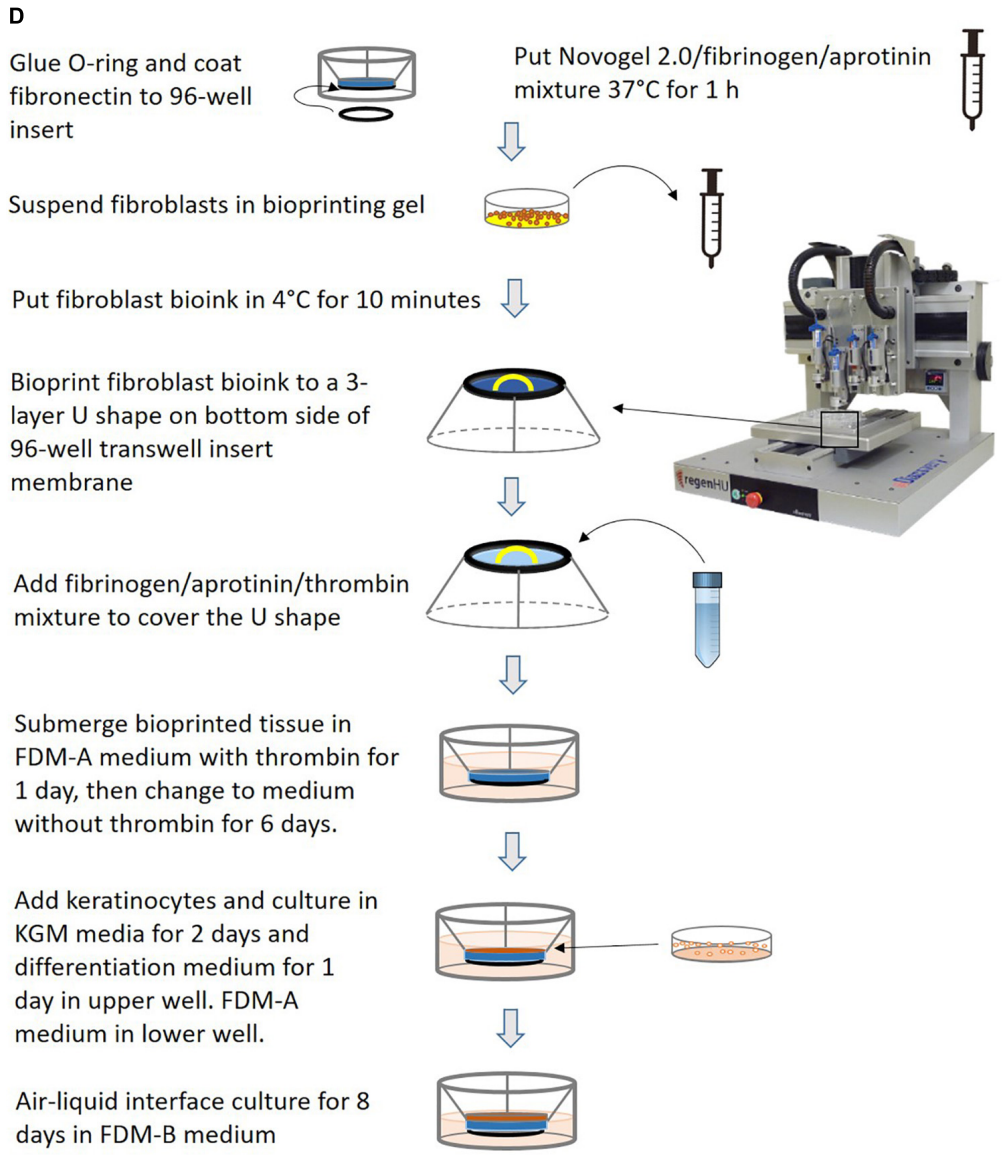

FIGURE 1 | (A) A flowchart for the identification of potential irritants. **(B)** A schematic signifying the comparison of test timelines and endpoints between the 2D monolayer culture and 3D bio-fabricated tissues. **(C)** A diagram of the generation of the bio-fabricated RhE model. **(D)** A schematic drawing of the bio-printing method for the FTS model.

Waltham, MA, United States). The cells within passage 3–4 were used. All the cells were maintained at 37°C under a humidified atmosphere and 5% CO_2. All the cultures were routinely monitored for mycoplasma contamination using MycoAlert™ PLUS mycoplasma detection kit (Lonza, Walkersville, MD, United States).

Cell Viability Assays in Human Primary Neonatal Keratinocytes and Normal Human Epidermal Keratinocytes

Human primary neonatal keratinocytes and normal human epidermal keratinocytes were seeded at 2000 cells/well/4 μL of culture medium into 1536-well black wall, clear bottom plates (Greiner Bio-One, Monroe, NC, United States) using a Multidrop™ Combi (Thermo Fisher Scientific). The cells were incubated at 37°C for 5 h for attachment. Then 23 nL of the compounds were transferred to the assay plates to reach final concentrations from 0.4 nM to 92 μM. The cells were treated for 24 h.

The cell viability of human primary neonatal keratinocytes and normal human epidermal keratinocytes was measured by using a Cell Counting Kit (WST8, Dojindo, Rockville, MD, United States) multiplexed with CellTiter-Glo® Luminescent Cell Viability Assay (Promega, Madison, WI, United States). Tetra-octylammonium bromide was the positive control for data

normalization. After compound treatment for 22 h, 1 μL WST8 reagent was added into each well. The plates were incubated at 37°C for 2 h before measuring absorbance at 450 nm by PHERAstar™ microplate reader. After measuring absorbance reading, 4 μL CellTiter-Glo® reagent was added to each well. The luminescence signal was measured with a ViewLux™ plate reader after a 30 min incubation at room temperature.

Generation of RhE Model

RhE was generated as previously described (Smits et al., 2017). A schematic of the process is shown in **Figure 1C**. In brief, HTS-96 transwell inserts with 0.4 μm pore size polycarbonate membranes (HTS Transwell-96, 3381, Corning, NY, United States) were treated with 50 μL of rat tail collagen (100 μg/mL) in (PBS, Corning, NY, United States) for 1 h at room temperature. The collagen solution was kept cold before usage. The transwell insert was then rinsed once with 100 μL of sterile cold PBS. Fifty μL of a human neonatal primary keratinocytes suspension (2×10^5 cell/cm^2 in KGM media) were seeded by pipetting on top of the membrane of the transwell insert. The cells were cultured submerged in 50 μL KGM media for 2 days. Afterward, the media was changed to keratinocyte differentiation media for another 24 h. The keratinocyte differentiation media consists of CnT-PR-3D media (Zen-Bio, Research Triangle Park, NC, United States) and Dulbecco's Modified Eagle Medium (DMEM, Thermo Fisher Scientific) with a 3:2 ratio. The tissues were then cultured in an ALI with 400 μL of keratinocyte differentiation medium in the base plate well, with no media in the transwell, for 8 days. The transwell insert was placed on a custom lifter (6 mm height), between the base plate and the insert tray, in order to add enough volume of media in the base plate well. The culture medium was changed every other day. All the cultures were routinely monitored for mycoplasma contamination using a MycoAlert™ PLUS mycoplasma detection kit (Lonza).

Bio-Printing of 3D Human Dermis in 96-Well Plate

The schematics for the bio-printing of the dermis are shown in **Figure 1D**. A custom 3D-printed polycarbolactone (PCL) O-ring (outside diameter 6 mm, inside diameter 5 mm, height 700 μm) was glued with bio-friendly silicon glue (Kwik-cast sealant, World Precision Instrument, Sarasota, FL, United States) onto the bottom of each well of a Corning® HTS Transwell® plate -96 Permeable Supports with 1 μm polyester pore size membrane (Catalog number 3381, Corning, NY, United States). The O-ring provided a sealed wall around the dermis compartment. The membranes of the transwell inserts were coated with 50 μL of fibronectin solution (0.03 mg/mL in distilled water) for 1 h at room temperature the night before printing. A mixture of Novogel 2.0 (60 mg/mL, Organovo, San Diego, CA, United States), fibrinogen (2.5 mg/mL) and aprotinin (0.075 unit/mL in DPBS, Sigma-Aldrich, St. Louis, MO, United States) was prepared as bioprinting hydrogel. On the day of printing, the prepared bioprinting hydrogel was kept in a 37°C water bath for 1 h before use. Neonatal fibroblasts were suspended with 1 mL printing hydrogel at a concentration of 8×10^6 cells/mL in a 2.5 mL syringe (RegenHU, Villaz-Saint-Pierre, Switzerland). The cell mixture was refrigerated at 4°C for 10 min to allow gelation before mounting on to the bioprinter (RegenHU, Villaz-Saint-Pierre, Switzerland). A 3-layer U-shaped pattern was bioprinted with the cell/hydrogel mixture, with a total volume of 5 μL/transwell, onto the bottom side of the transwell insert membrane. This structure was covered with 25 μL fibrinogen (4.5 mg/mL), aprotinin (0.075 unit/mL), and thrombin mixture (1 unit/mL) solution in DPBS using a pipet. The freshly bioprinted tissues were kept at room temperature for 15 min before adding 200 μL of fully supplemented dermal medium A (FDM-A; supplemented components in **Supplementary Table 3**) with 1 unit/mL thrombin in the basal side. This hydrogel mixture provided a proper ECM for the fibroblasts to migrate. The cells in the printed structure together with the added hydrogel formed the 3D structure of the dermis. Fifty μL of the same FDM-A media supplemented with thrombin was then added in the apical side. The tissues were incubated at room temperature for 2 h and moved to the 37°C with 5% CO_2, 95% humidity incubator afterward. The tissues were maintained in FDM-A supplemented with thrombin for 24 h. The media was then switched to FDM-A without thrombin and incubated for another 6 days. The medium of tissues cultured in the base plate and transwell was changed every other day.

Generation of FTS Model

The schematics for the generation of FTS are shown in **Figure 1D**. On day 8 of dermis tissue incubation, 50 μL of a human neonatal primary keratinocytes suspension (2.0×10^5/cm^2 in KGM) were pipetted into the apical side of the transwell insert while the bioprinted dermis remained on the bottom side. The transwell insert was rested on a custom lifter (6 mm height) between the base plate and the insert tray in order to leave enough room for the ALI step. The tissue was incubated with 450 μL FDM-A medium (see **Supplementary Table 3**) in the base plate well and 100 μL KGM medium in the apical insert well. After 48 h, the apical medium was changed to differentiation medium (see section "Generation of RhE Model") for another 24 h. Then the tissue was ALI cultured for 8 days with 350 μL FDM-B medium (see **Supplementary Table 3**) in the base plate well compartment and no media in the apical insert. All the cultures were routinely monitored for mycoplasma contamination using MycoAlert™ PLUS mycoplasma detection kit (Lonza, Walkersville).

Tissue Embedding and Cryosectioning

Reconstructed human tissues were fixed in 4% paraformaldehyde overnight at 4°C. The tissue was washed in PBS three times for 15 min each. The tissue was then taken through a gradient of 15% and 30% weight/volume sucrose in PBS. Whole tissues were removed from sucrose, blotted dry, and embedded in Tissue-Tek CRYO-OCT Compound (Andwin Scientific, Tryon, NC, United States). Blocks were stored at −80°C, sectioned on a Leica

CM3050 S cryostat into 12 μm thick sections, and placed on SuperFrost™ Plus slides (Thermo Fisher Scientific).

Immunostaining and Imaging

The immunostaining of the tissue was prepared using fully automated IHC machine (BOND RXm, Leica Biosystems, IL, United States). Tissue sections were incubated for 3 min with 1X Leica Bond Wash solution (10X Bond wash was diluted using deionized water, Leica Microsystems, Catalog number AR9590) and blocked for 20 min with 2% normal goat serum in PBS. The slides were incubated with primary antibodies (dilution factor and resources in **Supplementary Table 3**) at 150 μL/slide using Leica Microsystems M211518 for 1.5 h, followed by three washes with 1X Leica Bond Wash solution at room temperature. Thereafter, the slides were incubated with secondary antibodies at room temperature with 1:2000 Hoechst for 20 min followed by three washes with 1X Leica Bond Wash solution. Images of the slides were captured using Leica TCS SP8 MP multiphoton microscope with a 25x water objective lenses and processed using Leica LAS X software.

For H&E staining, sections were placed at room temperature for 10 min. The sections then underwent standard H&E (Thermo Fisher Scientific) staining. Brightfield photographs (20X or 40X) were made with an EVOS® Life technology microscope.

Transepithelial Electrical Resistance Measurements

Transepithelial electrical resistance measurements were acquired from the ALI on day 8 using an automated TEER measurement system (World Precision Instruments, Sarasota, FL, United States). The transwell was filled with 100 μL DPBS in the apical region. The contribution of the PET membrane was measured and subtracted from the sample values. TEER final values in Ω^*cm^2 were obtained by multiplying the electrical resistance with the skin surface area. Any tissue with a TEER value lower than 500 Ω^*cm^2 was not used in this research (Matsusaki et al., 2015).

Cell Viability in RhE and FTS Models

Tissue viability was measured by using CellTiter-Glo® 3D (CTG-3D) luminescent cell viability assay (Promega). CTG-3D was mixed with DPBS at 1:2 volume to volume ratio; 100 μL of the diluted CTG-3D was added to the upper compartment of each transwell and 200 μL of the diluted CTG-3D was added to the lower compartment. The tissues were incubated at 37°C for 30 min before harvesting by puncturing the tissues with 20 μL pipet tips. The whole plate was shaken on a rocker for 30 min at room temperature to mix the liquids in the upper and lower compartments. Fifty μL of the liquid was transferred to white solid 96-well plates and the luminescence activity was read by Viewlux™ plate reader.

Measurement of Secreted Cytokine Level

The medium from each well with tissue was collected before tissue harvesting and stored at −80°C in aliquots. According to the U-PLEX manufacturer's protocol, antibodies against IL-1α and IL-18 were coated onto MSD 96-well plates and the plates were shaken at room temperature for 1 h. Fifty μL of experimental samples and cytokine standards were added to each well after washing off the excessive unbound antibodies with PBS and Tween 20® (PBST; 0.05% Tween 20®) three times. Detection antibody was added to each well after shaking the whole plate on an orbital shaker at the speed of 700 rpm/min overnight at 4°C. Each well was washed three times with 0.05% PBST before adding 2X reading buffer. Electrochemiluminescence was measured using a MESO QuickPlex SQ 120 reader.

Data Analysis

Monolayer Cell Viability Data Analysis

Data normalization and concentration-response curve fitting for the data from the qualitative high throughput screen (qHTS) and follow up studies were performed as previously described (Huang, 2016). Briefly, raw plate reads for each titration point were first normalized relative to the positive control compound and DMSO-only wells (Benzalkonium chloride = −100%, DMSO = 0%) as follows:% Activity = $[(V_{compound} - V_{DMSO})/(V_{pos} - V_{DMSO})] \times 100$, where $V_{compound}$ denotes the compound well values, V_{pos} denotes the median value of the positive control wells, and V_{DMSO} denotes the median values of the DMSO-only wells, and then corrected by applying an NCATS in-house pattern correction algorithm using compound-free control plates (such as, DMSO-only plates) at the beginning and end of the compound plate stacks. Concentration-response titration points for each compound were fitted to a four-parameter Hill equation yielding concentrations of half-maximal inhibitory activity (IC_{50}) and maximal response (efficacy) values.

Tissue Viability Data Analysis

The luminescence activity was normalized to the fold of change over 1% DMSO (vehicle control). The means and SDs were calculated by three replicate plates and reported as fold-change over vehicle control.

Tissue TEER Data Analysis

Raw reads of the TEER value (Ω^*cm^2) for tissue were reported for the 46 compounds in 3 replicate plates. The means and SDs of TEER values in concentration-response curves of selected compounds were normalized to 1% DMSO and reported as fold of change over vehicle control.

Cytokine Data Analysis

Interleukin 1 alpha and IL-18 cytokine level of each well was calculated according to the standard curves by DISCOVERY WORKBENCH Software v 4.0 (Meso-Scale Discovery, Rockville, MD, United States). The relative increase or decrease of cytokine levels was normalized to the fold-change over 1% DMSO (vehicle control). The means and SDs were calculated by three replicate plates and reported as fold-change over vehicle control.

Statistical analyses were performed using GraphPad Prism software 7.0 (San Diego, CA, United States). Student *t*-test with

the Holm–Sidak posttest was used for statistically significant analyses that involved three experimental groups.

RESULTS

Cytotoxic Effects of Topical-Use Chemicals in 2D Monolayer Cell Cultures

A total of 396 topical chemicals from the Tox21 10K library and 55 OECD reference chemicals were tested in neonatal primary keratinocytes (NKTC) and immortalized human keratinocytes (NHEK) for cytotoxic activity. Keratinocytes growing as a monolayer were treated with chemicals at 11 concentrations ranging from 100 nM to 92 μM in 1536-well plates for 24 h. Cell viability was then measured using CellTiter-Glo® and WST-8 reagents. The 46 chemicals showing cytotoxicity in both cell lines (efficacy > 50% cell death) were selected and further tested in RhE and FTS models. The IC_{50} and % efficacy values of 46 chemicals are reported in **Supplementary Table 1**, and the cytotoxic activity of all 451 chemicals is reported in **Supplementary Table 4**.

Characterization of Skin Morphogenesis in RhE and FTS Models

H&E and IHC staining were performed to verify the generation of typical human epidermal morphological features for the biofabricated RhE and FTS. One of the critical hallmarks of skin maturation is the formation of a cornified envelop in the SC (Sriram et al., 2018). As shown in **Figure 2**, H&E staining of RhE displayed the stratified outermost layer, SC, which is a characteristic of normal human epidermis. The appearance of polarized columnar basal keratinocytes and several layers of spinous granular keratinocytes in the H&E staining indicated the formation of the SB and the SG. Desmoglein-1, a calcium-binding transmembrane glycoprotein component of desmosomes in vertebrate epithelial cells, and claudin-1, an important component in tight junctions, were strongly expressed, showing well-developed cell-cell junction in the viable epidermis. Loricrin and filaggrin, localized in the lamellar body of the SG, also showed strong expression and verified the maturation of the RhE. Expression of KRT 10 indicated post-mitotic terminal differentiation of the RhE. Histological staining of the bio-printed FTS sections also demonstrated fully differentiated epidermis with several viable epidermal layers. As shown in **Figure 2B**, H&E staining highlighted the complex architecture of the FTS for both dermis and epidermis. The formation of the epidermal barrier function was further verified by staining claudin-1 and desmoglein-1 junction proteins that appear in the upper layers of the epithelium. Early differentiation marker KRT-10 indicated an advanced epidermal maturation. The expression of filaggrin and loricrin demonstrated the stratification and cornification of the epidermis. The deposition of basement membrane proteins, collagen IV and collagen VII, showed appropriate anchorage between the epidermis and the dermis.

Verification of Skin Barrier Function of the Biofabricated RhE and FTS Models

To establish that the biofabricated RhE and FTS models had a matured skin barrier function, the TEER assay, a well-established measurement of the integrity of skin barrier function, was conducted (Abdayem et al., 2015; Niehues et al., 2018). Tissues with TEER values above 500 Ω^*cm^2 were used in the compound screening, for both RhE and FTS models (**Figures 2C,D**). As shown in **Figure 2C**, RhE models had TEER values of 2134.9 ± 530.2 Ω^*CM^2 (plate 1, n = 60), 2291.1 ± 346.1 Ω^*CM^2 (plate 2, n = 60), and 2731.0 ± 294.3 Ω^*CM^2 (plate 3, n = 60), which denoted normal skin barrier function. In the FTS models shown in **Figure 2D**, TEER values were 831.5 ± 156.1 Ω^*CM^2 (plate 1, n = 60), 831.7 ± 156.1 Ω^*CM^2 (plate 2, n = 60), and 767.5 ± 184.5 Ω^*CM^2 (plate 3, n = 58). Noticeably, these values from the FTS models were above 500 Ω^*cm^2, though they were lower than the TEER values from RhE models.

Effect of Compounds on Cell Viability and TEER in RhE and FTS Models

To assess the responsiveness of RhE to corrosive substances and irritants, we first examined tissue viability with a few compounds categorized as corrosion substances and irritants (**Supplementary Figures 1A,B**) using the RhE model, as suggested by OECD test guidelines 431 and 439. The benchmark substances, including two corrosives and three irritants from the OECD test guidelines, were tested in triplicate. The relative cell viability was normalized to the PBS-only tissues. Since the application of raw compounds is not possible in an HTS platform, the compounds were dissolved in DMSO and diluted, using PBS, to reach a 200 μM concentration (1% DMSO); they were then added topically for 3 days. We compared our modified protocol (3-day treatment) with the 1 h treatment plus 2-day post incubation protocol from the OECD test guideline 439. As shown in **Supplementary Figure 1C**, continuous treatment for 3 days did not affect the tissue viability in the vehicle control. Interestingly, the intensive washing steps recommended, in the OECD test guideline 439, appears to decrease the tissue viability, as seen in the 1% DMSO vehicle control wells.

We then proceeded to test whether the 46 most cytotoxic chemicals tested in monolayer keratinocytes reduced cell viability in the biofabricated skin tissue models. Seven compounds – pentachlorophenol, methyl violet, D&C red 27, benzethonium chloride, hexachlorophene, benzyldimethyldodecylammonium chloride, and methylrosaniline chloride, – reduced tissue viability in RhE at 200 μM (red bars in **Figure 3A** and * in **Supplementary Table 2**). When these chemicals were tested in the FTS model, only methylrosaniline chloride caused a significant reduction in viability (* in **Figure 3B** and # in **Supplementary Table 2**). The effects of the compounds on TEER were more pronounced in FTS, but heatmap plots (**Figure 5A**) showed a higher concordance between TEER and viability in the RhE model (R^2 = 0.33) than for FTS (R^2 = 0.13).

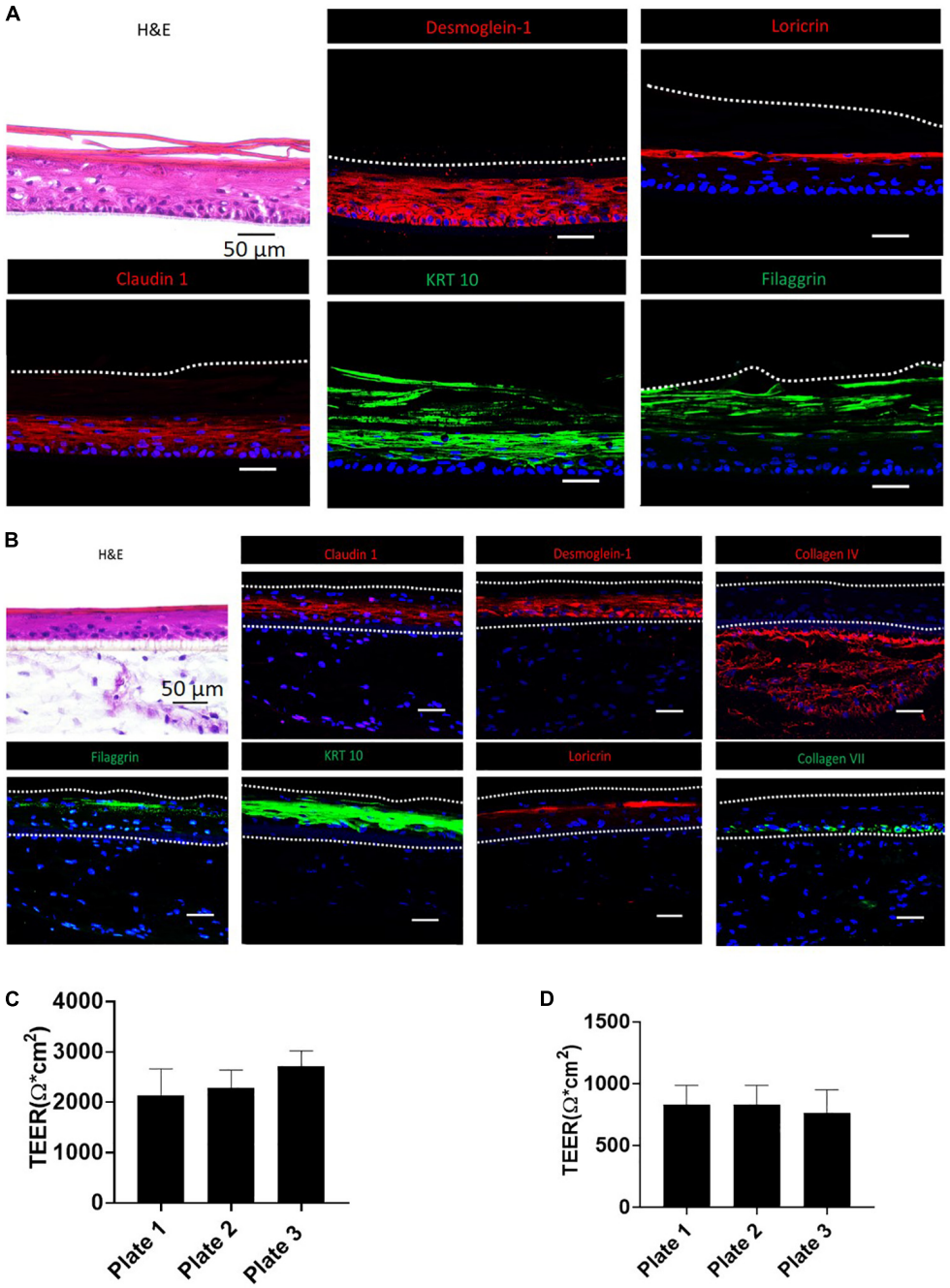

FIGURE 2 | Validation of RhE and FTS models by morphological staining and TEER measurement. **(A)** RhE was harvested at ALI day 8 and cryosectioned or cryopreserved for H&E and biomarker staining of claudin-1, desmoglein-1, filaggrin, keratin-10, and loricrin. **(B)** FTS was harvested at day 21 and cryosectioned or cryopreserved for H&E and biomarker staining of claudin-1, desmoglein-1, collagen IV, filaggrin, keratin-10, loricrin, and collagen VII. **(C)** TEER values, demonstrating barrier function, of RhE models which were replicated in different 96-well HTS plates. **(D)** TEER values of FTS models replicated in different 96-well HTS plates.

Effect of Compounds on IL-1α and IL-18 Secretion in RhE and FTS Models

Interleukin 1 alpha is a central mediator of innate immunity and inflammation (Corsini and Galli, 1998). Additionally, IL-18 secreted by keratinocytes has been proven to be a biomarker for an allergic response (Corsini et al., 2009; Hänel et al., 2013). To evaluate the potential of a compound to induce irritation and sensitization, we used a multiplex electrochemiluminescence assay to quantify the amounts of IL-1α and IL-18 secretion in RhE and FTS models. As shown in **Figure 4A**, hexachlorophene, methyl violet, 1-chloro-2,4-dinitrobenzene, pentachlorophenol, benzyldimethyldodecylammonium chloride, and benzethonium

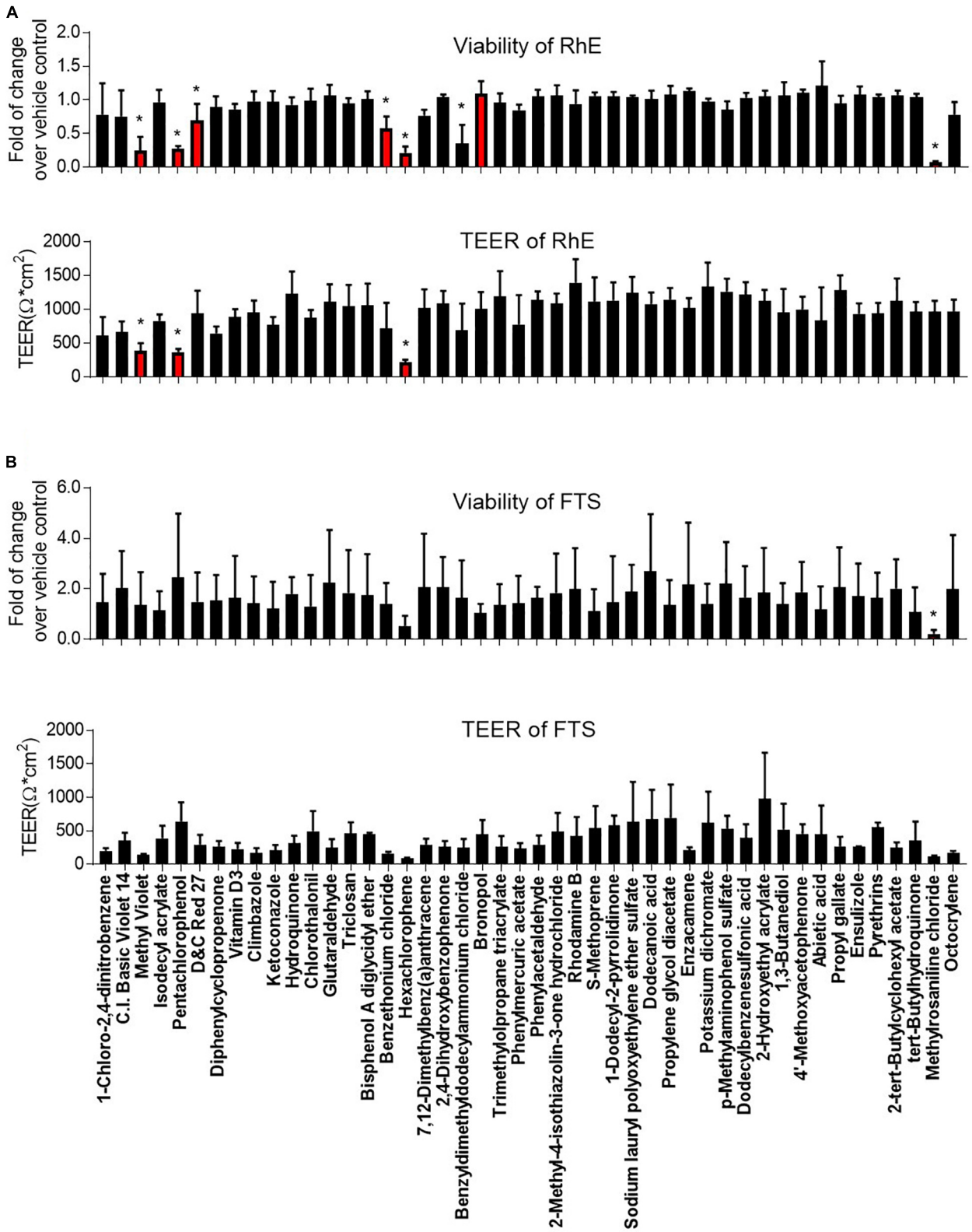

FIGURE 3 | Comparison of viability and TEER in **(A)** RhE and **(B)** FTS models upon treatment of 46 chemicals. The relative increase/decrease of viability level was normalized to the fold of change over 1% DMSO (vehicle control). The mean and SD of viability were calculated by three replicate plates and reported as fold of change over vehicle control. After compound treatment, raw readings of TEER values (Ω*cm2) for three replicate plates of tissues, in each model, were reported. Data are expressed as mean ± SD from triplicate experiments. (*$p < 0.05$).

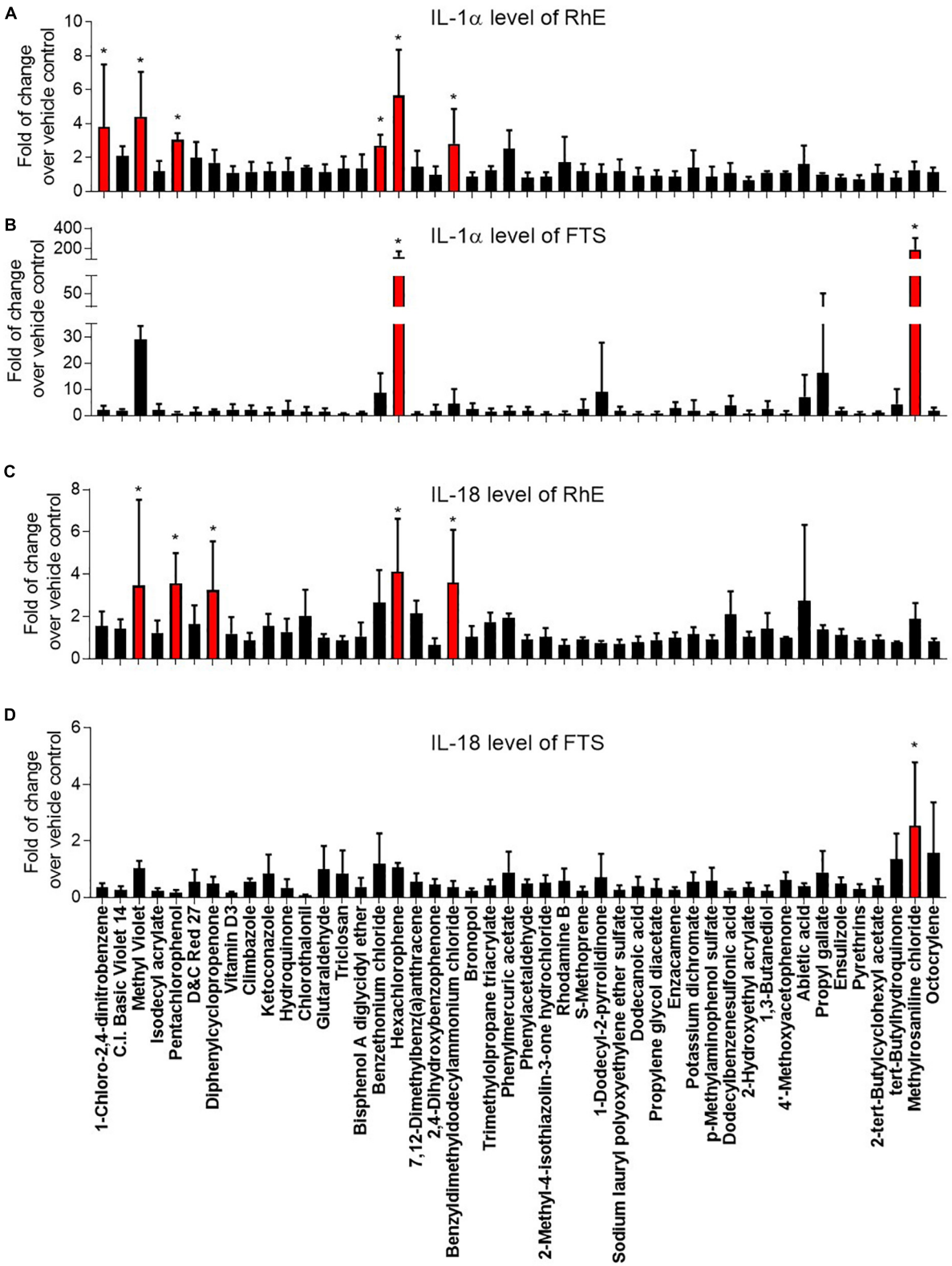

FIGURE 4 | Comparison of secreted IL-1α levels in **(A)** RhE and **(B)** FTS models as well as IL-18 levels in **(C)** RhE and **(D)** FTS models upon treatment of 46 chemicals. The relative increase or decrease of cytokine levels were normalized to the fold of change over 1% DMSO (vehicle control). Data are expressed as mean ± SD from triplicate experiments (*$p < 0.05$).

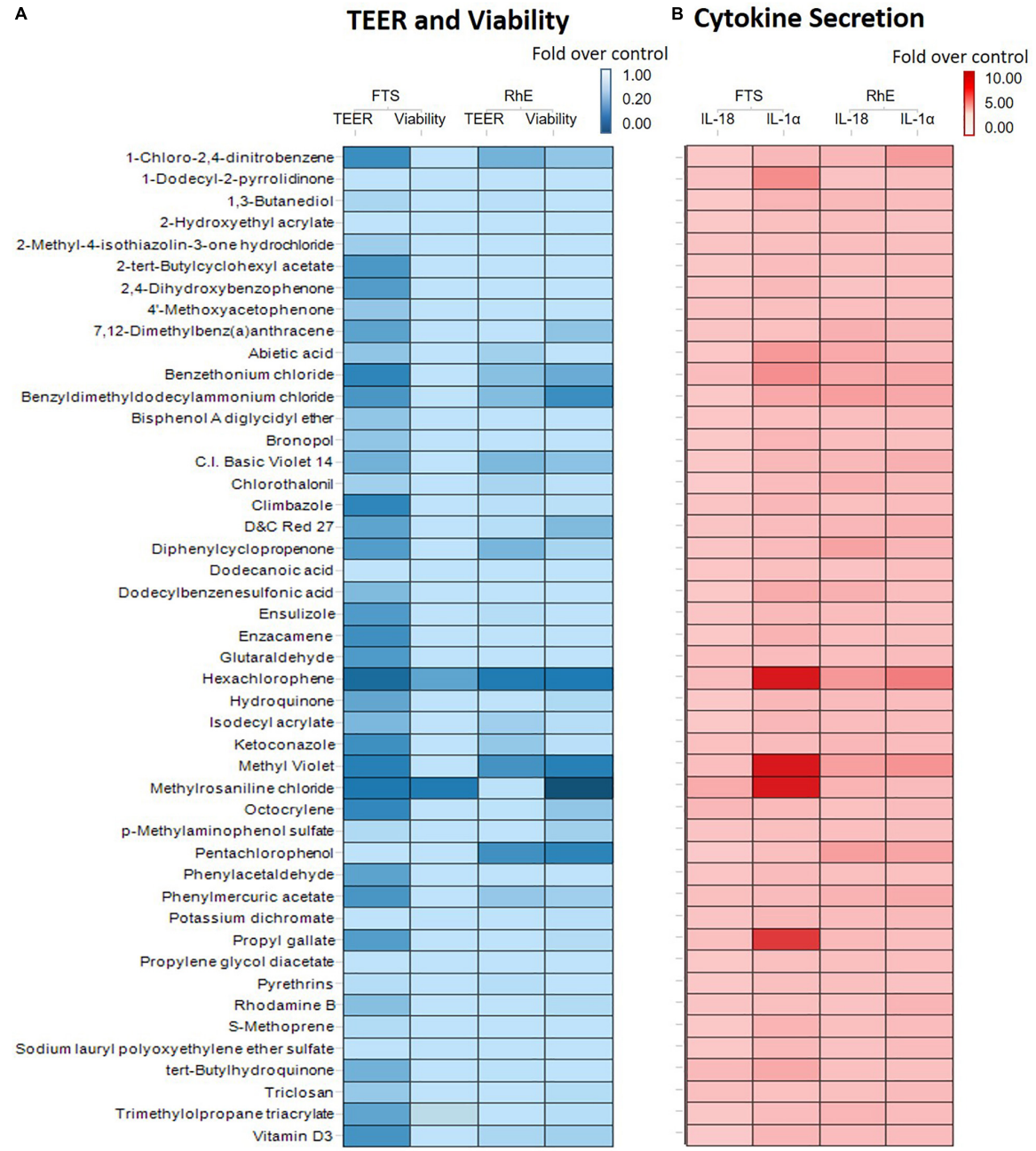

FIGURE 5 | (A) Comparison of viability and TEER using RhE and FTS models. The lightest blue color in the gradient represents 100% barrier integrity in the TEER assay and 100% viable tissue in the viability assay, while the darkest blue color signifies 0% barrier integrity (completely disrupted tight junction) in the TEER assay and 0% viability (dead skin). **(B)** Comparison of secreted IL-1α and IL-18 levels in RhE and FTS models. The lightest red color in the gradient denotes no fold change compared with the vehicle control, symbolizing healthy skin. The darkest red color represents a fold change of 10 or more compared with the vehicle control.

chloride significantly induced IL-1α secretion in the RhE model by 5.7-, 4.4-, 3.8-, 3.0-. 2.8-, and 2.7-fold, respectively. Interestingly, methylrosaniline chloride and hexachlorophene significantly increased IL-1α secretion in the FTS model by 193- and 123-fold, respectively (**Figure 4B**). As shown in **Figure 4C**, hexachlorophene, benzyldimethyldodecylammonium chloride, pentachlorophenol, methyl violet, and diphenylcyclopropenone induced IL-18 secretion, in the RhE model, by 4.1-, 3.6-, 3.6-, 3.5-, and 3.3-fold, respectively. Methylrosaniline chloride elevated the IL-18 level 2.5-fold greater than the vehicle control in the FTS model (**Figure 4D**). Interestingly, the IL-1α secretion was more prominent in the FTS model, while IL-18 elevation was more obvious in the RhE model (**Figure 5B**).

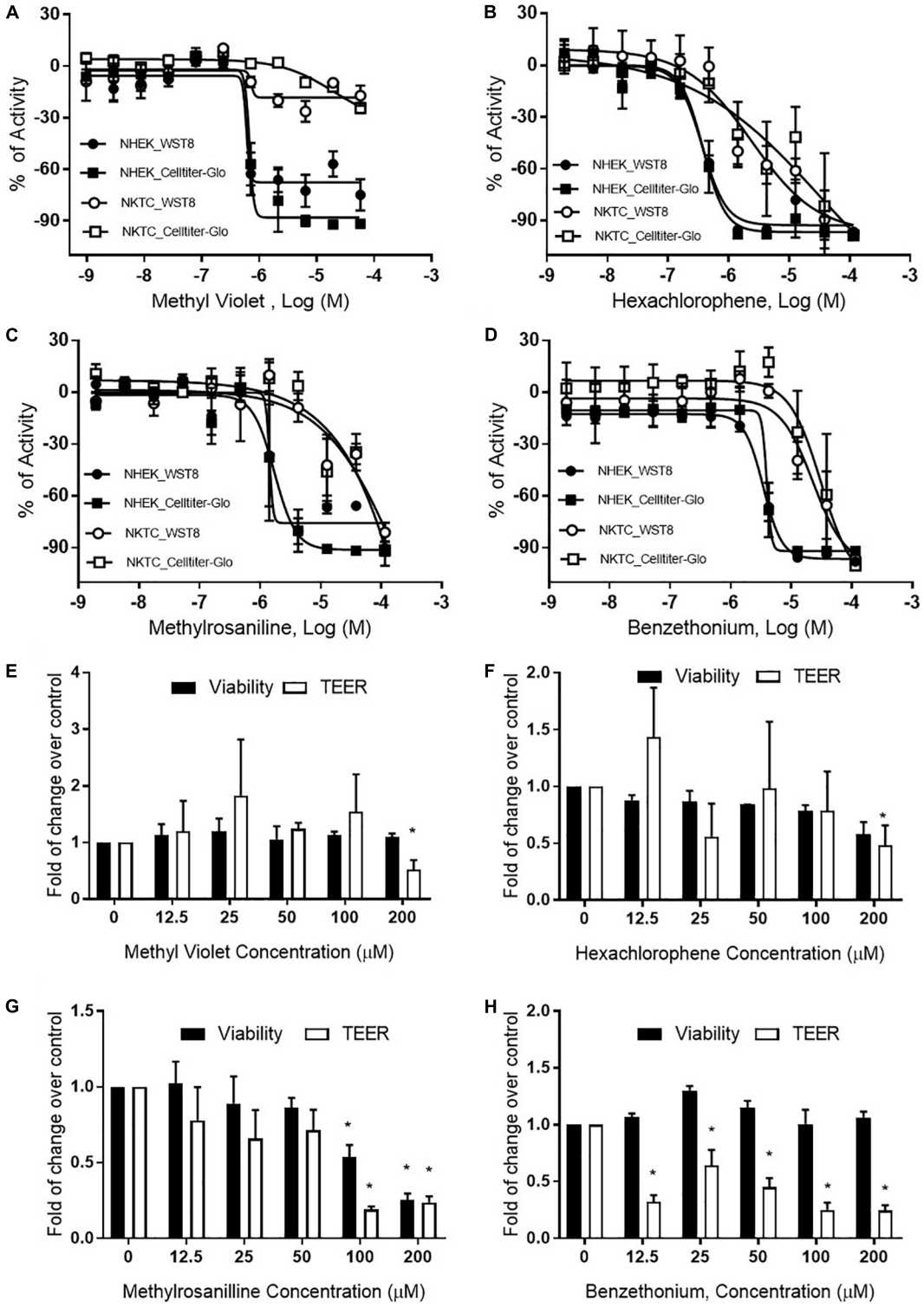

FIGURE 6 | Viability and TEER values of selected chemicals. Cytotoxic effects of **(A)** methyl violet, **(B)** hexachlorophene, **(C)** methylrosaniline, and **(D)** benzethonium in NHEK and NKTC. The viability of each cell type was measured by WST8 and CellTiter-Glo® assays and the percent activity was normalized to the positive control. Concentration-responses of tissue viability and TEER experiments, in FTS, upon treatment of **(E)** methyl violet, **(F)** hexachlorophene, **(G)** methylrosaniline and **(H)** benzethonium. The viability and TEER values were normalized to 1% DMSO (vehicle control). Concentration response curves and bar graphs were expressed as mean ± SD from three biological replicates (*$p < 0.05$).

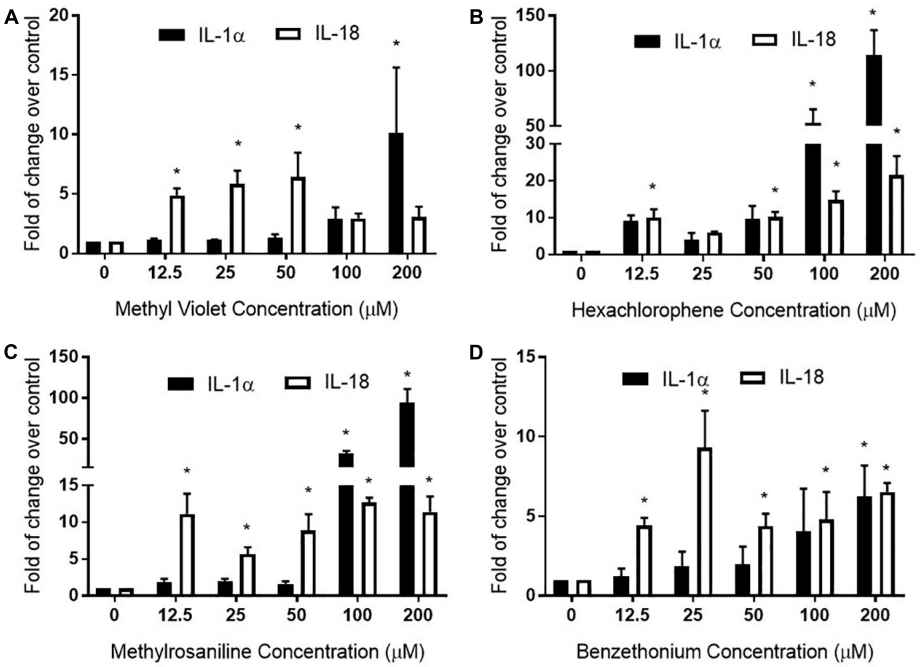

FIGURE 7 | Full thickness skin was treated with **(A)** methyl violet, **(B)** hexachlorophene, **(C)** methylrosaniline, and **(D)** benzethonium in a concentration-dependent manner and the secreted levels of IL-1α and IL-18 were measured. The relative increase or decrease of cytokine levels was normalized to the fold change over 1% DMSO (vehicle control). Concentration-responses were expressed as mean ± SD from three biological replicates (*$p < 0.05$).

Concentration-Response Effects of Selected Compounds in FTS Model

Methyl violet, methylrosaniline, hexachlorophene, and benzethonium which were significantly active in two endpoints compared to vehicle controls, in both RhE and FTS models, were further tested in five concentrations ranging from 12.5 to 200 μM. These compounds had similar IC_{50} values in viability when tested in monolayer keratinocytes (**Figures 6A–D**) but exhibited different cytotoxicity in FTS (**Figures 6E–H**) and distinct cytokine secretion profiles (**Figure 7**). The TEER assay was more sensitive than the viability assay when measuring the integrity of the FTS model; this became evident when 200 μM methyl violet (**Figure 6E**), 200 μM hexachlorophene (**Figure 6F**), and benzethonium (**Figure 6H**) significantly decreased TEER values but did not reduce the tissue viability. Methylrosaniline was the only chemical which significantly reduced TEER and viability. All four of these compounds displayed significant increases in IL-1α and IL-18 secretion levels in a concentration-response manner (**Figure 7**). Of note, the highest concentrations of each compound tested were able to significantly increase IL-1α secretion. Interestingly, only IL-18 level was increased upon the treatment of low concentrations (12.5–50 μM) (**Figure 7**).

DISCUSSION

This study established an integrated monolayer and 3D tissue assay in HTS platform, which enables large-scale dermal toxicology testing. We started with a screen of 451 topical compounds at 11 concentrations using monolayer keratinocyte viability assays. The chemicals showing cytotoxicity in these assays were selected for a single concentration test in bio-fabricated skin tissues. Several dermal toxicants were then selected and studied at multiple concentrations in FTS model. Our results showed the following main findings: (1) RhE is a sensitive model to detect irritant-induced cytotoxicity; (2) FTS model is a better model to detect irritant-induced IL-1α secretion; and (3) the secretion of IL-1α and IL-18 may distinguish chemical's irritation and sensitization potential. Overall, the monolayer culture system accommodates the need of large high throughput primary screening, while RhE and FTS models address more functional endpoints such as barrier function and inflammatory response.

Our study used several novel techniques to produce RhE and FTS models. First, the organotypic skin constructs, produced by bio-printing technology, allowed for controlled spatial cell layering with consistent cellular composition, cellular distribution, and extracellular matrix (ECM) organization. Second, the use of fibrin gel as a bio-printing ink has shown advantages in long term (over 12 weeks) cultures by preventing contraction when compared to conventional collagen-based models (Boehnke et al., 2007; Sriram et al., 2015; Derr et al., 2019). This feature also allows for the topical application of compounds without leakage from the side of the well occurring. When measuring TEER values, a tissue surface coverage of less than 99.6% has previously been shown to cause an 80% drop in barrier function (Florin et al., 2005). The consistent and high TEER values, from both RhE and FTS models developed in this

study, further emphasized that a proper bio-printing ink can provide a full surface area without shrinkage; this accommodates accurate TEER measurements which indicate barrier function integrity. Third, the bio-printed structure can accommodate different research needs by permitting custom printing of tissue onto various sizes of transwell inserts.

OECD test guidelines 431 and 439 use RhE as the *in vitro* model for skin corrosion and irritation tests (Co-operation and Development, 2013; OECD, 2015). In this study, we introduced a novel bio-technique to produce 96-well plate RhE and FTS models for HTS applications. The bio-fabricated RhE is capable of detecting corrosives, by applying raw material as suggested in OECD test guidelines 431 and 439 (**Supplementary Figure 1**). Due to the limited concentration (highest equaled 200 μM) of test chemicals in the compound library, some reported irritants (see global harmonized system (GHS) hazard information with H315 (indicating skin irritation) labeled in **Supplementary Table 2**) did not reduce viability in RhE. Also, most compounds that showed a reduction in tissue viability in RhE were not detected in FTS. Only methylrosaniline chloride showed disruption of tight junction through a decrease of TEER values in RhE model and a decrease of viability in both RhE and FTS models. This unexpected observation may be due to less of the compound being able to penetrate the dermis, which in turn causes fibroblast death. It also explains the greater concordance between viability and TEER endpoints in the RhE model over the FTS (**Figure 5A**). The endpoint of TEER values in the FTS appeared to be a more sensitive endpoint of skin corrosion or irritation rather than tissue viability. For example, TEER identified benzethonium as an irritant in the FTS, independent of cytotoxicity. However, TEER is very sensitive and may generate false positive irritation effects. Therefore, other readouts, such as tissue viability and IL-1α secretion level, should be considered in conjunction when studying TEER values.

Hexachlorophene is used as a topical anti-infective and anti-bacterial agent in soaps and toothpaste. It is also used in agriculture as a soil fungicide, plant bactericide, and acaricide (Fiege et al., 2000). Studies have shown that some patients tested with a concentration range of 0.3% to 6% transdermal patches (7–147 μM) were allergic to this substance (Schoppelrey et al., 1997). At a high concentration (200 μM), hexachlorophene dramatically increased the IL-1α secretion in the RhE and FTS models (**Figure 4A**). Further concentration-response testing in the FTS model, showed that IL-1α was not elevated at lower concentrations (12.5–50 μM), whereas IL-18 was elevated at these lower concentrations (**Figure 7B**). The IL-18 elevation indicated the sensitization potential of hexachlorophene which explained the allergic response in clinic.

Methylrosaniline chloride (also known as gentian violet) and methyl violet are the most frequently used topical skin agents among the triphenylmethane dyes (Torres et al., 2009). We have observed that both compounds elicited an increase in IL-18 secretion at the lowest concentration (12.5 μM), but not IL-1α when treated in the FTS model (**Figures 7A,C**). Interestingly, even though methylrosaniline differs from methyl violet by only a methyl group, it causes more severe tissue damage than the latter (**Figures 6E,G**). Methyl violet has been reported as a carcinogen and eye irritant in mice (Littlefield et al., 1985), as well as a few reports of contact sensitization to this dye (Bielicky and Novák, 1969; Bajaj and Gupta, 1986). The first report of methylrosaniline-caused allergy was as early as 1940 (Goldstein, 1940). At that time, 3% methylrosaniline solution was applied in an intertriginous space; meaning that the observed response could be due to toxicity or irritancy rather than a physical allergy. In 2009, there was a case report about irritant contact dermatitis caused by a methylrosaniline patch at the therapeutic concentration of 0.5% (Torres et al., 2009); this percentage is close to the 12.5 μM concentration which we observed a significant IL-18 elevation, but not IL-1α.

Based on the elevated IL-18 secretion from methyl violet and methylrosaniline treatment, both compounds could be considered sensitizers at low concentrations (less than 50 μM) and irritants at high concentrations. In addition, methylrosaniline's sensitizing effect of increasing IL-18 were only observed in FTS, not in the RhE model (**Figures 4C,D**), suggesting that a more complex model will better characterize inflammatory response upon chemical treatment.

Fibroblasts play an important role in skin tissue morphogenesis, homeostasis, and various histopathological conditions (Sriram et al., 2015). Adding dermis to the tissue fits the need for *in vitro* skin tissue to mimic physiological architecture of human native skin. Dermal fibroblasts interact with keratinocytes through direct cell-cell communications, cell-matrix interactions, and secretion of growth factors and cytokines (Werner et al., 1992; Werner et al., 1994; Mueller and Fusenig, 2002). The heatmap in **Figure 5B** indicated that RhE was more responsive to IL-18 secretion, while FTS captured more dramatic changes in IL-1α secretion. Cell-cell signaling between epidermal and dermal cells influence toxicological effects of compounds, specifically cytokine secretions (Maas-Szabowski et al., 2001). When investigating with the selected compounds, our data confirmed that fibroblasts and keratinocytes have cell to cell communication; this modulates the keratinocytes' response to environmental insults in a more physiologically relevant pattern. For example, methylrosaniline chloride and hexachlorophene generated a greater IL-1α secretion level in FTS than in RhE. We speculate that this is due to the dramatic increase of IL-1α secretion when in the presence of fibroblasts, and was therefore mediated by cell-cell signaling between the fibroblasts and keratinocytes.

During the production of FTS, we observed a drastic decrease in TEER values when using FTS after 11 days of tissue culture (data not shown). These lower TEER values suggested that the tight junction barrier formed between the keratinocytes and fibroblasts affected barrier function; this may be due to cell-cell interactions and signaling between both types of cells. Another possibility is the different medium used for FTS; using another type of medium introduced in a previous article (Sriram et al., 2018), the TEER values reached maximum at day 12 with a value of $1022.7 \pm 246\ \Omega^{*}cm^{2}$ ($n = 60$) (data not shown). Therefore, the bio-printing technique for each assay must be optimized, since the FTS maturation can occur at different times when different media is being used.

Our study tested 46 prioritized compounds related to topical products on monolayer keratinocytes, RhE, and FTS models. Each platform holds the potential for identifying dermal hazards, but each of these assays need extensive confirmation testing to be able to rely on their predictive ability. The scientific community generally accepts using the endpoints of TEER, cell viability, and IL-1α for assessing irritation potential, and IL-18 secretion levels for assessing sensitization potential. The integrated measurement of barrier function, inflammatory response, and tissue damage, combined these readouts and provided a comprehensive way to evaluate irritation potential. This novel approach could be used as an evidence for hazard labeling in the Globally Harmonized System (GHS), pesticide registration in the United States Environmental Protection Agency (EPA), and consumer product regulation by U.S. Consumer Product Safety Commission (CPSC). We believe using human cells to generate bio-printed tissue is a quick and reliable method to model human skin in a high-throughput manner. This newly biofabricated skin tissue can be used for the safety profiling of topically applied compounds, as well as in the earlier stages of drug discovery. Eventually, the HTS biofabricated models described here will potentially be able to speed up the translation of new candidate therapeutics to the clinic and new consumer products to the market.

DATA AVAILABILITY STATEMENT

All datasets for this study are included in the article/**Supplementary Material**.

AUTHOR CONTRIBUTIONS

ZW, XL, MX, and MF designed the study. ZW, XL, MO, LZ, and MS executed the experiments. RH and NK select compounds and curate datasets. ZW, XL, MX, and MF wrote the manuscript. RH, AS, and NK edited the manuscript. All authors read and approved the final version of the manuscript.

FUNDING

This work was supported in part by the National Institutes of Health (NIH) Intramural Research Program and the Cure Acceleration Network program to the National Center for Advancing Translational Sciences (NCATS), and the interagency agreement IAG #NTR 12003 from the National Institute of Environmental Health Sciences/Division of the National Toxicology Program to the NCATS, NIH.

ACKNOWLEDGMENTS

The authors thank Drs. Caitlin Lynch, DeeAnn Visk, and Elizabeth Ottinger for critical reading and editing the manuscript.

SUPPLEMENTARY MATERIAL

The Supplementary Material for this article can be found online at: https://www.frontiersin.org/articles/10.3389/fbioe.2020.00109/full#supplementary-material

FIGURE S1 | Assessment of RhE model for **(A)** corrosion and **(B)** irritation test of benchmark chemicals from OECD test guidelines. **(C)** Comparison of tissue viability treated by 1% DMSO (vehicle control) and 5% SDS. OECD test guideline 439 protocol suggested 1 h treatment with raw material followed by 14 time intensive washing steps. Viability was measured after a 2-day post-treatment incubation. Modified treatment plan in the current study is continuous 3-day treatment of compounds at a lower concentration without intensive washing steps.

TABLE S1 | Cell viability of top 46 most toxic compounds in NKTC and NHEK cells measured by CellTiter-Glo and WST-8.

TABLE S2 | Comparison of RhE and FTS constructs on viability and TEER upon treatment with the 46 most toxic compounds.

TABLE S3 | Medium composition for bio-printed full-thickness skin construct and primary and secondary antibodies used in the study.

TABLE S4 | Cell viability of all topical-use compounds in NKTC and NHEK cells measured by CellTiter-Glo and WST-8.

REFERENCES

Abdayem, R., Callejon, S., Portes, P., Kirilov, P., Demarne, F., Pirot, F., et al. (2015). Modulation of transepithelial electric resistance (TEER) in reconstructed human epidermis by excipients known to permeate intestinal tight junctions. *Exp. Dermatol.* 24, 686–691. doi: 10.1111/exd.12750

Attene-Ramos, M. S., Miller, N., Huang, R., Michael, S., Itkin, M., Kavlock, R. J., et al. (2013). The Tox21 robotic platform for the assessment of environmental chemicals–from vision to reality. *Drug Discov. Today* 18, 716–723. doi: 10.1016/j.drudis.2013.05.015

Bajaj, A., and Gupta, S. (1986). Contact hypersensitivity to topical antibacterial agents. *Int. J. Dermatol.* 25, 103–105. doi: 10.1111/j.1365-4362.1986.tb04548.x

Bielicky, T., and Novák, M. (1969). Contact-group sensitization to triphenylmethane dyes: gentian violet, brilliant green, and malachite green. *Arch. Dermatol.* 100, 540–543. doi: 10.1001/archderm.100.5.540

Boehnke, K., Mirancea, N., Pavesio, A., Fusenig, N. E., Boukamp, P., and Stark, H.-J. (2007). Effects of fibroblasts and microenvironment on epidermal regeneration and tissue function in long-term skin equivalents. *Eur. J. Cell Biol.* 86, 731–746. doi: 10.1016/j.ejcb.2006.12.005

Companjen, A. R., van der Velden, V. H., Vooys, A., Debets, R., Benner, R., and Prens, E. P. (2000). Human keratinocytes are major producers of IL-18: predominant expression of the unprocessed form. *Eur. Cytokine Netw.* 11, 383–390.

Co-operation and Development, (2013). "Test No. 431," in *Vitro Skin Corrosion: Reconstructed Human Epidermis (RHE) Test Method*, Paris: OECD Publishing.

Corsini, E., and Galli, C. L. (1998). Cytokines and irritant contact dermatitis. *Toxicol. Lett.* 102, 277–282.

Corsini, E., Mitjans, M., Galbiati, V., Lucchi, L., Galli, C. L., and Marinovich, M. (2009). Use of IL-18 production in a human keratinocyte cell line to discriminate contact sensitizers from irritants and low molecular weight respiratory allergens. *Toxicol. Vitro* 23, 789–796. doi: 10.1016/j.tiv.2009.04.005

Derr, K., Zou, J., Luo, K., Song, M. J., Sittampalam, G. S., Zhou, C., et al. (2019). Fully three-dimensional bioprinted skin equivalent constructs with validated morphology and barrier function. *Tissue Eng. Part CMethods* 25, 334–343. doi: 10.1089/ten.TEC.2018.0318

Draize, J. H., Woodard, G., and Calvery, H. O. (1944). Methods for the study of irritation and toxicity of substances applied topically to the skin and mucous membranes. *J. Pharmacol. Exp. Ther.* 82, 377–390. doi: 10.1016/j.yrtph.2017.01.009

El Ghalbzouri, A., Jonkman, M. F., Dijkman, R., and Ponec, M. (2005). Basement membrane reconstruction in human skin equivalents is regulated by fibroblasts and/or exogenously activated keratinocytes. *J. Investig. Dermatol.* 124, 79–86. doi: 10.1111/j.0022-202x.2004.23549.x

El−Ghalbzouri, A., Gibbs, S., Lamme, E., Van Blitterswijk, C., and Ponec, M. (2002). Effect of fibroblasts on epidermal regeneration. *Br. J. Dermatol.* 147, 230–243. doi: 10.1046/j.1365-2133.2002.04871.x

Fiege, H., Voges, H. W., Hamamoto, T., Umemura, S., Iwata, T., Miki, H., et al. (2000). "Phenol derivatives," in *Ullmann's Encyclopedia of Industrial Chemistry*, ed. V. C. H. Wiley (Hoboken, NJ: John Wiley & Sons).

Florin, L., Maas-Szabowski, N., Werner, S., Szabowski, A., and Angel, P. (2005). Increased keratinocyte proliferation by JUN-dependent expression of PTN and SDF-1 in fibroblasts. *J. Cell Sci.* 118, 1981–1989. doi: 10.1242/jcs.02303

Galbiati, V., Papale, A., Galli, C. L., Marinovich, M., and Corsini, E. (2014). Role of ROS and HMGB1 in contact allergen–induced IL-18 production in human keratinocytes. *J. Investig. Dermatol.* 134, 2719–2727. doi: 10.1038/jid.2014.203

Goldstein, M. B. (1940). Sensitivity to gentian violet (methylrosaniline). *Arch. Dermatol. Syphilol.* 41, 122–122.

Griesinger, C., Barroso, J., Zuang, V., Cole, T., Genschow, E., and Liebsch, M. (2009). *Explanatory Background Document to the OECD Draft test Guideline on in Vitro Skin Irritation Testing. Organisation for Economic co-Operation and Development (OECD)*. Availalbe at: http://www.oecd.org/chemicalsafety/testing/43670220.pdf (accessed June, 2019).

Hänel, K., Cornelissen, C., Lüscher, B., and Baron, J. (2013). Cytokines and the skin barrier. *Int. J. Mol. Sci.* 14, 6720–6745. doi: 10.3390/ijms14046720

Huang, R. (2016). A quantitative high-throughput screening data analysis pipeline for activity profiling. *Methods Mol. Biol.* 1473, 111–122. doi: 10.1007/978-1-4939-6346-1_12

Lee, V., Singh, G., Trasatti, J. P., Bjornsson, C., Xu, X., Tran, T. N., et al. (2013). Design and fabrication of human skin by three-dimensional bioprinting. *Tissue Eng. Part CMethods* 20, 473–484. doi: 10.1089/ten.tec.2013.0335

Littlefield, N. A., Blackwell, B.-N., Hewitt, C. C., and Gaylor, D. W. (1985). Chronic toxicity and carcinogenicity studies of gentian violet in mice. *Toxicol. Sci.* 5, 902–912. doi: 10.1016/0272-0590(85)90172-1

Liu, X., Cleary, J., and German, G. K. (2016). The global mechanical properties and multi-scale failure mechanics of heterogeneous human stratum corneum. *Acta Biomater* 43, 78–87. doi: 10.1016/j.actbio.2016.07.028

Maas-Szabowski, N., Szabowski, A., Andrecht, S., Kolbus, A., Schorpp-Kistner, M., Angel, P., et al. (2001). Organotypic cocultures with genetically modified mouse fibroblasts as a tool to dissect molecular mechanisms regulating keratinocyte growth and differentiation. *J. Investig, Dermatol.* 116, 816–820. doi: 10.1046/j.1523-1747.2001.01349.x

Matsusaki, M., Fujimoto, K., Shirakata, Y., Hirakawa, S., Hashimoto, K., and Akashi, M. (2015). Development of full−thickness human skin equivalents with blood and lymph−like capillary networks by cell coating technology. *J. Biomed.i Mater. Res. Part A* 103, 3386–3396. doi: 10.1002/jbm.a.35473

Mueller, M. M., and Fusenig, N. E. (2002). Tumor-stroma interactions directing phenotype and progression of epithelial skin tumor cells. *Differentiation* 70, 486–497. doi: 10.1046/j.1432-0436.2002.700903.x

Ng, W. L., Qi, J. T. Z., Yeong, W. Y., and Naing, M. W. (2018). Proof-of-concept: 3D bioprinting of pigmented human skin constructs. *Biofabrication* 10, 025005. doi: 10.1088/1758-5090/aa9e1e

Niehues, H., Bouwstra, J. A., El Ghalbzouri, A., Brandner, J. M., Zeeuwen, P. L., and van den Bogaard, E. H. (2018). 3D skin models for 3R research: The potential of 3D reconstructed skin models to study skin barrier function. *Exp. Dermatol.* 27, 501–511. doi: 10.1111/exd.13531

OECD, (2004). "430: In vitro skin corrosion: transcutaneous electrical resistance test (TER)," in *OECD Guidelines for the Testing of Chemicals* Section 4, Paris: OECD.

OECD, (2015). "439: In vitro skin irritation: reconstructed human epidermis test method," in *OECD Guidelines for the Testing of Chemicals* Section 4, Paris: OECD.

Poumay, Y., Dupont, F., Marcoux, S., Leclercq-Smekens, M., Hérin, M., and Coquette, A. (2004). A simple reconstructed human epidermis: preparation of the culture model and utilization in in vitro studies. *Arch. Dermatol. Res.* 296, 203–211.

Safety and Administration (2012). "Appendix A TO §1910.1200—health hazard criteria (Mandatory)".

Schoppelrey, H. P., Mily, H., Agathos, M., and Breit, R. (1997). Allergic contact dermatitis from pyoctanin. *Contact Dermat.* 36, 221–224. doi: 10.1111/j.1600-0536.1997.tb00274.x

Smits, J. P., Niehues, H., Rikken, G., van Vlijmen-Willems, I. M., van de Zande, G. W., Zeeuwen, P. L., et al. (2017). Immortalized N/TERT keratinocytes as an alternative cell source in 3D human epidermal models. *Sci. Rep.* 7, 11838. doi: 10.1038/s41598-017-12041-y

Srinivasan, B., Kolli, A. R., Esch, M. B., Abaci, H. E., Shuler, M. L., and Hickman, J. J. (2015). TEER measurement techniques for in vitro barrier model systems. *J. Lab Autom.* 20, 107–126. doi: 10.1177/2211068214561025

Sriram, G., Alberti, M., Dancik, Y., Wu, B., Wu, R., Feng, Z., et al. (2018). Full-thickness human skin-on-chip with enhanced epidermal morphogenesis and barrier function. *Materials Today* 21, 326–340. doi: 10.1016/j.mattod.2017.11.002

Sriram, G., Bigliardi, P. L., and Bigliardi-Qi, M. (2015). Fibroblast heterogeneity and its implications for engineering organotypic skin models in vitro. *Eur. J. Cell Biol.* 94, 483–512. doi: 10.1016/j.ejcb.2015.08.001

Tice, R. R., Austin, C. P., Kavlock, R. J., and Bucher, J. R. (2013). Improving the human hazard characterization of chemicals: a Tox21 update. *Environ. Health Perspect.* 121, 756–765. doi: 10.1289/ehp.1205784

Tornier, C., Rosdy, M., and Maibach, H. I. (2006). In vitro skin irritation testing on reconstituted human epidermis: reproducibility for 50 chemicals tested with two protocols. *Toxicol. Vitro* 20, 401–416. doi: 10.1016/j.tiv.2005.09.004

Torres, J., Sastre, J., las Heras De, M., Requena, L., and Cazorla, A. (2009). Irritative contact dermatitis due to gentian violet (methylrosaniline chloride) in an airplane passenger: a case report. *J. Investig. Allergol. Clin Immunol.* 19, 67–68.

Werner, S., Peters, K. G., Longaker, M. T., Fuller-Pace, F., Banda, M. J., and Williams, L. T. (1992). Large induction of keratinocyte growth factor expression in the dermis during wound healing. *Proc. Natl. Acad. Sci. U.S.A.* 89, 6896–6900. doi: 10.1073/pnas.89.15.6896

Werner, S., Smola, H., Liao, X., Longaker, M. T., Krieg, T., Hofschneider, P. H., et al. (1994). The function of KGF in morphogenesis of epithelium and reepithelialization of wounds. *Science* 266, 819–822. doi: 10.1126/science.7973639

Wojtowicz, A. M., Oliveira, S., Carlson, M. W., Zawadzka, A., Rousseau, C. F., and Baksh, D. (2014). The importance of both fibroblasts and keratinocytes in a bilayered living cellular construct used in wound healing. *Wound Repair Regen.* 22, 246–255. doi: 10.1111/wrr.12154

Worm, M. (2014). Allergic contact dermatitis beyond IL−1β role of additional family members. *Exp. Dermatol.* 23, 151–152. doi: 10.1111/exd.12311

Disclaimer: The views expressed in this article are those of the authors and do not necessarily reflect the views or policies of the National Institute of Environmental Health Sciences, the National Center for Advancing Translational Sciences, National Institutes of Health, or the United States Government. Mention of trade names or commercial products does not constitute endorsement or recommendation for use.

Conflict of Interest: The authors declare that the research was conducted in the absence of any commercial or financial relationships that could be construed as a potential conflict of interest.

frontiers in Bioengineering and Biotechnology

ORIGINAL RESEARCH
published: 17 March 2020
doi: 10.3389/fbioe.2020.00163

Intestine-Liver Axis On-Chip Reveals the Intestinal Protective Role on Hepatic Damage by Emulating Ethanol First-Pass Metabolism

*Vincenza De Gregorio [1,2], Mariarosaria Telesco [1], Brunella Corrado [1], Valerio Rosiello [2], Francesco Urciuolo [2], Paolo A. Netti [1,2,3] and Giorgia Imparato [1]**

[1] Center for Advanced Biomaterials for HealthCare@CRIB, Istituto Italiano di Tecnologia, Naples, Italy, [2] Interdisciplinary Research Centre on Biomaterials (CRIB), University of Naples Federico II, Naples, Italy, [3] Department of Chemical, Materials and Industrial Production Engineering (DICMAPI) University of Naples Federico II, Naples, Italy

OPEN ACCESS

Edited by:
María García-Díaz, Institute for Bioengineering of Catalonia (IBEC), Spain

Reviewed by:
Tiziano Verri, University of Salento, Italy
Salman Khetani, University of Illinois at Chicago, United States
Christopher B. Forsyth, Rush University, United States

***Correspondence:**
Giorgia Imparato
giorgia.imparato@iit.it

Specialty section:
This article was submitted to Tissue Engineering and Regenerative Medicine, a section of the journal Frontiers in Bioengineering and Biotechnology

Received: *28 November 2019*
Accepted: *18 February 2020*
Published: *17 March 2020*

Citation:
De Gregorio V, Telesco M, Corrado B, Rosiello V, Urciuolo F, Netti PA and Imparato G (2020) Intestine-Liver Axis On-Chip Reveals the Intestinal Protective Role on Hepatic Damage by Emulating Ethanol First-Pass Metabolism. Front. Bioeng. Biotechnol. 8:163. doi: 10.3389/fbioe.2020.00163

Intestine-Liver-on-chip systems can be useful to predict oral drug administration and first-pass metabolism *in vitro* in order to partly replace the animal model. While organ-on-chip technology can count on sophisticated micro-physiological devices, the engineered organs still remain artificial surrogates of the native counterparts. Here, we used a bottom-up tissue engineering strategy to build-up physiologically functional 3D Human Intestine Model (3D-HIM) as well as 3D Liver-microtissues (HepG2-μTPs) *in vitro* and designed a microfluidic Intestine-Liver-On-Chip (InLiver-OC) to emulate first-pass mechanism occurring *in vivo*. Our results highlight the ethanol-induced 3D-HIM hyper-permeability and stromal injury, the intestinal prevention on the liver injury, as well as the synergic contribution of the two 3D tissue models on the release of metabolic enzymes after high amount of ethanol administration.

Keywords: first-pass metabolism of ethanol (Et-OH), intestine-liver-on-chip, bottom-up tissue engineering approach, endogenous ECM, 3D tissue

INTRODUCTION

Orally administered drugs and chemicals are primarily metabolized by the gastrointestinal (GI) tract and liver (de Sousa and Bernkop-Schnürch, 2014). The xenobiotics and their metabolites interact with the small intestine, causing damage, and a fraction of these is transported across the gut epithelium and absorbed into the bloodstream before reaching the liver by the portal vein (Maurice et al., 2013). Therefore, there is a need to understand how such compounds may affect function at the organ level. Traditionally, testing the toxic effects of chemicals or drugs has relied on large-scale animal studies (Council, 2007). In addition to being extremely expensive, the data obtained with animal models often cannot be extrapolated to humans (Esch et al., 2011). In this perspective, there is a need to design *in vitro* organotypic cultures to investigate toxicity. In the last few years, *in vitro* models of the GI tract (Huh et al., 2011; Bhatia and Ingber, 2014) and liver (Santaguida et al., 2006; Inamdar and Borenstein, 2011) have been developed individually, but single-organ systems lack the complex intercellular and inter-organ communication that occurs *in vivo* and therefore are unable to properly model the enterohepatic circulation and first-pass metabolism that have been shown to be critical for assessing drug and xenobiotics metabolism. For this reason, recently, multi-compartment microfluidic-based devices (organs-on-a-chip) have been proposed to increase safety and the efficacy of the drug development process. These platforms

consist of microfluidic cell culture devices, fabricated by means of microfabrication methods, which contain continuously perfused chambers inhabited by living cells arranged to simulate tissue- and organ-level physiology. By recapitulating the multicellular architectures, tissue–tissue interfaces, physicochemical microenvironments, and vascular perfusion of the body, these devices exceed the static conventional 2D or 3D culture systems (Esch et al., 2012). In an attempt to recapitulate the integration of the GI tract and the liver mimicking the first-pass metabolism, several *in vitro* models have been established. Choe et al. have recently developed a microfluidic device that consists of 2D cell models seeded into two separate compartments for gut epithelial cells (Caco-2) and liver cells (HepG2), respectively, designed so that drugs go through a sequential absorption in the gut chamber and metabolic reaction in the liver chamber (Choe et al., 2017). In another work, 3D gut model and Hepg2 layer were integrated into microfluidic device to recapitulate the complex process of absorption and metabolism of digested lipids on *in vitro* model of hepatic steatosis (Lee and Sung, 2018). Another noteworthy model built up by Shuler's group is based on pumpless modular GI–liver model to co-culture human intestinal cells and 3D hepatic cells in order to replicate human GI–liver physiology (Chen et al., 2018). On the other hand, van Midwoud et al. developed a microfluidic system for the sequential perfusion of rat intestinal and liver slices for metabolism studies (van Midwoud et al., 2010). However, this approach cannot be easily translated to the use of human tissue slices, whose viability dramatically decreases over a few days of culture, making this tissue model infeasible for organ-on-chip purposes. Other studies are based on first-pass metabolism of orally administered drugs by using multi-compartment pharmacokinetic models. In particular, Mahler et al. developed a microfluidic biochip in which HT-29 goblet-like cells are included in the GI-tract compartment lining the Caco-2 cell layer with mucous granules, in order to demonstrate absorption, distribution, metabolism, and toxicity (ADME-Tox) of acetaminophen (APAP) (Mahler et al., 2009). Also, Prot et al. analyzed the metabolism of paracetamol through a microfluidic device, which comprises the Caco-2 cells cultivated on a conventional cell culture insert introduced in a bioreactor and the liver cells modeled by HepG2/C3a isolated from rat/human primary hepatocytes. Their experiments were also supported by a mathematical model to estimate intrinsic *in vitro* parameters and to predict *in vivo* processes (Prot et al., 2014). In a recent work, an integrated gut–liver microphysiological systems was used to elucidate the inter-tissue cross-talk under inflammatory conditions, focusing on the long-term co-culture into the device to reproduce pathological conditions (Chen et al., 2017). However, even if these systems (Esch et al., 2014) provide important insights into the molecular mechanism of GI tract metabolism, they include over-simplified cell mono or co-culture models, thus failing in the replication of the 3D physiological ECM microenvironment with its dynamic complexity. Our studies have recently demonstrated the crucial role of the native ECM remodeling on the intestine adsorptive and metabolic function as well as the ECM involvement in the intestinal mucosal inflammation (De Gregorio et al., 2019). With the perspective of elucidating the inter-organs crosstalk with a more physiological functional 3D tissues, we reported a development of a novel Intestine-Liver-on-Chip (InLiver-OC) consisting of two directly interconnected chambers (Intestine-compartment and Liver-compartment) that enable the culture of a 3D Human Intestine Model (3D-HIM) as well as 3D liver microtissues (HepG2-μTPs) in order to simulate the physiological mechanism of the first-pass metabolism of orally-ingested compounds. Bottom-up approach was used to fabricate the 3D-HIM provided with an endogenous ECM (Imparato et al., 2013) and HepG2-μTPs, as previously reported (Corrado et al., 2019). The combination of such physiological relevant 3D models with microfluidic technology allowed us to investigate the protective role of the intestine on liver injury, analyzing the 3D-HIM hyper-permeability as well as the intestinal stroma remodeling. In addition, in this system, the integrated InLiver-OC was used to study the synergic contribution of the two 3D tissue models on the release of metabolic enzymes after high amount of ethanol (Et-OH) administration as exogenous stimulus mimicking the "binge drinking." This multifunctional system has a broad applicability toward advancing fundamental understanding of human pathophysiology and drug development processes.

MATERIALS AND METHODS

Cell Type

For 3D-HIM production, human intestinal myofibroblasts (H-InMyoFib) were purchased from Lonza and cultured in SMGMTM-2 BulletKitTM medium (Lonza). H-InMyoFibs at 3–5 passages were used. Human intestinal epithelial cells (Caco-2) were provided by American Type Culture Collection (ATCC) and were cultured in Dulbecco Modified Eagle Medium (DMEM, Microtech) with 10% of fetal bovine serum (FBS, Microtech), 100 $\mu g\ mL^{-1}$ L-glutamine, 100 $U\ mL^{-1}$ penicillin/streptomycin. For HepG2-μTPs production, hepatocellular carcinoma cells (HepG2) cells were purchased by ATCC and were cultured in Minimum Essential Medium Earle's Salt (MEM, Microtech), containing 10% fetal bovine serum, 100 $\mu g\ mL^{-1}$ L-glutamine, 100 $U\ mL^{-1}$ penicillin/streptomycin, 0.1 mM Non-Essential Amino Acid and 0.1 mM Sodium pyruvate. Cells were incubated at 37°C in a humidified atmosphere with 5% CO_2.

3D Human Intestine Model (3D-HIM) Production

Gelatine porous microscaffolds (GPMs) (75–150 μm diameter) were made-up by a slightly adapted double emulsion method (O/W/O) and stabilized with glyceraldehyde at 4% as previously described (Imparato et al., 2013). Briefly, 10 mL of water containing TWEEN 85 (6% w/v) were used to dissolve the gelatin powder (type B, Mw 176,654 Da) (Sigma Aldrich) at 60°C. Then, an oil in water (O/W) emulsion was produced by adding a solution of Toluene and SPAN 85 (3% w/v) to the aqueous gelatin solution (8% w/v) (Sigma Aldrich). To obtain gelatin micro-beads, 30 mL of additional toluene were added (O/W/O) and cooled to 5°C. At last, to obtain the toluene extraction and gelatin micro-beads stabilization, ethanol (20 mL) was poured. Dried GPMs were sterilized with ethanol,

washed with PBS, and then inoculated (2 mg/mL of GPMs; 5 × 10^3 beads/mg) with H-InMyoFibs (1.5 × 10^5 cell/mL) and cultured in a dynamic conditions in spinner flask bioreactor (CELLSPIN, 250 ml, Integra Biosciences) to obtain Human Intestine-μTPs (HI-μTPs) (De Gregorio et al., 2018a). In order to promote H-InMyoFibs adhesion, spinner flask operated with and intermittent stirring for 6 h post inoculation (5 min shaking, 40 min stationary) and continuous stirring at 20 rpm was set for 10 days. Spinner flask bioreactor operated in the cell incubator at 37°C and 5% CO_2; the media replacement occurred every 2 days, and 2-O-alpha-D-Glucopyranosyl-L-ascorbic Acid 0.5 mM (TCI Europe) was added at each culture media change. After 10 days of spinner flask bioreactor culture, HI-μTPs were transferred into a maturation chamber bioreactor where HI-μTPs assembling took place forming disc-shaped (1 mm thick, 6 mm diameter) 3D Intestinal stroma (3D-ISs) (De Gregorio et al., 2018a). The maturation chamber was inserted into a spinner flask programmed at 60 rpm. After 2 weeks of culture, the maturation chamber was opened, the 3D-ISs were withdrawn and washed 2-folds with PBS solution, then transferred into a transwell insert (6.5 mm diameter; Corning), and left to dry for 5 min under laminar hood. Further, Caco-2 cells suspension (2 × 10^5 cells in 50 μL) was seeded on each 3D-IS in order to produce the intestinal epithelium. The samples were incubated for about 2 h at 37°C, 5% CO_2 to permit Caco-2 cells adhesion onto the 3D-IS apical surface. Further, submerged culture was performed by adding 200 μL of DMEM on the apical side of the 3D-IS and 600 μL of DMEM in the baso-lateral side for 7 days. Then, to induce the epithelial cells polarization and differentiation, the samples were cultured for 2 weeks in an air-liquid interface culture. Three times per week the culture medium was replaced. At the end of the experiment, the full-thickness intestinal equivalents (3D-HIMs) composed by 3D-IS overlapped by intestinal epithelium were taken from the transwell insert for further investigation or were loaded into the Intestine chamber of the Intestine-on-Chip (In-OC) or Intestine-Liver-on-Chip (InLiver-OC).

HepG2-μTPs Development

HepG2 cells were cultured on GPMs in spinner flasks (Integra), as previously reported with slight modifications (Corrado et al., 2019). Briefly, 35 mg of GPMs were loaded with 5.25 × 10^6 cells (30 cell/GPM ratio). To promote cell seeding on GPMs an intermittent stirring regime (30 min at 0 rpm, 5 min at 30 rpm) was applied for 24 h. Afterwards, the stirring speed was kept at a continuous 20 rpm for up to 7 days. Culture medium was changed three times per week. All cultures were maintained at 37°C in a humidified 5% CO_2 incubator for 6–7 days, and then HepG2-μTPs were loaded into microfluidic Liver-On-Chip (Liver-OC) or into InLiver-OC.

Microfluidic Device Fabrication

The microfluidic InLiver-OC device was fabricated by a rapid prototyping procedure. The PMMA master mold was designed by AutoCAD and carved with micromilling machine (Minithech CNC Mini-Mill) making a relief positive geometry. A mixture of PDMS pre-polymer and curing agent 10:1 (w/w) was prepared, degassed under vacuum for 20 min to remove air bubbles, and then poured on PMMA master. The set-up was incubated at 80°C for 60 min, then peeled off from master molds. The device consists of two compartments, the intestine compartment ($Intestine_c$) and the liver compartment ($Liver_c$), which are connected by a central microchannel. The $Intestine_c$ was designed with a central microchannel (1.2 mm wide × 40 mm long × 0.6 mm high), which transported the medium into an intestine chamber (9.5 mm diameter × 5 mm high). The $Liver_c$ communicated with the $Intestine_c$ by a central microchannel, which was separated from three parallels chambers (0.5 mm wide × 0.6 mm high × 1 mm long) by micro-pillars (0.100 mm diameter × 0.09 mm pillar interspace). A collection channel (0.5 mm wide × 0.3 high) was used to collect tissue supernatants. Culture medium inlet and outlet, as well as inlet for HepG2-μTPs loading in the $Liver_c$, were punched with a 2.5 mm biopsy punch (DifaCooper), while intestine chamber of the $Intestine_c$ was punched using a 9.5-mm puncher (Am-Tech) (**Figure S1**). Then, a transwell insert was placed into the 9.5-mm holes of the biochip of the $Intestine_c$. To ensure the selective transport of fluid through the 3D-HIM, a silicon gasket and a PMMA cylinder were fabricated. In detail, PDMS gasket was fabricated by punching 1-mm-thick PDMS layer, first with a 4-mm puncher (for the inner hole) and then with a 6.5-mm puncher (for the outer hole). PMMA hollow cylinder (5 mm high, 1 mm thick) was made up with micromilling machine. The PDMS biochip was sterilized by autoclave, while PDMS gasket and PMMA cylinder were sterilized by UV light. Before the experiments, InLiver-biochip was washed twice with PBS and then was filled with cell culture medium without encapsulating air bubbles. Then, the 3D-HIM was inserted in the transwell insert of the $Intestine_c$, the PDMS gasket was placed on the surface of the 3D-HIM, and the PMMA cylinder was placed on the PDMS gasket. In addition, to avoid bacterial contaminations, the $Intestine_c$ was closed by laying a 100-μm sterile PDMS sheet fabricated by spin coating of PDMS (750 rpm × 30 s) onto transwell insert of the $Intestine_c$. The entire set-up was connected to a syringe pump that worked at flow rate of 5 μL/min, a reservoir was connected to the basal $Intestine_c$, and another one was connected to the In-Liver outlet in order to collect the cell supernatants from each compartment. For each experiment, two parallel devices were used. To simulate oral ingestion and toxic damage to both $Intestine_c$ and $Liver_c$, Et-OH dissolved into 300 μL of culture medium (400 mM) was added on the apical side of the $Intestine_c$. The InLiver-OCs were incubated for 24 h at 37°C in a humidified atmosphere containing 5% CO_2. The control group InLiver-OC without Et-OH treatment was named "–Et-OH;" the 400-mM Et-OH treated sample was named "+Et-OH." 3D-HIMs and HepG2-μTPs were collected and processed for immune-histotypical and molecular characterizations. In addition, the media collected were analyzed for metabolites produced on the apical side of the $Intestine_c$, on the lower side of the $Intestine_c$ as well as on the outlet of the InLiver-OC.

Mathematical Model CFD Simulation

The commercial CFD COMSOL Multiphysics vers. Five was used to verify the experimental setup, the three-dimensional velocity and the oxygen gradients in the InLiver-OC. In the CDF analysis,

TABLE 1 | Mathematical modeling variables.

3D HIM properties	
Equilibrium O_2 concentration [C_0]	0.22 mol/m^3
3D HIM Cell density [ρ]	0.2×10^{14} cell/m^3
Diffusion coefficient (D_t)	10^{-10} m^2/s
Dynamic permeability [k_{dv}]	0 m^2
Porosity of the tissue [ε]	0.7
Effective viscosity in the fluid [μ_t]	0.0016 Pa s
Effective hydraulic conductivity [k_t]	10^{-11} m^2
Maximum oxygen consumption rate (V_{max})	10^{-18} mol/cells*s
O_2 concentration at $V_{max}/2$ (K_m)	10^{-3} mol/m3
HepG2-μTPs properties	
Effective hydraulic conductivity [k_t]	10^{-11} m^2
Porosity of the tissue [ε]	0.7
Dynamic permeability [k_{dv}]	0 m^2
Diffusion coefficient (D_t)	10^{-10} m^2/s
Effective viscosity in the fluid [μ_t]	0.0016 Pa s
HepG2-μTPs cell density [ρ]	2.4×10^{13} cell/m^3
Maximum oxygen consumption rate (Vmax)	2.77×10^{-17} mol/cells*s
O_2 concentration at $V_{max}/2$ (K_m)	6.3×10^{-3} mol/m^3
Culture media properties	
Oxygen diffusivity [D_f]	10–9 m^2/s
Dynamic viscosity [μ_f]	0.001 Pa s

the entire InLiver-OC bioreactor was divided into two different parts, a fluid domain, indicated by "f" (culture medium), and a tissue domain, indicated by "t" (tissue equivalents). The oxygen transport and the three-dimensional velocity were evaluated by combining different physics. Fluid flow in tissue-free regions was modeled by using steady state Navier–Stokes Equation (1); fluid flow in tissue domains was modeled by using transport in porous media Equation (2); oxygen transport was modeled by using Mass Transport-Convection/Diffusion application mode Equation (3); the generation term for oxygen was modeled by using Michelis-Menten kinetic Equation (4). Reference pressure was considered at device outlet ($p = 0$ Pa); no slip condition was adopted at the walls; up to the intestine chamber a fixed concentration of O_2 was imposed to simulate an open chamber; equality for velocity and pressure was imposed at the Navier–Stokes (u, v, w, p)/Brinkman (u_2, v_2, w_2, p_2) interfaces. All values utilized in the simulation are reported in **Table 1**. Laminar flow with different flow rates was set at the inlet, and zero pressure was set at the outlet.

$$\mu_f \nabla^2 v_f = \nabla P_f \tag{1}$$

Where μ_f is the dynamic viscosity, v_f is the fluid velocity, and P_f is the pressure. Brinkman Equation (2) was used to describe the flow through the porous medium:

$$\mu_t \nabla^2 v_t - K_t \mu_t = \nabla P_t \tag{2}$$

Where K_t is the hydraulic permeability, μ_t is the viscosity of the tissue, and P_t is the pressure.

The oxygen concentration within the system was calculated using the following mass balance Equation (3):

$$D\nabla^2 C - \nabla(Cv) = -R \tag{3}$$

Where C is the oxygen concentration, v is the fluid velocity field that was set equal to vf in the domain "f" and v_t in the domain "t," respectively. D is the diffusion coefficient of the oxygen, set as D_f in the domain "f" and D_t in the domain "t," respectively. R is the volumetric oxygen consumption rate expressed by the Michaelis–Menten law, according to the following Equation (4):

$$R = \frac{\rho V_{max} C}{K_m + C} \tag{4}$$

where V_{max} is the maximum oxygen consumption rate, and K_m is the concentration at which the oxygen consumption rate is half of V_{max}, ρ is the cell density in the perfusion chamber. For each tissue, corresponding values were considered. The HepG2 setting values were established from Weise et al. (2013). R was set to 0 only in the fluid domain, since cells are present only in the tissue domain.

Culture Media Selection for Co-culture in InLiver-OC

Two culture media (DMEM and EMEM) and different supplements were used for 3D-HIMs and HepG2-μTPs, respectively. In order to determine the optimal medium composition to flow into InLiver-OC, different media were tested such as: In-medium (Enriched_DMEM), Liver-medium (Enriched_EMEM), and their combination at the following ratio 1:1, 1:2, and 2:1 ratio (v/v). MTT and LDH assays were used to establish the medium condition that guarantees the highest cell viability and lowest toxicity.

Et-OH Curve and Cell Viability Assessment on 2D vs. 3D Liver Models

In order to evaluate the cell viability after Et-OH treatment in 2D as well as in HepG2-μTPs culture, 3-(4,5-dimethylthiazol-2-yl)-2,5-diphenyltetrazolium bromide (MTT) and Lactate dehydrogenase (LDH) assays were used according to the manufacturer's instructions (Dojindo Molecular Technologies Inc., Rockville, MD). For MTT assay 2D cell cultures (HepG2 cells) were seeded at 5 x 10^3 cells for each well in 96-well cell culture plate and cultured for 3 days prior to the start of the experiments. Based on the generation time of the HepG2, the total number of the cells at the beginning of the MTT test was $\sim 2.52 \times 10^4$. For 3D culture, HepG2-μTPs (∼15 microtissues, 2.32×10^4 total cells) were collected from the spinner flask at culture day 6 and loaded in 96-well cell culture plate. All samples were starved in culture medium with 0.2% FBS overnight and then, the medium with different Et-OH concentrations (0, 100, 200, 300, 400, 500, and 600 mM) was administered to 2D HepG2 and 3D HepG2-μTPs and were cultured for 24 h. For MTT assay, the optical density of each well sample was measured with a microplate spectrophotometer reader at 550 nm. Then, to evaluate the LDH release, the culture supernatants from

2D and 3D HepG2-Microtissues LDH activity was performed, using LDH Detection Kit (Sigma-Aldrich) according to the manufacturer's protocol. Briefly, 50 μL of sample or NADH standard were added to a 96-well. Then, reaction mix was added to each well, and after 2–5 min, the absorbance at 450 nm was measured using a microplate reader; in this way a $T_{initial}$ was fixed. Subsequent measurements were performed once every 5 min. The final measurement [(A450) final] was the penultimate reading or the value before the most active sample was near or exceeds the end of the standard curve. The time of the penultimate reading was T_{final}. The LDH activity was evaluated by the following Equation (5):

$$LDH = \frac{B \times Sample\ diluition\ factor}{Reaction\ time} \times V \quad (5)$$

Where B is the amount (nmole) of NADH generated between $T_{initial}$ and T_{final}, reaction time is the difference between T_{final} and $T_{initial}$, and V is the sample volume. ADH was expressed as mUnit/mL.

Cytotoxicity Assessment of Intestine-Metabolized Et-OH on HepG2-μTPs

An indirect estimation of the undigested Et-OH that crosses the 3D-HIM, and of the Et-OH metabolites produced by EtOH-treated, 3D-HIM were determined by collecting supernatants from apical ($3D\text{-}HIM_{apical\ supernatants}$) and basal side ($3D\text{-}HIM_{basal\ supernatants}$) of 3D-HIM treated or not with 400 mM Et-OH at T_0 or at 24 h. MTT was performed on HepG2-μTPs treated with the 3D-HIM supernatants. In addition, zone of Inhibition Test on *L. rhamnosus* were performed after the treatment of the bacteria with the 3D-HIM supernatants. For Zone of Inhibition assay, transparent zones of bacterial grown inhibition indicated the antibacterial activity of the Et-OH. Image J software was used for the measurement of the diameter of the inhibition zones.

Cytotoxic and Immunohistotypical Analyses of 3D-HIM Cultured in InLiver-OC

3D-HIMs cultured in InLiver-OC were either treated or not treated with 400 mM Et-OH for 24 h, then supernatants were collected, and LDH was performed as reported in section Et-OH Curve and Cell Viability Assessment on 2D vs. 3D Liver Models. Moreover, 3D-HIMs (control groups and Et-OH-treated) were fixed in a solution of 10% neutral buffered formalin for 1 h, rinsed in PBS, dehydrated in an incremental series of alcohol (75, 85, 95, and 100% twice, each step 30 min at RT), then treated with xylene (30 min twice) and embedded in paraffin. Tissue sections of 5 μm thick were stained with Hematoxylin and Eosin (H&E) or Alcian blue, mounted with Histomount mounting solution (Bioptica) on coverslips, and the morphological features of 3D-HIMs were observed with a light microscope. To quantify the mucus secretion, samples were processed by using color deconvolution plugin (Image J®). Automatic thresholding was applied, and blue staining (indicating mucus secretion) was separated from other colors. Further, the mucus deposition was quantified as the mean percentage of blue-stained region. Ten sections were used, and at least five different fields were randomly examined in each section for each time point. For immunofluorescence assay, 3D-HIMs were withdrawn from the InLiver-OC and fixed with 4% paraformaldehyde for 20 min and then rinsed with PBS. The samples were then incubated with a permeabilization solution (0.2% Triton X-100 + 3% BSA + PBS) for 10 min. After blocked for 1 h at RT, primary antibody (Claudin-1, 1/40, Abcam Laminin V, 1/50, Abcam; MMP-9, 1/250, Abcam) was incubated for 1 h at RT. Then, secondary antibody incubation, donkey AlexaFluor 546-conjugated anti-rabbit IgG antibodies, for Claudin-1 and Laminin V and goat AlexaFluor 546-conjugated anti-mouse for MMP-9 were incubated for 1 h. Cells nuclei were detected by DRAQ5 staining (5 μm/mL, Sigma Aldrich).

Quantification of Tight Junction Formation

For epithelial barrier evaluation, the 3D-HIMs were withdrawn from the InLiver-OC, and the quality of tight junctions was assessed by means of Claudin-1 staining. Cell samples were immune-stained for Claudin-1 and examined with Leica (Confocal Leica TCS SP5 II femtosecond laser scanning system, Leica) confocal microscope. For each sample, the number of tight junction structures, defined as a completely enclosed ring of smooth, contiguous, apical Claudin-1 staining, were counted in three different fields under 20 X magnification (>50 cells per field), and the mean number of tight junction structures per field was determined. Experiments were performed three times, and the mean number of tight junction structures per field from three independent experiments was calculated.

Transepithelial Electrical Resistance

The transepithelial electrical resistance (TEER) of the 3D-HIM cultured in InLiver-OC was measured by using an Autolab PGSTAT101 (potentiostat/galvanostat, Metrohm) equipped with FRA32M module (frequency response analysis module), which allowed for obtaining values of electrical impedance on a proper range of frequencies (10 Hz−10 kHz). Measurements were carried out using the two electrodes setup in potentiostatic mode, with an amplitude of 0.3 V_RMS and an AC current range of 10 μA (to avoid damage of the 3D-HIM); two platinum electrodes (0.38 mm diameter and 99.9% purity) were used. In order to obtain TEER values, impedance curve (40 data, 10 points per decade) was fitted with non-linear least-square method using software Nova2.1. In particular, the adopted model consisted of a series of a resistor (resistance of blank solution), CPE element (interaction between solution and electrodes), and a parallel between a resistor (TEER) and a capacitor (cell membrane) (**Figure S2**).

ECM Microarchitecture of 3D-HIM

Two-photon microscopy (Leica TCS SP5 II coupled with a multiphoton microscope where the NIR femtosecond laser beam was derived from a tunable compact mode locked titanium: sapphire laser-Chamaleon Compact OPO-Vis, Coherent) was used to produce Second Harmonic Generation (SHG) images in which unstained collagen in 3D-HIMs (untreated or Et-OH-treated) were highlighted. We used an excitation wavelength of

$\lambda_{ex} = 840$ nm (two photon) and collected the signal at emission wavelength in the range $\lambda_{em} = 420 \pm 5$ nm. ImageJ was used for the quantification of the collagen fraction (CF) by measuring the collagen portion in the ECM space in a selected region of interest (ROI). The collagen portion in the ECM corresponds to bright pixels with respect to black pixels, which represent the non-collagen portion. The CF was expressed as the ratio of bright pixels to total pixels (bright pixels + black pixels) in terms of percent in the selected ROI. In addition, the collagen assembly degree (CAD) was evaluated by analyzing the intensity of the SHG signal. All SHG images were subjected to noise subtraction, and the average intensity was evaluated as described by Equation (6):

$$CAD \propto \bar{I} = \frac{\sum_{i=1}^{255}(I_i p_i)}{\sum_{i=1}^{255}(p_i)} \quad (6)$$

where $\bar{I}$ is the average intensity, I_i is the intensity corresponding to the pixel, p_i, while the index, $i = x_i, y_i$, runs in the gray value interval from 1 to 255. The intensity $\bar{I}$ of the collagen network is known to be proportional to the degree of assembly of the newly synthesized collagen (De Gregorio et al., 2019). To quantify the stroma related changes, we performed Gray-level-Co-occurrence Matrix (GLCM) texture analysis, by using the Image J plug-in "Texture" on SHG images. In this work, we calculated the correlation curve (COR) for distances ranging from 1 to 100 pixels in the horizontal (0°) and vertical (90°) direction of each optical section that cover a length of interest of 40 μm. In such spatial windows, the distance at which the correlation function falls off represents the correlation length of the texture. In particular, correlation curve was calculated vs. neighbor index, and correlation length was obtained by fitting data with an exponential law. The Equation (7) of COR is given, below:

$$COR = \sum_{i,j} \frac{(i - \mu_i)\,(j - \mu_j)\,p(i,j)}{\sigma_i\,\sigma_j} \quad (7)$$

where μ_i, μ_j, σ_i, and σ_j are given by Equations (3–6):

$$\mu_i = \sum i,j\, i * p(i,j) \quad (8)$$

$$\mu_j = \sum i,j\, j * p(i,j) \quad (9)$$

$$\sigma_i = \sqrt{\sum i,j\,(1 - \mu_i)^2 p(i,j)} \quad (10)$$

$$\sigma_j = \sqrt{\sum i,j\,(1 - \mu_j)^2 p(i,j)} \quad (11)$$

In particular $p(i,j)$ is the probability of gray level i occurring next to gray level j, μ_i, μ_j, σ_i, and σ_j are the means μ and standard deviations σ of column i and line j of the matrix, respectively. All parameters have a maximum value of 1 and a minimum value of 0 or −1. The COR curve is an index of the architecture of the network, with a fast decay for fine textures and slow decay for coarse structure. From the COR curve, it is possible to obtain the correlation length, λ, defined as the distance at which the COR decay is equal to 0.5.

Morphological, Functional and Immunohistotypical Analyses on HepG2-μTPs Cultured in Liver-OC or InLiver-OC

HepG2-μTPs (control groups and Et-OH-treated) withdrawn from the Liver-OC or InLiver-OC were processed for histological and immunofluorescence analyses, as reported in section Cytotoxic and Immunohistotypical Analyses of 3D-HIM Cultured in InLiver-OC. For immunofluorescence assay, primary antibody (Claudin-1, 1/40, Abcam; P-gp, 1/50, Abcam) and secondary antibody (donkey AlexaFluor 546-conjugated anti-rabbit IgG antibodies for Claudin-1, goat Alexa Fluor 488-conjugated anti-mouse IgG antibodies for P-gp) were used. Cells nuclei were detected by DRAQ5 staining (5 μm/mL, Sigma Aldrich). Furthermore, in order to measure albumin and urea released by HepG2-μTPs, culture media were collected after Et-OH administration on HepG2-μTPs cultured in Liver-OC. Specifically, the supernatants were centrifuged at 2,000 g for 10 min in order to remove cell debris. They were then stored at −20°C before being analyzed. Albumin secretion in cell culture supernatants was quantified by a sandwich enzyme-linked immunosorbent assay (ELISA) kit (Abcam), according to the manufacturer's instructions. All experiments were performed in triplicate. Urea levels in cell supernatants were determined by Quanti Chrom TM Urea Assay Kit (DIUR-500) according to the manufacturer's instruction.

Oil Red Staining on HepG2-μTPs

In order to evaluate the lipids production and localization in HepG2-μTPs within InLiver- and Liver-OC treated or not treated with 400 mM Et-OH for 24 h, oil red staining was performed. A group of samples was stained directly into the device, and another group was fixed in formalin 10%. The paraffin embedded samples were cut into 4-μm-thick sections, which were mounted on coating slides, unmasked with antigen retrieval and stained with oil red (Sigma Aldrich). Briefly all the samples were incubated for 5 min with 60% isopropanol at room temperature, rinsed in dH_2O, and stained for 30 min with oil red working solution. Then, the samples were counterstained with hematoxylin, washed thoroughly with dH_2O, and transferred to mounting medium (Bio Optica).

Reactive Oxygen Species (ROS) Production on HepG2-μTPs

HepG2-μTPs were collected from InLiver- or Liver-OC with or without 400 mM Et-OH treatment for 24 h, in order to assess Reactive Oxygen Species (ROS) production. After the incubation, all samples were washed with PBS and incubated with 10 μM CM-DCFDA (5-6)-chloromethyl-2,7 dichlorodihydrofluoresceine diacetate (ROS indicator, Invitrogen) at 37°C for 60 min in dark condition. For positive control groups, the samples were incubated with H_2O_2 400 μM

for 30 min. Then, all samples were washed in PBS, returned in pre-warmed growth medium, and visualized under confocal microscope (Confocal Leica TCS SP5 II femtosecond laser scanning system, Leica), using excitation appropriate source for fluorescein (FITC). For quantitative analysis, 20 images were processed by using ImageJ software, and the green signal (ROS indicator excitation at 485 nm) was normalized to the surface area.

Metabolic and Molecular Assay on 3D-HIMs and HepG2-μTPs Cultured in InLiver-OC

Alcohol Dehydrogenase Release Assay

In order to evaluate the alcohol dehydrogenase (ADH) release, the culture supernatants from In-Liver-OC treated or not treated with 400 mM Et-OH for 24 h were collected and stored at −20°C before being analyzed. ADH activity was performed, using Alcohol Dehydrogenase Activity Detection Kit (Abcam), according to the manufacturer's protocol. Briefly, 50 μL of sample or NADH standard were added to a 96-well. Then reaction mix was added to each well, and the absorbance at 450 nm was measured using a microplate reader after 2–5 min; in this way, a $T_{initial}$ was fixed. Subsequent measurement was performed after 2 h. The ADH activity was evaluated by the following Equation (12):

$$ADH = \frac{B \times Sample\ diluition\ factor}{Reaction\ time} \times V \qquad (12)$$

where B is the amount (nmole) of NADH generated between $T_{initial}$ and T_{final}, reaction time is the difference between T_{final} and $T_{initial}$, and V is the sample volume. ADH was expressed as mUnit/mL. All experiments were performed in triplicate.

Reverse Transcription-Polymerase Chain Reaction Analysis

FFPE tissues blocks (3D-HIMs and HepG2-μTPs) was deparaffinized, digested, and total RNA was extracted by using RNeasy FFPE kit (Qiagen, Valentia, CA). Agarose gel electrophoresis assessed RNA integrity, and RNA concentrations were determined by UV light BioRad Imaging System (Biorad). 0.2 μg of total cellular RNA were reverse-transcribed (Expand Reverse Transcriptase, Roche Diagnostics; Milan, Italy) into complementary DNA (cDNA) using random hexamer primers (Random hexamers, Roche Diagnostics; Milan, Italy), at 42°C for 45 min. Two microliter of cDNA was amplified in a final volume of 50 μl composed by 10 mM Tris-HCl (pH 8.3), 1.5 mM $MgCl_2$, 50 mM KCl, 200 μm dNTP and 2.5 U of Taq DNA polymerase (Roche Diagnostics). The reaction was carried out in a DNA thermal cycler (Applied Biosystem). The expression of the following genes was examined: MRP, P-gp, and glyceraldehyde-3-phosphate dehydrogenase (GAPDH) used as a housekeeping gene. The primers used for amplification were: MRP, 5′-tgatgagccgtatgttttgc−3′ and 5′- cttcggaacggacttgacat−3′; P-gp, 5′- atatcagcagcccacatcat−3′ and 5′- gaagcactgggatgtccggt−3′; GAPDH, 5′- ccacccatggcaaattccatggca−3′, and 5′-tctagactggcaggtcaggtccacc−3′. PCR products were analyzed by electrophoresis on 1.8% agarose gel in TBE. Densitometric analysis of ethidium bromide-stained agarose gel was carried out using Image J analysis and normalized by the housekeeping gene GAPDH. Each data point represented the mean-standard error of the mean of three biological replicates.

Solid Biomass Evaluation

In order to determine the biomass weight of dehydrated samples, supernatants from In-OC, Liver-OC, or In-Liver-OC were collected and centrifuged at 13,000 rpm per 15 min. All pellets were dehydrated in an incremental series of alcohol [30, 50, 75, 85, 95, and 100% twice], each step 30 min at RT, and then were made to evaporate under a chemical hood for 24 h. After that, they were weighed on an analytical balance (Xs105 dual range, Mettler Toledo).

Statistical Analyses

Results were expressed as the mean ± standard deviation (s.d.) from three or more independent experiments ($n \geq 3$). For section staining, three specimens were used for each experiment and five sections were stained per specimen, then about five ROIs were examined for each section. All results were then statistically analyzed by the Student's t-test. The differences between two or more groups were evaluated using one-way analysis of variance (ANOVA) followed by the Tukey's post-test. Statistical significance was set at a value of $p < 0.05$.

RESULTS

Assessment of Intestinal and Epithelial Markers in 3D-HIM and HepG2-μTPs

Immunofluorescence staining was performed to verify the expression and localization of a representative intestinal epithelial marker, such as villin. As depicted in **Figure 1a**, the positivity for villin signal suggested the Caco-2 differentiation toward enterocytes cells showing highly polarized epithelial cells. In addition, the presence of microvilli structure on the free surface of the epithelial cells was also evidenced by ultrastructural SEM analysis, as showed in **Figure 1a** inset, confirming the epithelial polarization. The morphological features of the HepG2-μTPs was investigated via immune-histochemical analysis. A detectable expression of the Cyt P450, a membrane-associated protein correlated with toxic compounds metabolism, was displayed (**Figure 1b**, *high magnification inset).

InLiver-OC Assembly, Operation, and Comsol Simulation

The designed InLiver-OC device allowed the co-culture of the two 3D organ models (3D-HIM in the $Intestine_c$ and HepG2-μTPs in the $Liver_c$) into separate compartments connected by means of microfluidic channel allowing an efficient unidirectional transport from the 3D-HIM to the HepG2-μTPs, mimicking the first-pass metabolism (**Figures 2A,B**). The $Intestine_c$ presents a central hole to accommodate a commercially available transwell insert in order to obtain two separate Intestine side (apical and basal). The $Liver_c$ was located downstream to

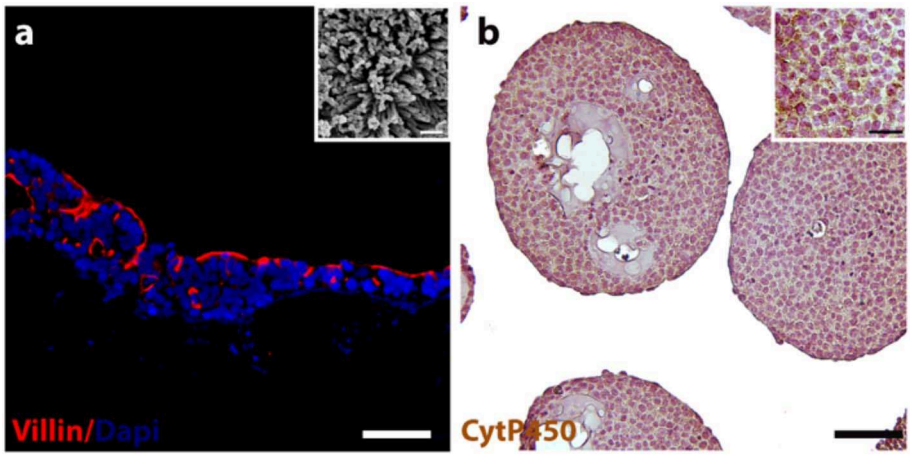

FIGURE 1 | 3D-HIM and HepG2-μTPs functionality. Immunofluorescence analysis reveals the epithelial cells marker stained in red (villin) and nuclei in blue (DAPI) **(a)**; scale bar, 75 μm. High magnification SEM micrograph shows the brush border on the apical side of the villi-like structures of the 3D-HIM (**a**, inset); scale bar 200 nm; representative immune-histochemical image of Cyt P450 on HepG2-μTPs **(b)** and high magnification inset, scale bar 75 and 50 μm, respectively.

the $Intestine_c$ and was connected through a microchannel to the basal side of the $Intestine_c$. 3D-HIM and HepG2-μTPs were produced as previously reported (De Gregorio et al., 2018a; Corrado et al., 2019), and when the best performance in terms of viability and functionality (5 weeks for 3D-HIM and 5–7 days for HepG2-μTPs) were detected, 3D-HIM was aseptically transferred into the apical side of the $Intestine_c$, and HepG2-μTPs were loaded in each chamber of the $Liver_c$ by pipetting. In order to assure the optimal conditions for cell survival, CFD (**Figure 2**) was used for simulating fluid dynamic conditions and oxygen concentration profile inside the InLiver-OC device. The flow rate at inlet (5 μL/min) assured the oxygen supply to both 3D models. As showed in **Figure 2C**, the O_2 concentration in the 3D-HIM was 0.16 mol/m^3, while the minimum O_2 concentration in the HepG2-μTPs was 0.12 mol/m^3. In **Figure 2D**, the velocity profile was shown, the maximum value of the fluid flow along the central channel was 5.4×10^{-4} m/s which is safe for cell viability according to literature (Sibilio et al., 2019).

Selection of Medium Mixing for the Optimal 3D Co-culture in InLiver-OC

Preliminary experiments were carried out in order to select the optimal media combination that did not cause the metabolic waste accumulation into the $Liver_c$. MTT and LDH assays (**Figures 3A,B**, respectively) were performed to establish the best medium combinations. We found that when 3D-HIM was cultured with the Liver-medium (Enriched_EMEM) or with InLiver-media (Enriched_DMEM:Enriched_EMEM at ratio 1:2), the viability of 3D-HIM was marginally reduced (86 ± 7.12% and 88 ± 6.22%, respectively), and low value of LDH was detected (0.2 ± 0.04 and 0.16 ± 0.02 munits/mL, respectively). At the same media combination, the HepG2-μTPs viability was slightly affected (87 ± 4.44% and 90.5 ± 4.2%, respectively), and a small but significant amount of LDH (0.35 ± 0.18 and 0.21 ± 0.07 munits/mL, respectively) was detected, indicating that the 3D-HIM probably produced a small amount of metabolic waste that slightly induced the epithelial cell injury of the HepG2-μTPs. In addition, when HepG2-μTPs were cultured with In-medium (Enriched_DMEM) or with InLiver-media (Enriched_DMEM:Enriched_EMEM at ratio 2:1), a slight amount of LDH was revealed (0.12 ± 0.02 and 0.11 ± 0.04 munits/mL, respectively), although these values were not indicative of cellular damage. Therefore, the optimal media combination resulted in the InLiver-media (Enriched_DMEM:Enriched_EMEM at ratio 1:1) that did not affect viability (96 ± 8.3% for 3D-HIM, 98 ± 6.5% for HepG2-μTPs) and did not lead to the production of LDH (0.04 ± 0.01 for 3D-HIM and 0.02 ± 0.005 munits/mL for HepG2-μTPs, respectively) as reported in **Figures 3A,B**, respectively.

Selection of the Optimal Et-OH Concentration for Evaluating HepG2-μTPs Damage

Initial experiments were focused on understanding how the HepG-2 cells respond to different concentration of Et-OH. In this experimental phase, the cytotoxic effect of Et-OH was assessed on standard culture dishes (2D HepG-2 monolayer) or in 3D configuration (3D HepG2-μTPs) (**Figure 3C**) by MTT viability assay. In detail, the 2D HepG-2 monolayer were seeded in 96 multiwell plate for 60 h in order to obtain 2.5×10^4 cells for each well. Instead, the 3D HepG2-μTPs were cultured in a spinner flask in dynamic conditions in order to obtain 1,550 cell/μTPs; then on the sixth day, 5 HepG2-μTPs were added for each liver chamber for a total of 15 HepG2-μTPs (2.32×10^4 total number of cells), as shown in the **Figure S3**. For 2D HepG-2 monolayer, a dose-dependent reduction of cell viability was reported from 0 to 600 mM Et-OH. For 3D HepG2-μTPs, a slight reduction of viability was revealed by adding 200 mM Et-OH, but an increase in cell cytotoxicity was shown at concentration over 300 mM. Specifically, when 2D HepG-2 monolayer was

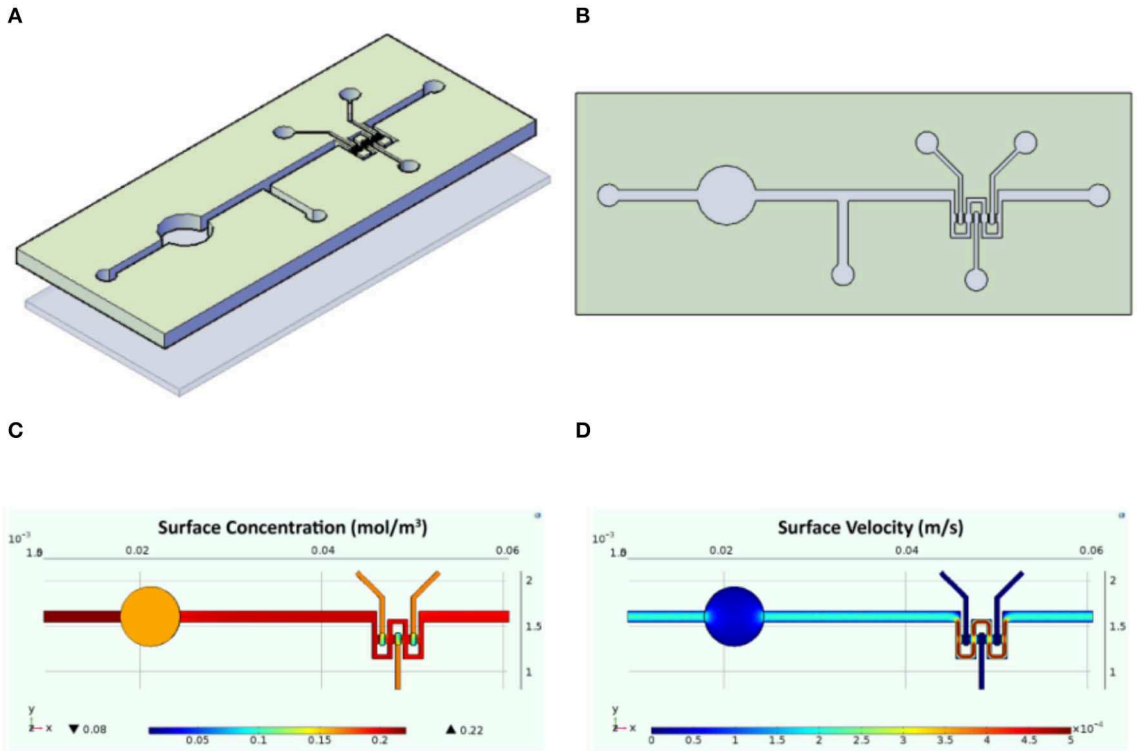

FIGURE 2 | Schematic representation of the InLiver-OC and CFD study. Lateral **(A)** and top **(B)** view of the InLiver biochip with Intestine$_c$ (In$_c$) and Liver$_c$ (Liv$_c$); fluid dynamic simulation indicates the velocity field in the device system at a flow rate of 5 μL/min **(C)** and the oxygen concentration field in the device working at a flow rate of 5 μL/min **(D)**.

treated with Et-OH 400 mM, a significant reduction in cell vitality (44 ± 4.08%) compared to 3D HepG2-μTPs treated with the same concentration (61.9 ± 5.02%) was revealed. In the groups treated with 500 mM Et-OH, the viability percentage of the cells decreased at 32 ± 4.3% in 2D HepG-2 monolayer and at 49.07 ± 5.32% in 3D HepG2-μTPs. Finally, the cells treated with 600 mM showed a mortality that exceeds 80% in 2D HepG-2 monolayer and was around 60% in 3D HepG2-μTPs. In order to perform the experiment in conditions that guarantee the cells functionality by preserving more than 50% of cell viability, the Et-OH concentration of 400 mM was selected.

400 mM Et-OH Effect on HepG2-μTPs Metabolic Activity in Liver-OC

In order to determine the liver functionality, the response of the HepG2-μTPs to Et-OH treatment at 24 h was analyzed by measuring albumin and urea production. As shown in **Figures 3E,F**, the untreated samples (–Et-OH) exhibited high levels of albumin (51.84 ± 3.9 ng) and urea (20.52 ± 2.3 μg). In contrast, there was a significant decrease in the metabolic activity in 400 mM Et-OH-treated samples (+Et-OH). In particular, albumin production decreased at value of 13.56 ± 3.81 ng and urea at 8.39 ± 1.48 μg, demonstrating that the HepG2-μTPs responded to the toxic stimulus by reducing their metabolic activity.

Intestine-Metabolized Et-OH Affects HepG2-μTPs Viability and *L. rhamnosus* Growth

An indirect estimation of the undigested Et-OH crossing the 3D-HIM was evaluated by treating HepG2-μTPs and *L. rhanmosus* with tissue supernatants in order to perform cell viability assay (MTT) and Zone of Inhibition Test, respectively (**Figures 4A,B**). Specifically, HepG2-μTPs were treated with the 3D-HIM supernatants collected from apical (3D-HIM$_{\text{apical supernatants}}$) or basal side (3D-HIM$_{\text{basal supernatants}}$) of the Intestine$_c$ at T_0 or after 24 h of 400 mM Et-OH treatment. The results indicated that at T_0 the 3D-HIM$_{\text{apical supernatants}}$ slightly reduced HepG2-μTPs viability, resulting in cell vitality of 62.5 ± 5.2%. This value corresponded in the Et-OH dose response curve to an Et-OH concentration of 400 mM (**Figure S4**). No significant reduction in cell viability was induced by treating HepG2-μTPs with 3D-HIM$_{\text{basal supernatants}}$ harvested at T_0. HepG2-μTPs treated with 3D-HIM$_{\text{apical supernatants}}$ collected at 24 h, revealed a very slight reduction of cell viability (87 ± 5.4% cell viability), while HepG2-μTPs treated with 3D-HIM$_{\text{basal supernatants}}$ harvested after 24 h of Et-OH treatment, presented a more pronounced reduction in cell viability (74 ± 5.3% cell viability). The latter value corresponded in the dose response curve (**Figure 3D**) to an Et-OH concentration of 350 mM, suggesting that a small amount of Et-OH was metabolized by the 3D-HIM (**Figure 4A**) at 24 h.

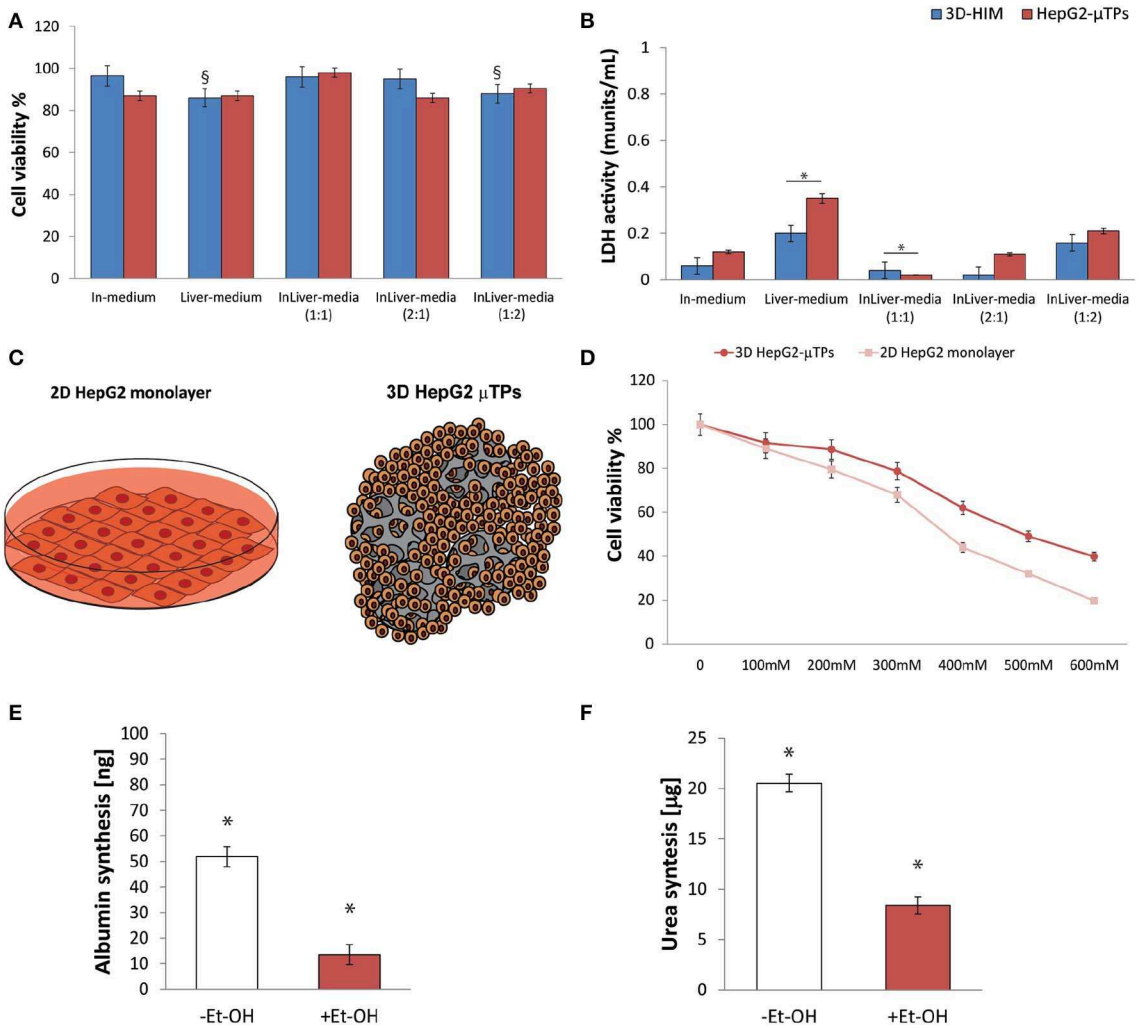

FIGURE 3 | Selection of optimal media combination in InLiver-OC, HepG-2 cytotoxicity under different Et-OH concentrations and 3D HepG2-μTPs metabolic activity under 400 mM Et-OH. MTT cell viability **(A)** and LDH **(B)** assays on 3D-HIM and HepG2-μTPs cultured with different media combinations ($^{\S}p < 0.05$; $^{*}p < 0.05$); schematic representation of standard culture dishes (2D HepG2 monolayer) and 3D configuration (3D HepG2-μTPs) **(C)**; dose response on 2D HepG2 monolayer vs. 3D HepG2-μTPs at different Et-OH concentrations (0–600 mM) **(D)**; comparison of Albumin **(E)** and urea production **(F)** on untreated (–Et-OH) and 400 mM Et-OH-treated (+Et-OH) 3D HepG2-μTPs. The Albumin amount is expressed in "ng" and the urea synthesis is indicated in "μg." All the experiments were performed in triplicate ($n = 3$), Values represent the mean and the standard deviation ($^{*}p < 0.05$).

Further, the antibacterial action of Et-OH was evaluated by analyzing the supernatants collected from 3D-HIM$_{apical}$ treated or not treated with 400 mM Et-OH at T_0 and 24 h. The maximum zone of *L. rhamnosus* strain inhibition growth (2.1 ± 0.51 cm) was found by using supernatants collected at T_0 from Et-OH treated 3D-HIM$_{apical}$ while a relatively lower (0.8 ± 0.66 cm) growth inhibition zone was found by using supernatants collected from Et-OH treated 3D-HIM$_{apical}$ at 24 h. Moreover, there was no antibacterial effect of the 3D-HIM$_{basal\ supernatants}$ at T_0, but an inhibition of the growth zone (1.5 ± 0.5 cm) was observed when 3D-HIM$_{basal\ supernatants}$ at 24 h was used. Taken together, these results demonstrate that Et-OH or Et-OH products such as acetaldehyde reduce the growth of *L. rhamnosus* strain (**Figure 4B**).

Et-OH-Induced 3D-HIM Hyper-Permeability and Stromal Injury in InLiver-OC

In order to evaluate the harmful effect of 400 mM Et-OH on 3D-HIM, the cell damage was assessed by LDH assay. The Et-OH was given on the apical side of the 3D-HIM, and at this dose, an LDH release of 0.92 ± 0.07 mU/mL at 24 h was found (**Figure 4C**), suggesting slight Et-OH-induced cell damage. This Et-OH concentration also impacted 3D-HIM's morphology and functional performance. In order to evaluate the effect in terms of the intestinal barrier integrity, intestinal tight junctions were investigated. High intensity of Claudin-1 signal, a tight junction marker, was observed on untreated samples (–Et-OH) compared to the Et-OH-treated ones (+Et-OH), in which the higher amount of acetaldehyde compromises the tight

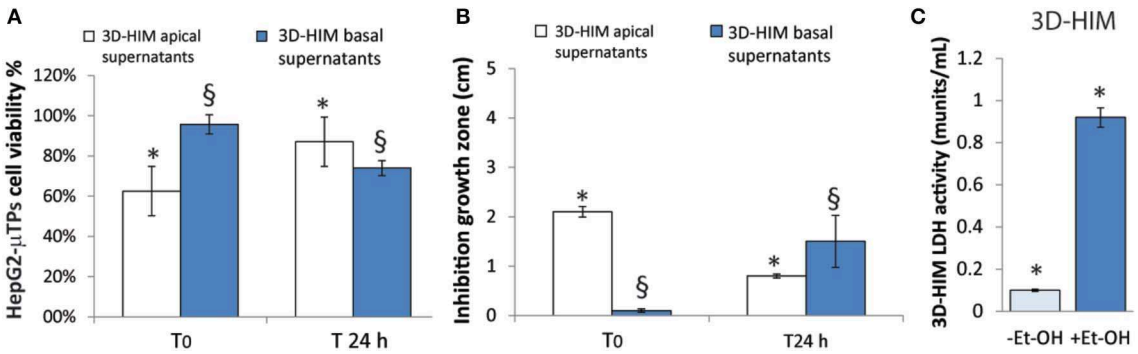

FIGURE 4 | 3D-HIM-metabolized Et-OH effect on HepG2-μTPs cytotoxicity and *L. rhamnosus* growth and Et-OH damage on 3D-HIM. MTT cell viability assay displays indirect estimation of the indigested Et-OH treating HepG2-μTPs with 3D-HIM supernatants (3D-HIM$_{apical}$ and $_{basal\ supernatants}$) at two different time points (T_0 and 24 h) (*$p < 0.001$; §$p < 0.05$) **(A)**; Zone of Inhibition Test shows the antimicrobial activity of the indigested Et-OH treating HepG2-μTPs with 3D-HIM supernatants (3D-HIM$_{apical}$ and $_{basal\ supernatants}$) on *L. rhamnosus* growth at two different time points (T_0 and 24 h) (*$p < 0.001$; §$p < 0.05$) **(B)**; LDH assay indicates the 3D-HIM toxicity after 400 mM Et-OH treatment **(C)** (*$p < 0.01$).

junction between the Caco-2 cells, determining an increase in barrier permeability (**Figures 5a,b**, respectively). Quantitative immunofluorescence analysis showed that the number of the tight junctions found on the untreated samples (189 ± 14.8, number of tight junctions per field) was higher compared to Et-OH-treated 3D-HIM (82 ± 8.01, number of tight junctions per field) (**Figure 5c**). Further, immunofluorescence staining for the Laminin V along the interface between stroma and epithelium indicated the presence of an intact basement membrane with a polarized epithelium on the untreated sample (-Et-OH, **Figure 5d**). In contrast, Et-OH treatment compromised the basement membrane integrity, as shown by pixelated signal of Laminin V and revealed the separation of the supra-basal epithelium from the basal lamina, which ultimately could cause the epithelium rupture (**Figure 5e**). In addition, an altered epithelial organization was also detected in Et-OH-treated 3D-HIM. TEER measurements were performed in order to confirm the damage at epithelium permeability. In agreement with immunofluorescence results, the untreated 3D-HIM (–Et-OH) expressed higher TEER values (4.72 kΩ) compared to Et-OH-treated 3D-HIM (43.4Ω) (**Figure 5f**), confirming that Et-OH treatment affected paracellular junctions. On the contrary, the capacitance measurements on untreated and treated samples resulted comparable (1.1 and 1.34 μF, respectively), suggesting that the membranes of the epithelial cells remain intact. Furthermore, in order to evaluate the mucus secretion on untreated (–Et-OH) and Et-OH-treated samples (+Et-OH), Alcian blue staining was performed. 3D-HIM respond to Et-OH treatment by overproducing mucus on Et-OH-treated 3D-HIM compared with the untreated one (**Figures 5g,h**, respectively). Quantification analysis of the Alcian blue images further confirmed the qualitatively observation of the histological images (**Figure 5i**). Moreover, analysis of the composition and architecture of the ECM was performed. **Figure 6** reported the Second Harmonic Generation (SHG) images rising from newly formed collagen signal on the untreated (–Et-OH, **Figure 6a**) and Et-OH-treated 3D-HIM (+Et-OH, **Figure 6b**). The SHG images were exploited to estimate the CF, the CAD, and the correlation length of collagen network in the ECM (**Figures 6c–e**). Statistically significative differences were found between the values of untreated and Et-OH-treated samples. Both CF and CAD were affected by Et-OH treatment, 43.64 ± 6.6% vs. 32.48 ± 5.0%, the former, and 31.00 ± 7.6 vs. 24.43 ± 3.0 a.u, the latter. In addition, the correlation length highlights differences in collagen texture, reporting a value for untreated samples of 52.34 ± 2.50 a.u. and a value for Et-OH-treated samples of 37.40 ± 2.10 a.u (**Figure 6e**). Lastly, Et-OH treatment induced MMP-9 overexpression, as reported in **Figures 6f,g**.

Protective Role of 3D-HIM on Et-OH-Induced Hepatic Cytotoxicity in InLiver-OC

In order to determine the intestine contribution to Et-OH metabolism, 400 mM Et-OH was administrated in three configurations of the device: Control group samples (untreated), Et-OH-treated Liver-OC (HepG2-μTPs without 3D-HIM), and Et-OH-treated InLiver-OC (device with both HepG2-μTPs and 3D-HIM). Histological characterization of untreated samples using H&E staining displayed a homogenous cell distribution around the microbeads surface of the HepG2-μTPs with the typical liver-like histotypic features, such as cuboidal hepatocyte cell shape with tight cell–cell contacts. In the Liver-OC configuration, HepG2-μTPs, although preserving the 3D epithelial organization, showed a high amount of lipid accumulation, as indicated by the black arrowheads. In contrast, in InLiver-OC configuration, HepG2-μTPs showed a small amount of lipid accumulation with a well-polarized epithelium (**Figures 7a–c**). Immunofluorescence staining showed that the Claudin-1 expression was higher in control groups than in Liver-OC, in which a completely damaged tight junction network was detected (**Figures 7d,e**, respectively). In contrast, a continuous network of tight junction was found in some

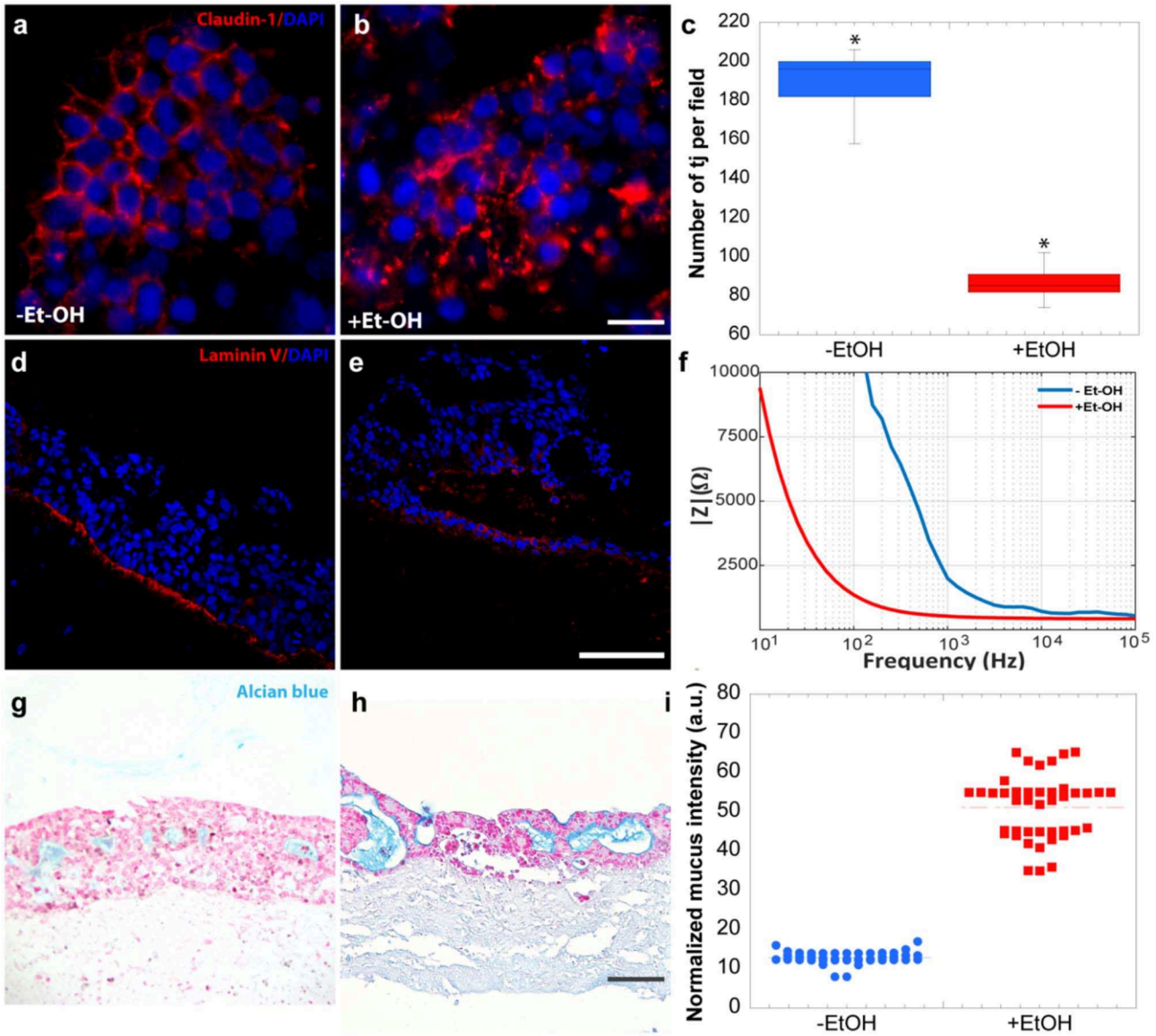

FIGURE 5 | Et-OH-induced 3D-HIM hyper-permeability at epithelial level. Comparison of the expression of the intestinal epithelial tight junction cell marker (Claudin-1) on untreated (–EtOH) 3D-HIMs **(a)** and 400 mM Et-OH-treated (+Et-OH) 3D-HIMs **(b)**; scale bar 50 μm. Quantitative analysis of tight junction per field (*$p < 0.05$) **(c)**; confocal microscope analysis of immunofluorescence staining shows the Laminin V signal on untreated (–EtOH) 3D-HIMs **(d)** and 400 mM Et-OH treated (+Et-OH) 3D-HIMs **(e)**; cell nuclei stained with DAPI scale bar 75 μm; Quantitative analysis of TEER values **(f)**; Alcian blue-stained cross-sections reveals the mucus deposition in untreated (–EtOH) 3D-HIMs **(g)** and 400 mM Et-OH-treated (+Et-OH) 3D-HIMs **(h)**; scale bar 100 μm; Quantitative analysis of Alcian blue-stained samples reveals the mucus production **(i)**. All the experiments were performed in triplicate ($n = 3$); values represent the mean and the standard deviation.

area of HepG2-μTPs in InLiver-OC (**Figure 7f**). Moreover, in order to better characterize the liver functionality, HepG2-μTPs were stained with P-Glycoprotein (P-gp) antibody—a membrane's protein that guides the transport of the substance across the epithelium—and a qualitative analysis of the P-gp expression for untreated samples, Liver-OC, and InLiver-OC was performed, as highlighted in **Figures 7g–i**. Specifically, as depicted in **Figure 7g**, the formation of canalicular-like structures was evidenced in untreated samples. However, a slight signal of P-gp was detected in Liver-OC, which indicated no assembly of the membrane protein (**Figure 7h**) in this condition, while the InLiver-OC showed higher expression of this protein, well-organized both in the core and on the external surface of the microtissue (**Figure 7i**). Furthermore, in order to determine the lipid accumulation on HepG2-μTPs, oil red staining was assessed directly into the biochip (**Figure S5**) or cross-sections after withdrawing the sample from the device (**Figures 7j–l**). In particular, untreated samples

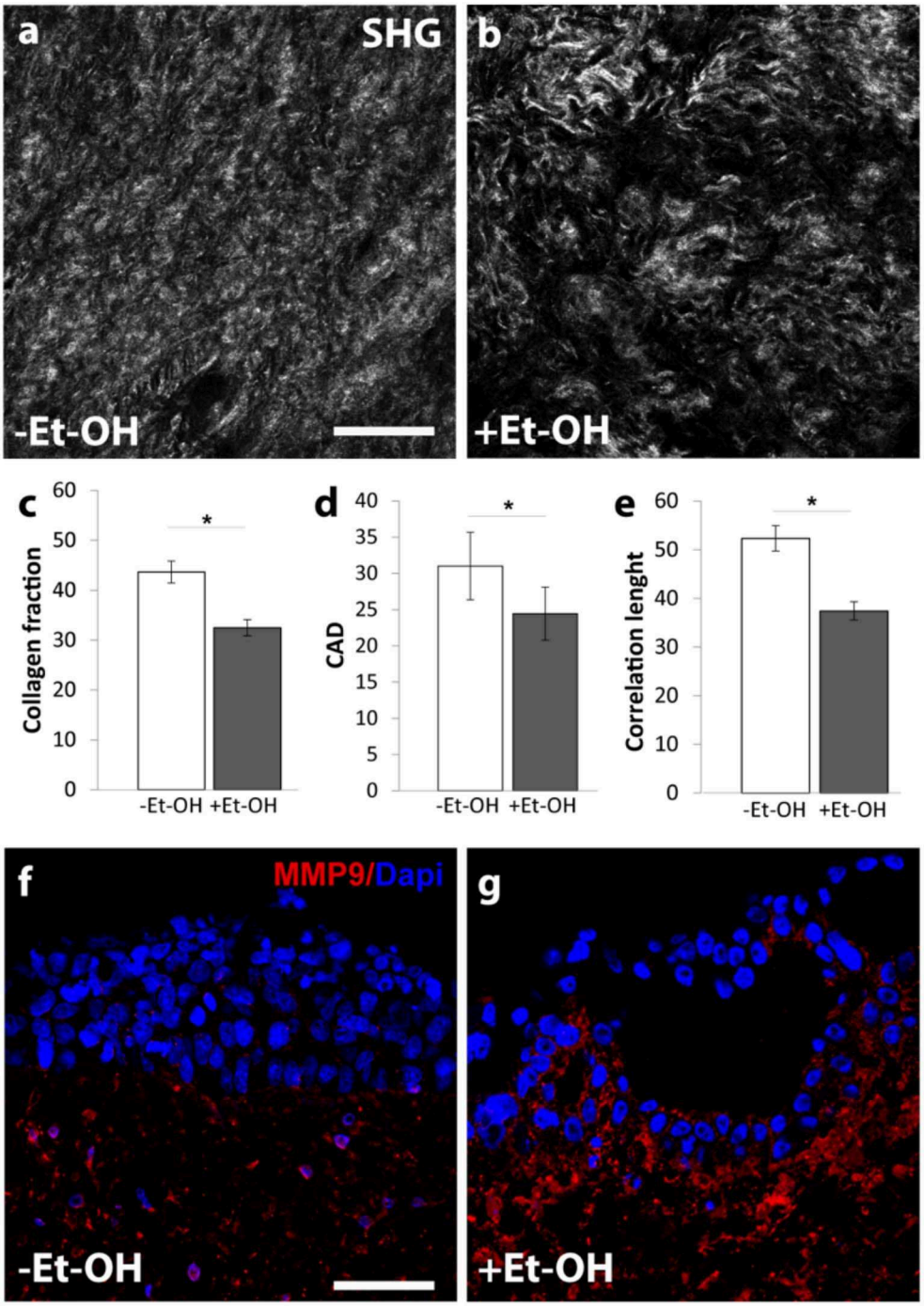

FIGURE 6 | Et-OH-induced 3D-HIM stromal injury. Representative high magnification SHG images (gray scale) of the auto-produced collagen in untreated (–EtOH) 3D-HIMs **(a)** and 400 mM Et-OH-treated (+Et-OH) 3D-HIMs **(b)**; scale bar 75 μm; **(c)** Collagen fraction, **(d)** CAD and **(e)** GLCM analysis in untreated (–EtOH) and 400 mM Et-OH-treated (+Et-OH) 3D-HIMs (*$p < 0.001$); immunofluorescence images indicate different protein expression stained in red (MMP9) on untreated (–EtOH) 3D-HIMs **(f)** and 400 mM Et-OH-treated (+Et-OH) 3D-HIMs **(g)**; scale bar is 75 μm; DAPI (blue fluorescence). All the experiments were performed in triplicate ($n = 3$); values represent the mean and the standard deviation.

showed a small amount of lipid accumulation. In contrast, high amount of lipid drops (stained in red, black arrowheads) were displayed in Liver-OC, and a small quantity of lipid drops was found in InLiver-OC cross-sections, as reported in **Figures 7j–l**.

Finally, ROS were found to be over-expressed in Liver-OC compared to untreated and InLiver-OC. **Figure S6** shows that the ROS expression on the Liver-OC was higher than on the InLiver-OC.

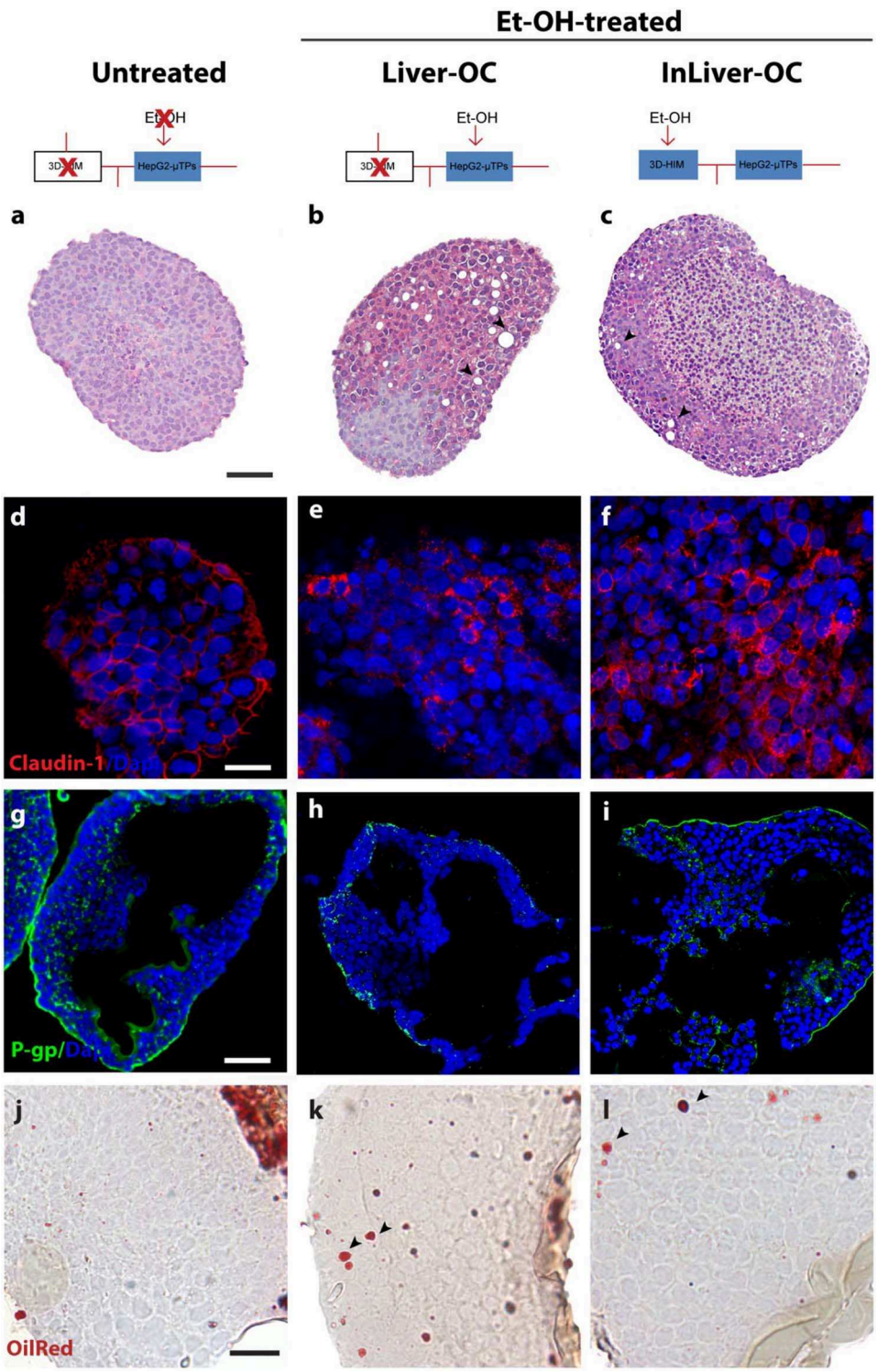

FIGURE 7 | Protective role of 3D-HIM on Et-OH-induced liver cytotoxicity. Schematic representation of Et-OH administration in different configurations [untreated **(a)**, Et-OH-treated Liver-OC **(b)** and Et-OH-treated InLiver-OC**(c)**]; representative images of the histological analysis display H&E staining of untreated **(a)** Et-OH-treated Liver-OC **(b)** and Et-OH-treated InLiver-OC **(c)**; black arrowheads indicate the lipid accumulation; scale bar 100 μm; representative immunofluorescence of tight junction marker Claudin-1 of untreated **(d)**, Et-OH-treated Liver-OC **(e)** and Et-OH-treated InLiver-OC **(f)**; scale bar 50 μm; immunofluorescent staining of the protein transporter P-gp of untreated **(g)**, Et-OH-treated Liver-OC **(h)** and Et-OH-treated InLiver-OC **(i)**; scale bar 100 μm. Oil red staining reveals the lipid drop (black arrowheads) on untreated **(j)**, Et-OH-treated Liver-OC **(k)** and Et-OH-treated InLiver-OC **(l)**; scale bar 50 μm. All the experiments were performed in triplicate ($n = 3$); values represent the mean and the standard deviation.

Synergic Response of 3D-HIM and HepG2-μTPs After Et-OH Administration in InLiver-OC

In order to determine the 3D-HIM as well as the HepG2-μTPs response to the Et-OH treatment in the device, three configurations were explored: In-OC (device loaded with 3D-HIM without HepG2-μTPs), Liver-OC (device loaded with HepG2-μTPs without 3D-HIM), and InLiver-OC (device with both HepG2-μTPs and 3D-HIM). In the In-OC configuration, the tissue supernatants were collected from the apical compartment of the $Intestine_c$ and from the sampling channel between the $Intestine_c$ and $Liver_c$. In the Liver-OC configuration, the tissue supernatants were collected downstream to the $Liver_c$. And, in the InLiver-OC configuration, the tissue supernatants were collected only downstream to the $Liver_c$ (**Figure 8A**). The detection of ADH activity was used as indication of acute cell damage (**Figure 8B**). As deduced from the results obtained after treatment with 400 mM Et-OH, a high amount of ADH was detected in the $Intestine_{apical}$ (In_{apical}) (2.42 ± 0.65 mU/mL), indicating the enzyme activity of 3D-HIM. In addition, a slight but significant release of ADH was revealed in the sampling channel (In_{basal}) (1.33 ± 0.32 mU/mL). Further, a higher amount of ADH (4.27 ± 0.42 mU/mL) was detected downstream to the $Liver_c$ in the Liver-OC configuration, mimicking what occurs during acute alcoholic liver injury. At last, InLiver-OC showed the highest ADH value (7.2 ± 0.56 mU/mL) compared to the other configuration, suggesting a synergic activity of both intestinal and hepatic tissue co-cultured into the device. Meanwhile, experiments were performed to evaluate whether the Et-OH injury induced MDRs gene expression modulation. 3D-HIM as well as the HepG2-μTPs samples cultured in Liver-OC or InLiver-OC were processed to quantify the MDR gene expression by means of molecular analysis. The results indicated that MDR4 expression on 3D-HIM decreased after Et-OH injury (5.3 ± 0.6 a.u.) compared to untreated samples (7.9 ± 2.4 a.u.) (**Figure 8C**). Likewise, Et-OH-treated HepG2-μTPs cultured in Liver-OC displayed low values of the MDR4 gene expression (3.8 ± 0.9 a.u.) compared to untreated samples (7.2 ± 1.5). On the other hand, when HepG2-μTPs were cultured in InLiver-OC, they displayed higher values in the MDR4 gene expression (8.1 ± 1.6 a.u.) compared to Et-OH-treated Liver-OC, suggesting a protective action of intestine on hepatic function. Furthermore, an increase of P-gp gene expression (9.8 ± 2.6) was revealed on 3D-HIM after Et-OH injury, in agreement with the *in vivo* situation. P-gp gene expression slightly increased on Et-OH-treated Liver-OC (7.9 ± 1.7) but reached higher values on Et-OH treated InLiver-OC (9.2 ± 2.8) compared to untreated samples (7.5 ± 1.7) (**Figures 8D,E**). Lastly, the biomass production after 400 mM Et-OH treatment was measured, showing the amount of cell debrides collected in the tissue supernatants. In particular, Et-OH-treated Liver-OC showed highest biomass compared to the other conditions, indicating the major cell debrides accumulation due to the cell damage in this configuration. The biomass quantification of InLiver-OC Et-OH-treated samples correspond to the sum of the two organs contributions: 20% of Liver-OC debrides (extrapolated from the HepG2-μTPs viability assay) and In-OC debrides (**Figure S7**).

DISCUSSION

It is widely recognized that the intestinal and hepatic first-pass metabolism may depress extensively the bioavailability of drugs and xenobiotic compounds (Rowland, 1972), highlighting the urgent need for robust *in vitro* models able to recapitulate this process to support drug and nutraceutics discovery and testing. Here, an integrated microfluidic intestine–liver device (InLiver-OC) has been proposed to investigate the *in vivo* route of orally ingested Et-OH by connecting directly the two main organs (intestine and liver) involved in the first-pass metabolism. The InLiver-OC device was designed in order to allow the inter-organs crosstalk recapitulating the key features of human intestine–liver physiology and functionality. A previously established modular tissue assembling approach to fabricate the intestinal stroma (3D-ISM) composed by H-InMyoFibs embedded in their own ECM has been exploited, and then full-thickness 3D-HIM has been obtained after Caco-2 seeding and culture (De Gregorio et al., 2018a,b). Then, 3D HepG2-μTPs have been obtained by using dynamic cells seeding in a spinner flask bioreactor (Corrado et al., 2019). The microfluidic device (InLiver-OC) was designed to host the two 3D physiologically relevant *in vitro* models (3D-HIM and HepG2-μTPs) and to provide a direct link between them by connecting in a continuous fluid stream the basal side of the $Intestine_c$ and the $Liver_c$. As first issue, the optimization of culture media mixture to perform the organ-on-chip co-culture was faced. As reported in literature, some researchers solved the problems by using multi-organ-on-chip composed by independent modules and transferring the media from one organ module to the subsequent in a physiological sequence, which allows each organ module to be operated independently (Tsamandouras et al., 2017). However, this method leads the dilution of the culture media from one module to another, avoiding the metabolic waste accumulation, which could lead to the loss of metabolic products that are crucial for experimental purposes. In this perspective, in our InLiver-OC, the modules are directly connected and the culture medium opportunely optimized. Et-OH was selected as harmful stimulus, and the Et-OH concentration to mimic alcohol-induced liver damage was selected by performing cytotoxicity assay under different Et-OH concentration on HepG2 cells in both 2D and 3D configurations. The results indicated that Et-OH significantly increases the death rate in 2D HepG-2 monolayer samples compared to 3D HepG2-μTPs that maintained high cell vitality, suggesting that the 3D configuration was more reliable than 2D for cytotoxicity assay (Edmondson et al., 2014). In general, the main issue in reproducing the first-pass mechanism is the maintenance of a selective transport route from the apical to the basal side of the $Intestine_c$. To achieve this, we fabricated a sealed chamber by using a PDMS gasket and a PMMA cylinder accommodated over the 3D-HIM. As it is well-known, once consumed, alcohol is absorbed mainly in the upper intestinal tract by diffusion and then enters the liver

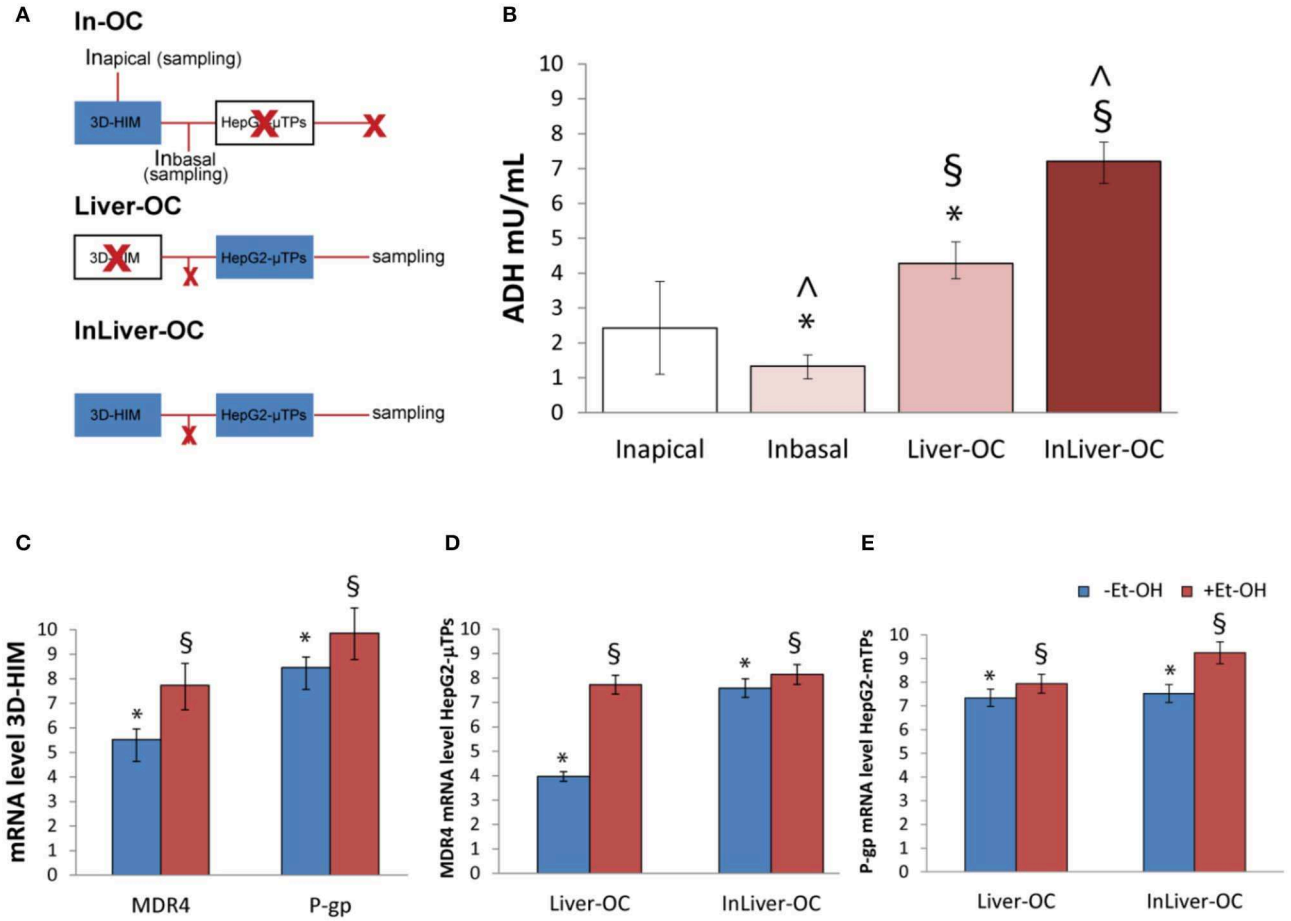

FIGURE 8 | Synergic response of 3D-HIM and HepG2-μTPs after Et-OH administration. Overview of the experimental design: In-OC (device loaded with 3D-HIM without HepG2-μTPs), Liver-OC (device loaded with HepG2-μTPs without 3D-HIM) and InLiver-OC (device with both HepG2-μTPs and 3D-HIM); In_{apical} sampling indicates the tissue supernatants collected from the apical compartment of the $Intestine_c$, In_{basal} indicates the tissue supernatants collected between the $Intestine_c$ and $Liver_c$ and sampling indicates the tissue supernatants collected downstream to the $Liver_c$ **(A)**; quantification analysis of ADH activity in the $Intestine_{apical}$ (In_{apical}), in the sampling channel (In_{basal}), Liver-OC, and Liver-OC; "∧" indicates that the group samples Inbasal and InLiver-OC are considered to be statistically significant ($p < 0.001$) **(B)**; quantification analysis of P-gp and MDR4 genes expression on untreated (–Et-OH) and Et-OH-treated (+Et-OH) 3D-HIM (*$p < 0.0001$; §$p < 0.05$) **(C)**; MDR4 **(D)**; and P-gp **(E)** gene expression of untreated (–Et-OH) and Et-OH-treated (+Et-OH) HepG2-μTPs (*$p < 0.001$; §$p < 0.05$) in the two different device configurations: Liver-OC or InLiver-OC. All the experiments were performed in triplicate ($n = 3$); values represent the mean and the standard deviation.

via the portal vein (Bishehsari et al., 2017). However, although the majority of alcohol metabolism occurs in hepatocytes, the enzymes involved in the oxidative or non-oxidative metabolism of alcohol are also present in the intestinal mucosa (Cederbaum, 2012). Mounting evidence suggests that alcohol, particularly if consumed chronically or in larger amounts, induces a deleterious effect at the intestinal district that in turn promotes inflammation through various pathways, including changes in intestinal microbiota composition and function (Mutlu et al., 2012; Engen et al., 2015), increased permeability of the intestinal mucosa (Günzel and Yu, 2013), and disruptions of the immune system of the intestinal mucosa (Bishehsari et al., 2017), as well. With this perspective, we deeply investigated the 3D-HIM response to Et-OH treatment by analyzing supernatants from apical and basal side of 3D-HIM. Surprisingly, we found that Et-OH is partly digested by 3D-HIM after 24 h, protecting HepG2-μTPs from cell mortality. In addition, in line with the literature reporting a correlation between alcohol and dysbiosis (Canesso et al., 2014), our results demonstrated the antibacterial activity on the *L. rhamnosus* strain growth of supernatants withdrawn from $3D\text{-}HIM_{apical}$ at T_0 due to the presence of undigested Et-OH and of supernatants from $3D\text{-}HIM_{apical}$ and -_{basal} at 24 h due to the presence of Et-OH or its metabolites. Alcohol has been known for a long time to interfere with the absorption of several nutrients and to lead to small intestinal mucosal damage, thereby contributing to the increase of the intestinal trans-epithelial as well as para-cellular permeability by acting on the tight junction complex (Bode and Bode, 2003). Intestinal epithelial tight junctions' integrity is fundamental in the studies of absorption and permeation of compounds, because

they form a physical barrier to the diffusion of macromolecules (Günzel and Yu, 2013). Previous studies demonstrated that the acetaldehyde, rather than Et-OH, can cause the disruption of tight junctions in Caco-2 monolayer (Atkinson and Rao, 2001). As predictable, the 3D-HIM-epithelial damage was found after Et-OH administration in InLiver-OC by analyzing the Claudin-1 signal, a transmembrane protein of the tight junctions, that form a barrier to macromolecular diffusion (Günzel and Yu, 2013). Specifically, the Et-OH-treated 3D-HIM presented a lower number of tight junctions with less organized protein structure. In addition, the TEER measurements on Et-OH-treated 3D-HIM confirmed the Et-OH deleterious effect on the epithelial barrier showing a very low TEER value compared to untreated samples. Further, the acute alcohol administration elicits basement membrane alterations determining in severe cases the separation of the epithelium from the basal lamina with the formation of sub-epithelial blisters, which ultimately cause the epithelium rupture (Singer and Brenner, 2006). In agreement, we found that in Et-OH-treated InLiver-OC, the 3D-HIM showed a basement membrane impairment reported as pixelated immunofluorescence signal of the main protein of basal lamina (Laminin V) (Haas et al., 2001). In addition, in Et-OH-treated 3D-HIM, a high quantifiable amount of mucus was produced, due to the self-defense to the high concentration of the Et-OH and its metabolites. This is in agreement with previous studies showing that chronic alcohol feeding increased mucin production in the small intestine due to alcohol-induced qualitative changes (Valatas and Kolios, 2009). However, the damage induced to the small intestine by the Et-OH involves not only the epithelial layer but also affects the stromal compartment (Casini et al., 1999). From this perspective, the availability of a 3D-HIM provided with an endogenous stroma allows to assess the complex response of the small intestine to Et-OH, otherwise not observable with the over-simplistic existing intestinal mucosa model. SHG microscopy on 3D-HIM provided high-resolution 3D images of collagen fibers in thick samples without the need for sample staining and processing and allowed us to detect the non-centrosymmetrical structure of fibrillar collagen and the textural change at stromal level resulting from Et-OH treatment (De Gregorio et al., 2019). The results indicated that Et-OH-treated 3D-HIM experienced a decrease of both the total collagen amount and of the degree of the collagen assembly, as well as a collagen stretching in the intestinal mucosa. It is reasonable to assume that ECM remodeling contributes to Et-OH intestinal mucosa injury. In terms of liver damage due to Et-OH administration we assessed the role of intestine in reducing the toxic effects by analyzing morphological and functional hepatic markers in InLiver-OC vs. Liver-OC. Our results showed a protective role of intestine able to impair the lipid accumulation and maintain quite intact the tight junction's network in Et-OH-treated HepG2-μTPs cultured in InLiver-OC. Some *in vivo* studies suggested that intestinal drug efflux transporters are involved in pharmacokinetic alterations caused by chronic alcohol exposure (Artursson and Karlsson, 1991; Sambuy et al., 2005). Here, we reported a strong increase of P-gp gene expression on 3D-HIM after Et-OH injury according to the *in vivo* situation. High value of P-gp gene expression in Et-OH-treated HepG2-μTPs in InLiver-OC indicate once again the preservation of biochemical liver function from intestine. Furthermore, in terms of protein expression, we found the correct signal of P-gp that pointed out the formation of canalicular-like structures in InLiver-OC. In addition, the high value of MDR4 gene expression indicated a physiological liver protection from toxic accumulation of bile acids and a low cytosolic ROS production in Et-OH treated HepG2-μTPs cultured in InLiver-OC samples, corroborating once again the intestine prevention to the liver injury. Even if the majority of alcohol metabolism in humans occurs in the hepatocytes cells in the liver, some enzymes involved in the oxidative metabolism of alcohol such as alcohol dehydrogenase (ADH) are also present in the intestinal mucosa. In line with the *in vivo* situation, ADH was detected in the 3D-HIM as well as HepG2-μTPs, indicating the enzyme activity of InLiver-OC after Et-OH treatment. Liver-OC also showed high amount of ADH indicating acute alcoholic liver injury. These data confirmed the synergic contribution of both tissues when co-cultured into InLiver-OC together. Lastly, it should also be noted that the biomass production after Et-OH treatment indicated the comparable debris accumulation when single tissues culture (In-OC or Liver-OC) or co-culture (InLiver-OC) were performed in the device. These results suggested that the culture medium guaranteed the physiological function of both intestine and hepatic equivalent tissues and did not induce hepatic damage due to intestinal metabolic waste accumulation in InLiver-OC. Taken together, these results point out the stromal and epithelial damage of the 3D-HIM under orally administrated xenobiotic and the protective intestinal role in attenuating the Et-OH-induced liver cytotoxicity.

CONCLUSION

In conclusion, in this study, we developed a microfluidic InLiver-OC with the aim of reproducing the first pass metabolism. We have observed the intestine–liver crosstalk in the metabolic and absorptive properties. By using the Et-OH as a harmful stimulus, we have shown that this device can be used as a tool to reproduce the first-pass metabolism of drugs and xenobiotics. Our proposed model is a more predictive platform than the 2D cell culture, resembling the physiological way route of the *in vivo* first-pass metabolism. It is also suitable to study the interaction of the gastrointestinal tract, the effects of nutraceutical substances, and the uptake of compounds. InLiver-OC can be adapted to co-culture human gut microbiome to provide a versatile platform to investigate host-microbiome interaction in a multi-organs platform. Finally, this microdevice is expected to reduce the number of drug candidates and accelerate the pre-clinical screening process reducing animal testing.

DATA AVAILABILITY STATEMENT

The datasets generated for this study are available on request to the corresponding author.

AUTHOR CONTRIBUTIONS

GI and PN conceived the idea and critically revised the manuscript with input from the entire team. VD, GI, and FU worked on the study conception and design, analyzed and interpreted the data, and drafted the manuscript. VD and MT carried out biological experiments. VR performed electrophysiological measurements. BC designed and microfabricated the device. FU performed fluidodynamic simulations experiments. All authors have read and approved the final draft.

ACKNOWLEDGMENTS

The authors thank Dr. La Rocca Alessia for her precious contribution during the experimental phase. The authors thank Dr. Sibilio Sara for her contribution in Comsol studies.

SUPPLEMENTARY MATERIAL

The Supplementary Material for this article can be found online at: https://www.frontiersin.org/articles/10.3389/fbioe.2020.00163/full#supplementary-material

REFERENCES

Artursson, P., and Karlsson, J. (1991). Correlation between oral drug absorption in humans and apparent drug permeability coefficients in human intestinal epithelial (Caco-2) cells. *Biochem. Biophys. Res. Commun.* 175, 880–885. doi: 10.1016/0006-291X(91)91647-U

Atkinson, K., and Rao, R. (2001). Role of protein tyrosine phosphorylation in acetaldehyde-induced disruption of epithelial tight junctions. *Am. J. Physiol. Gastrointest. Liver Physiol.* 280, G1280–G1288. doi: 10.1152/ajpgi.2001.280.6.G1280

Bhatia, S. N., and Ingber, D. E. (2014). Microfluidic organs-on-chips. *Nat. Biotechnol.* 32, 760–772. doi: 10.1038/nbt.2989

Bishehsari, F., Magno, E., Swanson, G., Desai, V., Voigt, R. M., Forsyth, C. B., et al. (2017). Alcohol and gut-derived inflammation. *Alcohol Res.* 38, 163–171.

Bode, C., and Bode, J. C. (2003). Effect of alcohol consumption on the gut. *Best Pract. Res. Clin. Gastroenterol.* 17, 575–592. doi: 10.1016/S1521-6918(03)00034-9

Canesso, M. C. C., Lacerda, N., Ferreira, C., Gonçalves, J., Almeida, D., Gamba, C., et al. (2014). Comparing the effects of acute alcohol consumption in germ-free and conventional mice: the role of the gut microbiota. *BMC Microbiol.* 14:240. doi: 10.1186/s12866-014-0240-4

Casini, A., Galli, A., Di Lollo, S., Orsini, B., Arganini, L., Jezequel, A. M., et al. (1999). Ethanol-induced alterations of matrix network in the duodenal mucosa of chronic alcohol abusers. *Virchows Arch.* 434, 127–135. doi: 10.1007/s004280050316

Cederbaum, A. I. (2012). Alcohol metabolism. *Clin. Liver Dis.* 16, 667–685. doi: 10.1016/j.cld.2012.08.002

Chen, H. J., Miller, P., and Shuler, M. L. (2018). A pumpless body-on-a-chip model using a primary culture of human intestinal cells and a 3D culture of liver cells. *Lab Chip* 18, 2036–2046. doi: 10.1039/C8LC00111A

Chen, W. L., Edington, C., Suter, E., Yu, J., Velazquez, J. J., Velazquez, J. G., et al. (2017). Integrated gut/liver microphysiological systems elucidates inflammatory inter-tissue crosstalk. *Biotechnol. Bioeng.* 114, 2648–2659. doi: 10.1002/bit.26370

Choe, A., Ha, S. K., Choi, I., Choi, N., and Sung, J. H. (2017). Microfluidic Gut-liver chip for reproducing the first pass metabolism. *Biomed. Microdevices* 19:4. doi: 10.1007/s10544-016-0143-2

Corrado, B., De Gregorio, V., Imparato, G., Attanasio, C., Urciuolo, F., and Netti, P. A. (2019). A three-dimensional microfluidized liver system to assess hepatic drug metabolism and hepatotoxicity. *Biotechnol. Bioeng.* 116, 1152–1163. doi: 10.1002/bit.26902

Council, N. R. (2007). *Toxicity Testing in the 21st Century: A Vision and a Strategy*. Washington, DC: National Academies Press.

De Gregorio, V., Corrado, B., Sbrescia, S., Sibilio, S., Urciuolo, F., Netti, P. A., et al. (2019). Intestine-on-chip device increases ECM remodeling inducing faster epithelial cell differentiation. *Biotechnol. Bioeng.* 117, 556–566. doi: 10.1002/bit.27186

De Gregorio, V., Imparato, G., Urciuolo, F., and Netti, P. A. (2018a). 3D stromal tissue equivalent affects intestinal epithelium morphogenesis *in vitro*. *Biotechnol. Bioeng.* 115, 1062–1075. doi: 10.1002/bit.26522

De Gregorio, V., Imparato, G., Urciuolo, F., and Netti, P. A. (2018b). Micro-patterned endogenous stroma equivalent induces polarized crypt-villus architecture of human small intestinal epithelium. *Acta Biomater.* 81, 43–59. doi: 10.1016/j.actbio.2018.09.061

de Sousa, I. P., and Bernkop-Schnürch, A. (2014). Pre-systemic metabolism of orally administered drugs and strategies to overcome it. *J. Control. Release* 192, 301–309. doi: 10.1016/j.jconrel.2014.08.004

Edmondson, R., Broglie, J. J., Adcock, A. F., and Yang, L. (2014). Three-dimensional cell culture systems and their applications in drug discovery and cell-based biosensors. *Assay Drug Dev. Technol.* 12, 207–218. doi: 10.1089/adt.2014.573

Engen, P. A., Green, S. J., Voigt, R. M., Forsyth, C. B., and Keshavarzian, A. (2015). The gastrointestinal microbiome: alcohol effects on the composition of intestinal microbiota. *Alcohol Res.* 37, 223–236.

Esch, M., King, T., and Shuler, M. (2011). The role of body-on-a-chip devices in drug and toxicity studies. *Annu. Rev. Biomed. Eng.* 13, 55–72. doi: 10.1146/annurev-bioeng-071910-124629

Esch, M. B., Mahler, G. J., Stokol, T., and Shuler, M. L. (2014). Body-on-a-chip simulation with gastrointestinal tract and liver tissues suggests that ingested nanoparticles have the potential to cause liver injury. *Lab Chip* 14, 3081–3092. doi: 10.1039/C4LC00371C

Esch, M. B., Sung, J. H., Yang, J., Yu, C., Yu, J., March, J. C., et al. (2012). On chip porous polymer membranes for integration of gastrointestinal tract epithelium with microfluidic 'body-on-a-chip'devices. *Biomed. Microdevices* 14, 895–906. doi: 10.1007/s10544-012-9669-0

Günzel, D., and Yu, A. S. (2013). Claudins and the modulation of tight junction permeability. *Physiol. Rev.* 93, 525–569. doi: 10.1152/physrev.00019.2012

Haas, M. K., Berndt, A., Stiller, K. J., Hyckel, P., and Kosmehl, H. (2001). A comparative quantitative analysis of laminin-5 in the basement membrane of normal, hyperplastic, and malignant oral mucosa by confocal immunofluorescence imaging. *J. Histochem. Cytochem.* 49, 1261–1268. doi: 10.1177/002215540104901008

Huh, D., Hamilton, G. A., and Ingber, D. E. (2011). From 3D cell culture to organs-on-chips. *Trends Cell Biol.* 21, 745–754. doi: 10.1016/j.tcb.2011.09.005

Imparato, G., Urciuolo, F., Casale, C., and Netti, P. A. (2013). The role of microscaffold properties in controlling the collagen assembly in 3D dermis equivalent using modular tissue engineering. *Biomaterials* 34, 7851–7861. doi: 10.1016/j.biomaterials.2013.06.062

Inamdar, N. K., and Borenstein, J. T. (2011). Microfluidic cell culture models for tissue engineering. *Curr. Opin. Biotechnol.* 22, 681–689. doi: 10.1016/j.copbio.2011.05.512

Lee, S. Y., and Sung, J. H. (2018). Gut–liver on a chip toward an *in vitro* model of hepatic steatosis. *Biotechnol. Bioeng.* 115, 2817–2827. doi: 10.1002/bit.26793

Mahler, G. J., Esch, M. B., Glahn, R. P., and Shuler, M. L. (2009). Characterization of a gastrointestinal tract microscale cell culture analog used to predict drug toxicity. *Biotechnol. Bioeng.* 104, 193–205. doi: 10.1002/bit.22366

Maurice, C. F., Haiser, H. J., and Turnbaugh, P. J. (2013). Xenobiotics shape the physiology and gene expression of the active human gut microbiome. *Cell* 152, 39–50. doi: 10.1016/j.cell.2012.10.052

Mutlu, E. A., Gillevet, P. M., Rangwala, H., Sikaroodi, M., Naqvi, A., Engen, P. A., et al. (2012). Colonic microbiome is altered in alcoholism. *Am. J. Physiol. Gastrointest. Liver Physiol.* 302, G966–G978. doi: 10.1152/ajpgi.00380.2011

Prot, J. M., Maciel, L., Bricks, T., Merlier, F., Cotton, J., Paullier, P., et al. (2014). First pass intestinal and liver metabolism of paracetamol in a

microfluidic platform coupled with a mathematical modeling as a means of evaluating ADME processes in humans. *Biotechnol. Bioeng.* 111, 2027–2040. doi: 10.1002/bit.25232

Rowland, M. (1972). Influence of route of administration on drug availability. *J. Pharm. Sci.* 61, 70–74. doi: 10.1002/jps.2600610111

Sambuy, Y., De Angelis, I., Ranaldi, G., Scarino, M., Stammati, A., and Zucco, F. (2005). The caco-2 cell line as a model of the intestinal barrier: influence of cell and culture-related factors on caco-2 cell functional characteristics. *Cell Biol. Toxicol.* 21, 1–26. doi: 10.1007/s10565-005-0085-6

Santaguida, S., Janigro, D., Hossain, M., Oby, E., Rapp, E., and Cucullo, L. (2006). Side by side comparison between dynamic versus static models of blood–brain barrier *in vitro*: a permeability study. *Brain Res.* 1109, 1–13. doi: 10.1016/j.brainres.2006.06.027

Sibilio, S., De Gregorio, V., Urciuolo, F., Netti, P. A., and Imparato, G. (2019). Effect of peristaltic-like movement on bioengineered intestinal tube. *Mater. Today Bio.* 4:100027. doi: 10.1016/j.mtbio.2019.100027

Singer, M. V., and Brenner, D. (2006). *Alcohol and the Gastrointestinal Tract*. Basel: Karger Medical and Scientific Publishers.

Tsamandouras, N., Chen, W. L. K., Edington, C. D., Stokes, C. L., Griffith, L. G., and Cirit, M. (2017). Integrated gut and liver microphysiological systems for quantitative *in vitro* pharmacokinetic studies. *AAPS J.* 19, 1499–1512. doi: 10.1208/s12248-017-0122-4

Valatas, V., and Kolios, G. (2009). Ethanol effects on mucin glycosylation: another kick in the gut? *Ann. Gastroenterol.* 22, 138–140.

van Midwoud, P. M., Merema, M. T., Verpoorte, E., and Groothuis, G. M. (2010). A microfluidic approach for *in vitro* assessment of interorgan interactions in drug metabolism using intestinal and liver slices. *Lab Chip* 10, 2778–2786. doi: 10.1039/c0lc00043d

Weise, F., Fernekorn, U., Hampl, J., Klett, M., and Schober, A. (2013). Analysis and comparison of oxygen consumption of HepG2 cells in a monolayer and three-dimensional high density cell culture by use of a matrigrid®. *Biotechnol. Bioeng.* 110, 2504–2512. doi: 10.1002/bit.24912

Conflict of Interest: The authors declare that the research was conducted in the absence of any commercial or financial relationships that could be construed as a potential conflict of interest.

frontiers in Bioengineering and Biotechnology

ORIGINAL RESEARCH
published: 07 April 2020
doi: 10.3389/fbioe.2020.00294

Imaging the Cell Morphological Response to 3D Topography and Curvature in Engineered Intestinal Tissues

Gizem Altay[1], Sébastien Tosi[2], María García-Díaz[1] and Elena Martínez[1,3,4]**

[1] Biomimetic Systems for Cell Engineering, Institute for Bioengineering of Catalonia, The Barcelona Institute of Science and Technology, Barcelona, Spain, [2] Advanced Digital Microscopy Core Facility, Institute for Research in Biomedicine, The Barcelona Institute of Science and Technology, Barcelona, Spain, [3] Centro de Investigación Biomédica en Red en Bioingeniería, Biomateriales y Nanomedicina, Madrid, Spain, [4] Department of Electronics and Biomedical Engineering, University of Barcelona, Barcelona, Spain

OPEN ACCESS

Edited by:
Ivan Martin,
University of Basel, Switzerland

Reviewed by:
Sourabh Ghosh,
Indian Institute of Technology Delhi, India
Vanessa L. S. LaPointe,
Maastricht University, Netherlands

***Correspondence:**
María García-Díaz
mgarcia@ibecbarcelona.eu
Elena Martínez
emartinez@ibecbarcelona.eu

Specialty section:
This article was submitted to Tissue Engineering and Regenerative Medicine, a section of the journal Frontiers in Bioengineering and Biotechnology

Received: *30 November 2019*
Accepted: *19 March 2020*
Published: *07 April 2020*

Citation:
Altay G, Tosi S, García-Díaz M and Martínez E (2020) Imaging the Cell Morphological Response to 3D Topography and Curvature in Engineered Intestinal Tissues. Front. Bioeng. Biotechnol. 8:294. doi: 10.3389/fbioe.2020.00294

While conventional cell culture methodologies have relied on flat, two-dimensional cell monolayers, three-dimensional engineered tissues are becoming increasingly popular. Often, engineered tissues can mimic the complex architecture of native tissues, leading to advancements in reproducing physiological functional properties. In particular, engineered intestinal tissues often use hydrogels to mimic villi structures. These finger-like protrusions of a few hundred microns in height have a well-defined topography and curvature. Here, we examined the cell morphological response to these villus-like microstructures at single-cell resolution using a novel embedding method that allows for the histological processing of these delicate hydrogel structures. We demonstrated that by using photopolymerisable poly(ethylene) glycol as an embedding medium, the villus-like microstructures were successfully preserved after sectioning with vibratome or cryotome. Moreover, high-resolution imaging of these sections revealed that cell morphology, nuclei orientation, and the expression of epithelial polarization markers were spatially encoded along the vertical axis of the villus-like microstructures and that this cell morphological response was dramatically affected by the substrate curvature. These findings, which are in good agreement with the data reported for *in vivo* experiments on the native tissue, are likely to be the origin of more physiologically relevant barrier properties of engineered intestinal tissues when compared with standard monolayer cultures. By showcasing this example, we anticipate that the novel histological embedding procedure will have a positive impact on the study of epithelial cell behavior on three-dimensional substrates in both physiological and pathological situations.

Keywords: hydrogel scaffold, confocal microscopy, substrate curvature, cell morphology, cell orientation, histological section, small intestine, villus

INTRODUCTION

Many epithelial tissues exhibit complex morphologies that are mostly dominated by curved surfaces such as those found in lung alveoli and intestinal villi (Torras et al., 2018; Baptista et al., 2019). These three-dimensional (3D) topographies generate gradients in biochemical signals and mechanical tension that play a key role in cell polarization, morphology, and function (Farin et al., 2016; Krndija et al., 2019). While traditionally ignored in flat *in vitro* models, 3D topographies are distinctive elements in the emergence and further development of a new generation of tissue-engineered cell culture substrates (Griffith and Swartz, 2006). These 3D models are capable of capturing the complex physiological responses of tissue *in vitro* and have been employed to systematically study the effects of *in vivo*-like tissue geometry and curvature on cell fate (Griffith and Swartz, 2006; Baptista et al., 2019).

Hydrogels are widely used as scaffold materials for tissue engineering and 3D cell culture applications (Slaughter et al., 2009; Caliari and Burdick, 2016). Due to their porous network structure and soft mechanical properties, hydrogels mimic important elements of the native extracellular matrix. Also, their rich water content facilitates the diffusion of biochemical factors and oxygen and also enables long-term maintenance of mammalian cell cultures (Peppas et al., 2006; DeForest and Anseth, 2012; Caliari and Burdick, 2016). Hydrogels can be engineered with different topographies and can thus be used to reproduce the 3D architecture of native tissues (Khademhosseini and Langer, 2007; Torras et al., 2018). In the case of the small intestine, several strategies have been proposed to fabricate villus-like hydrogels such as replica molding or stereolithography-based 3D printing (Wang et al., 2017; Creff et al., 2019). Using a different approach, we have recently developed a method to fabricate microstructured hydrogel scaffolds mimicking the small intestinal villi by using a photolithography-based microfabrication technique (Castaño et al., 2019). This moldless approach yielded high aspect ratio, finger-like hydrogel microstructures with the physiological shape and dimensions of the native villi. Moreover, not only did these scaffolds support the growth and differentiation of intestinal epithelial Caco-2 cells along the villi but they also induced improved cell polarization and tissue barrier properties compared to the standard monolayer cell cultures. These benefits were attributed to the more physiologically realistic environment provided by the 3D model.

Recently, it has been reported that, *in vivo*, parameters such as cell density and cell anisotropy differ significantly along the crypt-villus axis of the intestinal epithelium (Krndija et al., 2019). This raises the question if analogous effects can also be observed *in vitro* on engineered intestinal tissue models. For that purpose, the optical visualization of individually resolved cells along the vertical axis of 3D villus-like microstructures is required. Confocal fluorescence microscopy is the most widespread imaging technique used in the field of life sciences and enables optical sectioning for *in situ* cell imaging (Graf and Boppart, 2010; Leferink et al., 2016). However, imaging large tissue-engineered constructs with high resolution is technically challenging due to sample thickness and high scattering (Pampaloni et al., 2007). In particular, engineered intestinal tissues contain relatively large finger-like microstructures with a high aspect ratio (∼500 μm in height, ∼100 μm in diameter). As such, due to the working distance restrictions of high magnification objective lenses, the total thickness of the scaffolds (often ∼1000 μm) precludes high-resolution imaging along the whole structure (Smith et al., 2010; Short et al., 2017). To overcome this problem, advanced techniques such as multiphoton microscopy, light sheet microscopy, or optical coherence tomography can be used. However, the sophisticated equipment needed is often not widely available in standard tissue engineering laboratories (Graf and Boppart, 2010; Leferink et al., 2016).

Histological processing is the gold standard for tissue characterization in medical practice and is often available as a support facility at most research centers. When applied to cells grown on 3D tissue-engineered constructs, it can provide crucial information on parameters such as their viability, proliferation, and differentiation. However, due to their high water content, hydrogels are very sensitive to routine histology procedures (James et al., 2004; Yang et al., 2007). In standard paraffin processing, the exchange of tissue water by ethanol, followed by a hydrophobic solvent (e.g., xylene), results in the collapse of the hydrogel scaffolds (Loebsack et al., 1999). Cryosectioning is another standard technique for tissue processing. It is performed at very low temperatures (about −20 to −30°C) after embedding the tissue in a gel-like medium called optimum cutting temperature (OCT). Then again, the water-rich hydrogel samples show the formation of ice crystals within the hydrogels themselves, resulting in sample brittleness and poor cryosection quality, even after infiltration with a 30% sucrose solution for cryoprotection (Ruan et al., 2013). Different strategies have been pursued to improve the sectioning of hydrogel scaffolds. Among them, improved cryosections were obtained by including, as an additional step in the protocol, an overnight incubation with non-protein-based solutions such as polyvinyl alcohol or the same OCT medium that is later used for embedding (Ruan et al., 2013). In another approach, it was recently reported that the integrity of the hydrogels during sectioning was preserved by employing vibrating microtomy, which is commonly used in sectioning soft tissues such as the brain (Short et al., 2017). Nevertheless, despite their potential, these techniques have rarely been applied to the characterization of microstructured hydrogel scaffolds (Sung et al., 2011; Costello et al., 2014b). In fact, our previous attempts to produce histological sections of engineered intestinal tissues by using either cryosectioning or vibrating microtomy resulted in the collapse of the delicate villus-like microstructures.

In this study, we present a new method to preserve complex hydrogel microstructures in histological sections by employing a photopolymerisable polyethylene glycol diacrylate (PEGDA) polymer as the embedding medium. This resulted in hydrogel blocks that were suitable for processing by either cryosectioning or vibrating microtomy and that yielded undistorted sections of the engineered 3D hydrogels. By using this method, the cell morphological response of intestinal epithelial Caco-2 cells to villi-like hydrogel microstructures was successfully evaluated. High-resolution imaging was performed and revealed that cell

morphology and nuclear orientation changes significantly along the vertical axis of the villus-like microstructures while also being dramatically impacted by the curvature of the structures. Also, the expression of epithelial polarization markers, such ZO-1, were remarkably higher toward the tips of the villi than at their bases. Altogether, these findings demonstrate that, similar to what has been reported *in vivo*, the complex topographies and curvatures recreated by the engineered *in vitro* models significantly affect cell shape and polarization. As such, this methodology paves the way to gain better insights about the growth of epithelial cells on 3D artificial structures and to study the effects of tissue curvature in physiological events, such as morphogenesis or homeostasis, and pathological situations such as wound healing processes.

MATERIALS AND METHODS

Fabrication of Villus-Like Microstructured Hydrogels and Cell Culture

The villus-like microstructured scaffolds were fabricated by photolithography, as previously described (Castaño et al., 2019) (**Figure 1A**). Briefly, a prepolymer solution containing 6.5% w/v 6 kDa PEGDA, 0.3% w/v acrylic acid (AA), and 1% w/v Irgacure D-2959 photoinitiator in phosphate-buffered saline (PBS) (all from Sigma-Aldrich) was flown into a chip fabricated with a 1 mm thick polydimethylsiloxane (PDMS) (Sylgard 184, Dow Corning) stencil containing an array of pools of 6.5 mm diameter. Silanized glass coverslips or Tracketch polyethylene terephthalate (PET) membranes of 5 μm pore size (Sabeu GmbH & Co.) were used as substrates. The microstructured PEGDA-AA scaffolds were fabricated by exposure to UV light under patterned photomasks with transparent windows of 100 μm in diameter and a density of 25 windows/mm^2. The photolithography was performed in an MJBA mask aligner (SUSS MicroTech) using a power density of 25 mW/cm^2. The prepolymer solution was exposed for 140–220 s to form the villus-like micropillars (**Figure 1B**). For the samples fabricated on glass coverslips, a second exposure of 15 s was performed to form a hydrogel base holding the microstructures together. After UV exposure, unreacted polymer and photoinitiator were washed out with PBS and the hydrogels were kept submerged at 4°C for at least 3 days to reach equilibrium swelling. Samples fabricated onto PET membranes were assembled on modified Transwell inserts using double-sided pressure-sensitive adhesive rings as detailed in Castaño et al. (2019). After swelling, and to provide the scaffolds with cell-adhesion motifs, the PEGDA-AA hydrogels were functionalized with 0.01% w/v collagen type I (Sigma Aldrich) via an *N*- (3-Dimethylaminopropyl)-*N*′-ethylcarbodiimide (EDC)/*N*-Hydroxysuccinimide (NHS) (Sigma Aldrich) mediated coupling.

Caco-2 cells (ATCC HTB-37) from passages 75–85 were expanded and maintained in 75 cm^2 flasks containing DMEM-Glutamax medium (Gibco, Thermofisher), supplemented with 10% v/v fetal bovine serum (Gibco, Thermofisher), 1% v/v penicillin/streptomycin (Sigma-Aldrich), and 1% v/v non-essential amino acids (Gibco, Thermofisher). Cells were kept in an incubator at 37°C and 5% CO_2 and passaged weekly. Cells were seeded in the villus-like scaffolds at a density of 2.5 × 10^5 cells/cm^2 and cultured for 21 days while changing media every other day. At different time points during culturing, cells were fixed with 10% neutral buffered formalin solution (Sigma-Aldrich) at RT for 30 min and kept in PBS at 4°C until further sectioning.

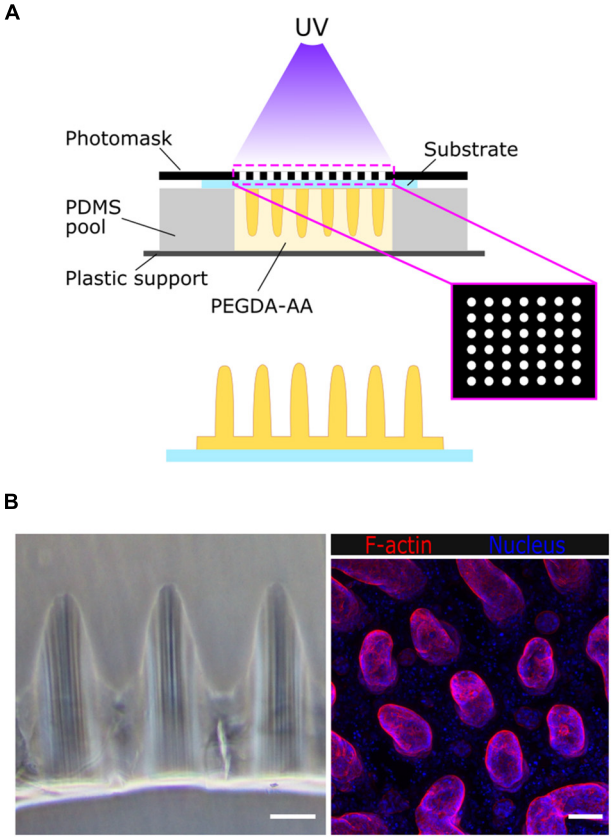

FIGURE 1 | (A) Schematic drawing of the fabrication of villus-like microstructured PEGDA-AA hydrogel scaffolds. **(B)** Left: bright field microscope image of the cross-section of the villus-like microstructured hydrogel scaffolds. Right: confocal maximum intensity projection showing F-actin and nuclei staining of Caco-2 cells grown on top of the villus-like scaffold. Scale bars: 100 μm.

Embedding Microstructured Hydrogels With Low Molecular Weight PEGDA

The embedding medium was prepared by dissolving 10% w/v 575 Da PEGDA (P575) (Sigma-Aldrich) and 1% w/v Irgacure D-2959 photoinitiator in PBS. The solution was mixed at 65°C for 1 h, filtered and stored at 4°C until further use. Prior to light-induced embedding, microstructured scaffolds were incubated with the embedding medium overnight at 4°C. To facilitate the formation of P575 blocks, a PDMS chip was made. Briefly, the PDMS prepolymer was mixed with the curing agent in a 10:1 w/w ratio and degassed under vacuum. Then, it was cast to 4-well

rectangular culture dishes (Thermo Fisher Scientific) to obtain PDMS slabs of 2 mm in height, which were cured for at least 2 h at 65°C. A pool of 10 mm in diameter was carved into the PDMS using a 10 mm diameter punch (Acuderm). Then, the pool was placed on top of a 24 mm × 60 mm glass coverslip (Menzel-Glaser). The pool was filled with the P575 embedding solution and the microstructured hydrogel samples grown on the glass coverslips or on the PET membranes (cultured with cells or not) were placed onto the pool upside down. The P575 embedding medium was then crosslinked by UV exposure using a UV lamp source (Mask aligner SUSS MicroTec MJB4 calibrated to a constant intensity of 25 mW/cm^2 at 365 nm). First, the chip was irradiated for 100 s on one side and then flipped and exposed again for 100 s on the other (**Figure 2A**). For the hydrogel scaffolds prepared on PET membranes, a hydrogel support base was formed by first exposing 10% w/v P575 solution to UV for 40 s. The samples on the membrane were placed onto this support base and embedded in P575, as explained above. With this procedure, translucent blocks of P575 with the microstructured PEGDA-AA scaffolds inside were obtained (**Figure 2B**). The samples were kept in PBS at 4°C until sectioning, remaining unaltered for at least 1 month.

Hydrogel Sectioning

For vibrating microtome sectioning, the P575 blocks were re-embedded in agarose to provide structural support. This second embedding medium was prepared by dissolving 8% w/v of low melting point agarose (CONDA) in PBS, boiling it twice in a microwave oven, and shaking it at 65°C for at least 30 min. A cryomold (Tissue-Tek) was filled halfway with the agarose solution and the P575 block was placed inside, orienting the sample properly for the desired section. Then, additional agarose solution was used to completely fill the mold. The agarose block was solidified at 4°C for 4 min, affixed to the specimen holder with Loctite super glue adhesive, and placed within a Leica VT1000S vibrating blade microtome, while ensuring that the tips of the villus-microstructures were facing the blade. The buffer tray bottom was filled with ice-cold PBS and the temperature was maintained by applying ice cubes to the outer holding chamber. The microtome was operated at the following parameters: 0.075 mm/s sectioning speed, 81 Hz oscillation frequency, 1 mm amplitude, and 300–350 μm section thickness. The cuts were recovered from the bath and kept in PBS at 4°C until further use, remaining unaltered for at least 1 month.

For cryotome sectioning, the P575 blocks were cut in half and incubated with OCT (VWR) overnight at 4°C. Thereafter, samples were transferred to cryomolds filled with OCT, frozen with liquid nitrogen and ice-cold 2-methylbutane (Sigma-Aldrich), and stored at −80°C. Histological cuts of 7–10 μm were obtained using a Leica CM1950 cryostat and air-dried for 15 min. Samples were stored at −20°C until further use, remaining unaltered for at least 1 month.

Microstructural Assessment of Embedded and Sectioned Microstructured Hydrogels

To evaluate the morphology of the hydrogel villus-like microstructures after the embedding and sectioning processes,

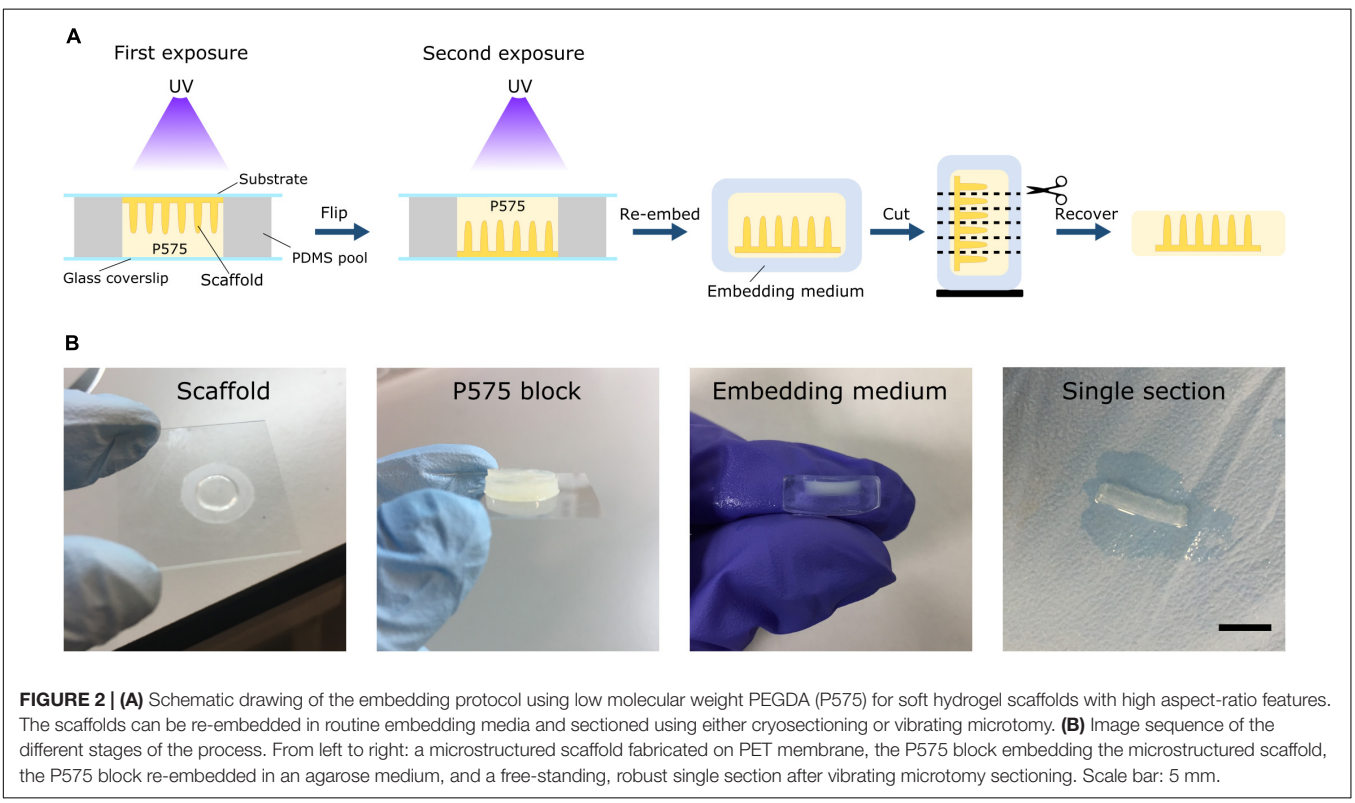

FIGURE 2 | (A) Schematic drawing of the embedding protocol using low molecular weight PEGDA (P575) for soft hydrogel scaffolds with high aspect-ratio features. The scaffolds can be re-embedded in routine embedding media and sectioned using either cryosectioning or vibrating microtomy. **(B)** Image sequence of the different stages of the process. From left to right: a microstructured scaffold fabricated on PET membrane, the P575 block embedding the microstructured scaffold, the P575 block re-embedded in an agarose medium, and a free-standing, robust single section after vibrating microtomy sectioning. Scale bar: 5 mm.

microstructured PEGDA-AA hydrogels were selectively stained by taking advantage of the flanking carboxylic groups from the acrylic acid polymer. For that, two strategies were used: Alcian Blue staining and functionalization with a fluorescent protein. Alcian Blue is a dye that has an affinity for acidic elements, such as the carboxylic acid residues of the PEGDA-AA hydrogels, so it should selectively stain the microstructured scaffold but not the embedding medium, which does not contain acrylic acid. The sections were incubated in a solution of 1% w/v Alcian Blue 8GX (Sigma-Aldrich) in 3% v/v acetic acid for 10 min at RT. Then, the sections were washed thoroughly with tap water for at least 10 min. Sections were visualized using bright field microscopy (Nikon Eclipse Ts2). Additionally, the flanking carboxylic groups of the microstructured hydrogels were functionalized with bovine serum albumin conjugated with Texas Red dye (BSA-TxRED) (Invitrogen) by EDC/NHS crosslinking chemistry. The vibratome sections were submerged into the EDC/NHS solution and incubated for 1 h at RT. Subsequently, the hydrogels were washed with PBS and incubated with 500 μg/mL BSA-TxRED solution in PBS for 1.5 h at RT. Then, the sections were washed again with PBS and visualized using a confocal laser scanning microscope (LSM 800, Zeiss).

Immunofluorescence Staining

In order to prove that the standard cell immunostaining protocols can be applied to the tissue sections obtained with the P575 embedding medium, we used fixed cell samples of Caco-2 cells grown on microstructured PEGDA-AA hydrogels as described in Section "Fabrication of Villus-Like Microstructured Hydrogels and Cell Culture." Antigen retrieval was performed in the recovered sections by boiling them in 10 mM citrate buffer and 0.05% v/v Tween 20 at pH 6.0 for 10 min in a microwave oven. Then, the cells were permeabilized with 0.5% v/v Triton X-100 (Sigma-Aldrich) for 30 min and blocked with a buffer containing 1% w/v BSA (Sigma-Aldrich), 3% v/v donkey serum (Millipore), and 0.2% v/v Triton X-100 in PBS for at least 3 h. The sections were then incubated with the primary and secondary antibodies for 72 and 24 h, respectively. Increased antibody incubation times allowed better penetration of large antibody molecules through the hydrogels. The primary antibodies and their dilutions were: mouse anti-villin (5 μg/mL, Abcam ab201989), rabbit anti-β-catenin (2 μg/mL, Abcam ab2365), mouse anti-β-catenin (2.5 μg/mL, BD Biosciences 610154), and rabbit anti-*zonula occludens* 1 (ZO-1) (2.5 μg/mL, Invitrogen 40-2200). As secondary antibodies, Alexa Fluor® 488 donkey anti-mouse (Invitrogen A-21202), Alexa Fluor® 647 donkey anti-rabbit (Jackson ImmunoResearch 111-607-003), and Alexa Fluor® 568 donkey anti-goat (Invitrogen A-11057) diluted at 4 μg/mL, were used. The primary and secondary antibodies were diluted in a working buffer containing 0.1% w/v BSA, 0.3% v/v donkey serum, and 0.2% v/v Triton X-100 in PBS. Nuclei were stained with 4′, 6-diamidino-2-phenylindole (DAPI) (5 μg/mL, Invitrogen D1306) for 1–2 h. For the staining of filamentous actin (F-actin), no antigen retrieval was performed as it interfered with the staining. Therefore, after the sections were recovered, samples were permeabilized and blocked as explained above. Then, samples were incubated with Acti-stain 535 Phalloidin (100 nM, Tebu-bio) for 2 h and counterstained with DAPI for 1 h. All the incubations were performed at 4°C under shaking.

Image Acquisition

For imaging, histological sections obtained with the vibrating microtome were mounted with PBS, whereas cryosections were mounted using the standard mounting medium Fluoromount-G (Thermo Fisher Scientific). Fluorescence images were acquired at randomly selected locations using either a confocal laser scanning microscope (LSM 800, Zeiss) with 10x dry (N.A. = 0.3), 20x dry (N.A. = 0.8), and 40x glycerol (N.A. = 1.3) objectives or a super-resolution inverted confocal microscope (LSM 880 – Airyscan Elyra PS1, Zeiss) in fast airyscan mode and with 63x oil (N.A. = 1.4) objective. The laser excitation and emission light spectral collections were optimized for each fluorophore, especially for the four-color scans, where the emission bands were carefully adjusted to avoid overlapping channels. The pinhole diameter was set to 1 Airy Unit (AU). For all images acquired, the optimal z-step was used as indicated by the equipment software. The bright field images were obtained by an inverted optical microscope (Eclipse Ts2, Nikon).

Image Analysis

Confocal microscopy z-stacks were processed using ImageJ software (NIH). All images were corrected for brightness and contrast while maximum intensity projections, or single focal planes, were represented as indicated in the figure legends. For the z-stacks from immunostainings, a background subtraction with a rolling ball radius of 150 pixels and a median filter with a radius of 3 pixels were applied to ZO-1 and β-catenin channels in order to remove the background noise.

To estimate the height of the cells, intensity profile plot measurements along line segments orthogonal to the cell walls were performed using the F-actin staining. For each sample, each villus-like micropillar to be analyzed was selected and rotated into an upright vertical position with the central axis of the pillar being parallel to the y-axis. The single focal plane that provided the best segmentation of the cellular membrane by visual inspection was selected from the acquired z-stacks. To mitigate the effect of noise in the images, the profiles were endowed with a width of 10 pixels to average the intensity across (ImageJ Plot Profile function). The cell height was estimated as the distance between the two most significant intensity maxima found along the intensity profile. The intensity maxima were required to have a minimum significance of 5–10 grayscale levels (i.e., the minimum altitude of the maxima with respect to the two adjacent valleys). This process was assisted by an ImageJ macro where the only manual step was adjusting the line segments. The (x, y) coordinates of the line segments (by default taken from the center) were also recorded. The cell heights were plotted as a function of the normalized position along the vertical axis (y-axis) of the villus (0: base, 1: tip). A total of 386 cells in 21 pillars were analyzed for samples obtained from two independent experiments with two technical replicas each ($N = 2$, $n = 2$).

Cell nuclei were segmented from single focal planes extracted from the z-stacks acquired from DAPI staining. Micropillars were

individually oriented into a vertical position, as above, by rotating the image accordingly. Then, an ImageJ macro was used for implementing the following steps: (1) forcing very low values (background) to zero, (2) filtering the image by Laplacian of Gaussian filter with a radius adapted to the characteristic size of the nuclei, (3) detecting the nuclei as regional intensity minima (user-defined detection tolerance), (4) editing the detected nuclei markers manually, (5) performing watershed segmentation from these markers on an edge detected version of the original image (magnitude of intensity gradient after slight Gaussian filtering) and, (6) analyzing connected particles in the resulting binary mask while keeping the particles within a user-defined area range (25 to 300 pixels). The measurements of the connected particles (nuclei) included the position (centroid) as well as the major and minor axes of the ellipses fitted to the particles. The aspect ratio (elongation) of nuclei was determined from the ratio of the major to the minor axis of the fitted ellipses. The cell nuclei aspect ratios were plotted as a function of the normalized position along the villus axis. A total of 473 cell nuclei in 11 micropillars were analyzed.

The orientation of the cell nuclei was also estimated from the single focal planes. First, the micropillars were individually oriented into a vertical position and toward the top of the image by rotating the image accordingly. Next, the major axes (direction of orientation) of several nuclei were manually marked by drawing line segments. Then, another line segment was drawn along the orientation of the hydrogel surface in the vicinity of the nuclei. The angle (0–90°) between these two-line segments was calculated using an ImageJ macro. The measurements also report the nuclei locations as the rescaled villus axis (0: base, 1: tip). The orientations of the nuclei (expressed as the angle), with respect to the hydrogel surface, were plotted as a function of the normalized position along the villus. A total of 440 cell nuclei in 11 micropillars were analyzed.

Statistical Analysis

Graphs were plotted using GraphPad software. The data are presented in the figures as the mean ± standard error of the mean (SEM). The error bars represent the SEM of at least two independent experiments with two technical replicas. Statistical comparisons were performed using ANOVA test and p-values < 0.05 were considered to be significant.

RESULTS

Poly(ethylene) Glycol Diacrylate Embedding Preserves the Structural Integrity of Villus-Like Hydrogel Scaffolds During Sectioning

3D villus-like hydrogel scaffolds were fabricated by lithography-based dynamic photopolymerization of PEGDA-AA prepolymer solutions, as described in Castaño et al. (2019). The microstructures were fabricated either on glass coverslips or on flexible porous PET membranes ready to be assembled into Transwell insert supports. The villus-like micropillars were 480 ± 40 μm in height and there were 2330 ± 30 micropillars/cm^2. After reaching equilibrium swelling, the hydrogel scaffolds were functionalized with Collagen-I via EDC/NHS chemistry. Caco-2 cells seeded on top of the hydrogels covered the micropillars by forming a monolayer. After 3 weeks of culturing, cells were fixed and sectioned.

The villus-like microstructured hydrogels were embedded in 10% w/v low molecular weight PEGDA, P575, by UV-initiated crosslinking (**Figure 2A**). The formed P575 block embedded the finger-like structures in a conformal manner, providing the delicate structures with good mechanical stability. Then, the P575-embedded microstructured hydrogels were successfully re-embedded in routine embedding media (e.g., OCT and agarose) for cryosectioning or vibrating microtomy. In vibrating microtomy, minimum damage is made to fragile tissues as it does not require dehydration or freezing steps. However, the sections obtained by this technique are thick (≥50 μm) (Short et al., 2017). The P575-embedded hydrogel sections recovered from the vibratome were mechanically robust, which enabled further manipulation, immunostaining and imaging procedures (**Figure 2B**). On the contrary, sectioning the microstructured hydrogels with the vibratome was not possible without the P575 embedding. Furthermore, the standard embedding medium, agarose, did not sufficiently penetrate the hydrogel network to hold it within the block (**Supplementary Figure 1**). On the other hand, sectioning scaffolds fabricated onto porous membranes with vibrating microtomy was not possible, even after the P575 embedding. The difference in stiffness between the soft hydrogel and the hard PET membrane resulted in the sample being dragged by the blade, which ruined it. Instead, the scaffolds on membranes were processed with the cryotome. In cryosectioning, very thin tissue sections (5–15 μm) can be obtained, allowing for the visualization of fine details of the cells (Fischer et al., 2008). The P575 blocks containing the villus-like microstructures were embedded in OCT after overnight infiltration (Ruan et al., 2013). Cryosection sections of these samples were then successfully recovered on glass slides and were suitable for further processing.

To evaluate if the P575 embedding, and further sectioning steps, affected the morphology of the villus-like microstructures, vibratome sections were stained with Alcian Blue and fluorescently labeled BSA proteins. Both molecules bind selectively to the flanking carboxylic groups from the acrylic acid polymer and therefore allows the morphology of the micropillars (made of PEGDA-AA) within the P575 embedding block to be properly distinguished. **Figure 3A** shows that the villus-like features of the hydrogels were unaffected by the P575 embedding and further sectioning. In addition, the BSA fluorescence images demonstrate the suitability of the embedding medium for the staining with large proteins (**Figure 3A**, right panel).

Then, the compatibility of the embedding method with sectioning samples covered by epithelial cells was also tested. **Figure 3B** shows that vibrating microtomy sections of villus-like microstructured hydrogels, with an epithelial cell monolayer grown on top, can be obtained without damaging the structural integrity of the microstructures. Such structural integrity was also observed for the samples fabricated on porous membranes and used in cryosectioning. In this case, compared to the

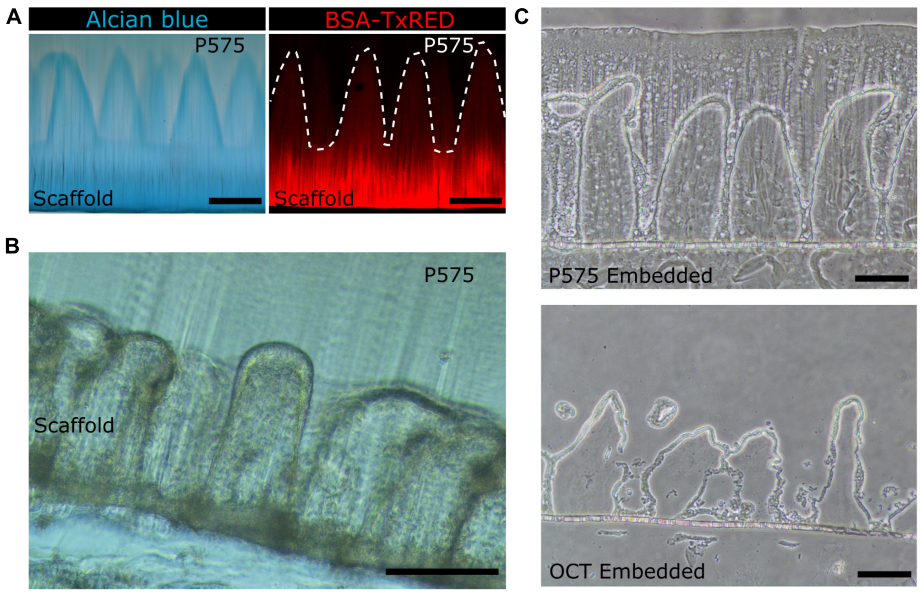

FIGURE 3 | (A) Bright field microscopy image of villus-like microstructured PEGDA-AA hydrogels stained with Alcian Blue (left panel) and confocal maximum intensity projection image of the PEGDA-AA microstructures functionalized with BSA-Texas Red (right panel) after P575 embedding and sectioning. White dashed lines mark the border of the microstructures. Scale bars: 200 μm. **(B)** Bright field microscopy image of a vibratome section of the P575 embedded villus-like hydrogel scaffold with Caco-2 cells grown on top. Scale bar: 200 μm. **(C)** Bright field microscopy images of cryosectioned villus-like hydrogel scaffolds with Caco-2 cells grown on top. The upper panel shows the hydrogel embedded in P575 and then in OCT; the lower panel shows the control only with the OCT embedding. Scale bars: 100 μm.

control sections, the P575 embedding significantly improved the preservation of the villi-like micropillars (OCT embedding) (**Figure 3C** and **Supplementary Figure 2**). More importantly, it should be noted that the sections obtained using the novel embedding technique were fully compatible with standard immunostaining and imaging procedures.

High Magnification Imaging Reveals the Impact of Villus-Like Topography and Local Curvature on Intestinal Epithelial Cell Polarization and Orientation

Cell–cell and cell-substrate interactions determining cell fate are affected by substrates containing 3D curved features with micron-scale dimensions (Assoian et al., 2019; Baptista et al., 2019). Previously, we have demonstrated that the villus-like 3D topography of PEGDA-AA hydrogels affects cell growth and improves the functional performance of the epithelial monolayers as tissue barriers, representing better tissue physiological permeability (Castaño et al., 2019). To explore the origin of such an improvement, histological sections of the scaffolds were obtained and imaged at high magnification by employing the new embedding method described here (**Figure 4A** and **Supplementary Video 1**). The Caco-2 monolayers grown on the 3D microstructures were stained for filamentous actin (F-actin) and DAPI at different time points during culturing. After 1 week of culture, cells covering the microstructures exhibited a cuboidal morphology but without a pronounced apicobasal polarity. After 2 weeks, and especially after 3 weeks of culturing, cells showed the columnar morphology characteristic of the differentiated intestinal epithelium (**Supplementary Figure 3**). After 3 weeks of culture, cell and nuclei morphology were quantitatively evaluated along the villi vertical axis and correlated with their position with respect to the base of their corresponding villus. High magnification images (**Supplementary Figure 4**) provided the necessary resolution for both proper cell segmentation and quantitative analysis of these cell features. Through these measurements, changes in the cell height, nuclear aspect ratio (elongation), and orientation along the vertical axis of the villi were revealed. Cell height, determined from the F-actin staining, significantly increases by more than twofold, from 7 ± 4 to 18 ± 5 μm (mean ± SD), when measured from cells located at the bases of the villi to the cells located at their tips (**Figure 4B**). On the other hand, cell nuclei orientation, expressed as the angle θ between the major axis of an ellipse fitting nucleus shapes and the tangent to the hydrogel surface at the place where each nucleus is located (**Figure 4C**, upper panel), were also quantified. It was found that the nuclei of cells located on the lateral surfaces of the villus-like structures, which have a planar topography, were mostly oriented parallel to these surfaces ($\theta < 20°$, **Figure 4D**). Conversely, the nuclei of cells located closer to the regions of maximum surface curvature (close to the tips) exhibited orientations which are significantly more perpendicular to the surface ($\theta > 60°$) (**Figure 4D**). An additional parameter often related to epithelial polarization, i.e., the elongation of cell nuclei, was also calculated along the villus-like axis (base to tip) of the different microstructures analyzed. The obtained values, expressed as the nuclei aspect ratio between the major and the minor axes of the fitted ellipse (**Figure 4C**, lower panel), did not change significantly along the vertical axis of the villi.

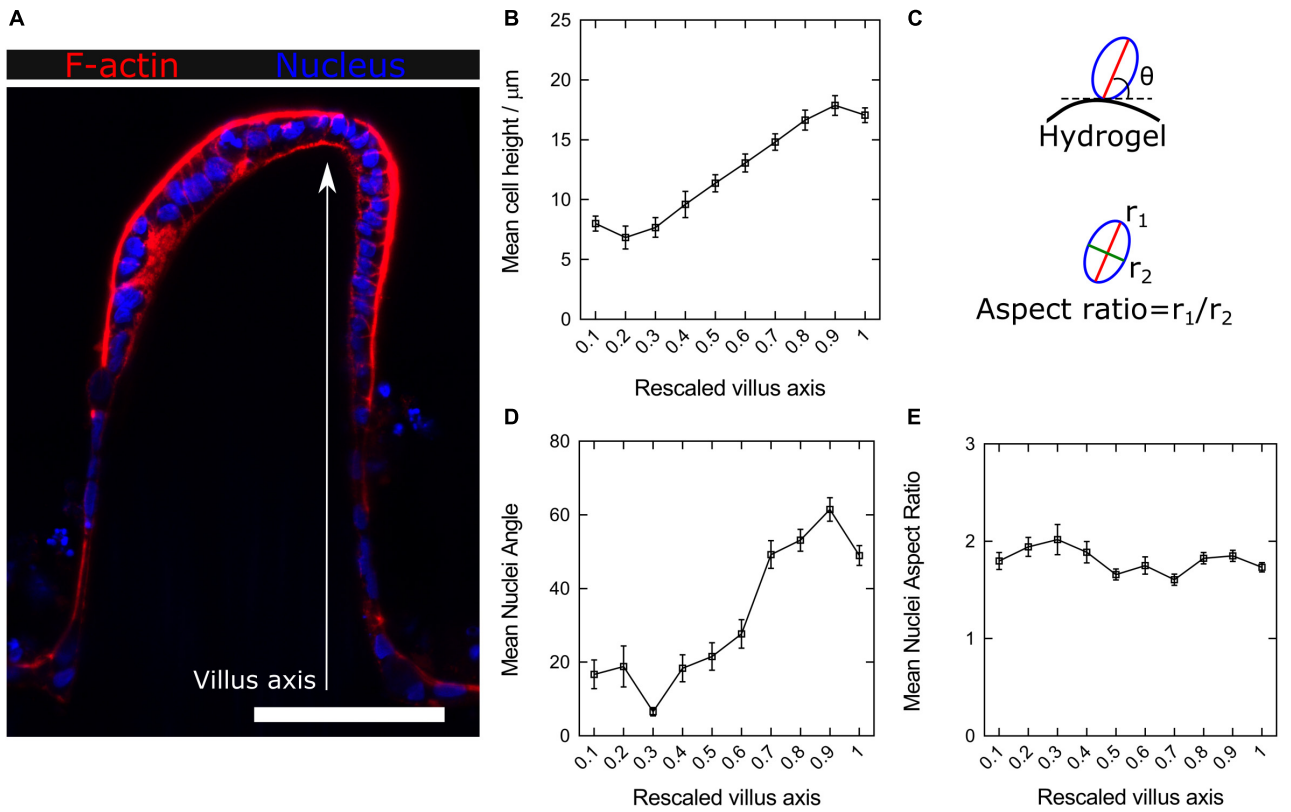

FIGURE 4 | (A) Confocal microscopy image of F-actin and nuclei staining of the Caco-2 monolayer formed on top of microstructured hydrogels after 21 days in culture. Scale bar: 100 µm. **(B)** Average cell heights along the rescaled villus axis. **(C)** Schematic drawing showing the nuclei orientation (the major axis angle of the fitted ellipse with respect to the hydrogel surface) and elongation (the ratio between the major to the minor axes of the fitted ellipse) analysis. **(D)** Change in the mean nuclei angle (nuclei orientation) and **(E)** nuclei aspect ratio (nuclei elongation) along the rescaled villus axis. Data presented as mean ± standard error of the mean (SEM).

Remarkably, all the cell nuclei analyzed were elliptically elongated with values ranging from 1.6 to 2.0, where 1 being the value of a circle (**Figure 4E**).

To further assess in greater detail the specific cell-morphology effects of the local curvature, high-resolution images were acquired using the fast Airyscan modality of a super-resolution inverted confocal microscope equipped with a 63x oil objective lens. Tile scans were performed to image the entire microstructure (**Figure 5**, upper row). High magnification images performed at precise locations displaying convex (tip apex), planar (lateral walls), and concave (base) curvatures showed a progressive change in cell morphology which adapts to the curvature of the hydrogel surfaces (**Figure 5**, middle row). Cells were found to be basally constricted and thus wedge-shaped at the convex surfaces (villi tips), possessed a cuboidal morphology on the planar surfaces (villi walls), and be apically constricted at the concave surface of villi bases (**Figure 5**, lower row), revealing differential apicobasal tensions along the villus-like microstructures. Altogether, these results demonstrate that cells on the villus-like structures were all polarized (nuclei elongated, accumulation of actin at the apical side), but that their polarization state (according to cell height, nuclei orientation, visual differences of apical actin and cell morphology) changes along the vertical axis of the villus-like microstructures, suggesting a good correlation with the local changes in surface curvature.

High-Resolution Imaging of Intestinal Epithelial Cell Markers Suggests a Differential Expression Along the Vertical Axis of Villus-Like Structures

On the one hand, we had previously reported that Caco-2 cell monolayers grown onto 3D villus-like scaffolds of PEGDA-AA showed barrier properties that were more similar to physiological tissues than those grown onto standard 2D flat cell cultures (Castaño et al., 2019). On the other hand, the results presented in the previous section showed significant changes in epithelial cell height and morphology along the vertical axis of the villus-like structures. Therefore, this raised the question if the morphological changes observed correlated with the differential expression of epithelial markers, indicating that cell polarization and cell–cell tight junctions might be the origin of the improved barrier performance reported.

In order to visualize the intestinal epithelial cell marker distribution along the villus axis of the microstructures,

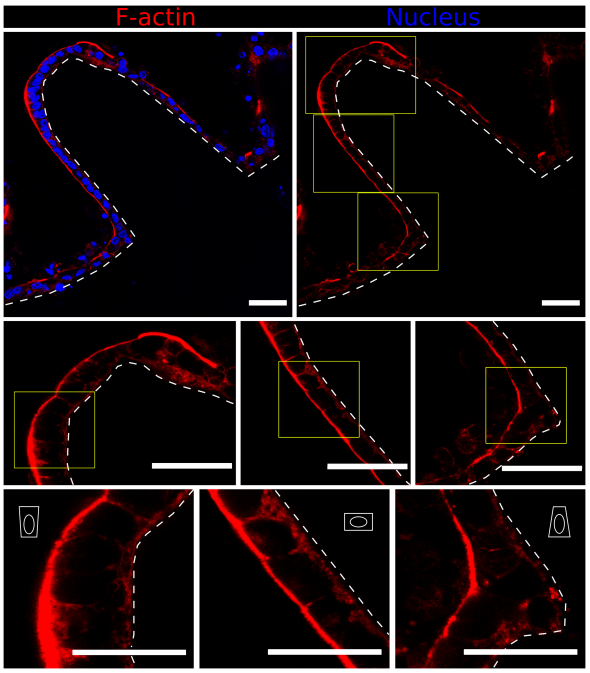

FIGURE 5 | Fast Airyscan confocal images showing F-actin and nuclei staining of the Caco-2 monolayer formed on top of microstructured hydrogels after 21 days in culture (upper row). Yellow boxed regions are shown in high magnification (middle and lower rows). Different cell shapes are observed: basally constricted wedge-shaped at the villi tips, cuboidal along the walls and apically constricted at the base, as represented by the white drawings. Scale bars (upper and middle rows): 50 μm, (lower row): 30 μm.

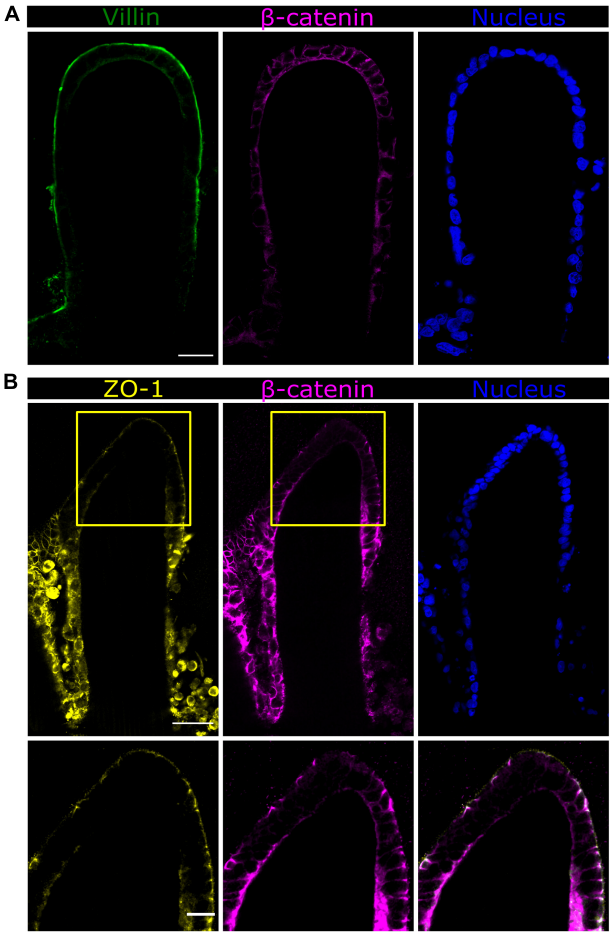

FIGURE 6 | Fast Airyscan confocal images of the Caco-2 monolayer formed on top of the microstructured hydrogels after 21 days in culture showing the expression of **(A)** villin in green or **(B)** ZO-1 in yellow, β-catenin in magenta, and nuclei in blue. Yellow boxed regions are shown in high magnification. Scale bars (upper and middle rows): 50 μm, (lower row): 20 μm.

vibratome sections of P575-embedded villus-like hydrogels were stained using a minimally adapted routine immunostaining procedure. Sections were then imaged at high resolution (63x magnification) and tile scans spanning the entire microstructure were acquired. Caco-2 cells, grown for 21 days on top of the villus-like scaffolds, expressed the epithelial cell markers located at their proper locations. Specifically, villin protein was found in the microvilli at the cell apical membrane while β-catenin was shown to accumulate in the lateral and basolateral cell membranes (**Figure 6A**). Remarkably, the expression of the tight junction protein *zonula occludens*-1 (ZO-1) was spatially encoded along the villus-like structures. Cells located at the tip of the villi showed ZO-1 localization at the apex of the lateral membrane (**Figure 6B**). This spatially coincides with the convex surfaces displaying the most columnar morphology, as determined in the previous section. More importantly, the images show ZO-1 exquisitely located at the top of the β-catenin staining (**Figure 6B**), just as in native intestinal epithelium (Zihni et al., 2016), thus also indicating the good polarization of the intestinal epithelial cells on the PEGDA-AA villi-like hydrogel scaffolds.

DISCUSSION

Over the last two decades, 3D culture models have been developed to provide cells with a more physiologically relevant *in vitro* environment with the aim to reduce the gap between two-dimensional cell cultures and live tissues for studying healthy and disease states as well as for preclinical drug screening (Pampaloni et al., 2007; Booij et al., 2019). The effect of surface topography on cell behavior has been explored in numerous studies where it was mostly conducted on single cells and focused on the cellular and subcellular scale (Martínez et al., 2009; Théry, 2010). However, most physiological occurring structures, such as glands, alveoli, or intestinal villi, have topographies in the range of hundreds of micrometers and they are inherently curved. Furthermore, there is increasing evidence that substrate topography and curvature on a micron-scale also affects cell fate and cell–cell interactions (Broaders et al., 2015; Yevick et al., 2015; Assoian et al., 2019; Baptista et al., 2019). In our previous study, we fabricated microstructured 3D hydrogel scaffolds containing finger-like protrusions mimicking the architecture of small intestinal epithelium (Castaño et al., 2019). We observed that, compared to flat monolayer cultures, the growth of Caco-2

intestinal epithelial cells on these villus-like microstructures of physiological dimensions improved both cell polarization and cell nuclei elongation (Castaño et al., 2019). However, due to the limitations of the optical microscopy methods, these analyses were performed over a collection of low magnification z-stack confocal images acquired along the villi-like structure.

At present, there is a need to adapt the conventional handling and imaging techniques developed for flat cultures to more suitable for 3D cultured microtissues (Montanez-Sauri et al., 2015; Booij et al., 2019). Microengineered 3D samples, such as these villus-like microstructures, are typically several hundreds of micrometers thick and yield high light scattering, thus limiting the imaging of the whole construct with standard optical techniques such as confocal fluorescence microscopy. Some of the limitations include a reduced penetration depth when using high numerical aperture lenses and photobleaching, which is induced by the illumination of the entire object (Smith et al., 2010). The histological sectioning of the engineered constructs might overcome some of these drawbacks. By obtaining thin cross-sections of the samples, high magnification imaging can be achieved while cell behavior and morphology can be evaluated along the sample vertical axis in a single focal plane. However, standard histology procedures should be adapted for the special characteristics of tissue-engineered scaffolds.

In the case of villus-like hydrogel scaffolds, these high aspect-ratio structures should be well-preserved and their water-rich nature and soft mechanical properties should also be considered. Since the paraffin wax embedding method is incompatible with these structures, we investigated the microstructure integrity after sectioning with a vibrating microtome or cryotome. Both methods require the specimen to be embedded into agarose or OCT, respectively. Several authors have optimized the embedding and sectioning protocols for tissue-engineered hydrogel samples (James et al., 2004; Yang et al., 2007; Ruan et al., 2013; Short et al., 2017). However, those materials were prepared in bulk, leading to 3D flat constructs with no complex topographical features. In the presence of such delicate structures, these methods were unsuitable as the villus-like micropillars were not well-preserved after sectioning. In one instance, the agarose embedding did not sufficiently penetrate to hold the microstructured sample in place and sectioning could not be performed. Instead, the agarose acted as a molding material, a strategy previously used in the literature for the fabrication of villus-like structures (Costello et al., 2014a,b). In the case of the samples processed by cryosectioning, after overnight incubation with OCT following the protocol by Ruan et al. (2013), thin sections could be obtained but the hydrogel pillars showed obvious shrinkage and the microstructures collapsed. Thus, we developed a method in which the 3D microstructured hydrogel was transformed into a non-structured hydrogel block that can further be embedded into the standard media for histological sectioning without the risk of collapsing the structures. The microstructures were embedded using a light-based approach and a low molecular weight P575 prepolymer, creating a hard hydrogel block after UV exposure. The short polymer chains penetrated the pores of the microstructured hydrogels and, upon polymerization, the topography and dimensions of the microstructures remained unaltered. We demonstrated that this embedding method can be applied to cell-free and cell covered scaffolds fabricated in different substrates, such as glass coverslips or porous membranes, and that it is compatible with vibratome or cryotome sectioning upon second embedding in the corresponding standard media. This versatility allows for the selection of an adequate method for the desired end-use application.

By using this novel embedding protocol, the longitudinal core section of the villus-like micropillars could be obtained and imaged via high-resolution, high-magnification confocal microscopy. Thus, we analyzed, in a spatially resolved manner, the cellular and nuclear morphology along the villi. Moreover, a clear difference was observed in cell height and shape at different regions of the villi that presented distinguished curvatures. Cells at the base experienced a negative curvature and exhibited a trapezoidal shape with an apical constriction. Cells then transitioned to the flat region of the villus, adopting a cuboidal shape. In addition, cell height steadily increased toward the tip where it reached a maximum in the section of the tip with maximum convex curvature. The evolution of cell height along the villus structures was in agreement with the mechanical model of epithelial folds (Štorgel et al., 2016) and the quantification of cell morphology along the crypt-villus axis of *ex vivo* intestinal tissue in mice (Krndija et al., 2019). The orientation of nuclei along the villi showed a significant change in the angle when cells were at the curved region of the villi ($x > 0.6$). Yu et al. (2018), also reported effects on cell height and alignment of renal epithelial cells when cultured on curved surfaces. In that study, they also observed an increased ZO-1 expression when cells were exposed to a highly concave curvature. For the villus-like microstructures reported here, polarization markers of intestinal epithelial cells, such as ZO-1 and β-catenin, were differentially expressed at the tip of the villi, again highlighting that the 3D curvature is crucial for cell morphology and differentiation. This differential expression along the vertical axis of the villus-like features might impact the permeability of the epithelial barrier formed and, thus, explains the experimental differences measured in the functional assays between cells grown on 3D curved surfaces and those grown on flat substrates (Castaño et al., 2019).

In summary, we examined the cell morphological response to villus complex topography in a microengineered hydrogel scaffold using a novel embedding method to preserve these complex features. This versatile photopolymerization-based method, compatible with both cryosectioning and vibrating microtomy, yields well-preserved microstructures that can be further analyzed with high-resolution and high-magnification microscopy. Analysis of the cellular and nuclear morphology of epithelial cells demonstrated that the topography and curvature along villus-like microstructures can have a significant effect. The combination of new sample processing methods, such as the one here described, with state-of-the-art 3D *in vitro* models would help to study the physiological events observed in *in vivo* models in a systematic and reproducible manner. This method would also be useful for *in vitro* models of morphogenesis, for mechanistic studies such as curvotaxis, as well as for pathological situations in which there are changes in the physiological

structures. For example, some enteropathies such as celiac disease, present villus atrophy as the histopathologic hallmark, which has been related to defective intestinal permeability and an altered distribution of the tight junction proteins (Schumann et al., 2017; Jansson-Knodell et al., 2018). This work would significantly contribute to the widespread implementation of 3D microengineered tissues for those applications, ultimately leading to more effective discovery of new drugs.

DATA AVAILABILITY STATEMENT

The raw data supporting the conclusions of this article will be made available by the authors upon request.

AUTHOR CONTRIBUTIONS

GA performed the experiments and analyzed the data. ST developed the macros for image analysis. GA together with MG-D designed the experiments. MG-D provided hydrogel scaffolds cultured with Caco-2 cells. EM and MG-D coordinated the project and together with GA wrote the manuscript.

FUNDING

Funding for this project was provided by the European Union's Horizon 2020 ERC Grant Agreement No. 647863 (COMIET), the CERCA Programme/Generalitat de Catalunya (2017-SGR-1079), and the Spanish Ministry of Economy and Competitiveness (TEC2017-83716-C2-1-R and the Severo Ochoa Program for Centers of Excellence in R&D 2016-2019). GA was funded through an FI-DGR 2014 predoctoral fellowship from the Agència de Gestió d'Ajuts Universitaris i de Recerca (AGAUR). MG-D was funded through the BEST Postdoctoral Programme, as part of the European Commission's Horizon 2020's MSCA COFUND scheme (Grant Agreement No. 712754) and by the Severo Ochoa programme of the Spanish Ministry of Science and Competitiveness (Grant SEV-2014-0425). The results presented here reflect only the views of the authors; the European Commission is not responsible for any use that may be made of the information it contains.

ACKNOWLEDGMENTS

The authors would like to thank the MicroFabSpace and Microscopy Characterization Facility, unit 7 of the CIBER in Bioengineering, Biomaterials, and Nanomedicine (CIBER-BBN) at the Institute for Bioengineering of Catalonia (IBEC). The authors also acknowledge the support provided by the histopathology and advanced digital microscopy core facility of the Institute for Research in Biomedicine (IRB) in Barcelona.

SUPPLEMENTARY MATERIAL

The Supplementary Material for this article can be found online at: https://www.frontiersin.org/articles/10.3389/fbioe.2020.00294/full#supplementary-material

REFERENCES

Assoian, R. K., Bade, N. D., Cameron, C. V., and Stebe, K. J. (2019). Cellular sensing of micron-scale curvature: a frontier in understanding the microenvironment. *Open Biol.* 9:190155. doi: 10.1098/rsob.190155

Baptista, D., Teixeira, L., van Blitterswijk, C., Giselbrecht, S., and Truckenmüller, R. (2019). Overlooked? Underestimated? Effects fof substrate curvature on cell behavior. *Trends Biotechnol.* 37, 838–854. doi: 10.1016/j.tibtech.2019.01.006

Booij, T. H., Price, L. S., and Danen, E. H. J. (2019). 3D cell-based assays for drug screens: challenges in imaging, image analysis, and high-content analysis. *SLAS Discov.* 24, 615–627. doi: 10.1177/2472555219830087

Broaders, K. E., Cerchiari, A. E., and Gartner, Z. J. (2015). Coupling between apical tension and basal adhesion allow epithelia to collectively sense and respond to substrate topography over long distances. *Integr. Biol.* 7, 1611–1621. doi: 10.1039/c5ib00240k

Caliari, S. R., and Burdick, J. A. (2016). A practical guide to hydrogels for cell culture. *Nat. Methods* 13, 405–414. doi: 10.1038/nmeth.3839

Castaño, A. G., García-Díaz, M., Torras, N., Altay, G., Comelles, J., and Martínez, E. (2019). Dynamic photopolymerization produces complex microstructures on hydrogels in a moldless approach to generate a 3D intestinal tissue model. *Biofabrication* 11:025007. doi: 10.1088/1758-5090/ab0478

Costello, C. M., Hongpeng, J., Shaffiey, S., Yu, J., Jain, N. K., Hackam, D., et al. (2014a). Synthetic small intestinal scaffolds for improved studies of intestinal differentiation. *Biotechnol. Bioeng.* 111, 1222–1232. doi: 10.1002/bit.25180

Costello, C. M., Sorna, R. M., Goh, Y., Cengic, I., Jain, N. K., and March, J. C. (2014b). 3-D intestinal scaffolds for evaluating the therapeutic potential of probiotics. *Mol. Pharm.* 11, 2030–2039. doi: 10.1021/mp5001422

Creff, J., Courson, R., Mangeat, T., Foncy, J., Souleille, S., Thibault, C., et al. (2019). Fabrication of 3D scaffolds reproducing intestinal epithelium topography by high-resolution 3D stereolithography. *Biomaterials* 221:119404. doi: 10.1016/j.biomaterials.2019.119404

DeForest, C. A., and Anseth, K. S. (2012). Advances in bioactive hydrogels to probe and direct cell fate. *Annu. Rev. Chem. Biomol. Eng.* 3, 421–444. doi: 10.1146/annurev-chembioeng-062011-080945

Farin, H. F., Jordens, I., Mosa, M. H., Basak, O., Korving, J., Tauriello, D. V. F., et al. (2016). Visualization of a short-range Wnt gradient in the intestinal stem-cell niche. *Nature* 530, 340–343. doi: 10.1038/nature16937

Fischer, A. H., Jacobson, K. A., Rose, J., and Zeller, R. (2008). Cryosectioning tissues. *Cold Spring Harb. Protoc.* 3:pdb.prot4991. doi: 10.1101/pdb.prot4991

Graf, B. W., and Boppart, S. A. (2010). Imaging and analysis of three-dimensional cell culture models. *Methods Mol. Biol.* 591, 211–227. doi: 10.1007/978-1-60761-404-3_13

Griffith, L. G., and Swartz, M. A. (2006). Capturing complex 3D tissue physiology *in vitro*. *Nat. Rev. Mol. cell Biol.* 7, 211–224. doi: 10.1038/nrm1858

James, R., Jenkins, L., Ellis, S. E., and Burg, K. J. L. (2004). Histological processing of hydrogel scaffolds for tissue-engineering applications. *J. Histotechnol.* 27, 133–139. doi: 10.1179/his.2004.27.2.133

Jansson-Knodell, C. L., Hujoel, I. A., Rubio-Tapia, A., and Murray, J. A. (2018). Not all that flattens villi is celiac disease: a review of enteropathies. *Mayo Clin. Proc.* 93, 509–517. doi: 10.1016/j.mayocp.2017.10.025

Khademhosseini, A., and Langer, R. (2007). Microengineered hydrogels for tissue engineering. *Biomaterials* 28, 5087–5092. doi: 10.1016/j.biomaterials.2007.07.021

Krndija, D., El Marjou, F., Guirao, B., Richon, S., Leroy, O., Bellaiche, Y., et al. (2019). Active cell migration is critical for steady-state epithelial turnover in the gut. *Science* 365, 705–710. doi: 10.1126/science.aau3429

Leferink, A. M., Van Blitterswijk, C. A., and Moroni, L. (2016). Methods of monitoring cell fate and tissue growth in three-dimensional scaffold-based

strategies for *in vitro* tissue engineering. *Tissue Eng. B Rev.* 22, 265–283. doi: 10.1089/ten.teb.2015.0340

Loebsack, A. B., Halberstadt, C. R., Holder, W. D., Culberson, C. R., Beiler, R. J., Greene, K. G., et al. (1999). The development of an embedding technique for polylactide sponges. *J. Biomed. Mater. Res.* 48, 504–510. doi: 10.1002/(sici)1097-4636(1999)48:4<504::aid-jbm16>3.0.co;2-y

Martínez, E., Engel, E., Planell, J. A., and Samitier, J. (2009). Effects of artificial micro- and nano-structured surfaces on cell behaviour. *Ann. Anat.* 191, 126–135. doi: 10.1016/j.aanat.2008.05.006

Montanez-Sauri, S. I., Beebe, D. J., and Sung, K. E. (2015). Microscale screening systems for 3D cellular microenvironments: platforms, advances, and challenges. *Cell. Mol. Life Sci.* 72, 237–249. doi: 10.1007/s00018-014-1738-5

Pampaloni, F., Reynaud, E. G., and Stelzer, E. H. K. (2007). The third dimension bridges the gap between cell culture and live tissue. *Nat. Rev. Mol. Cell Biol.* 8, 839–845. doi: 10.1038/nrm2236

Peppas, N. A., Hilt, J. Z., Khademhosseini, A., and Langer, R. (2006). Hydrogels in biology and medicine: from molecular principles to bionanotechnology. *Adv. Mater.* 18, 1345–1360. doi: 10.1002/adma.200501612

Ruan, J., Tulloch, N. L., Muskheli, V., Genova, E. E., Mariner, P. D., Anseth, K. S., et al. (2013). An improved cryosection method for polyethylene glycol hydrogels used in tissue engineering. *Tissue Eng. C Methods* 19, 794–801. doi: 10.1089/ten.tec.2012.0460

Schumann, M., Siegmund, B., Schulzke, J. D., and Fromm, M. (2017). Celiac disease: role of the epithelial barrier. *CMGH* 3, 150–162. doi: 10.1016/j.jcmgh.2016.12.006

Short, A. R., Czeisler, C., Stocker, B., Cole, S., Otero, J. J., and Winter, J. O. (2017). Imaging cell–matrix interactions in 3D collagen hydrogel culture systems. *Macromol. Biosci.* 17, 1–8. doi: 10.1002/mabi.201600478

Slaughter, B. V., Khurshid, S. S., Fisher, O. Z., Khademhosseini, A., and Peppas Biomaterials, N. A. (2009). Hydrogels in regenerative medicine. *Adv. Mater.* 21, 3307–3329. doi: 10.1002/adma.200802106

Smith, L. E., Smallwood, R., and Macneil, S. (2010). A comparison of imaging methodologies for 3D tissue engineering. *Microsc. Res. Tech.* 73, 1123–1133. doi: 10.1002/jemt.20859

Štorgel, N., Krajnc, M., Mrak, P., Štrus, J., and Ziherl, P. (2016). Quantitative morphology of epithelial folds. *Biophys. J.* 110, 269–277. doi: 10.1016/j.bpj.2015.11.024

Sung, J. H., Yu, J., Luo, D., Shuler, M. L., and March, J. C. (2011). Microscale 3-D hydrogel scaffold for biomimetic gastrointestinal (GI) tract model. *Lab Chip* 11, 389–392. doi: 10.1039/c0lc00273a

Théry, M. (2010). Micropatterning as a tool to decipher cell morphogenesis and functions. *J. Cell Sci.* 123, 4201–4213. doi: 10.1242/jcs.075150

Torras, N., García-Díaz, M., Fernández-Majada, V., and Martínez, E. (2018). Mimicking epithelial tissues in three-dimensional cell culture models. *Front. Bioeng. Biotechnol.* 6:197. doi: 10.3389/fbioe.2018.00197

Wang, Y., Gunasekara, D. B., Reed, M. I., DiSalvo, M., Bultman, S. J., Sims, C. E., et al. (2017). A microengineered collagen scaffold for generating a polarized crypt-villus architecture of human small intestinal epithelium. *Biomaterials* 128, 44–55. doi: 10.1016/j.biomaterials.2017.03.005

Yang, C. C., Jenkins, L., and Burg, K. J. L. (2007). Adapted cryosectioning method for hydrogels used in regenerative medicine. *J. Histotechnol.* 30, 185–191. doi: 10.1179/his.2007.30.3.185

Yevick, H. G., Duclos, G., Bonnet, I., and Silberzan, P. (2015). Architecture and migration of an epithelium on a cylindrical wire. *Proc. Natl. Acad. Sci. U.S.A.* 112, 5944–5949. doi: 10.1073/pnas.1418857112

Yu, S. M., Oh, J. M., Lee, J., Lee-Kwon, W., Jung, W., Amblard, F., et al. (2018). Substrate curvature affects the shape, orientation, and polarization of renal epithelial cells. *Acta Biomater.* 77, 311–321. doi: 10.1016/j.actbio.2018.07.019

Zihni, C., Mills, C., Matter, K., and Balda, M. S. (2016). Tight junctions: from simple barriers to multifunctional molecular gates. *Nat. Rev. Mol. Cell Biol.* 17, 564–580. doi: 10.1038/nrm.2016.80

Conflict of Interest: The authors declare that the research was conducted in the absence of any commercial or financial relationships that could be construed as a potential conflict of interest.

frontiers in Bioengineering and Biotechnology

ORIGINAL RESEARCH
published: 05 May 2020
doi: 10.3389/fbioe.2020.00405

Development of a New 3D Hybrid Model for Epithelia Morphogenesis

Filippos Ioannou[1,2], *Malik A. Dawi*[3], *Robert J. Tetley*[1,2], *Yanlan Mao*[1,2,4] *and José J. Muñoz*[3]*

[1] Institute for the Physics of Living Systems, University College London, London, United Kingdom, [2] MRC Laboratory for Molecular Cell Biology, University College London, London, United Kingdom, [3] Laboratori de Càlcul Numèric (LaCàN), Universitat Politècnica de Catalunya, Barcelona–Tech, Barcelona, Spain, [4] College of Information and Control, Nanjing University of Information Science and Technology, Nanjing, China

Many epithelial developmental processes like cell migration and spreading, cell sorting, or T1 transitions can be described as planar deformations. As such, they can be studied using two-dimensional tools and vertex models that can properly predict collective dynamics. However, many other epithelial shape changes are characterized by out-of-plane mechanics and three-dimensional effects, such as bending, cell extrusion, delamination, or invagination. Furthermore, during planar cell dynamics or tissue repair in monolayers, spatial intercalation between the apical and basal sides has even been detected. Motivated by this lack of symmetry with respect to the midsurface, we here present a 3D hybrid model that allows us to model differential contractility at the apical, basal or lateral sides. We use the model to study the effects on wound closure of solely apical or lateral contractile contributions and show that an apical purse-string can be sufficient for full closure when it is accompanied by volume preservation.

Keywords: wound healing, vertex, modeling, three dimensions, morphogenesis

OPEN ACCESS

Edited by:
Núria Torras,
Institute for Bioengineering of Catalonia (IBEC), Spain

Reviewed by:
Alexander Fletcher,
University of Sheffield, United Kingdom
Satoshi Yamashita,
Université Paris Diderot, France

***Correspondence:**
José J. Muñoz
j.munoz@upc.edu

Specialty section:
This article was submitted to Tissue Engineering and Regenerative Medicine, a section of the journal Frontiers in Bioengineering and Biotechnology

Received: *16 October 2019*
Accepted: *09 April 2020*
Published: *05 May 2020*

Citation:
Ioannou F, Dawi MA, Tetley RJ, Mao Y and Muñoz JJ (2020) Development of a New 3D Hybrid Model for Epithelia Morphogenesis. Front. Bioeng. Biotechnol. 8:405. doi: 10.3389/fbioe.2020.00405

1. INTRODUCTION

Many morphogenetic events in epithelia can be successfully described with two-dimensional models. Some examples include tissue intercalation (Munjal et al., 2015), jamming transitions (Bi et al., 2016), or collective cell migration (Sunyer et al., 2016). However, monolayers are also subjected to observable out of plane deformations like tissue folding (Tozluoğlu et al., 2019), invagination (Bielmeier et al., 2016), extrusion (Deforet et al., 2014), or delamination (Eisenhoffer et al., 2012). In these cases, two-dimensional models with folding capabilities (Misra et al., 2016), or purely three-dimensional models, usually implemented in the continuum context, seem necessary to capture the underlying contractile mechanisms.

There are also other problems that, despite being studied extensively in two-dimensions, contain three-dimensional contributions that have not been included in their modeling and description. Some examples are neural crest zippering (Hashimoto et al., 2015) or wound healing in monolayers (Antunes et al., 2013; Brugués et al., 2014). The former in fact originates from a precedent tissue folding, while experimental observations of the latter indicate that wound closure has some variations along the cell apicobasal axis (Zulueta-Coarasa et al., 2014). Understanding forces in these processes requires models that are able to reproduce both junctional mechanics and deformations that are different at the apical and basal sides of the monolayer. The present paper introduces a vertex model that includes these ingredients.

The discrete nature of tissues makes vertex modeling an ideal approach that has been successfully employed to simulate cell dynamics of monolayers and study, for example, T1 transitions

(Bi et al., 2015), phase transformations (Bi et al., 2016), and wound healing (Brugués et al., 2014; Staddon et al., 2018; Tetley et al., 2019). For further reference on vertex models see for instance the recent review (Alt et al., 2017).

Three-dimensional versions are more scarce, but have been also recently developed to study curved monolayers (Gómez-Gálvez et al., 2018), cyst formation in monolayers (Bielmeier et al., 2016), folding in epithelial shells (Misra et al., 2016), or general morphogenesis (Okuda et al., 2013, 2015).

We here extend a previous version of our 2D hybrid model to three dimensions (Mosaffa et al., 2018), with the ability to uncouple intercalation on the apical and basal sides of the monolayer. Differential intercalation and the geometrical definition of the cell poses special computational challenges. The analysis of shape transitions between the two sides of a monolayer have been analyzed for curved monolayers (Gómez-Gálvez et al., 2018). Differential apical and basal intercalation has also been seen in the *Drosophila* salivary gland–termed "interleaving" (Sánchez-Corrales et al., 2018). A similar idea is employed here in flat geometries by defining an intermediate vertex that facilitates neighbors changes.

In our model, we resort to a hybrid approach, where the cell-centers of the apical and basal layer are the main degrees of freedom. As is customary in vertex models, each cell-center is surrounded by a set of vertices, where mechanical balance is also imposed between all connected bar elements (Barton et al., 2017). Vertex positions are constrained by the triangulation of the cell-centers. By inserting these constraints into the equilibrium equations, we manage to reduce the computational size of the model, which is solely described by cell-center positions, and thus simplifies the topological definition of the monolayer. We note though that despite this reduction, our final equations still include vertex equilibrium.

Illustrative results are shown by applying the model for the analysis of wound healing, with specific contractility evolution at the wound edge. Each bar element of the model adopts a viscoelastic rheology, which is based on a dynamic change of the rest-length (Muñoz and Albo, 2013; Staddon et al., 2018), and allows calibrating the short term recoil process.

2. METHODOLOGY

2.1. Three-Dimensional Vertex Model

2.1.1. Monolayer Geometry

The cells in the monolayer are initially defined by the centers (*nodes*) of their surfaces at the apical (top) and basal (bottom) sides, respectively denoted by $\boldsymbol{x}_A^i$ and $\boldsymbol{x}_B^i$, $i = 1, \ldots, N_{cells}$. In our simulations, these cell centers are equal at the apical and basal sides, and correspond to the measured experimental locations of the cell center of mass.

After applying a 2D Delaunay triangulation on each side, the cell apical, and basal boundaries are then constructed by joining the *vertices* $\boldsymbol{y}^I, I = 1, \ldots, N_y$ *on each side. These vertices are located at the barycenters of the triangles that surround each cell center*. The two 2D layers are then joined with vertical and diagonal segments that join apical and basal nodes, and also basal and apical vertices, forming prism-like polyhedra. As a result, each cell is formed by an apical and basal center (node) and two sets of vertices defining the apical and basal boundaries. **Figure 1** shows the construction process and final polyhedra.

The initial position of the apical and basal cell-centers (nodes) are taken from two dimensional experimental images, where cell center positions are measured. The cell boundaries are located at the barycenters of the resulting triangles computed from a Delaunay triangulation of the cell centers. Consequently, the initial cell-center locations and shape of the cell areas at the apical and basal surfaces are equal. However, they are allowed to change their connectivity independently in subsequent time-steps, forming polyhedra that may have different polygonal shapes and number of sides at each apical and basal surface. The apico-basal transition between two polygons with different number of segments is facilitated by the definition of *intermediate vertices*, located between the apical and basal surfaces, as shown in **Figure 2**.

More specifically, the positions of the vertices at the apical and basal surfaces are computed from the interpolation of the corresponding cell-centers by using the following constraint equation,

$$\boldsymbol{y}^I = \sum_{i=1}^{3} N^i(\boldsymbol{\xi}^I)\boldsymbol{x}_I^i s, I = 1, \ldots, N_{tri} \tag{1}$$

where $N^i(\boldsymbol{\xi}^I)$ are interpolation functions associated to each one of the nodes $\boldsymbol{x}_I^1, \boldsymbol{x}_I^2, \boldsymbol{x}_I^3$ forming triangle I, and $\boldsymbol{\xi}^i$ a parametric coordinate. Hereafter we set $N^i(\boldsymbol{\xi}^I) = 1/3$, so that vertices are located at the triangle barycenters. As a consequence, the model is a hybrid version between a cell-centered and a purely vertex model. Vertices are used for defining the cell boundary (cortex), but cell-centers are kept as degrees of freedom (DOF) describing the whole cell kinematics. Similar approaches can be found in Barton et al. (2017) and Mosaffa et al. (2018).

The resulting geometrical construction is formed by two coupled networks: the set of segments *ij* joining nodes *nodal network*, and the segments *IJ* joining the vertices *vertex network*. The motivation of the hybrid approach is threefold: (i) it reduces the number of DOF, and thus the size of the resulting system of equations to solve at each time-step, (ii) it allows us to model mechanical interactions between cell-centers (nodal network of triangles) and joint mechanics (vertex network of polygonal cell boundaries), and (iii) it also provides a mechanical coupling between the two networks.

In order to define the vertices at the boundary of the patch, we add a set of boundary nodes which are not the center of any cell. We note also that intermediate vertices are free to move as independent DOF, so that they are not interpolated according to Equation (1). Furthermore, we will also relax the constraint in Equation (1) for those vertices that are at the edge of the wound, and let all those free vertices, denoted by $\boldsymbol{y}_w^I$, to be additional DOFs. As a result, the kinematics of the monolayer is fully defined by the cell centers positions $\boldsymbol{x}^i$ and the coordinates of the relaxed vertices $\boldsymbol{y}_w^I$. We note that this relaxation is introduced in order to avoid zig-zag effects at the wound edge. The reader is referred to Mosaffa et al. (2018) for further analysis on this effect.

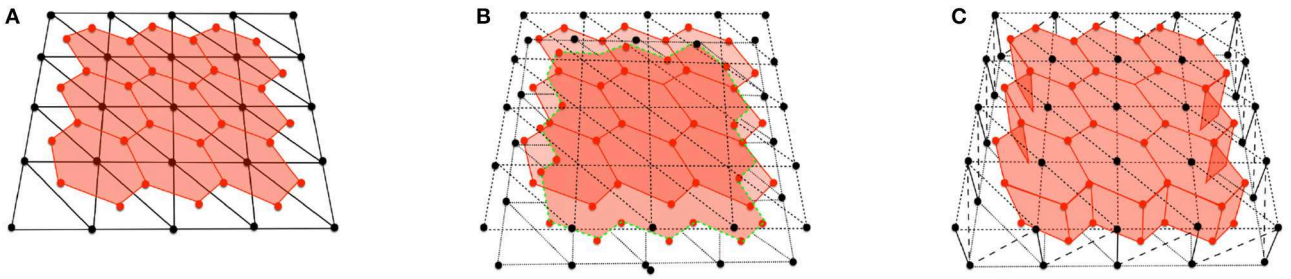

FIGURE 1 | (A) Scheme of a cell with vertex bar elements (red) and nodal bar elements (black). **(B)** Adding apical vertex (red) and nodal (black) network. **(C)** Construction of cells with vertical bar elements. Diagonal elements in vertex network have been omitted for clarity.

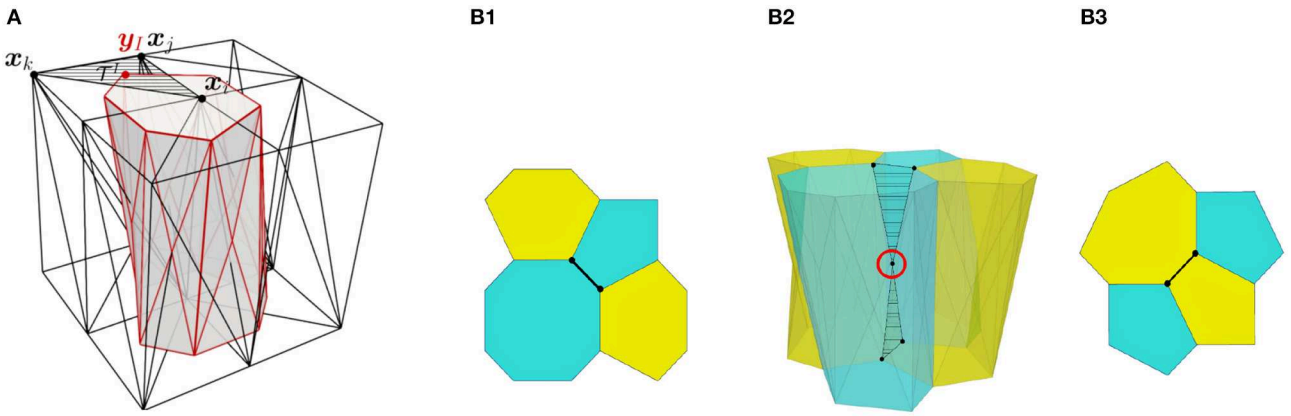

FIGURE 2 | (A) Scheme of a cell with vertex bar elements (red) and nodal bar elements (black). **(B)** Definition of intermediate vertices in order to ease different connectivity at basal surface **(B1)** and apical surface **(B3)**.

2.1.2. Mechanical Equilibrium

In each one of the nodal and vertex network, we distinguish apical, basal and lateral segments. The total energy of the system $W(\boldsymbol{x}, \boldsymbol{y}_w)$ is defined by the sum of nodal and vertex elastic contributions, and a volume penalization as,

$$W(\boldsymbol{x}, \boldsymbol{y}_w) = W_N(\boldsymbol{x}) + W_V(\boldsymbol{y}(\boldsymbol{x}), \boldsymbol{y}_w) + W_{Vol}(\boldsymbol{y}(\boldsymbol{x}), \boldsymbol{y}_w) \quad (2)$$

Each term is defined by,

$$W_N(\boldsymbol{x}) = \frac{k_N}{2} \sum_{ij} (l^{ij} - L^{ij})^2$$

$$W_V(\boldsymbol{y}(\boldsymbol{x}), \boldsymbol{y}_w) = \frac{k_V}{2} \sum_{IJ} (l^{IJ} - L^{IJ})^2$$

$$W_{Vol}(\boldsymbol{y}(\boldsymbol{x}), \boldsymbol{y}_w) = \frac{\lambda_{Vol}}{2} \sum_{i=1}^{N_{cells}} \left(\frac{V^i - V_0^i}{Vi_0} \right)^2$$

The material parameters k_N and k_V measure the stiffness of the nodal and vertex segments, respectively. The measures $l^{ij} = ||\boldsymbol{x}^i - \boldsymbol{x}^j||$ and $l^{IJ} = ||\boldsymbol{y}^I - \boldsymbol{y}^J||$ correspond to the current observable lengths of each nodal and vertex segment. The rest-lengths L^{ij} and L^{IJ} are internal variables, not necessarily constant. Their evolution will furnish viscous properties to the monolayer, and will be defined in section 2.1.3. The penalization parameter λ_{Vol} is set to a value such that relative volume difference $|V^i - V_0^i|/V_0^i$ at each cell i is kept between 5 and 10%, as experimentally measured (Gelbart et al., 2012).

Mechanical equilibrium is achieved by minimizing the total energy with respect to the positions of the nodes and the relaxed vertices, i.e.,

$$\frac{\partial W_N}{\partial \boldsymbol{x}^i} + \frac{W_V}{\partial \boldsymbol{y}^I} \frac{\partial \boldsymbol{y}^I}{\partial \boldsymbol{x}^i} + \frac{\partial W_{Vol}}{\partial \boldsymbol{y}^I} \frac{\partial \boldsymbol{y}^I}{\partial \boldsymbol{x}^i} = \boldsymbol{0}, \; i = 1, \ldots, N_{nodes} \quad (3)$$

$$\frac{W_V}{\partial \boldsymbol{y}_w^I} + \frac{\partial W_{Vol}}{\partial \boldsymbol{y}_w^I} = \boldsymbol{0}, I = 1, \ldots, N_{relax} \quad (4)$$

The terms $\frac{\partial \boldsymbol{y}^I}{\partial \boldsymbol{x}^i}$ are computed from the constraint equation in (1) as, $\frac{\partial \boldsymbol{y}^I}{\partial \boldsymbol{x}^i} = N^i(\boldsymbol{\xi}^I)\mathbf{I} = 1/3\mathbf{I}$, with $\mathbf{I} = \frac{\partial \boldsymbol{x}^i}{\partial \boldsymbol{x}^i}$ the three-dimensional identity matrix. Due to the non-linearity of the equations in (3), the solution is found using a Newton-Raphson strategy enhanced with line-search strategies.

After each converged step at time t_n, with connectivity C_n and nodal and vertex positions $\boldsymbol{x}_n^i$ and $\boldsymbol{y}_w^I$, we compute new nodal and vertex positions, $\boldsymbol{x}_{n+1}^i$ and $\boldsymbol{y}_{w,n+1}^I$, respectively, and a new connectivity C_{n+1} using a modified Delaunay triangulation of

the apical and basal surfaces. New triangles are formed if their aspect ratio at time t_{n+1}, denoted by r_{n+1}, is improved according to the relation

$$r_{n+1} < (1 + tol_r)r_n$$

with tol_r a non-negative numerical parameter. When $tol_r = 0$, the standard Delaunay algorithm is recovered, while for $tol_r > 0$, suboptimal stretched triangles and cells are permitted.

2.1.3. Rheological Model

Each vertex segment in the model has the ability to respond according to a viscoelastic rheological law. This law is implemented by resorting to a variable rest-length L^{ij} or L^{IJ}, which evolves with the following equation:

$$\frac{1}{L}\frac{dL}{dt} = \gamma\left(\frac{l-L}{L} - \varepsilon^c\right) \tag{5}$$

This law reflects the fact that as far as the strain measure $(l-L)/L$ is different from a contractility ε^c, the rest-length will evolve, and that L will remain unchanged when the strain reaches the value ε^c. It has been proved that for $\varepsilon^c = 0$, such evolution law gives a similar response to a Maxwell viscous model (Muñoz and Albo, 2013). The intrinsic contractility ε^c has been included in order to mimic the contractile state of cells (Khalilgharibi et al., 2019; Wyatt et al., 2020).

In addition, we also consider the local actin concentration at the wound edge. This is implemented through an additional contractility $\hat{\Upsilon}^c$, which increases the tension at the elastic branch of the vertex segment as

$$\sigma_V = k_{V0}(\varepsilon^e + \Upsilon^c)$$

We will use time-varying values of $\hat{\Upsilon}^c$ at the apical and lateral sides of the cells, as it is explained in section 2.2. As a result, an additional tension equal to $k_{V0}\hat{\Upsilon}^c$ is being applied on those vertex segments.

Figure 3 depicts the rheological model employed at the nodal and vertex segment. The purely elastic behavior is obtained by the minimization of energies W_N and W_V using, respectively, stiffnesses k_N and k_{V0}, while the viscous response results from the implementation of the evolution law in (5) in an additional energy term W_V with stiffness k_V. For simplicity and to avoid having to fit too many parameters, we have set $\gamma = 0$ for the nodal elements, which yields a purely elastic behavior, as depicted in **Figure 3**. The calibration of the material parameters will be explained in section 3.1.

2.1.4. Numerical Solution

The set of non-linear equations in (3) depends non-linearly on the nodal positions $\boldsymbol{x}^i$ and on the relaxed vertices $\boldsymbol{y}_w^I$. In addition, these equations, which may be expressed as,

$$\boldsymbol{g}(\boldsymbol{x}, \boldsymbol{y}_w) = \boldsymbol{0} \tag{6}$$

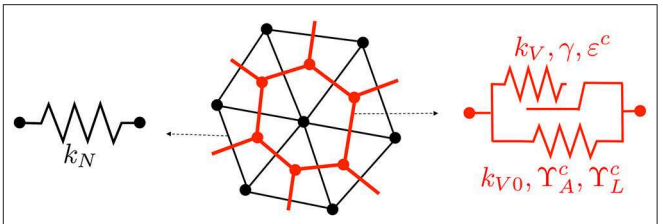

FIGURE 3 | Rheological model for nodal **(left)** and vertex **(right)** segments. Contractility parameters Υ_A^c and Υ_L^c are only used at the wound edge.

also include the rest-lengths L of each bar element. These rest-lengths obey the differential equation in (5), which is discretized in time using a θ − *weighted* scheme,

$$L_{n+1} - Ln = \Delta t L_{n+\theta}\gamma\left(\frac{l_{n+\theta} - L_{n+\theta}}{L_{n+\theta}} - \varepsilon^c\right) \tag{7}$$

with $(\bullet)_{n+\theta} = (1-\theta)(\bullet)_n + \theta(\bullet)_{n+1}$. We used the value $\theta = 0.5$, which yields a second-order accurate and unconditionally stable scheme in linear systems. The relation in (7) allows obtaining an expression of L_{n+1} as a function of l_{n+1} and other values at time t_n. This expression is inserted in the system of equations in (6) at each time t_{n+1}, and solved in an implicit manner with a fully Newton-Raphon iterative process. We set the convergence tolerance $tol = 1E-10$ and impose the convergence condition $||\delta \boldsymbol{x}|| < tol$ and $||\boldsymbol{g}(\boldsymbol{x}, \boldsymbol{y}_w)|| < tol$. We have used the time-step size $\Delta t_1 = 0.6$ min during the recoil process (up to $t = 6$ min), and $\Delta t_2 = 1$ min during the closure process. In some simulations, the latter time-step was halved in some of the increment in order to achieve convergence. The total simulation when using a patch of 205 cells took around 150 increments, and a run time of approximately 20 min in Matlab R2018a in a Windows machine with Intel(R) Core(TM) i7-6700 CPU @ 3.4 GHz, and 16 GB RAM memory, working with 2 processors.

2.2. Wounding and Contractility

The *Drosophila* larval wing imaginal disc is a pseudostratified epithelium containing highly columnar cells. This tissue is therefore an ideal experimental system for investigating wound healing cell behaviors in 3-dimensions. We wounded wing disc epithelia by ablating multiple tricellular junctions at the level of adherens junctions using a pulsed TiSa laser (Tetley et al., 2019). We then imaged the wound healing response in wing discs expressing a GFP tagged form of non-muscle Myosin II using 3D time-lapse confocal microscopy with intervals of 3 min between successive time points. A representative sequence of images is shown in **Figure 5**.

We simulate the *in silico* wounding of the vertex model by degrading the stiffness of the ablated cells down to 1% of their initial value, and removing the volume penalization term in the total energy for these cells, that is, reducing λ_{Vol} to 0 on those ablated cells. This softening, together with the subsequent removal of these degraded cells and the progressive intercalation of the cells at the wound edge allows us to simulate progressive wound closure.

We explicitly implement the evolution of an actomyosin purse-string at the wound edge by applying a decreasing trend to the apical vertex segments, while applying a constant value at the lateral sides. In the model, the contractilities are explicitly given by,

$$\hat{\Upsilon}_A^c = \begin{cases} \Upsilon_A^c\left(1 - \frac{t-t_w}{400}\right), & t > t_w \\ 0, & \text{otherwise} \end{cases}$$

$$\hat{\Upsilon}_L^c = \begin{cases} \Upsilon_L^c, & t > t_w \\ 0, & \text{otherwise} \end{cases}$$

where $t_w \approx 6$ min is the time at which purse-string contractility is activated, with $t = 0$ the time for tissue ablation. Our simulations last in average around 150 min, so that the factor 1/400 in $\hat{\Upsilon}_A^c$ aims at reducing the purse-string contractility with a similar trend of the concentration of Myosin II measured and showed in **Figure 4**. Model parameters Υ_A^c and Υ_L^c will be calibrated in section 3.1.

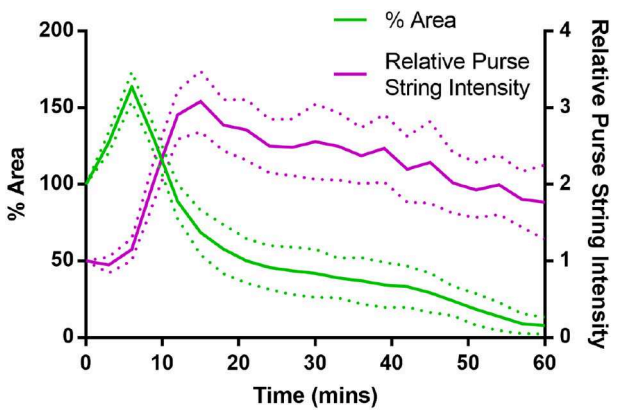

FIGURE 4 | Purse-string Myosin II intensity and wound area evolution during the first hour of wound closure, averaged over 5 wing disc wounds. Myosin II intensity in the purse-string gradually reduces over time, as the wound closes (Error bars = S.D.).

2.3. Experimental Measurements

Experimental quantifications were averaged across wounds in five separate wing discs. We quantified the evolution of wing disc apical wound area by manually tracing the periphery of the wound for the first 72 min after wounding. The wound periphery was particularly clear while wound healing progressed, due to the formation of an apical actomyosin purse-string (**Figure 5**). To quantify the evolution of wound apical indentation depth, we first generated orthogonal image views and fitted a line between the highest points of the apical surface either side of the wound edge. We then calculated the distance along the apicobasal axis between this line and the position of the wound periphery (most clearly marked by the actomyosin purse-string, **Figure 5**). The relative height was computed from the depth measurements by assuming that the monolayer had an average height of 35 μm.

We also quantified the number of T1 transitions by analysing the gradual reduction in the number of cells at the wound edge. The evolution of the latter will be compared with our simulations in the next section. **Figure 6** demonstrates that T1 transitions also occur spatially, along the apicobasal axis in a single timeframe, as well as temporally in the plane of the epithelium. This justifies our inclusion of intermediate vertices (**Figure 2**).

3. RESULTS

3.1. Model Calibration

We use the recoil process for calibrating tissue contractility ε^c, vertex stiffness k_{V0}, and the remodeling rate γ, which measures

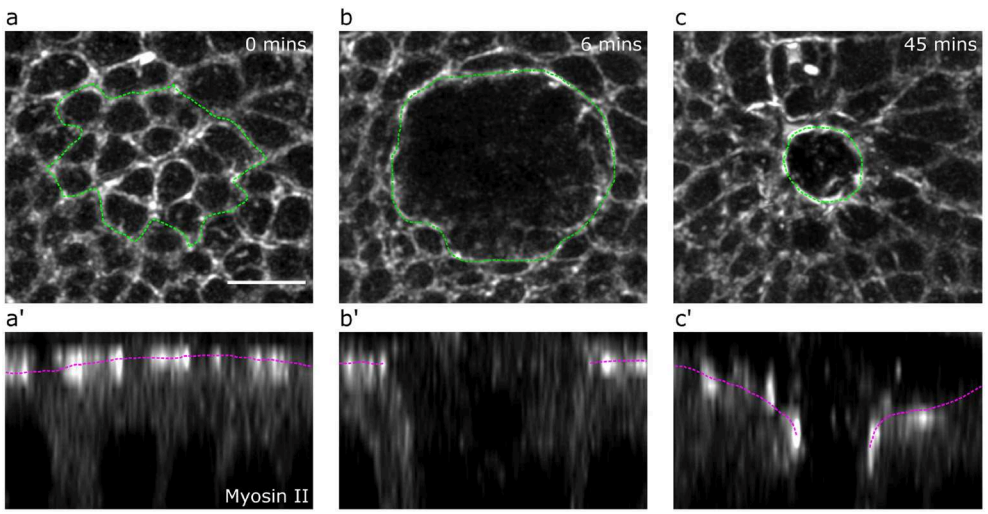

FIGURE 5 | *Drosophila* wing disc wound evolution. Apical **(a,b,c)** and lateral views **(a',b',c')** of a *Drosophila* wing disc expressing a GFP-tagged form of non-muscle Myosin II at 0 min **(a,a')**, 6 min (maximum recoil, **b,b'**) and 45 min (partial closure, **c,c'**) after wounding. The margin of killed cells **(a)** and the wound **(b,c)** are marked by a green dotted line. The apical surface of the tissue is marked by a magenta dotted line **(a',b',c')**. Scale bar = 5μm.

the viscous response. In order to avoid stiffness redundancy between vertex and nodal networks, we fix $k_N = 0.5$. **Figure 7** shows the sensitivity of the recoil to these material parameters.

Tissue contractility ε^c increases the asymptotic line tension in cells, and as such increases the final apical and basal areas after recoil. Larger values of recoil for MyoII activation and higher tension have been reported experimentally (Tetley et al., 2019), supporting this effect. Material stiffness has an inverse trend, reducing recoil for larger values of k_{V0}, which increases the relative energy cost of length changes. In our formulation, mechanical equilibrium is reached through energy minimization, which is proportional to material stiffness and line strains. Consequently, when stiffness increases, line stretching is in general reduced.

The remodeling rate mimics the viscous and fluid response of the cells. For higher values of γ, the characteristic time and the viscosity of the fluid is reduced, in agreement with the model (Muñoz and Albo, 2013). Consequently, the area after recoil increases for a fixed time. The final values of the tissue are given in **Table 1**. Other values of nodal and vertex stiffness, k_N and k_V have been manually fitted so that the final wound area remains stable at the experimental values, and that no element is under compression. Although there is some redundancy on their values (multiple combinations giving similar wound area), we have chosen the values $k_N = 0.3$ and $k_V = 1.0$.

3.2. Wound Healing Simulations

We tested squared patches with different size, from 80 to 205 cells, and generated for each case cell positions similar to those measured experimentally. We fixed the positions of the cell-centers at the patch boundary. For the tested sizes of ablation (from 5 to 11 cells) and patch dimensions, the assumption of zero displacements on those external cells agreed also with the observed deformations. We measured the experimental displacements of the boundary cell centers, and the mean of their norm was in all cases below 1% of the side of the patch.

In order to test the effects of the wound edge contractility after ablation, we measured the time evolution of the relative projected area and the relative height at the wound edge in the *in silico* model and *in vivo*. **Figure 8** shows snapshots of the full simulated tissue. Two videos showing apical and basal view of the simulation can be found in the Supplemental Material (**Supplementary Videos 1**, **2**). **Figure 9** shows cross-sections through the wounded region, where unequal closure at the apical and basal sides can be observed. **Figure 10** shows the standard deviation of the experimental and simulated wound area evolutions, when using the same cell center positions and similar areas for each one of the patches tested. The deviations from the mean trend are similar, but the mean values of the numerical simulations close slightly earlier than the *in vivo* wounds. More sophisticated contractility profiles were needed in order to delay the simulated closure.

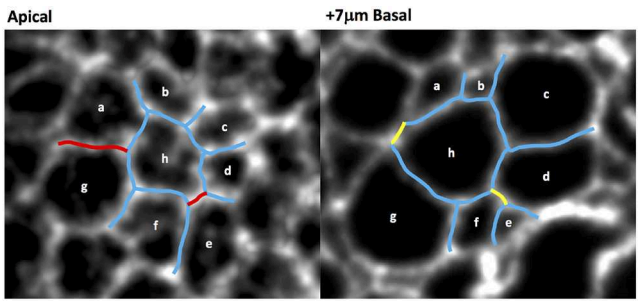

FIGURE 6 | Wing disc cell outlines (cells a–h, marked by CAAX-GFP) at two different apicobasal positions, demonstrating that neighbor exchanges occur along the apicobasal axis at a single time point. Persistent cell-cell junctions are in blue, lost junctions in red and gained junctions in yellow.

TABLE 1 | Values of parameters fitted in recoil phase.

Parameter	Value
Contractility ε^c	1.3
Vertex stiffness k_{V0}	0.05
Remodeling rate γ	0.2

Fixed values are $k_N = 0.3$ and $k_V = 1$.

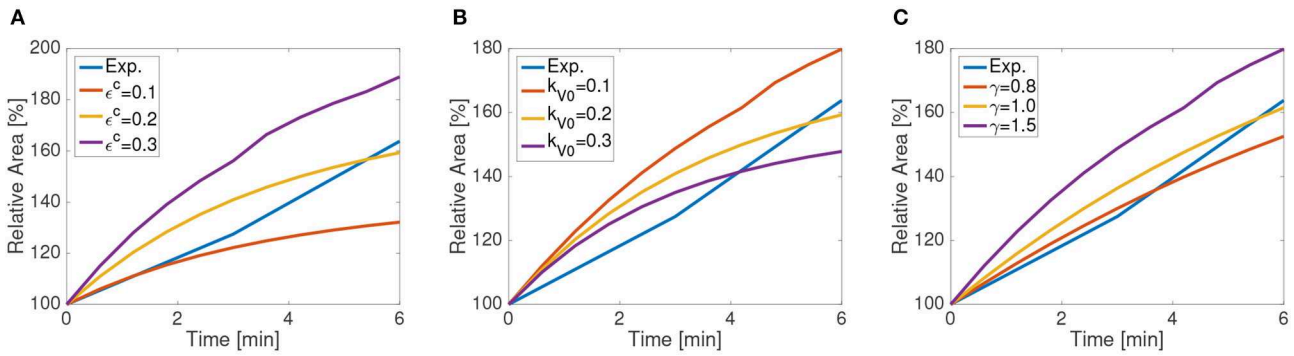

FIGURE 7 | Apical wounded area as a function of time for the first 6 min following ablation as simulated using a 65 cell computational tissue. Different values of **(A)** background contractility ε^c, **(B)** vertex stiffness k_V, and **(C)** and remodeling rates γ.

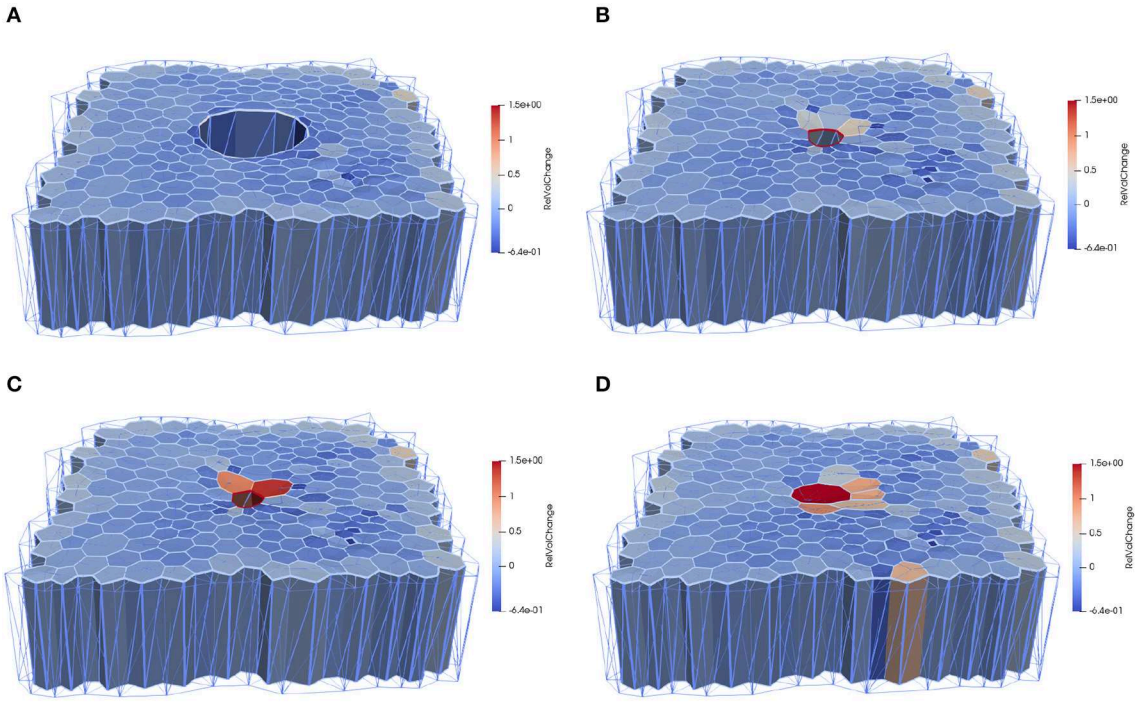

FIGURE 8 | Computational epithelial tissue with 205 cells and 8 ablated cells, shown in side view for applied apical contractility of $\Upsilon_A^c = 2.3$. **(A)** Apical view of epithelial computational tissue shows the maximum recoil ($t = 10$ min). **(B)** Wound edge cell before intercalation $t = 30$ min. **(C)** Wound edge cell after intercalation $t = 32$ min. **(D)** Final time step of wound closure process $t = 52$ min. The color map illustrates the relative volume change. Videos of the simulation showing the apical and basal view can be found in the **Supplemental Material**.

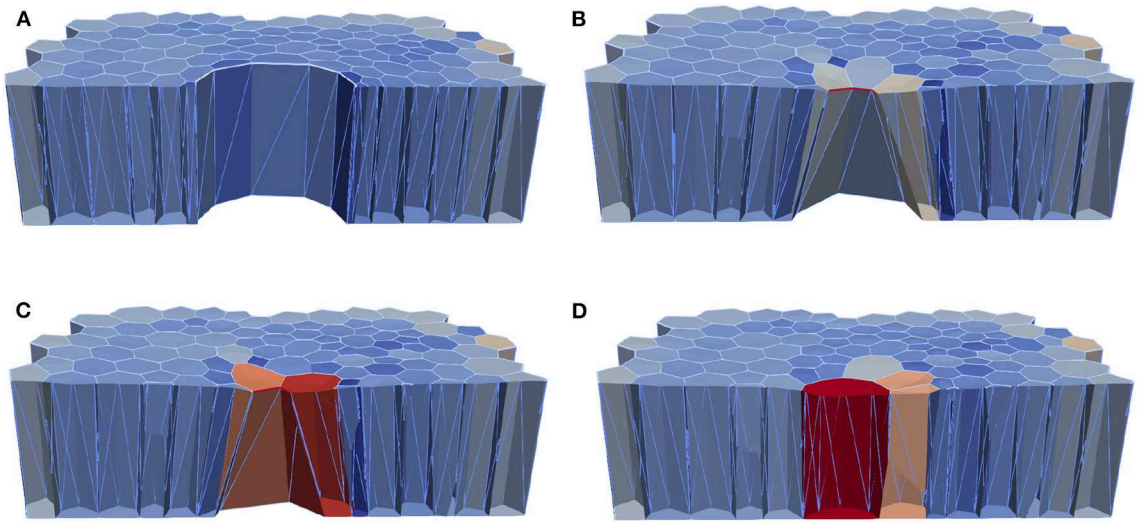

FIGURE 9 | Computational epithelial tissue with 205 cells and 8 ablated cells, shown in cross-section view for applied apical contractility of $\Upsilon_A^c = 2.3$. **(A)** Apical of epithelial computational tissue shows the maximum recoil $t = 10$ min. **(B)** Wound edge cell before intercalation $t = 30$ min. **(C)** Wound edge cell after intercalation $t = 52$ min. **(D)** Final time step of wound closure process. The color map illustrates the relative volume change.

The parameter study of apical contraction Υ_A^c in **Figure 11** shows that below a threshold value of $\approx$ 2.2, contractility is insufficient to close the wound, for the tested material parameters. However, the changes on the purse-string tension have a minimal effect on the relative height evolution (see **Figure 11B**). We remark that the material parameters also have an effect on the closure time and profile: higher values of stiffness and tissue contractility ε^c delay or may prevent closure, while

higher viscosity (lower value of γ) may also delay the closure process. These material properties have been calibrated in order to match the recoil, but also the rate of closure.

Recently, it has been shown that changes in tissue height occur as a result of increased apicobasal contractility (Monier et al., 2015; Sui et al., 2018). We therefore also tested the effect of increased lateral contractility on wound closure. For increasing values of Υ_L^c, the height diminishes, as expected, and the closure of the area is in turn also accelerated (see the plots in **Figure 12**). Despite the fact that lateral edges are inclined due to the higher area reduction in the apical side, and oppose closure, their global effect is to contribute to closure due to the volume constraint.

We also analyse the evolution of the transitions, or equivalently, the number of cells at the wound edge. **Figure 13A** shows the evolution of the number of cells at the wound edge. While the experimental evolution is progressive, our simulations exhibit a more sudden concentration of the transitions. This may be due to the geometrical control of the transitions in the vertex discretization. We are currently investigating more accurate cell descriptions in order to obtain less drastic T1 transitions.

In order to measure the effect of the volume constraint, we checked the evolution of the apical area for different values of λ_{Vol}. **Figure 13B** shows that in fact, to strict or too relaxed volume preservation may impede wound closure. In our simulations, when $\lambda_{Vol} = 25$ or $\lambda_{Vol} = 10$, the wound does not close. In the first case this is due to the need to increase the cell size to some extent in order to recover the same sized patch with fewer cells (we do not simulate cell proliferation). In the second case, when λ_{Vol} is too low, the recoil is too large and cell adapt to the purse-string by changing size instead of closing the wound through intercalation. In our simulations we used $\lambda_{Vol} = 20$, which garantees that the mean deviation of each cells remains below 10%.

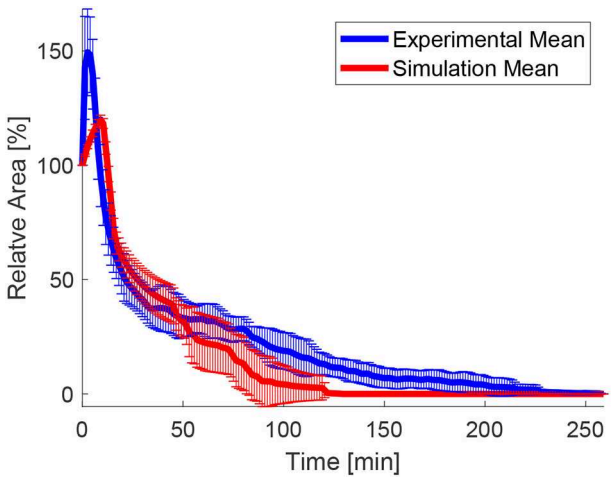

FIGURE 10 | Mean values and standard deviation of the experimental and numerical area evolution.

4. CONCLUSIONS AND DISCUSSION

Recent experimental analyses have shown that wound closure is not only driven by tissue tension and contractility, but also by the rate of intercalation, so-called tissue fluidity (Tetley et al., 2019). The present model aims at extending this analysis to three dimensions, by including lateral contractility, and allowing the simulation of different intercalation at the apical and basal side.

We used the recoil process to calibrate the material parameters that characterize tissue viscoelastic properties. The rate of wound expansion just after ablation is a useful measure of tissue viscosity, which we simulated through a variable rest-length $L(t)$ that adapts according to a remodeling rate γ. This parameter, and tissue contractility ε^c have been experimentally measured *in vitro* (Wyatt et al., 2020) for suspended monolayers. We showed that ε^c takes the value ≈ 0.3, which is close to our fitted value from the *in vivo* measurements of the area evolution. We here also showed that the recoil can be employed to evaluate this material property and that it indeed determined the final expansion.

Based on experimental observations of the evolution of myosin concentration, we applied non constant trends on the

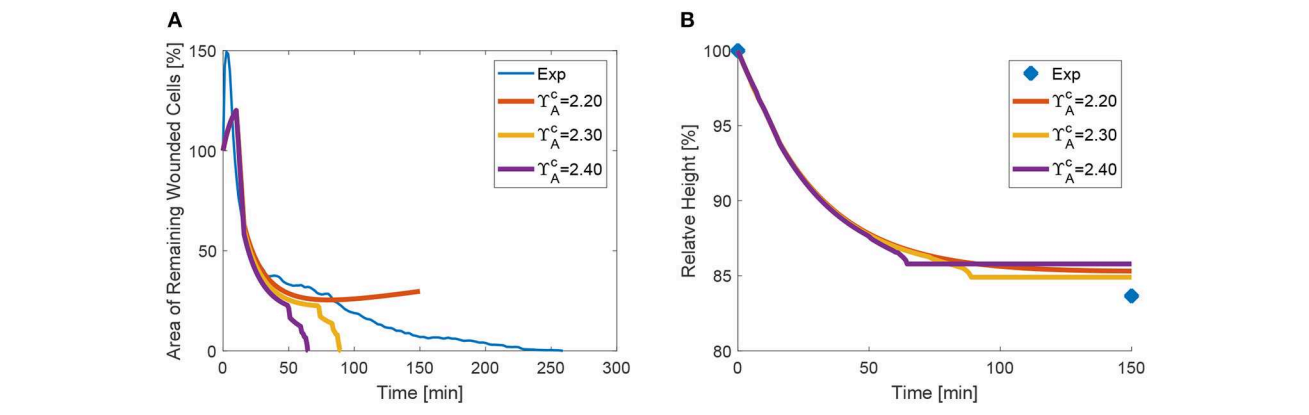

FIGURE 11 | Area **(A)** and height **(B)** evolution as a function of apical purse-string contractility Υ_A^c.

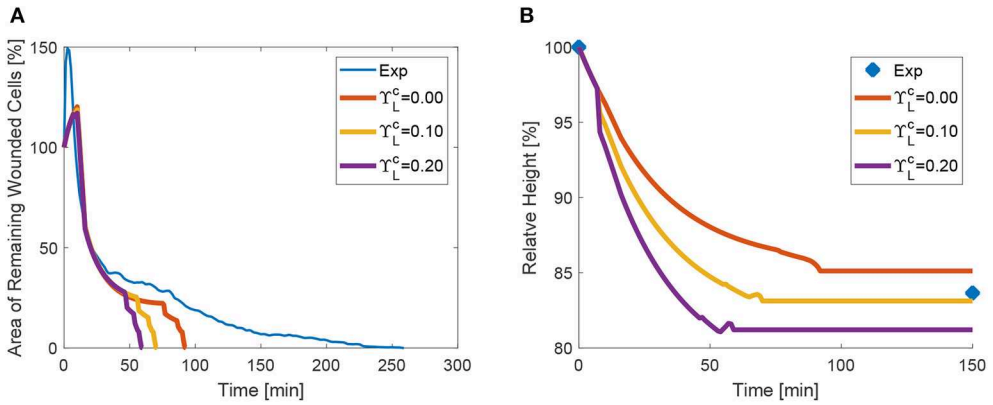

FIGURE 12 | Area **(A)** and height **(B)** evolution as a function of lateral purse-string contractility Υ_L^c.

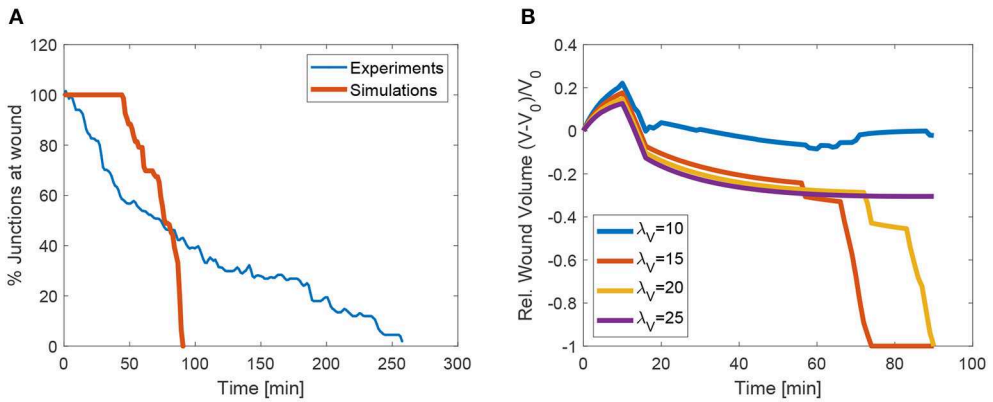

FIGURE 13 | (A) Evolution of the mean number of junctions at apical wound perimeter *in vivo* and in the simulations. **(B)** Evolution of volume in the wounded region as a function penalization factor λ_{Vol}. The cases with $\lambda_1 0$ and $\lambda_2 5$ did not converge.

apical and lateral surfaces of the wound. We encountered a minimum value of apical tension at the wound edge, below which no closure takes place. When Υ_A^c is lower than approximately 2.3, the tissue in unable to surmount line tension between cells, given by ε^c in the model. It appears thus that the ratio between purse-string tension (given in the model by Υ_A^c) and cell line tension (in the model represented by ε^c) modulates the speed of closure, and that for too low values, closure may not succeed. Experimentally, too high values of line tension have been also shown to slow down or even prevent closure (Tetley et al., 2019).

We additionally observed that although lateral tension contributes in general to wound closure, depending on the tissue thickness, the net contribution of lateral purse-string contractility, regulated by Υ_L^c, the duration of the healing process is shortened. Further inspection of the whole shape and cross-section of the wound along the apicobasal axis and accurate measurements of the height profile are necessary to corroborate this fact. This is a challenging task, given the high aspect ratio (thickness/diameter) of the cells and their high light scattering. We also note that purse-string apical tension has very minor effects on the height evolution, but lateral contractility does modify the values of tissue thickness and importantly, also area evolution (see **Figure 12**).

Our numerical results indicated that apical purse-string tension, when applied together with volume preservation induced a reduction of the height, due to the expansion of the tissue. We point out though that in our model, lateral contractility is applied on the whole height of the tissue. This may not be so in the real tissue, where lateral myosin may not be homogeneous along the thickness. Further discretization of the monolayer along the apicobasal axis seems necessary to simulate the specific localization of lateral myosin on the apical side. We expect that more accurate experimental measurements and model enhancements will allow us to quantify cell mechanical contribution and regulation more closely during wound closure, which as shown, are more complex than a 2D analysis may reveal.

The evolution of relative height *in vivo* and *in vitro* plotted in **Figures 11B**, **12B** also revealed that the initial height of the monolayer was not recovered, even when the wound was fully

closed. In our model, this fact can be explained by the reduced number of cells in the patch after ablation. The reduction in the total volume reduction is compensated by a height reduction, since the patch area is fixed. In the experiments, whether the patch recovers the initial height after a sufficiently long period is still under study. This analysis, and the evolution of the material properties after successive re-wounding is left for further investigations.

DATA AVAILABILITY STATEMENT

The data generated and analyzed for this study can be provided upon request to the corresponding authors.

AUTHOR CONTRIBUTIONS

YM conceived the project and designed the experiments. JM conceived the *in silico* model. FI, MD, and JM developed the numerical simulations. RT carried out experiments and performed experimental quantification. All authors participated in the discussions of the experiments and the modeling. JM, FI, and YM drafted the manuscript, which was completed and revised by all the authors.

FUNDING

JM and MD have been financially supported by the Spanish Ministry of Science, Innovation and Universities (MICINN) with grant DPI2016-74929-R and by the local government *Generalitat de Catalunya* with grant 2017 SGR 1278. RT was funded by a Medical Research Council Skills Development Fellowship (MR/N014529/1). YM was funded by a Medical Research Council Fellowship MR/L009056/1, a Lister Institute Research Prize, and EMBO Young Investigator Programme. FI was funded by a Marie Curie ITN PolarNet. This work was also supported by MRC funding to the MRC LMCB University Unit at UCL, award code MC_U12266B.

SUPPLEMENTARY MATERIAL

The Supplementary Material for this article can be found online at: https://www.frontiersin.org/articles/10.3389/fbioe.2020.00405/full#supplementary-material

Supplementary Video 1 | Apical view of the wound healing simulation using fitted parameters.

Supplementary Video 2 | Basal view of the wound healing simulation using fitted parameters.

REFERENCES

Alt, S., Ganguly, P., and Salbreux, G. (2017). Vertex models: from cell mechanics to tissue morphogenesis. *Philos. Trans. R. Soc. Lond. B* 372:20150520. doi: 10.1098/rstb.2015.0520

Antunes, M., Pereira, T., Cordeiro, J. V., Almeida, L., and Jacinto, A. (2013). Coordinated waves of actomyosin flow and apical cell constriction immediately after wounding. *J. Cell Biol.* 202, 365–379. doi: 10.1083/jcb.201211039

Barton, D., Henkes, S., Weijer, C., and Sknepnek, R. (2017). Active vertex model for cell-resolution description of epithelial tissue mechanics. *PLoS Comput. Biol.* 13:e1005569. doi: 10.1371/journal.pcbi.1005569

Bi, D., Lopez, J., Schwarz, J., and Manning, M. (2015). A density-independent rigidity transition in biological tissues. *Nat. Phys.* 11, 1074–1079. doi: 10.1038/nphys3471

Bi, D., Yang, X., Marchetti, M. C., and Manning, M. L. (2016). Motility-driven glass and jamming transitions in biological tissues. *Phys. Rev. X* 6:021011. doi: 10.1103/PhysRevX.6.021011

Bielmeier, C., Alt, S., Weichselberger, V., Fortezza, M., Harz, H., Jülicher, F., et al. (2016). Interface contractility between differently fated cells drives cell elimination and cyst formation. *Curr. Biol.* 25, 563–574. doi: 10.1016/j.cub.2015.12.063

Brugués, A., Anon, E., Conte, V., Veldhuis, J., Gupta, M., Collombelli, J., et al. (2014). Forces driving epithelial wound healing. *Nat. Phys.* 10, 683–690. doi: 10.1038/nphys3040

Deforet, M., Hakim, V., Yevick, H., Duclos, G., and Silberzan, P. (2014). Emergence of collective modes and tri-dimensional structures from epithelial confinement. *Nat. Commun.* 5:3747. doi: 10.1038/ncomms4747

Eisenhoffer, G., Loftus, P., Yoshigi, M., Otsuna, H., Chien, C. B., Morcos, P. A., et al. (2012). Crowding induces live cell extrusion to maintain homeostatic cell numbers in epithelia. *Nature* 484, 546–549. doi: 10.1038/nature10999

Gelbart, M., He, B., Martin, A., Thiberge, S., Wieschaus, E., and Kaschube, M. (2012). Volume conservation principle involved in cell lengthening and nucleus movement during tissue morphogenesis. *Proc. Natl. Acad. Sci. U.S.A.* 109, 19298–19303. doi: 10.1073/pnas.1205258109

Gómez-Gálvez, P., Vicente-Munuera, P., Tagua, A., Forja, C., Castro, A., Letrán, M., et al. (2018). Scutoids are a geometrical solution to three-dimensional packing of epithelia. *Nat. Commun.* 9:2960. doi: 10.1038/s41467-018-05376-1

Hashimoto, H., Robin, F., Sherrard, K., and Munro, E. (2015). Sequential contraction and exchange of apical junctions drives zippering and neural tube closure in a simple chordate. *Dev. Cell* 32, 241–255. doi: 10.1016/j.devcel.2014.12.017

Khalilgharibi, N., Fouchard, J., Asadipour, N., Barrientos, R., Duda, M., Bonfanti, A., et al. (2019). Stress relaxation in epithelial monolayers is controlled by the actomyosin cortex. *Nat. Phys.* 15, 839–847. doi: 10.1038/s41567-019-0516-6

Misra, M., Audoly, B., Kevrekidis, I., and Shvartsman, S. (2016). Shape transformations of epithelial shells. *Biophys. J.* 110, 1670–1678. doi: 10.1016/j.bpj.2016.03.009

Monier, B., Gettings, M., Gay, G., Mangeat, T., Schott, S., Guarner, A., et al. (2015). Apico-basal forces exerted by apoptotic cells drive epithelium folding. *Nature* 7538, 245–248. doi: 10.1038/nature14152

Mosaffa, P., Rodríguez-Ferran, A., and Muñoz, J. (2018). Hybrid cell-centred/vertex model for multicellular systems with equilibrium-preserving remodelling. *Int. J. Num. Methods Biomed. Eng.* 34, 1–24. doi: 10.1002/cnm.2928

Munjal, A., Philippe, J., Munro, E., and Lecuit, T. (2015). A self-organized biomechanical network drives shape changes during tissue morphogenesis. *Nature* 524, 351–355. doi: 10.1038/nature14603

Muñoz, J., and Albo, S. (2013). Physiology-based model of cell viscoelasticity. *Phys. Rev. E* 88:012708. doi: 10.1103/PhysRevE.88.012708

Okuda, S., Inoue, Y., Eiraku, M., Adachi, T., and Sasai, Y. (2015). Vertex dynamics simulations of viscosity-dependent deformation during tissue morphogenesis. *Biomech. Model. Mechanobiol.* 14, 413–425. doi: 10.1007/s10237-014-0613-5

Okuda, S., Inoue, Y., Eiraku, M., Sasai, Y., and Adachi, T. (2013). Modeling cell proliferation for simulating three-dimensional tissue morphogenesis based on a reversible network reconnection framework. *Biomech. Model. Mechanobiol.* 12, 987–996. doi: 10.1007/s10237-012-0458-8

Sánchez-Corrales, E., Blanchard, G., and Röper, K. (2018). Radially patterned cell behaviours during tube budding from an epithelium. *eLife* 7:e35717. doi: 10.7554/eLife.35717

Staddon, M., Bi, D., Tabatabai, A. P., Ajeti, V., Murrell, M., and Banerjee, S. (2018). Cooperation of dual modes of cell motility promotes epithelial stress relaxation to accelerate wound healing. *PLoS Comput Biol.* 14:e1006502. doi: 10.1371/journal.pcbi.1006502

Sui, L., Alt, S., Weigert, M., Dye, N., Eaton, S., Jug, F., et al. (2018). Differential lateral and basal tension drive folding of *drosophila* wing discs through two distinct mechanisms. *Nat. Commun.* 4320, 1–13. doi: 10.1038/s41467-018-06497-3

Sunyer, R., Conte, V., Escribano, J., Elosegui-Artola, A., Labernadie, A., Valon, L., et al. (2016). Collective cell durotaxis emerges from long-range intercellular force transmission. *Science* 353, 1157–1161. doi: 10.1126/science.aaf7119

Tetley, R., Staddon, M., Banerjee, S., and Mao, Y. (2019). Tissue fluidity promotes epithelial wound healing. *Nat. Phys.* 15, 1195–1203. doi: 10.1038/s41567-019-0618-1

Tozluoğlu, M., Duda, M., Kirkland, N., Barrientos, R., Burden, J., Muñoz, J., et al. (2019). Planar differential growth rates initiate precise fold positions in complex epithelia. *Dev. Cell* 51, 299–312. doi: 10.1016/j.devcel.2019.09.009

Wyatt, T. J., Fouchard, J., Lisica, A., Khalilgharibi, N., Baum, B., Recho, P., et al. (2020). Actomyosin controls planarity and folding of epithelia in response to compression. *Nat. Mat.* 19, 109–117. doi: 10.1101/422196

Zulueta-Coarasa, T., Tamada, M., Lee, E., and Fernandez-Gonzalez, R. (2014). Automated multidimensional image analysis reveals a role for Abl in embryonic wound repair. *Development* 141, 2901–2911. doi: 10.1242/dev.106898

Conflict of Interest: The authors declare that the research was conducted in the absence of any commercial or financial relationships that could be construed as a potential conflict of interest.

frontiers in Bioengineering and Biotechnology

REVIEW
published: 31 July 2020
doi: 10.3389/fbioe.2020.00725

Human Microphysiological Models of Intestinal Tissue and Gut Microbiome

Steven N. Steinway[1], Jad Saleh[2], Bon-Kyoung Koo[3], Delphine Delacour[2†] and Deok-Ho Kim[1,4*†]*

[1] Department of Medicine, Johns Hopkins University School of Medicine, Baltimore, MD, United States, [2] Cell Adhesion and Mechanics, Institut Jacques Monod, CNRS UMR 7592, Paris Diderot University, Paris, France, [3] Institute of Molecular Biotechnology, Austrian Academy of Sciences (IMBA), Vienna Biocenter (VBC), Vienna, Austria, [4] Department of Biomedical Engineering, Johns Hopkins University School of Medicine, Baltimore, MD, United States

The gastrointestinal (GI) tract is a complex system responsible for nutrient absorption, digestion, secretion, and elimination of waste products that also hosts immune surveillance, the intestinal microbiome, and interfaces with the nervous system. Traditional *in vitro* systems cannot harness the architectural and functional complexity of the GI tract. Recent advances in organoid engineering, microfluidic organs-on-a-chip technology, and microfabrication allows us to create better *in vitro* models of human organs/tissues. These micro-physiological systems could integrate the numerous cell types involved in GI development and physiology, including intestinal epithelium, endothelium (vascular), nerve cells, immune cells, and their interplay/cooperativity with the microbiome. In this review, we report recent progress in developing micro-physiological models of the GI systems. We also discuss how these models could be used to study normal intestinal physiology such as nutrient absorption, digestion, and secretion as well as GI infection, inflammation, cancer, and metabolism.

Keywords: microphysiological model, gut-on-a-chip, organ chip, microbiome, intestinal tissue, organoid, microfluidics

OPEN ACCESS

Edited by:
María García-Díaz, Institute for Bioengineering of Catalonia (IBEC), Spain

Reviewed by:
Murat Cirit, Javelin Biotech, Inc., United States
Sasan Jalili-Firoozinezhad, Koch Institute for Integrative Cancer Research at MIT, United States

****Correspondence:***
Delphine Delacour
delacour.delphine@gmail.com
Deok-Ho Kim
dhkim@jhu.edu

† These authors share senior authorship

Specialty section:
This article was submitted to Tissue Engineering and Regenerative Medicine, a section of the journal Frontiers in Bioengineering and Biotechnology

Received: *25 February 2020*
Accepted: *09 June 2020*
Published: *31 July 2020*

Citation:
Steinway SN, Saleh J, Koo B-K, Delacour D and Kim D-H (2020) Human Microphysiological Models of Intestinal Tissue and Gut Microbiome. Front. Bioeng. Biotechnol. 8:725. doi: 10.3389/fbioe.2020.00725

INTRODUCTION

The human gastrointestinal (GI) tract is the site of ingestion and digestion of nutrients, nutrient absorption, secretory function, and elimination of waste product (Trowers and Tischler, 2014). The GI tract is a tubular structure which is composed of three main compartments: a muscular layer surrounding a mucous membrane and a lumen.

The GI tract is divided into four layers: the mucosa (epithelium, lamina propria, and muscular mucosae), the submucosa, the muscularis propria (inner circular muscle layer, intermuscular space, and outer longitudinal muscle layer), and the serosa (Jaladanki and Wang, 2011). An intrinsic nervous system called the enteric nervous system (ENS) helps regulate the muscular compartment and epithelial cells. The ENS is a dense network of neurons present throughout the GI. However, its composition, neuronal density and morphology varies according to the digestive segment. Together with the muscular layers, it regulates intestinal motility, peristalsis, which is responsible for migration of the food bolus along the digestive tract. Moreover, they provide a mechanical basis for the establishment of the mucosal architecture *per se* during development. In fact, Shyer et al. (2013) showed that, in addition to the endodermal signaling, smooth muscle differentiation is required for intestinal tissue shaping and villus formation (Walton et al., 2016). Further, there is growing evidence that gut microbiota contribute to gut motility (Quigley, 2011). Moreover, the ENS is part of the "gut-brain axis" and, because of its autonomous property, is nowadays considered a "second brain" (Cryan and Dinan, 2012; Mayer et al., 2015; Martin et al., 2018).

The mucous membrane is composed of a muscularis mucosae, a columnar epithelial monolayer and a mucus gel. This general structure is maintained throughout the GI tract, and most structural variations occur in the mucosal layer. For example, the stomach is made of a secretory mucosa for digestion, whereas crypt-villus subunits exist in the small intestine for absorption and secretion (**Figure 1**). In comparison to other epithelia, the epithelial monolayer lining the small intestine has a simple and regular architecture, where proliferative and differentiated cells are distributed in distinct areas (**Figure 1B**). It is characterized by its organization into finger-like tissue shapes protruding into the intestinal lumen and so-called villi, which are surrounded by tissue invaginations called crypts, which house the intestinal stem cell niche (**Figure 1B**). The epithelium of the small intestine turns over every 5 days in mice and constitutes the most rapidly regenerating tissue of adult mammals. Cell production starts at the crypt base, producing numerous progenies, which move up the crypt-villus axis. Intestinal stem cells are clustered at the bottom of the crypts, and cells moving up the crypt continue proliferating while in parallel becoming committed either to an absorptive (enterocytic) or a secretory fate (mainly goblet cells, Paneth cells, and enteroendocrine cells). Cells stop proliferating and differentiate while approaching the crypt-villus junction (**Figure 1B**). Upon reaching the villus tip a few day later cells are shed into the lumen of the intestine. Transit amplifying cells emanate from the bottom of the crypts. At the most apical part of the crypt, cells stop to divide and the epithelial sheet undergoes fine polarization and specific organization while progressing on the villus, called terminal differentiation, with the formation of a structural and functional additional feature at the apex, a brush border of microvilli, which increases the plasma membrane surface at the apex and thus enhances cell absorption at the interface of the gut lumen and epithelium (Barker, 2014; Delacour et al., 2016).

The epithelial layer of the GI tract is subjected daily to aggression from external elements present in the diet and the external world, and its erosion must be compensated by secretions from the mucosa to guarantee the integrity of the barrier, the first line of defense against external aggression. It is therefore coated with a lubricating protective barrier, the mucus gel, a viscoelastic gel which provides a physical barrier between the underlying luminal surface of the epithelial layer and microorganisms, the toxins they produce and other potentially harmful substances present in the intestinal lumen. Mucus gel is produced by goblet cells, which are disseminated between enterocytes in the upper two-thirds of the crypts but also along the villi. Reaching 15% of the total population of the duodenal epithelium, the proportion of goblet cells gradually increases to 40% in the distal colon (Wang et al., 2019a). Secretory granules produced by goblet cells contain the mucins, the main structural component of the mucus gel. MUC1, MUC2, MUC3, MUC4, and MUC5AC are the mostly expressed mucins in humans at the GI level, MUC2 being the main component of the intestinal mucus gel (Hollingsworth and Swanson, 2004; Okumura and Takeda, 2018). Mucins are responsible for its viscoelastic and gelling properties and display the common characteristics of being high molecular weight glycoproteins (up to 30,000 kDa) where carbohydrate chains represent up to 80% of the weight of the mucin (Pinho and Reis, 2015). This high glycosylation state gives mucins high density and viscosity properties. In addition

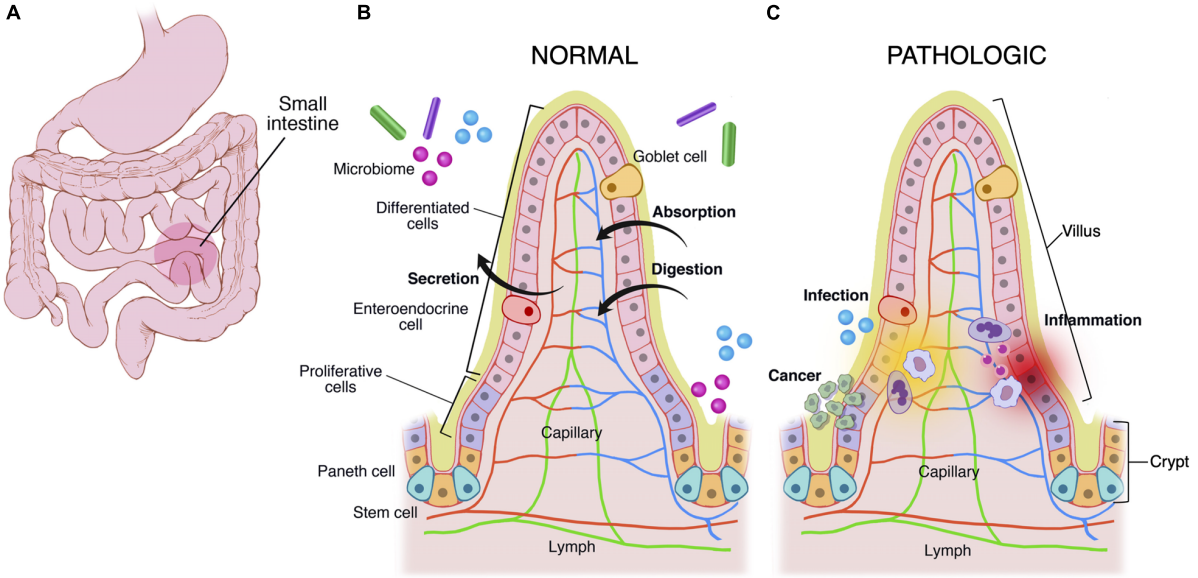

FIGURE 1 | Multiscale physiological features of small intestine of the gastrointestinal tract. The GI tract **(A)** grossly consists of the esophagus, stomach, small intestine, large intestine, and rectum. The small intestine is made of crypts and villi **(B,C)**. Crypts are home to the LGR5+ intestinal stem cell, which differentiates into paneth cells, enteroendocrine, goblet cells, and enterocytes. As cells differentiate they migrate up the villus. These cells are covered in a mucus layer and the microbiome, which are all involved in normal homeostatic functions of immune regulation, secretion, absorption, and digestion. **(C)** Infection, cancer, and inflammatory processes disrupt the gastrointestinal homeostasis.

to its physical and chemical protective function, the mucus gel is in symbiosis with the endogenous bacterial flora. It offers many benefits to bacteria in the intestinal lumen since mucins can provide a direct source of nutrients for bacterial growth, and the gel structure facilitates the colonization of the intestine by bacteria, which can survive and multiply (Sicard et al., 2017; He et al., 2018).

The GI tract is also a major site of immune surveillance and its lumen is inhabited by a microbial community called the gut microbiome (**Figure 1C**) (Round and Mazmanian, 2009; Garrett et al., 2010), which plays an important role in normal intestinal function and has been implicated in numerous intestinal diseases including inflammatory bowel disease, gastrointestinal malignancy, and celiac disease (Clemente et al., 2012; Lloyd-Price et al., 2016). Additionally there exist stroma, immune cells (e.g., Peyer's patches in small intestine, macrophages, and neutrophils), and an endothelium/blood supply (Drake et al., 2010). The immune system monitors for and suppresses pathologic gastrointestinal infections, and at times it acts aberrantly, leading to diseases like inflammatory bowel disease and celiac disease (**Figure 1C**).

In vivo and *in vitro* models of gastrointestinal function are important tools as they allow many experiments that are unfeasible and unethical to do in humans. *In vivo* studies on animal models such as mice or pigs have been extensively used to understand the normal and pathological development of the intestinal organ. However, they have been largely restricted due to ethical and financial problems, weak reproducibility, variability of individuals and the difficulty to isolate the influence of one given factor. Moreover, as the animal physiology differs from human physiology, animal models only reflect a few aspects of human diseases. As another option, *in vitro* 2D cell culture models, such as those using Caco-2, T84 cell or HT29 lines, are frequently used to study the GI tract, including nutrient transport, intestinal absorption, cell differentiation and human diseases including carcinogenesis (Hilgers et al., 1990; Nataro et al., 1996; Delacour et al., 2003). However, the use of established cell lines intrinsically displays several major drawbacks. They only contain the enterocytic cell type and do not allow functional analyses representative of the entire intestinal epithelium. Moreover, established intestinal epithelial cell lines such as Caco-2 cells are of cancer origin and harbor multiple gene mutations, which could incur problems in genome fidelity and personalized medicine approach (Kasendra et al., 2018). For all those reasons, development of alternate intestinal *in vitro* models is crucial for the progression of the gastroenterology field of research.

INTESTINAL ORGANOIDS AND THEIR LIMITATIONS

In 2009, Hans Clevers's work revolutionized the intestinal bioengineering field with the generation of a mouse intestinal organoid *in vitro* model system called "mini-gut" or "enteroid" (Sato et al., 2009), which was then followed by the establishment of a human version either from human adult stem cells (AdSC) or pluripotent stem cells (PSC) (Spence et al., 2011). Since then, organoids have become a very attractive tool for researchers to study intestinal morphogenesis (Sumigray et al., 2018) and homeostasis maintenance in such a dynamic tissue due to their physiological relevance compared to classical 2D cultures of immortalized cell lines. In fact, classical 2D cultures of established cell lines do not allow adequate studies on epithelial organ morphogenesis. Since *in vivo* epithelial cells organize into 2D monolayers experiencing various out-of-plane curvature and 3D geometries, it is essential to study the intestinal epithelium in a topography that is physiologically relevant. Over a decade ago cystogenesis in 3D Matrigel matrix emerged as a key experimental tool to study epithelial morphogenesis *in vitro* for cell line-based cultures. This system brought remarkable progress in the understanding of the sequential events of epithelial arrangement and lumen generation during the development of spherical structures such as tubules or acini (O'Brien et al., 2002). It has been useful in the understanding of different human pathologies based on spherical or tubular formation defects, such as polycystic kidney disease. Nevertheless, this 3D culture system is not appropriate to study epithelial layer maintenance in non-spherical or non-tubular shaped organs, such as along the architecture of the intestinal mucosa. More importantly, it only gives access to the dynamics of a single differentiated cell type during morphogenetic processes, and does not recapitulate the coordinated evolution of various stem and differentiated cell types that takes place in the native intestinal tissue. Initially generated from isolated crypts, intestinal organoids are three-dimensional *in vitro* systems, which house the intestinal stem cell niche. They are essentially "mini-organs" that retain most physiological conditions such as the spatial organization of cells, cell-cell interactions, and cell-matrix interactions (Yin et al., 2016). Organoid culture allows for monitoring of how intestinal tissues develop and maintain homeostasis through different conditions using live-imaging techniques such as two-photon or spinning disk microscopy.

With the identification of Lgr5-positive-intestinal stem cells (LGR5+ ISC) and the understanding of the signals controlling ISC behavior in the mouse, Sato et al. (2009, 2011b) were successful in developing *in vitro* murine intestinal organoids, representing a powerful breakthrough in the intestinal research field. Intestinal organoids can be derived from either a single LGR5+ stem cell or from transplanted intestinal crypts by embedding them in Matrigel, a 3D substrate that mimics the complex extracellular environment found in many tissues and is composed of ECM components such as laminin, Collagen IV, entactin, and heparin sulfate proteoglycans. The formation and maintenance of intestinal organoids inside the Matrigel is supported by the addition of a medium containing epidermal growth factor (EGF), R-Spondin-1, and Noggin, which are important to stimulate proliferation and maintenance of stem cells while blocking differentiation. A transplanted crypt in these conditions will close after a few hours to form a spheroid, which then starts budding to develop into a mature organoid with distinct crypt-like structures as seen *in vivo* (**Figure 2A**). These crypt-like budding structures include LGR5+ stem cells and Paneth cells, whereas in the main body of organoids contains

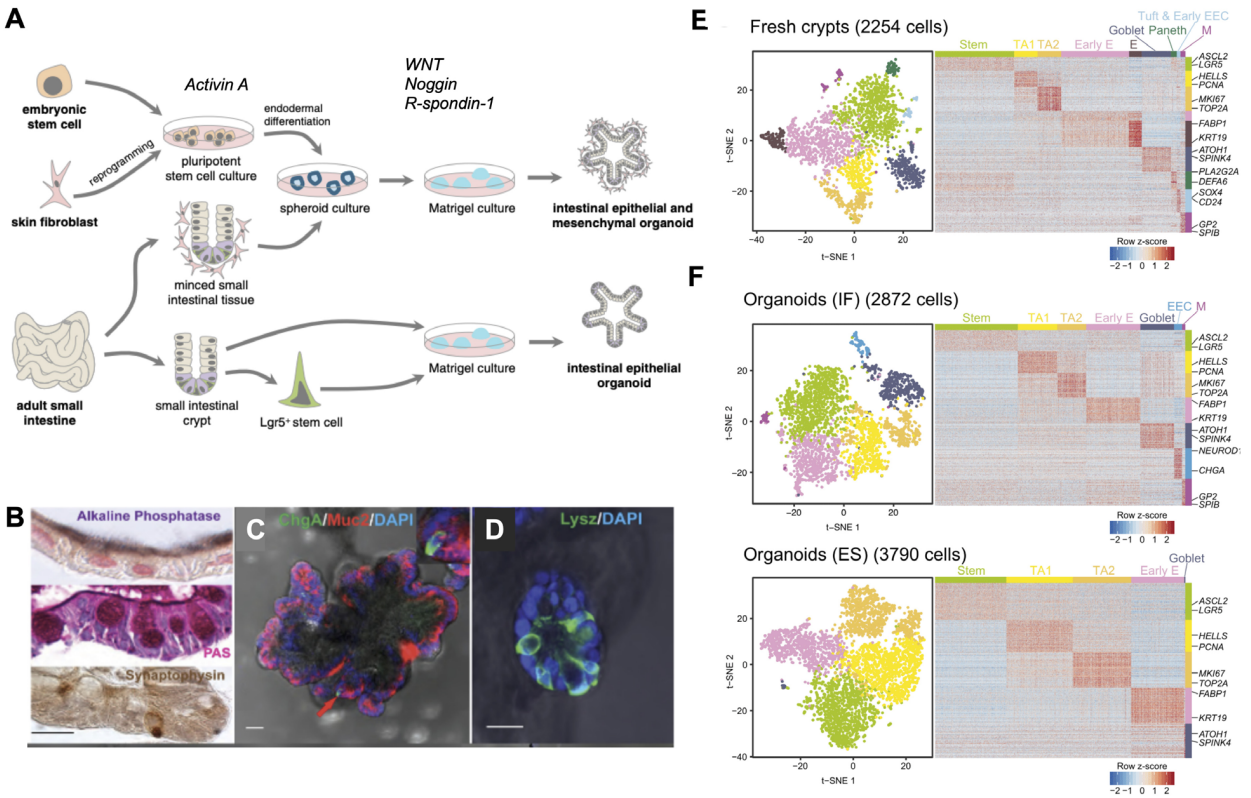

FIGURE 2 | State-of-the-art in intestinal organoids. **(A)** Organoids can be derived from either embryonic stem cells or induced pluripotent stem cells (iPSC) from reprogrammed differentiated cells. iPSCs grown in the presence of Activin A undergo endodermal development and in the presence of niche factors Noggin, EGF, and R-spondin-1, form intestinal organoids containing both epithelial and mesenchymal cell types. Small intestinal tissue samples can be directly cultured as spheroids to produce organoids or LGR5+ stem cells can be isolated from these tissues to produce epithelial organoids when grown in the presence of niche factors. **(B)** Alkaline phosphatase staining for mature enterocytes, periodic acid-Schiff (PAS) staining for goblet cells, synaptophysin staining for enteroendocrine cells. **(C)** Human intestinal organoids expressing Mucin 2 (red) a marker of goblet cells, chromogranin A (green) a marker of enteroendocrine cells, **(D)** lysozyme (green) a marker of Paneth cells. **(E)** Single cell RNA sequencing demonstrates cell types in conserved in fresh human ileal crypts and in **(F)** intestinal organoids cultured under two different conditions, standard organoids cultured with two different culturing conditions: traditional culture conditions (bottom panel) compared to a new set of culture conditions (IGF-1 and FGF-2). Scale bar demonstrates statistical association (*z*-score) of specific genes with specific cell types listed.

differentiated cells forming the villus-like areas (**Figure 1**). Other cell types including goblet cells, enterocytes, and enteroendocrine cells (Sato et al., 2009; Kretzschmar and Clevers, 2016) can be identified by immunohistochemistry (**Figures 2B–D**) and more recently by single cell RNA sequencing (**Figures 2E,F**) (Grün et al., 2015). Moreover, addition of Wnt3A to the combination of growth factors allowed indefinite growth of mouse colon organoids and addition of nicotinamide, along with an inhibitor of Alk and an inhibitor of p38 is required for long-term culture of human small intestine and colon organoids (Jung et al., 2011; Sato et al., 2011a). Recently, a p38 inhibitor was found to impair proper cellular differentiation in human gut organoids. An effort has been made to identify IGF-1 and FGF-2 as growth factors that can improve human intestinal organoid plating, recovery, self-renewal and differentiation capacity (Fujii et al., 2018).

Alternatively, it is also possible to develop human intestinal organoids using induced pluripotent stem cells (iPSCs) (Spence et al., 2011). Pioneered by S. Yamanaka in 2006, the introduction of defined transcription factors allow the reprogramming of differentiated adult cells from any tissue such as skin or blood pluripotent cells to immature pluripotent cells that have regained the capacity to differentiate into any type of cell in the body (Takahashi and Yamanaka, 2006; Takahashi et al., 2007). In the context of personalized medicine, iPSCs are very useful for constituting patient biobanks and specific therapeutic strategies without any rejection due to immune response (Takahashi and Yamanaka, 2013; Scudellari, 2016). For intestinal engineering, primary cells can be differentiated into endodermal cells in 2D cultures. Then the formation of a gut tube is provoked thanks to Wnt3 or FGF treatment, and gut tubes are transposed in 3D ECM matrix with culture medium complemented with notable EGF, Noggin and R-Spondin-1 factors. In comparison to the classical mini-guts, this alternate organoid culture system develops crypts but also villus-like structures and presents the advantage of an epithelial-mesenchyme co-culture (Wells and Spence, 2014). This human PSC-derived gut organoid often showed immature fetal organoid features that require further maturation *in vitro*. A cytokine-based maturation protocol has been introduced as a step for full maturation of human PSC-derived gut organoids (Jung et al., 2018).

Intestinal organoids have been shown to recapitulate normal intestinal physiology including ion, water, and nutrient absorption/secretion and have been used to model pathophysiologic processes, including intestinal infection and cancer. Importantly, organoids created from primary patient samples can be frozen and banked. These cryopreserved samples can be repeatedly thawed and grown, providing as sample source of human materials. Thus, organoids are a complementary model to cell lines and xenograft models, and very useful in the case of rare patient samples or personalized medicine (Van De Wetering et al., 2015). Because organoids are readily established from individual patient samples, they can be used for personalized medicine studies such as studying particular human mutations or individualized responses to drug treatments (Van De Wetering et al., 2015; Fatehullah et al., 2016; Yin et al., 2016). The versatility of intestinal organoids further allows the application of various biological methods of genetic modification to be performed on intestinal organoids in both mouse and human tissue using different tools such as siRNA, CRISPR/Cas9 editing, lentiviral infection, and inducible systems that incorporate both lentiviral infection and the efficiency of the CRISPR/Cas9 tool, to produce normal and pathological phenotypes with fluorescent markers (Koo et al., 2012; Schwank et al., 2013a,b; De Van Lidth Jeude et al., 2015; Drost et al., 2015; Fujii et al., 2015; Andersson-Rolf et al., 2016, 2017; Broutier et al., 2016; Driehuis and Clevers, 2017). These genetically modified organoids are used in fundamental biology to understand the role of certain proteins in maintaining the proper function and performance of the intestinal tissue. They are also widely used to model diseases such as the rare enteropathy microvillous-inclusion disease (MVID) (Mosa et al., 2018) or colorectal cancer (Drost et al., 2015; Matano et al., 2015). For proper gene-editing of intestinal organoids, researchers have described several protocols with some variations (Miyoshi and Stappenbeck, 2013; Andersson-Rolf et al., 2014; Fujii et al., 2015; Merenda et al., 2017; Fujii et al., 2018).

There are many advantages to organoids as stated above but still many limitations exist, such as (i) ethical aspects of the use of live human derivatives, (ii) the lack of repeatability and quality control of the variability of individual samples collected or used, (iii) the difficulty of isolating the influence of a particular factor in a complex environment. In addition, these culture systems do not consider the fact that cells have to integrate numerous factors of the microenvironment: (i) geometrical: topographical variations of the substrate, (ii) mechanical: substrate rigidity, and (iii) chemical: extracellular matrix proteins, morphogens, molecule diffusion. Importantly, while being appropriate for crypt morphogenesis and dynamics studies, AdSC-derived human intestinal organoids do not form villi *per se* in culture. PSC-derived human intestinal organoids do form villus-like structures but only contain a restricted differentiated compartment, and they have been recently reported to be immature and to actually be much closer to fetal villi. These two culture systems then cannot be used for correct villus epithelium organization analyses. In addition, they have very irregular shapes that can greatly vary from one organoid to another, which can be attributed to the lack of the underlying mesenchymal cells and basement membrane that is replaced with a soft Matrigel *in vitro*. Moreover, they only represent the epithelial layer of the GI tract and they lack other important constituents including immune, stromal, muscular, endothelial/vascular, and microbiome components, which are important for normal intestinal function and which have known roles in various diseases. Organoid models also do not incorporate mechanical motion (peristalsis) and fluid flows that are a part of the normal intestinal function. In addition, they form a closed lumen and the apical aspect of the lumen faces the interior of the organoid. Thus it is difficult to access the luminal component of the cells to study the mucus layer or to evaluate the effect of drugs, toxins, microbes, and other stimuli in these systems (Bein et al., 2018). In this context, microinjection techniques have been used with limited success since the procedure provokes damages to the organoid structure (Bartfeld et al., 2015; Forbester et al., 2015; Wilson et al., 2015; Heo et al., 2018; Williamson et al., 2018).

In summary, though holding great advantages compared to classical 2D cultures, intestinal organoids on their own cannot recapitulate every architectural and physiological aspects of the intestinal tissue. In addition, the need of new intestinal culture systems where one could precisely control as much as possible various physical and chemical parameters has emerged. Thus, the current trend in the field is to use the unique properties of the organoids and to adapt/combine them to material engineering techniques. Development of *in vitro* models of the intestine that recapitulates the structural, absorptive, mechanical, microbial, physiologic, and pathophysiological properties of the human gut could accelerate pharmaceutical development and potentially replace animal testing. This has been the driving force behind biomimetic intestinal engineering and microfluidic "gut on a chip" model development.

IMPORTANCE OF BIOPHYSICAL AND BIOCHEMICAL CUES IN DESIGNING *IN VITRO* INTESTINAL MODELS

A major challenge in the field remains to adapt synthetic surfaces to organoid primary cultures. Developed over the last decade, microfabrication techniques allowed the development of synthetic substrates with controlled chemistry and defined geometries at the micron scale, that can be used in cell culture systems (Le Digabel et al., 2010). Such approaches are now used to mimic biochemical and biophysical cellular environments and investigate intestinal epithelial morphogenesis *in vitro* in more physiological conditions. Widely used for culturing established cell lines, they offer the advantage of effectively breaking down cell behaviors in relation to specific and known conditions such as concentrations of adhesion molecules, tissue stiffness or geometric dimensions. However, adapting organoid primary cultures on such microfabricated surfaces is a way more difficult than culturing cancer cell lines, and thus requires a strong knowledge of the intestinal tissue to develop appropriate microfabricated surfaces. This challenge is currently taken up by combining biochemistry and

biomaterials to capsulize the heterogenous properties of the cellular intestinal environment.

Mimetism of the Intestinal Tissue Biochemistry

A difficult task in intestinal tissue engineering is to imitate the underlying lamina propria or extracellular matrix (ECM) which provides a biochemical support for cells within the intestinal tissue. The ECM is composed of the basement membrane, a very dense matrix mainly composed of collagen type IV, laminin and fibronectin, and the interstitial matrix, which constitutes a loose and porous fibrous scaffold constituted of collagens, elastin and fibronectin (Kular et al., 2014; Chen and Liu, 2016). The basement membrane exhibits direct interactions with cellular ECM receptors such as integrins in epithelial cells, influencing cell adhesion, cell growth, migration, gene expression, morphology and differentiation (Rozario and DeSimone, 2010). Indeed, abolishing the contacts between intestinal epithelium with the ECM often impinges on tissue integrity and homeostasis. For instance, the deletion of the integrin alpha-6, an ECM receptor, provokes defects in the epithelial barrier, as well as prolapse formation and colitis-associated adenocarcinoma development in mice (De Arcangelis et al., 2017). Moreover, conditional depletion of laminin gamma-1 in mouse leads to crypt hyperplasia and epithelium detachment along the villus (Fields et al., 2019).

It is important to mention that the ECM composition and architecture differ according to the tissue, and, within the intestinal tissue, additional spatio-temporal heterogeneities occur (Kedinger et al., 2000). Each intestinal segment exhibits a distinct ECM component mixture. For instance, an increasing gradient of collagen-VII has been reported along the antero-posterior axis of the gut (Leivo et al., 1996). Furthermore, differential deposition of ECM component isoforms takes place along the crypt-villus axis: as an example, laminin-1 and -2 being enriched at the level of crypts, whereas laminin-3 and -5 are prominent in villi (Simon-Assmann et al., 1995; Leivo et al., 1996; Simon-Assmann et al., 1998; Teller et al., 2007; Fields et al., 2019). In addition, gene expression of ECM proteins also varies during the gut development (Simon-Assmann et al., 1995). Whereas laminin-1 is downregulated after birth, laminin-3 expression increases at late embryonic and postnatal stages (Teller et al., 2007). It is worth mentioning that ECM composition is frequently altered in intestinal diseases. It is well described that abnormal ECM remodeling contributes to the progression of the inflammatory bowel disease (IBD) and Crohn's disease (Petrey and De La Motte, 2017). In the case of the congenital tufting enteropathy (CTE), a rare intestinal disease, patient duodenal biopsies display defects of laminin deposition in the basement membrane, which, at least in part, participates to the formation of characteristic epithelial tissue lesions in villi (Goulet et al., 1995; Righini-Grunder et al., 2017). Moreover, the composition, density and integrity of ECM components evolve concomitantly with tumor development and dynamics (Frantz et al., 2010). As an example, increase of collagen-X and alpha-3 chain of collagen-VI takes place in the development of colorectal cancers, making these ECM components potential diagnostic markers (Solé et al., 2014; Qiao et al., 2015). Thus, the choice of the appropriate ECM composition remains a crucial point in the biomimetic approach.

To recapitulate the intestinal native ECM, two approaches can be followed: either using natural ECM matrices or to produce synthetic ones. Natural ECM matrices can be produced upon cell removal from the native intestinal tissue. In fact, decellularized small intestinal submucosa samples from rat or pig has been used in the context of tissue repair or regeneration (Hodde, 2002; Andrée et al., 2013). This source of natural ECM scaffold has been tested for intestinal biomimetic cultures for *in vitro* fundamental research. Protocols have been adapted to generate from animal models or human samples decellularized intestinal tissue that keep crypt-villus structures (Totonelli et al., 2012; Giuffrida et al., 2019), and combination of such natural ECM scaffolds with intestinal organoid cultures allows the generation of a differentiated intestinal model *in vitro* (Finkbeiner et al., 2015).

In order to get closer to the tissue environment, natural biomaterials are used in microfabrication, though they are costly and control of their physical properties cannot be performed. For instance, collagen-based scaffolds give the possibility of more physiological culture systems since it is an intrinsic extracellular matrix (ECM) component and the 3D architecture of the collagen meshwork is close to the *in vivo* context (Millet et al., 2019). However, more complex ECM-based hydrogels can be used. In 1977, R. Orkin pioneered the field with the production of a basement membrane gel from Engelbreth-Holm-Swarm (EHS) chondrosarcoma mouse tumors (Orkin et al., 1977; Kleinman and Martin, 2005). Now known as Matrigel, this hydrogel is constituted of a cocktail of laminin, collagen IV, entactin, heparan sulfate proteoglycans and growth factors such as TGFbeta and FGF. More recently, Giobbe et al. (2019) proposed the preparation of ECM-derived hydrogels from decellularized intestinal submucosa which allows organoid cultures.

Another approach consists in the use of synthetic hydrogel scaffolds Generated as physical support structures, they can be modified by modulating surface biochemistry with addition of ECM components and will mimic, at least to some extent, the biological function of the ECM (Kular et al., 2014). Among the synthetic biomaterials, PEG hydrogels have been extensively used as scaffolds in tissue engineering. PEG is a non-adhesive material, so it constitutes an excellent base for bioactive modifications and selective incorporation of identified bio-functional oligopeptide sequences corresponding to proteins of the ECM whose concentration and spatial distribution can be easily modulated to provide fundamental insight of signaling events involved in specific cell-matrix interactions and repercussion on epithelial organization. Thus, the interaction between cell surface receptors and specific ligands of the ECM are replaced through the chemical attachment of peptides to the hydrogel scaffold. Synthetic peptides are able to bind to cell surface receptors and mediate cell adhesion with high affinity and specificity similar to that observed with intact proteins. Peptides are generally preferable to intact proteins as they are not subject to denaturation and may be less susceptible to proteolysis. The most extensively used peptide is the sequence Arg-Gly-Asp (RGD), which is found in many cell adhesion proteins

and binds to integrin receptors (Rozario and DeSimone, 2010; Leijten et al., 2017).

Furthermore, the ECM network stores and sequesters active molecules essential for tissue development and homeostasis (Frantz et al., 2010; Rozario and DeSimone, 2010). A growing body of literature has demonstrated that the spatial patterning of cellular behaviors, such as proliferation and differentiation, is important during tissue development. Control of intestinal cell fate and differentiation have been long shown to be triggered by downstream signaling pathways and morphogens in the crypt-villus axis (Sancho et al., 2004; Nelson et al., 2005; Crosnier et al., 2006). Morphogens are long-range signaling molecules such as growth factors and cytokines that can pattern developing tissues by inducing distinct cellular responses in a concentration-dependent manner. Their graded activity within tissues exposes cells to different signal levels and leads to region-specific transcriptional responses and cell fates. Responding cells often transduce morphogen levels in a linear fashion, which results in the graded activation of transcriptional effectors. The spatial distribution of Wingless/Int (Wnt), Hedgehog (Hh) and bone morphogenetic protein (BMP) has been longstanding reported to direct the organized formation of the intestinal unit (Sancho et al., 2004; Crosnier et al., 2006; Williamson et al., 2018). In tissue engineering, studies report the immobilization of growth factors in hydrogel biomaterials include EGF, bFGF, VEGF, NGF, TGF-beta, either by grafting on PEG framework or by alginate encapsulation and incorporation in the hydrogel scaffolds (Rozario and DeSimone, 2010; Leijten et al., 2017). More recently, Wang et al. (2017b) mimic the effect of the morphogen gradient taking place in the intestinal unit by culturing organoid-based biomimetic 3D substrates on Transwell filters and adding distinct culture media (either enriched in Wnt3a, R-Spondin and Noggin to maintain the stem cell niche, or in DAPT to stimulate epithelial differentiation) in the lower or upper insert compartments, respectively.

Mimetism of the Intestinal Tissue Stiffness

Besides chemistry, rigidity is another essential property of the ECM microenvironment controlling cell behavior. Cells interact with the environment through cell-substrate adhesions and sense the mechanical status of the ECM. Through the mechanotransduction process, cells can thus adapt in response to the physical properties of the tissue and modulate its organization and homeostasis (Iskratsch et al., 2014). For example, matrix rigidity regulates cell differentiation program. Soft matrices favor the differentiation of mesenchymal cells toward the neurogenic pathway, whereas stiff matrices orient toward the osteogenic pathway (Engler et al., 2006). According to the tissue, stiffness varies in a range from 100 Pa (brain) up to 1 GPa (bone). Recent analyses have determined the stiffnesses of the global human ileum and colon at 0.6 and 1 kPa, respectively (Stewart et al., 2018). However, precise stiffness measurements along the crypt-villus axis, the functional unit of the intestinal epithelium, remain to be performed.

In fact, the intestinal ECM should not be seen as a frozen structure, but rather as a dynamic network. Its stiffness is modulated by its composition and fiber density, the activation of myofibroblasts and their ability to contract ECM fibers, as well as the pathological state of the tissue (Tomasek et al., 2002). In inflammatory bowel disease (IBD) or Crohn's disease, the increase of ECM density provokes intestinal fibrosis and subsequently exacerbated ECM stiffness (Latella and Rieder, 2017; Stewart et al., 2018). In addition, during tumor development, the modification of the ECM participates in tumor growth, cancer stem cell modulation, propagation and extravasation (Kaushik et al., 2019). This process is enhanced by the additional enzymatic ECM remodeling by matrix metalloproteinases (MMPs). For instance, increase of MMP-9 expression and activity takes place in colorectal cancers, where it notably cleaves collagen-I fibers of the ECM (Biasi et al., 2012). In classical microfabrication approaches, the polydimethyl siloxane (PDMS) has been extensively used since it is cheap, easy to use and biocompatible. However, the PDMS material exhibits a stiffness (2 MPa) close to the bone tissue or glass material, making this material a poor candidate for the mimicry of the intestinal tissue stiffness (Barnes et al., 2017). Material replacement with hydrogels has made possible to tune culture device rigidity. For instance, it has been demonstrated that culture of Caco2-cells on PEG replicates improves their columnar organization and differentiation (Sung et al., 2011; Creff et al., 2019). To mimic *in vivo* ECM remodeling, Gjorevski et al. (2016); Blondel and Lutolf (2019), and Brassard and Lutolf (2019) pioneered the field by fine-tuning a enzymatically controlled modulation of PEG hydrogel rigidity. By culturing intestinal organoids in such dynamic matrices, they could show that a soft matrix favors intestinal differentiation. In sharp contrast, a stiff matrix promotes intestinal stem cells proliferation and organoid expansion. Thereby demonstrating that mechanical state of the ECM directly impinges on the intestinal tissue behavior.

Mimetism of Intestinal Tissue Geometry

In recent years, accumulating experimental evidence have led to recognition that topological tissue properties have the power of directing a variety of cell functions including cell migration, proliferation and differentiation (Nelson et al., 2006; Baptista et al., 2019; Hannezo and Heisenberg, 2019). However, to date few studies concern the intestinal epithelium. Wang et al. (2017b) have shown that when grown on 3D culture devices recapitulating the crypt-villus axis, intestinal stem cells preferentially colonize crypt-like shapes when placed under morphogen gradient. However, recent studies showed that organoid suspensions self-organize and spontaneously generate crypt-like domains in 2D cultures, without any geometrical clues (Thorne et al., 2018; Altay et al., 2019). Therefore, demonstration of the importance of crypt-villus geometry in intestinal tissue development and homeostasis remains to be provided.

Nevertheless, mimetism of the intestinal tissue geometry represents an active field of bioengineering research. Natural ECM-based 3D scaffolds can be directly produced from decellularized porcine intestinal tissue preparation where crypt-villus structures can be kept with adapted protocols. This system is suitable for further intestinal organoid suspension cultures (Maghsoudlou et al., 2013; Finkbeiner et al., 2015). Although this approach has been used in the clinic for

intestinal tissue repair (Andrée et al., 2013; Hoeppner, 2013), decellularized intestinal matrix may constitute a poor mechanical support for long-term cultures. In addition, its intrinsic heterogeneity weakens the expected reproducibility properties in bio-engineering experiments. In microfabrication approaches, topographical features that mimic tissue architecture are usually made by photolithography and soft lithography (Le Digabel et al., 2010; Qin et al., 2010; Xi et al., 2019). Shapes are usually obtained through the generation of wafers by photolithography, i.e., by polymerization of a photoresist or photosensitive material exposed to UV light through a patterned mask. Pattern refinement is obtained using deep reactive ion etching (DRIE) and tapered using the surface technology system inductive coupled plasma (STS-ICP) silicon etcher and oxide deposition (Tezcan et al., 2006; Dixit et al., 2012). Recently, spatial resolution of culture devices has been improved with the laser writing technique of 2-photon lithography with which 3D microstructures below 100 nm can be generated (Accardo et al., 2017; Lemma et al., 2019). Direct molding of 3D scaffolds can be performed by soft lithography using elastomers such as the PDMS. Alternatively, PDMS scaffolds can be used as molds for further 3D hydrogel scaffolds production. PDMS has many favorable properties for development of tissue/organ chips, including its optical clarity, and permeability. However, it is well-known to absorb small hydrophobic drugs, which limits its use in drug discovery and development (Berthier et al., 2012). A microfluidic cell culture system was recently developed from a tetrafluoroethylene-propylene (FEPM) elastomer, which was shown not to absorb several hydrophobic compounds, while maintaining other favorable properties of PDMS, thus making it a potentially useful platform for drug discovery and development in the future (Sano et al., 2019). Moreover, PEG is a non-adhesive polymer and is highly resistant to protein adsorption and cell adhesion. PEG hydrogels are biocompatible and hydrophilic, and they have been extensively used as scaffolds in tissue engineering. Crosslinked PEG hydrogel networks swell extensively in aqueous environments providing a 3D highly swollen network with viscoelastic properties similar to soft tissues enabling diffusive transport and interstitial flow characteristics (Lutolf and Hubbell, 2005). In addition, natural compounds such as collagen nicely mimic the chemistry and the 3D organization of ECM layer, and collagen-based 3D replicates have been used to imitate the 3D architecture of the intestinal tissue. However, low-concentration collagen gel is difficult to mold in microfabrication, and increasing collagen concentration subsequently modifies stiffness and porosity properties of the mimetic matrix (Frantz et al., 2010). Such techniques allow to recreate the surface topography of intestinal crypt-villus axis and to obtain well-defined and well-controlled environments for cell culture. We and others performed the first assays on 3D PDMS scaffolds recapitulating the intestinal villus topology and constraints using the Caco2 cell line (Kim et al., 2014; Salomon et al., 2017). Further improvements have been made through the implementation of the crypt geometry and the replacement of cell lines with primary organoid cells (Wang et al., 2017a,b).

In summary, this section recapitulates the various main approaches which have been developed to imitate as much as possible of the intrinsic biochemical and biophysical properties of the intestinal tissue. A further step is to apply and control the distinct elements of the microenvironment on the biomimetic cultures.

MICROFLUIDIC "ORGAN-ON-A-CHIP" MODELS OF THE INTESTINE

Organ chips are microfluidic models of biological systems, in which cells are grown in thin chambers using techniques similar to microchip manufacturing. Incorporation of microfluidics allow accurate control of perfusion of these systems. Over the past several years these systems have evolved to incorporate various channel shapes, multiple intestinal cell types, including primary cells, the microbiome, immune and vascular channels and have thus overcome many of the limitations of previous *in vitro* models (i.e., 2D cell culture, organoids, microbiome metagenomics) (Bhatia and Ingber, 2014; Bein et al., 2018).

Microfluidic Set-Up

Microfluidic devices contain small channels that cells can be grown on. Chips have been developed with multiple channels divided by a thin membrane, such that multiple cell layers can be seeded in different channels. They are thin enough to perform high resolution imaging and simultaneously provide enough cells to do quantitative biological assays. A polymer called polydimethylsiloxane (PDMS) has frequently been used construct gut chips given it is gas-permeable and its clarity permits high-resolution imaging (Huh et al., 2013). Fluids and gasses can be precisely perfused into these systems to mimic fluid flow parameters of the GI system through chambers flanking the microchannels (Huh et al., 2013). Additionally drugs, toxins, nutrients, and growth factors can be precisely delivered to the apical cell surface, a no limitation of spheroid organoid systems (Vickerman et al., 2008).

Initially immortalized cell lines were used to seed intestinal chip models. These models have been used to evaluate drug absorption (Kimura et al., 2015; Pocock et al., 2017), nutrient absorption (Imura et al., 2009), and barrier function (Odijk et al., 2015). To better simulate the intestinal morphology, methods have been developed to form villous shaped channels, with some preliminary suggestion that this better mimics physiologic intestinal cell behavior (Shim et al., 2017; Wang et al., 2017b).

Intestine Chip Models

Chip based models of the intestine were initially constructed with immortalized intestinal cell lines (e.g., colon cancer cell lines like Caco-2) (Kim et al., 2014; Salomon et al., 2017). However, these cell lines are of GI tumor origin, display a high degree of protein expression dysregulation and thus do not properly represent normal epithelial physiology. In addition, these cell lines only recapitulate the main differentiated cell type of the intestine, the absorptive enterocytes, meaning that notably no stem cell compartment can be studied using these cells. The primary cultures of organoids partly overcome these difficulties. They are developed using the stem cell compartment itself, the intestinal

crypts, meaning they contain the intestinal stem cell niche, made of LGR5-positive cells, Paneth and transit-amplifying (TA) cells, and will be able to produce all differentiated cell types present in the intestinal epithelial layer, notably enterocytes, goblet, enteroendocrine, tuft, and Paneth cells. But, as mentioned earlier, their closed lumens do not give easy access to their luminal side for drug, chemical, toxin treatment, and the inability to incorporate other aspects of the physiologic microenvironment (e.g., differential fluid flow and pulsatile flow) as well as co-culture with microbes.

To solve these issues, several authors have enzymatically lysed organoids into single cells and seeded them in monolayers onto 2D substrates made of collagen or Matrigel (Wang et al., 2017a; Thorne et al., 2018). Some went further with the use of Transwell plates coated with collagen or Matrigel matrix where dissociated cells from organoids are seeded (Tong et al., 2018). These monolayers demonstrated apical-basal organization, gave access for chemical or viral treatment of either cell side differentially (Foulke-Abel et al., 2014; Ettayebi et al., 2016). Altogether, organoid monolayers offer the simplicity of 2D culture, which makes it easier for scientists to investigate due to the diverse tools available to study 2D monolayers compared to complex 3D structures. An elegant study from Thorne et al. (2018) recently showed that dissociated organoids do not randomly arrange on 2D substrates. Quite the opposite, primary intestinal cultures are capable of self-organization, *de novo* segregate undifferentiated and differentiated compartments, and even locally form niche-like compartments (Thorne et al., 2018).

Moreover, 2D organoid monolayer cultures have been instrumental in developing biomimetic systems adapted for mucus secretion analyses. Often underestimated in intestinal bioengineering strategies, the mucus gel layer coating the intestinal epithelial layer nonetheless provides a physical barrier but also a permissive environment for bacterial growth. Classical *in vitro* culture models that are commonly used to study intestinal physiology such as Caco-2 cell lines are not suitable to study the mucus secretion process in the intestinal epithelial layer, since they do not produce the typical intestinal MUC2 normally secreted by goblet cells. However, since classical organoids have an enclosed lumen, the mucus produced is entrapped and inaccessible for proper physiological study. Wang et al. (2019a) recently reported a method to implement a mucus layer on top of a 2D organoid monolayer model. Briefly, this technique, reminiscent of studies applied to the respiratory epithelium, is based on the fact that classical medium-based culture systems dilute the secreted mucus on top of the epithelial layer. Switching to an air-liquid interface culture principle, together with treatment with an intestinal hormone modulating water secretion on the luminal side, allowed the accumulation of a mucus layer above organoid monolayers. More recently, D Sontheimer-Phelps et al. (2020) developed an organoid-based human colon-on-a-chip microfluidic device with a high number of differentiated MUC2-producing goblet cells, which allows the formation of a mucus bilayer. They show the presence of a protective inner mucus layer that is impenetrable to bacteria, and an outer penetrable layer where commensal microbes can be found, with a thickness similar to *in vivo* (Gustafsson et al., 2012). Their system is able to support the differentiation of large numbers of mucus-producing goblet cells similar to levels *in vivo*, while maintaining proliferative cells to ensure long-term culture. These data are crucial to improve the physiological relevancy of 2D organoid monolayers in the context of bacteria interaction or immune response.

Nevertheless, the 2D organoid monolayer models still lack tissue topographical properties as well as many characteristics employable in chip-based models including growing multiple cell types (mesenchymal, vascular endothelial, immune), incorporation of microbial organisms, and pulsatile flow. Intestinal chip models incorporating primary cells have then been developed. For example, fragmented human enteroids were seeded into one chamber of a two-chamber microchip, with primary vascular endothelial cells from the same biopsy sample seeded into the second channel. With incorporation of pulsatile fluid flow, the authors claim that these cells undergo villous-like differentiation, although this is quite a preliminary suggestion based on morphology under confocal microscopy and there are not good controls (i.e., no comparison to *in vivo* villi or comparison to epithelial cells cultured in traditional cell culture). More detailed physiologic evaluation of these suggested villi is needed to determine whether they are in fact physiologically resemble villi (Kasendra et al., 2018).

Microfluidic Devices to Mimic Peristalsis and Physicomechanical Cues

Application of pneumatic cyclic vacuum suction to the side chambers of microfluidic devices leads to pulsatile flow and mechanical deformations, which have been used to mimic peristaltic movements of the GI tract (**Figures 3A,B**). Evidence suggests that application of mechanical deformation in Caco-2 cells, which normally grow as an epithelial monolayer in 2D culture may undergo three-dimensional villus morphogenesis (**Figure 3C**) with differentiation into the four intestinal cell subtypes. Morphologically there appear to be villus-like tissue patterning but more rigorous testing is needed to determine how similar these villus-like structures are to actual villi. There is also suggestion of migration of proliferative cells from the basal crypt to the villus tip, formation of the apical brush border, increased cytochrome P450 activity, and enhanced mucus production relative to static cultures which mechanical deformation is applied (Kim et al., 2012; Huh et al., 2013) although we feel the criteria for villus formation needs to be carefully developed and the tissues grown in these models needs more analysis.

It was further found that in Caco-2 cells and intestinal organoid-derived primary epithelial cells, that specific cessation of basal flow, while maintaining luminal flow, halted intestinal morphogenesis and villi formation. By manipulating physical and biochemical cues in the gut chip model, it was identified that the Wnt antagonist DKK-1 was secreted in a polarized basolateral direction and that its removal by fluid flow in the basolateral microchannel is a critical factor that directly triggers intestinal 3D morphogenesis in this model using Caco-2 as well as the primary organoid-derived epithelial cells (Shin et al., 2019). Evaluation of differential stimuli on the luminal and basal sides of the

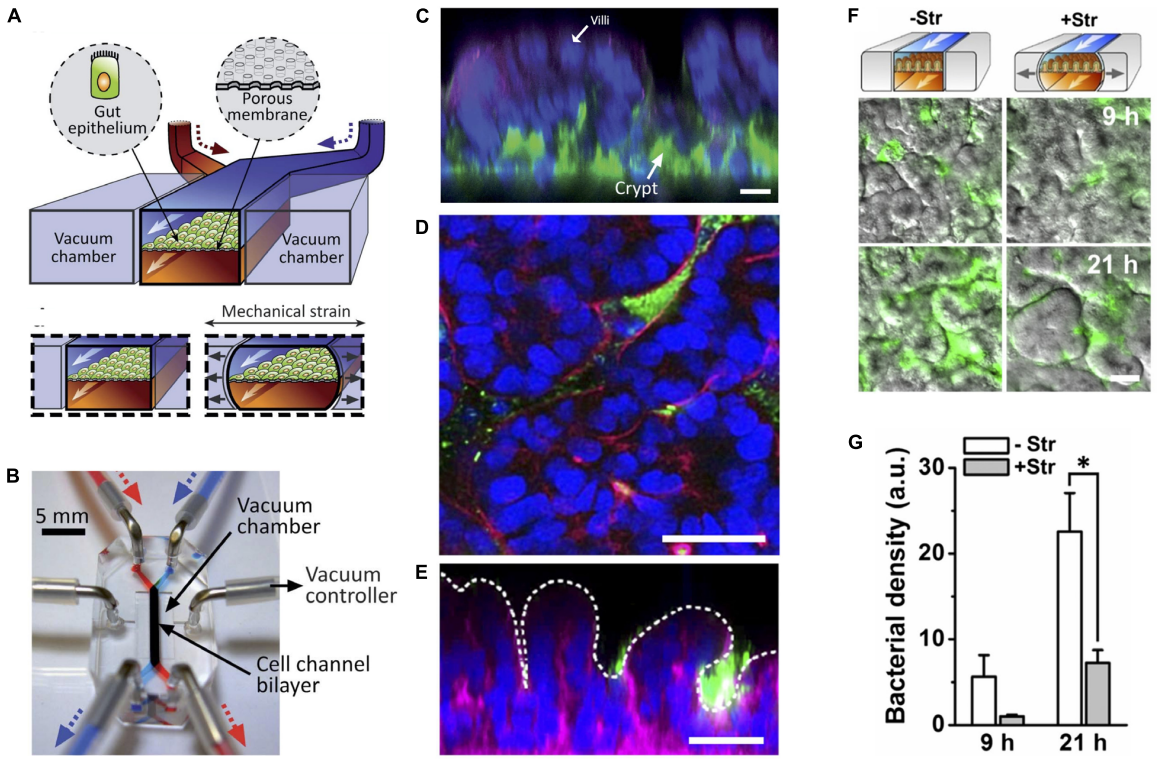

FIGURE 3 | State of the art in gut-on-a-chip platforms. **(A)** Illustration of the cross section of an organ chip with two chambers and flanking vacuum chambers, which are used to perform mechanical deformation. Gut epithelial cells are grown on top of a porous membrane. The upper (epithelial) chamber is perfused by the blue pump and the lower chamber is perfused by the red pump. Two lateral chambers allowed application of vacuum to the side chambers to produce cyclic mechanical strain in the direction of the arrows to mimic peristalsis (Reproduced from Huh et al., 2013 with permission from The Royal Society of Chemistry). **(B)** Photograph of the organ chip constructed from PDMS elastomer with the upper (epithelial) chamber infused by a syringe attached to a pump with a blue dye and the lower chamber being infused with a red dye. The direction of fluid flow is in the direction of the arrows. Cells are seeded in the labeled cell channel. Application of vacuum to produce cyclic mechanical deformation is performed through tubing attached to vacuum chambers flanking the main micro channel using a vacuum controller (Reproduced from Huh et al., 2013 with permission from The Royal Society of Chemistry). **(C)** Caco-2 cells grown under cyclic mechanical strain formed of three-dimensional "villus-like" structures and crypts. Immunofluorescence staining with DAPI nuclear staining (blue), f-actin (green), and mucin staining (magenta). (Reproduced from Huh et al., 2013 with permission from The Royal Society of Chemistry). **(D)** Horizontal and **(E)** vertical cross-sections of green fluorescent protein (GFP) expressing *E. coli* (green) co-cultured with Caco-2 cells on-a-chip (DAPI nuclear stain in blue; F-acin stain in magenta). Dotted line represents the villous surface of these intestinal cells. **(F)** Cessation of mechanical strain (deformation) leads to bacterial overgrowth as seen in Caco-2 cells grown with GFP expressing *E. coli*. **(G)** Quantification of bacterial overgrowth. + Str = cells and bacteria grown in the presence of mechanical strain. – Str = without mechanical strain. (Reproduced from Kim et al., 2016 with permission from The National Academy of Science). *Represents statistical significance as determined by p-value < 0.05.

cells was capable on organ chips but not in conventional cell culture, making organ chips a powerful tool for understanding morphogenesis and development. This was further confirmed in a paper by Sunuwar and colleagues which used human jejunal enteroids to show that luminal and basolateral flow produce a model of continual differentiation and NaCl absorption that mimics normal intestine that will be useful in modeling normal intestinal physiology (Sunuwar et al., 2020).

Application of pulsatile flow and mechanical deformation has allowed co-culture of microbes in direct contact with epithelial cells (instead of with a thin membrane) and for the ability to maintain systems for weeks, longer than any static cell culture systems (Kim et al., 2012; Huh et al., 2013). In fact, it was shown that specific cessation of pulsatile flow (stopping the peristalsis-like motion) while maintaining continuous flow, lead to bacterial overgrowth, demonstrating that the lack of pulsatility, not the lack of fluid flow, is the likely mechanism of bacterial overgrowth. This may have implications for the disease small intestinal bowel overgrowth (SIBO), which occurs in the setting of ileus and may suggest that the mechanism of overgrowth has more to do with decreased peristalsis rather than lack of fluid flow in the intestine and that restoring motility may help treat this disease (Kim et al., 2016).

Incorporation of the Microbiome Into Gut Chip Models

Gut microbiome study has been limited to genomic and metagenomic analysis given difficulty in culturing the largely anaerobic bacterial population. Conventional 2D models are unable to support co-culture of microbiome with cells for extended periods of time limiting analyses because the aerobic bacteria rapidly overgrow and contaminate the cultures in a

day. Additionally, obligate anaerobic bacteria are unable to be effectively cultured.

Kim et al. (2012) developed the first microfluidics-based system to co-culture human and microbial organisms using Caco-2 cells and *Lactobacillus rhamnosus* GG for greater than 1 week. Shin and Kim (2018) developed a more sophisticated model called HuMiX (human–microbial crosstalk), which again used co-culture of Caco-2 cells with *L. rhamnosus GG* or *Bacteroides caccae,* this time under anaerobic conditions. Their model demonstrated transcriptional, metabolic and immunologic responses that differed between the two different microbial species (Shah et al., 2016). Limitations of this model include physical separation of intestinal and microbial cells by a thin membrane and lack of pulsatile flow (Kim and Ingber, 2013).

A subsequent model allowed for direct contact between epithelial cells and microbes (**Figures 3D,E**). This was shown to be possible through the integration of pulsatile flow and mechanical deformation, which produced peristalsis-like waves of deformation (**Figures 3F,G**) (Kim et al., 2012, 2016) (see section on intestine chip models of peristalsis). They found that co-culture of *L. rhamnosus GG* with intestinal epithelial cells improved intestinal barrier function and also demonstrated that pathogenic bacteria such as enteroinvasive *Escherichia coli* can be integrated into this model (Kim et al., 2016).

One major hurdle to studying the interactions of the comprehensive gut microbiome and intestinal epithelia is that hundreds of bacteria species are obligate anaerobes that will not grow under aerobic conditions (>0.5% O_2) required to grow intestinal cells (Flint et al., 2012). A recent gut-on-a-chip model overcame this problem by incorporating physiologic oxygen gradients into a gut chip which included primary human ileum epithelium and endothelial layers. Their chip contained two chambers: the epithelial chamber was anaerobic and the vascular (endothelial) chamber grown in aerobic conditions. These chambers were separated by PDMS. Diffusion of oxygen from the aerobic chamber produced an oxygen gradient with oxygen concentration <0.3%. The authors fabricated oxygen sensors with embedded oxygen-quenched fluorescent particles along the epithelial and vascular channels to for real-time non-invasive monitoring of oxygen levels. They grew Caco-2 cells and primary ileal epithelium in this chip. They demonstrated that the obligate anaerobe *Bacteroides fragilis* was able to grow in this system and demonstrated improved growth when anaerobic conditions were applied. They used microbiota originally derived from healthy human stool specimens in order to produce the first *in vitro* microbiome epithelium co-culture. This oxygen gradient allowed for the stable co-culture of the microbiome community in the same channel as mucus-producing human villus intestinal epithelium for 5 days and again showed improved growth of obligate anaerobes in the anaerobic system (Jalili-Firoozinezhad et al., 2019).

Incorporation of the gut microbiome on-a-chip opens doors for many questions previously unanswerable such as how microbial composition differs on the cell surface versus lumen, how specific bacteria interact with host cells and tracking of these dynamics over time in response to stimuli. Additionally, immune cells, epithelium from different regions of the intestine, and specific microbial aspirates from those regions can be added to this system to model specific geographic regions along the GI tract (Poceviciute and Ismagilov, 2019).

Gut Inflammation On-a-Chip

Chip based models have been used to study gut inflammation and inflammatory bowel disease (IBD). Addition of lipopolysaccharide (LPS) endotoxin to a microfluidic model of the epithelial microchannel demonstrates secretion of proinflammatory cytokines interleukin (IL)-1beta, IL6, IL8, and tumor necrosis factor (TNF)-alpha which lead to increased expression of intercellular adhesion molecule (ICAM)-1, villous blunting, and intestinal barrier dysfunction similar to that seen in inflammatory bowel disease (Kim et al., 2016). An intestinal chip model was also used to study radiation induced gut injury (Jalili-Firoozinezhad et al., 2018).

More recently, in order to identify the initiating factors in gut inflammation, a gut chip incorporating the well-established dextran sodium sulfate (DSS)-induced colitis model (Solomon et al., 2010; Chassaing et al., 2014) was used to assess the effects of gut epithelial barrier dysfunction (DSS treatment), microbial pathogens (*E. coli* or its byproduct LPS), immune components [peripheral blood mononuclear cells (PBMC)], probiotics in various combinations. They demonstrated epithelial barrier dysfunction, pathogenic bacteria (*E. coli* or LPS), and immune cells were required to get gut inflammation and that pretreatment with a probiotic (VSL #3) was able to suppress gut inflammation (Shin and Kim, 2018).

Another study using an intestinal chip model demonstrated that LPS disrupted the intestinal barrier and that lactobacillus was able to protect against the invasion across the epithelium of the opportunistic pathogen *Candida albicans* in this model (Maurer et al., 2019). Another model of enterohemorrhagic E. coli (EHEC) infection, a pathogenic bacterium causing diarrheal illness, showed that addition of specific metabolites from the gut microbiome potentiate the pathogen's infection, providing a potential explanation for why certain organisms (e.g., mice) and certain human subpopulations (e.g., children) may have different susceptibilities to EHEC (Tovaglieri et al., 2019).

Recently, a gut-on-a-chip model was used to study the relationship of the entero-invasive intestinal pathogen *Shigella* and colonic mucosa. *Shigella* is a pathogen bacillary dysentery, a severe diarrheal illness, with a small inoculation, as few as a few hundred bacteria; however, *Shigella* are particularly hard to culture using traditional cell culture methods (Sansonetti et al., 1996). A gut-on-a-chip system with incorporation of peristalsis-like activity (as described above, see section on "Models of Peristalsis in Intestinal Chips Models") (Kim et al., 2016) was found to increase the capability of this bacterium to invade human colonic epithelium (Grassart et al., 2019). This provides an important animal-free model that more accurately models Shigella infection that traditional methods.

Models of Metabolism

The intestine is an important contributor to drug absorption and metabolism that is understudied. First pass metabolism — drug metabolism that occurs before systemic circulation of drugs is

a major barrier to drug bioavailability. Traditionally thought to occur in the liver, it has been more recently identified to occur in the intestine as well (Thummel, 2007; Thelen and Dressman, 2009). Animal models are not great for predicting bioavailability for numerous reasons (Martignoni et al., 2006; Paine et al., 2006; Komura and Iwaki, 2011). Human *in vitro* models of intestinal drug absorption have generally used Caco-2 cell lines in cell culture or Transwell plates. Issues with these systems include lack of three-dimensional cellular architecture, lack of other cell populations present in the gut, altered expression profiles of drug transporters and drug metabolizing enzymes, especially CYP450s, and aberrant CYP450 induction response, making use of these models challenging for predicting clinical human responses (Sun et al., 2008). Human intestinal microsomes are more commonly used for gut metabolism rather than Caco-2 cells since they lack CYP450 activity (Hatley et al., 2017).

Several intestinal chip models of drug metabolism were recently developed as possible low-cost, *in vitro* platforms for monitoring drug metabolism. The first used Caco-2 cells to evaluate bioavailability of two drugs (Guo et al., 2018). A second drug metabolism model was adapted from the primary cell human duodenum-on-a-chip model (Kasendra et al., 2018). This model demonstrated polarized cell architecture, intestinal barrier function, presence of specialized cell subpopulations, and expression, localization, and function of major intestinal drug transporters. Notably, when compared to Caco-2 cells, this model displayed improved CYP3A4 expression and induction capability (Kasendra et al., 2019). Lastly, a "functional coupling" organ chip model incorporating intestine, liver, kidney, blood–brain barrier, and skeletal muscle was used to screen drugs to identifying multi-organ toxicity and absorption, distribution, metabolism and excretion. In this publication, each microphysiologic system was run separately in labs across the US and the samples from each chip were shipped to each lab. This operation is not practical for drug screening and questionable to be useful for this purpose, which led to the development of multi-organ chips (Vernetti et al., 2017).

Gut Chips of the Different Regions of the Intestine

The gastrointestinal system from the mouth to anus is subdivided based on anatomic and physiologic function into the esophagus, stomach, small intestine (consisting of duodenum, jejunum, and ileum), large intestine, rectum, and anus. Organ chip models of the various gut regions have been constructed. A duodenum on a chip constructed using biopsy samples and was shown to transcriptionally more closely resemble *in vivo* duodenum than organoids (Kasendra et al., 2018). An organ chip derived from human ileum samples was used to understand mucosal microbiome interactions (Jalili-Firoozinezhad et al., 2019). This model is more extensively described in the above section entitled "*Incorporation of the Microbiome Into Gut Chip Models.*" More recently an organ chip constructed from human colonic mucosal tissue was developed to study mucus formation. This model demonstrated a subpopulation of proliferative epithelial cells, goblet cells, and the accumulation of a mucus bilayer with thickness similar to what is seen *in vivo*. In response to prostaglandin E2 the mucus layer underwent volume expansive. This model was responsive to prostaglandin in a Na-K-Cl cotransporter 1 dependent manner (Sontheimer-Phelps et al., 2020). There currently is not an organ chip model of the esophagus, although esophageal organoids have been developed from human pluripotent stem cells. Future development of an esophagus-on-a-chip will be an important direction. Another important future direction will be the further use of current region specific gut chips for investigation of specific physiology and disease processes pertaining to these regions.

Multi-Organ Chips

Multi-organ chips attempt to model multiple organ systems through the culture of multiple cell types that are connected in a microphysiologic system. In one of the seminal multi-organ chip models, Tsamandouras et al. (2017) demonstrate the quantitative contribution of gut and liver microphysiologic systems to drug absorption and metabolism as individual and interconnected MPSs. A three-compartment microfluidic "digestion-on-a-chip" model system was created to study digestion *in vitro*. This was constructed using three compartments in series to mimic the environments of the mouth, stomach, and small intestine. Each compartment was with specific pH, buffer, and mineral composition as well as saliva, gastric, and duodenal fluid in order to mimic their respective local physiologic environment. Digestion of starch, casein, and milk protein (lactoferrin) were used in the study as model nutrients and enzyme kinetics were monitored in real time across the system. Notably, no gut mucosa was used in these models, which limits its current use for the study of drug metabolism and bioavailability (De Haan et al., 2019).

Another study developed a microfluidic platform connecting the liver, stomach, and intestinal cells in a multi-organ-on-a-chip, with the goal of using this as an *in vitro* drugs screening platform, given that not only the liver, but the intestine and stomach play roles in drug metabolism (Jin et al., 2018).

Recent studies suggest peripheral inflammation and microbial pathogens could be triggers for neurologic diseases like Alzheimer's (AD) and Parkinson's disease (PD) (Dominy et al., 2019; Rekdal et al., 2019). Recently the European Research Council (ERC) funded a project called "MINERVA" aimed at evaluating the effect of intestinal microbiota on brain functionality through development of a gut-brain chip model. This model has five miniaturized organs (gut microbiota, gut epithelium, immune system, blood–brain-barrier, and the brain) connected hydraulically through a microfluidic system. The goal of this work is to test the effect of microbiota from AD versus healthy patients in the system (Raimondi et al., 2019).

CONCLUSION AND FUTURE PERSPECTIVES

In this review, we describe the recent efforts to develop microphysiological models of the GI system. The overarching goal

of organ-on-a-chip technology is to emulate *in vivo* system physiology in a highly controllable environment. Despite the significant listed efforts to model the GI tract *in vitro*, there remain significant challenges and room for improvement in model development.

We still can only model a handful of cell types at a time. Being able to interface numerous cell types at once will be a challenge but is important to recapitulate many processes. For example, modeling the microbiome interactions with epithelium is interesting but the human immune system is very important for pathogen response and in the induction of tolerance (Belkaid and Hand, 2014). Some incorporation of the immune system into organ chips is currently possible but it is largely limited to infusion of peripheral blood mononuclear cells and injection of various cytokines. Furthermore, future work needs to identify ways to integrate the ENS, which is recognized as having an increasingly important role in the regulation of stress response, blood flow, secretion, metabolism, and immune regulation (Sharkey et al., 2018).

Organ-on-a-chip technology will be quite powerful for advancing personalized medicine approaches. Organoids can be used to do some personalized studies, but they lack the ability to incorporate multiple tissue types and their luminal surface is on the interior of the organ and so not directly open to drug treatment (as described above); thus, they are limited in their use in personalized medicine approaches. Organ-on-a-chip technology will allow growth of patient-specific samples in the presence of microbiome and immune systems and so will more fully incorporate these factors in.

Organ-on-a-chip technology is creating a new wave of powerful *in vitro* tools that overcome many of the limitations of traditional cell culture and have begun to allow many complex biomedical questions to the asked that were unattainable with previous technology. There remain many avenues to improve this technology to make it more biologically relevant as it becomes an increasingly important tool in biomedical research.

AUTHOR CONTRIBUTIONS

SS, JS, B-KK, DD, and D-HK wrote the manuscript. SS constructed the figures. All authors contributed to the article and approved the submitted version.

FUNDING

This work was supported by grants from the Human Frontier Science Program (RGP0038/2018) (to D-HK and DD), the National Institute of Diabetes and Digestive and Kidney Diseases (T32 DK007632) (to SS and D-HK), and the CNRS Défi Biomimétisme (to DD), the Groupama Foundation – Research Prize for Rare Diseases 2017 (to DD), the LabEx "Who Am I?" #ANR-11-LABX-0071 and the Université de Paris IdEx #ANR-18-IDEX-0001 funded by the French Government through its "Investments for the Future" program (to DD).

ACKNOWLEDGMENTS

The authors would like to thank Dr. Mark Donowitz, from the Department of Medicine, Division of Gastroenterology and Hepatology at the Johns Hopkins School of Medicine for his insightful comments on the manuscript.

REFERENCES

Accardo, A., Blatché, M. C., Courson, R., Loubinoux, I., Thibault, C., Malaquin, L., et al. (2017). Multiphoton direct laser writing and 3D imaging of polymeric freestanding architectures for cell colonization. *Small* 13, 1–11. doi: 10.1002/smll.201700621

Altay, G., Larrañaga, E., Tosi, S., Barriga, F. M., Batlle, E., Fernández-Majada, V., et al. (2019). Self-organized intestinal epithelial monolayers in crypt and villus-like domains show effective barrier function. *Sci. Rep.* 9:10140. doi: 10.1038/s41598-019-46497-x

Andersson-Rolf, A., Fink, J., Mustata, R. C., and Koo, B. K. (2014). A video protocol of retroviral infection in primary intestinal Organoid culture. *J. Visualiz. Exp.* 51765. doi: 10.3791/51765

Andersson-Rolf, A., Merenda, A., Mustata, R. C., Li, T., Dietmann, S., and Koo, B. K. (2016). Simultaneous paralogue knockout using a CRISPR-concatemer in mouse small intestinal organoids. *Dev. Biol.* 420, 271–277. doi: 10.1016/j.ydbio.2016.10.016

Andersson-Rolf, A., Mustata, R. C., Merenda, A., Kim, J., Perera, S., Grego, T., et al. (2017). One-step generation of conditional and reversible gene knockouts. *Nat. Methods* 14, 287–289. doi: 10.1038/nmeth.4156

Andrée, B., Bär, A., Haverich, A., and Hilfiker, A. (2013). Small intestinal submucosa segments as matrix for tissue engineering: review. *Tissue Eng. Part B Rev.* 19, 279–291. doi: 10.1089/ten.teb.2012.0583

Baptista, D., Teixeira, L., van Blitterswijk, C., Giselbrecht, S., and Truckenmüller, R. (2019). Overlooked? Underestimated? Effects of substrate curvature on cell behavior. *Trends Biotechnol.* 37, 838–854. doi: 10.1016/j.tibtech.2019.01.006

Barker, N. (2014). Adult intestinal stem cells: critical drivers of epithelial homeostasis and regeneration. *Nat. Rev. Mol. Cell Biol.* 15, 19–33. doi: 10.1038/nrm3721

Barnes, J. M., Przybyla, L., and Weaver, V. M. (2017). Tissue mechanics regulate brain development, homeostasis and disease. *J. Cell Sci.* 130, 71–82. doi: 10.1242/jcs.191742

Bartfeld, S., Bayram, T., Van De Wetering, M., Huch, M., Begthel, H., Kujala, P., et al. (2015). In vitro expansion of human gastric epithelial stem cells and their responses to bacterial infection. *Gastroenterology* 148, 126–136.e6. doi: 10.1053/j.gastro.2014.09.042

Bein, A., Shin, W., Jalili-Firoozinezhad, S., Park, M. H., Sontheimer-Phelps, A., Tovaglieri, A., et al. (2018). Microfluidic organ-on-a-chip models of human intestine. *Cell. Mol. Gastroenterol. Hepatol.* 5, 659–668. doi: 10.1016/j.jcmgh.2017.12.010

Belkaid, Y., and Hand, T. W. (2014). Role of the microbiota in immunity and inflammation. *Cell* 157, 121–141. doi: 10.1016/j.cell.2014.03.011

Berthier, E., Young, E. W. K., and Beebe, D. (2012). Engineers are from PDMS-land, biologists are from polystyrenia. *Lab Chip* 12, 1224–1237. doi: 10.1039/c2lc20982a

Bhatia, S. N., and Ingber, D. E. (2014). Microfluidic organs-on-chips. *Nat. Biotechnol.* 32, 760–772. doi: 10.1038/nbt.2989

Biasi, F., Guina, T., Maina, M., Nano, M., Falcone, A., Aroasio, E., et al. (2012). Progressive increase of matrix metalloprotease-9 and interleukin-8 serum levels during carcinogenic process in human colorectal tract. *PLoS ONE* 7:e41839. doi: 10.1371/journal.pone.0041839

Blondel, D., and Lutolf, M. P. (2019). Bioinspired hydrogels for 3d organoid culture. *Chimia* 73, 81–85. doi: 10.2533/chimia.2019.81

Brassard, J. A., and Lutolf, M. P. (2019). Engineering stem cell self-organization to build better organoids. *Cell Stem Cell* 24, 860–876. doi: 10.1016/j.stem.2019.05.005

Broutier, L., Andersson-Rolf, A., Hindley, C. J., Boj, S. F., Clevers, H., Koo, B. K., et al. (2016). Culture and establishment of self-renewing human and mouse adult liver and pancreas 3D organoids and their genetic manipulation. *Nat. Protoc.* 11, 1724–1743. doi: 10.1038/nprot.2016.097

Chassaing, B., Aitken, J. D., Malleshappa, M., and Vijay-Kumar, M. (2014). Dextran sulfate sodium (DSS)-induced colitis in mice. *Curr. Protoc. Immunol.* 23, 6016–6029. doi: 10.1002/0471142735.im1525s104

Chen, F. M., and Liu, X. (2016). Advancing biomaterials of human origin for tissue engineering. *Prog. Polym. Sci.* 53, 86–168. doi: 10.1016/j.progpolymsci.2015.02.004

Clemente, J. C., Ursell, L. K., Parfrey, L. W., and Knight, R. (2012). The impact of the gut microbiota on human health: an integrative view. *Cell* 148, 1258–1270. doi: 10.1016/j.cell.2012.01.035

Creff, J., Courson, R., Mangeat, T., Foncy, J., Souleille, S., Thibault, C., et al. (2019). Fabrication of 3D scaffolds reproducing intestinal epithelium topography by high-resolution 3D stereolithography. *Biomaterials* 221:119404. doi: 10.1016/j.biomaterials.2019.119404

Crosnier, C., Stamataki, D., and Lewis, J. (2006). Organizing cell renewal in the intestine: stem cells, signals and combinatorial control. *Nat. Rev. Genet.* 7, 349–359. doi: 10.1038/nrg1840

Cryan, J. F., and Dinan, T. G. (2012). Mind-altering microorganisms: the impact of the gut microbiota on brain and behaviour. *Nat. Rev. Neurosci.* 13, 701–712. doi: 10.1038/nrn3346

De Arcangelis, A., Hamade, H., Alpy, F., Normand, S., Bruyère, E., Lefebvre, O., et al. (2017). Hemidesmosome integrity protects the colon against colitis and colorectal cancer. *Gut* 66, 1748–1760. doi: 10.1136/gutjnl-2015-310847

De Haan, P., Ianovska, M. A., Mathwig, K., Van Lieshout, G. A. A., Triantis, V., Bouwmeester, H., et al. (2019). Digestion-on-a-chip: a continuous-flow modular microsystem recreating enzymatic digestion in the gastrointestinal tract. *Lab Chip* 19, 1599–1609. doi: 10.1039/c8lc01080c

De Van Lidth Jeude, J. F., Vermeulen, J. L. M., Montenegro-Miranda, P. S., Van Den Brink, G. R., and Heijmans, J. (2015). A protocol for lentiviral transduction and downstream analysis of intestinal organoids. *J. Visualiz. Exp.* V98:52531. doi: 10.3791/52531

Delacour, D., Gouyer, V., Leteurtre, E., Ait-Slimane, T., Drobecq, H., Lenoir, C., et al. (2003). 1-Benzyl-2-acetamido-2-deoxy-α-D-galactopyranoside blocks the apical biosynthetic pathway in polarized HT-29 cells. *J. Biol. Chem.* 278, 37799–37809. doi: 10.1074/jbc.M305755200

Delacour, D., Salomon, J., Robine, S., and Louvard, D. (2016). Plasticity of the brush border-the yin and yang of intestinal homeostasis. *Nat. Rev. Gastroenterol. Hepatol.* 13, 161–174. doi: 10.1038/nrgastro.2016.5

Dixit, P., Vehmas, T., Vähänen, S., Monnoyer, P., and Henttinen, K. (2012). Fabrication and electrical characterization of high aspect ratio poly-silicon filled through-silicon vias. *J. Micromech. Microeng.* 22, 37–40. doi: 10.1088/0960-1317/22/5/055021

Dominy, S. S., Lynch, C., Ermini, F., Benedyk, M., Marczyk, A., Konradi, A., et al. (2019). Porphyromonas gingivalis in Alzheimer's disease brains: evidence for disease causation and treatment with small-molecule inhibitors. *Sci. Adv.* 5:eaau3333. doi: 10.1126/sciadv.aau3333

Drake, R. L., Vogl, A. W., and Mitchell, A. W. M. (2010). *Gray's Anatomy for Students*, 2nd Edn. Philadelphia: Churchill Livingstone Elsevier.

Driehuis, E., and Clevers, H. (2017). CRISPR/Cas 9 genome editing and its applications in organoids. *Am. J. Physiol. Gastroint. Liver Physiol.* 312:G257. doi: 10.1152/ajpgi.00410.2016

Drost, J., Van Jaarsveld, R. H., Ponsioen, B., Zimberlin, C., Van Boxtel, R., Buijs, A., et al. (2015). Sequential cancer mutations in cultured human intestinal stem cells. *Nature* 521, 43–47. doi: 10.1038/nature14415

Engler, A. J., Sen, S., Sweeney, H. L., and Discher, D. E. (2006). Matrix elasticity directs stem cell lineage specification. *Cell* 126, 677–689. doi: 10.1016/j.cell.2006.06.044

Ettayebi, K., Crawford, S. E., Murakami, K., Broughman, J. R., Karandikar, U., Tenge, V. R., et al. (2016). Replication of human noroviruses in stem cell-derived human enteroids. *Science* 353, 1387–1393. doi: 10.1126/science.aaf5211

Fatehullah, A., Tan, S. H., and Barker, N. (2016). Organoids as an in vitro model of human development and disease. *Nat. Cell Biol.* 18, 246–254. doi: 10.1038/ncb3312

Fields, B., DeLaForest, A., Zogg, M., May, J., Hagen, C., Komnick, K., et al. (2019). The adult murine intestine is dependent on constitutive laminin-γ1 synthesis. *Sci. Rep.* 9:19303. doi: 10.1038/s41598-019-55844-x

Finkbeiner, S. R., Freeman, J. J., Wieck, M. M., El-Nachef, W., Altheim, C. H., Tsai, Y. H., et al. (2015). Generation of tissue-engineered small intestine using embryonic stem cell-derived human intestinal organoids. *Biol. Open* 4, 1462–1472. doi: 10.1242/bio.013235

Flint, H. J., Scott, K. P., Louis, P., and Duncan, S. H. (2012). The role of the gut microbiota in nutrition and health. *Nat. Rev. Gastroenterol. Hepatol.* 9, 577–589. doi: 10.1038/nrgastro.2012.156

Forbester, J. L., Goulding, D., Vallier, L., Hannan, N., Hale, C., Pickard, D., et al. (2015). Interaction of *salmonella enterica* serovar Typhimurium with intestinal organoids derived from human induced pluripotent stem cells. *Infect. Immun.* 83, 2926–2934. doi: 10.1128/IAI.00161-15

Foulke-Abel, J., In, J., Kovbasnjuk, O., Zachos, N. C., Ettayebi, K., Blutt, S. E., et al. (2014). Human enteroids as an ex-vivo model of host–pathogen interactions in the gastrointestinal tract. *Exp. Biol. Med.* 239, 1124–1134. doi: 10.1177/1535370214529398

Frantz, C., Stewart, K. M., and Weaver, V. M. (2010). The extracellular matrix at a glance. *J. Cell Sci.* 123(Pt 24), 4195–4200. doi: 10.1242/jcs.023820

Fujii, M., Matano, M., Nanki, K., and Sato, T. (2015). Efficient genetic engineering of human intestinal organoids using electroporation. *Nat. Protoc.* 10, 1474–1485. doi: 10.1038/nprot.2015.088

Fujii, M., Matano, M., Toshimitsu, K., Takano, A., Mikami, Y., Nishikori, S., et al. (2018). Human intestinal organoids maintain self-renewal capacity and cellular diversity in niche-inspired culture condition. *Cell Stem Cell* 23, 787–793.e6. doi: 10.1016/j.stem.2018.11.016

Garrett, W. S., Gordon, J. I., and Glimcher, L. H. (2010). Homeostasis and inflammation in the intestine. *Cell* 140, 859–870. doi: 10.1016/j.cell.2010.01.023

Giobbe, G. G., Crowley, C., Luni, C., Campinoti, S., Khedr, M., Kretzschmar, K., et al. (2019). Extracellular matrix hydrogel derived from decellularized tissues enables endodermal organoid culture. *Nat. Commun.* 10:5658. doi: 10.1038/s41467-019-13605-4

Giuffrida, P., Cococcia, S., Delliponti, M., Lenti, M. V., and Di Sabatino, A. (2019). Controlling gut inflammation by restoring anti-inflammatory pathways in inflammatory bowel disease. *Cells* 8:397. doi: 10.3390/cells8050397

Gjorevski, N., Sachs, N., Manfrin, A., Giger, S., Bragina, M. E., Ordóñez-Morán, P., et al. (2016). Designer matrices for intestinal stem cell and organoid culture. *Nature* 539, 560–564. doi: 10.1038/nature20168

Goulet, O., Kedinger, M., Brousse, N., Cuenod, B., Colomb, V., Patey, N., et al. (1995). Intrac diarrhea of infancy with epithelial and basement membrane abnormalities. *J. Pediatr.* 127, 212–219. doi: 10.1016/S0022-3476(95)70297-0

Grassart, A., Malardé, V., Gobaa, S., Sartori-Rupp, A., Kerns, J., Karalis, K., et al. (2019). Bioengineered human organ-on-chip reveals intestinal microenvironment and mechanical forces impacting *shigella* infection. *Cell Host Microbe* 26, 435–444.e4. doi: 10.1016/j.chom.2019.08.007

Grün, D., Lyubimova, A., Kester, L., Wiebrands, K., Basak, O., Sasaki, N., et al. (2015). Single-cell messenger RNA sequencing reveals rare intestinal cell types. *Nature* 525, 251–255. doi: 10.1038/nature14966

Guo, Y., Li, Z., Su, W., Wang, L., Zhu, Y., and Qin, J. (2018). A biomimetic human gut-on-a-chip for modeling drug metabolism in intestine. *Artificial Organs* 42, 1196–1205. doi: 10.1111/aor.13163

Gustafsson, J. K., Ermund, A., Johansson, M. E. V., Schütte, A., Hansson, G. C., and Sjövall, H. (2012). An ex vivo method for studying mucus formation, properties, and thickness in human colonic biopsies and mouse small and large intestinal explants. *Am. J. Physiol. Gastroint. Liver Physiol.* 302, G430–G438. doi: 10.1152/ajpgi.00405.2011

Hannezo, E., and Heisenberg, C. P. (2019). Mechanochemical feedback loops in development and disease. *Cell* 178, 12–25. doi: 10.1016/j.cell.2019.05.052

Hatley, O. J. D., Jones, C. R., Galetin, A., and Rostami-Hodjegan, A. (2017). Quantifying gut wall metabolism: methodology matters. *Biopharm. Drug Dispos.* 38, 155–160. doi: 10.1002/bdd.2062

He, J., Guo, H., Zheng, W., and Yao, W. (2018). Effects of stress on the mucus-microbial interactions in the gut. *Curr. Protein Peptide Sci.* 20, 155–163. doi: 10.2174/1389203719666180514152406

Heo, I., Dutta, D., Schaefer, D. A., Iakobachvili, N., Artegiani, B., Sachs, N., et al. (2018). Modelling cryptosporidium infection in human small intestinal and lung organoids. *Nat. Microbiol.* 3, 814–823. doi: 10.1038/s41564-018-0177-8

Hilgers, A. R., Conradi, R. A., and Burton, P. S. (1990). Caco-2 cell monolayers as a model for drug transport across the intestinal mucosa. *Pharm. Res*. 7, 902–910. doi: 10.1023/A:1015937605100

Hodde, J. (2002). Review: naturally occurring scaffolds for soft tissue repair and regeneration. *Tissue Eng*. 8, 295–308. doi: 10.1089/107632702753725058

Hoeppner, J. (2013). Limited resection for duodenal gastrointestinal stromal tumors: surgical management and clinical outcome. *World J. Gastroint. Surg*. 5, 16–21. doi: 10.4240/wjgs.v5.i2.16

Hollingsworth, M. A., and Swanson, B. J. (2004). Mucins in cancer: protection and control of the cell surface. *Nat. Rev. Cancer* 4, 45–60. doi: 10.1038/nrc1251

Huh, D., Kim, H. J., Fraser, J. P., Shea, D. E., Khan, M., Bahinski, A., et al. (2013). Microfabrication of human organs-on-chips. *Nat. Protoc*. 8, 2135–2157. doi: 10.1038/nprot.2013.137

Imura, Y., Asano, Y., Sato, K., and Yoshimura, E. (2009). A microfluidic system to evaluate intestinal absorption. *Anal. Sci*. 25, 1403–1407. doi: 10.2116/analsci.25.1403

Iskratsch, T., Wolfenson, H., and Sheetz, M. P. (2014). Appreciating force and shape-the rise of mechanotransduction in cell biology. *Nat. Rev. Mol. Cell Biol*. 15, 825–833. doi: 10.1038/nrm3903

Jaladanki, R. N., and Wang, J.-Y. (2011). "Regulation of gastrointestinal mucosal growth," in *Colloquium Series on Integrated Systems Physiology: From Molecule to Function*, eds D. Neil Granger and J. P. Granger (San Rafael, CA: Morgan & Claypool Publishers), 1–114. doi: 10.4199/c00028ed1v01y201103isp015

Jalili-Firoozinezhad, S., Gazzaniga, F. S., Calamari, E. L., Camacho, D. M., Fadel, C. W., Bein, A., et al. (2019). A complex human gut microbiome cultured in an anaerobic intestine-on-a-chip. *Nat. Biomed. Eng*. 3, 520–531. doi: 10.1038/s41551-019-0397-0

Jalili-Firoozinezhad, S., Prantil-Baun, R., Jiang, A., Potla, R., Mammoto, T., Weaver, J. C., et al. (2018). Modeling radiation injury-induced cell death and countermeasure drug responses in a human Gut-on-a-Chip article. *Cell Death Dis*. 9:223. doi: 10.1038/s41419-018-0304-8

Jin, Y., Kim, J., Lee, J. S., Min, S., Kim, S., Ahn, D. H., et al. (2018). Vascularized liver organoids generated using induced hepatic tissue and dynamic liver-specific microenvironment as a drug testing platform. *Adv. Funct. Mater*. 28. doi: 10.1002/adfm.201801954

Jung, K. B., Lee, H., Son, Y. S., Lee, M. O., Kim, Y. D., Oh, S. J., et al. (2018). Interleukin-2 induces the in vitro maturation of human pluripotent stem cell-derived intestinal organoids. *Nat. Commun*. 9:3039. doi: 10.1038/s41467-018-05450-8

Jung, P., Sato, T., Merlos-Suárez, A., Barriga, F. M., Iglesias, M., Rossell, D., et al. (2011). Isolation and in vitro expansion of human colonic stem cells. *Nat. Med*. 17, 1225–1227. doi: 10.1038/nm.2470

Kasendra, M., Luc, R., Yin, J., Manatakis, D. V., Apostolou, A., Sunuwar, L., et al. (2019). Organoid-derived duodenum intestine-chip for preclinical drug assessment in a human relevant system. *BioRxiv Cell Biol.* [Preprint] doi: 10.1101/723015

Kasendra, M., Tovaglieri, A., Sontheimer-Phelps, A., Jalili-Firoozinezhad, S., Bein, A., Chalkiadaki, A., et al. (2018). Development of a primary human small intestine-on-a-chip using biopsy-derived organoids. *Sci. Rep*. 8, 1–14. doi: 10.1038/s41598-018-21201-7

Kaushik, N., Kim, S., Suh, Y., and Lee, S. J. (2019). Proinvasive extracellular matrix remodeling for tumor progression. *Arch. Pharm. Res*. 42, 40–47. doi: 10.1007/s12272-018-1097-0

Kedinger, M., Freund, J.-N., Launay, J. F., and Simon-Assmann, P. (2000). "Cell interactions through the basement membrane in intestinal development and differentiation," in *Development of the Gastrointestinal Tract*, eds I. R. Sanderson, and W. A. Walker (London: B.C. Decker), 83–102.

Kim, H. J., Huh, D., Hamilton, G., and Ingber, D. E. (2012). Human gut-on-a-chip inhabited by microbial flora that experiences intestinal peristalsis-like motions and flow. *Lab Chip* 12, 2165–2174. doi: 10.1039/c2lc40074j

Kim, H. J., and Ingber, D. E. (2013). Gut-on-a-Chip microenvironment induces human intestinal cells to undergo villus differentiation. *Integr. Biol. (United Kingdom)* 5, 1130–1140. doi: 10.1039/c3ib40126j

Kim, H. J., Li, H., Collins, J. J., and Ingber, D. E. (2016). Contributions of microbiome and mechanical deformation to intestinal bacterial overgrowth and inflammation in a human gut-on-a-chip. *Proc. Natl. Acad. Sci. U.S.A*. 113, E7–E15. doi: 10.1073/pnas.1522193112

Kim, S. H., Chi, M., Yi, B., Kim, S. H., Oh, S., Kim, Y., et al. (2014). Three-dimensional intestinal villi epithelium enhances protection of human intestinal cells from bacterial infection by inducing mucin expression. *Integr. Biol. (UK)* 6, 1122–1131. doi: 10.1039/c4ib00157e

Kimura, H., Ikeda, T., Nakayama, H., Sakai, Y., and Fujii, T. (2015). An on-chip small intestine–liver model for pharmacokinetic studies. *J. Labor. Automat*. 20, 265–273. doi: 10.1177/2211068214557812

Kleinman, H. K., and Martin, G. R. (2005). Matrigel: basement membrane matrix with biological activity. *Semin. Cancer Biol*. 15, 378–386. doi: 10.1016/j.semcancer.2005.05.004

Komura, H., and Iwaki, M. (2011). In vitro and in vivo small intestinal metabolism of CYP3A and UGT substrates in preclinical animals species and humans: species differences. *Drug Metabol. Rev*. 43, 476–498. doi: 10.3109/03602532.2011.597401

Koo, B. K., Stange, D. E., Sato, T., Karthaus, W., Farin, H. F., Huch, M., et al. (2012). Controlled gene expression in primary Lgr5 organoid cultures. *Nat. Methods* 9, 81–83. doi: 10.1038/nmeth.1802

Kretzschmar, K., and Clevers, H. (2016). Organoids: modeling development and the stem cell niche in a dish. *Dev. Cell* 38, 590–600. doi: 10.1016/j.devcel.2016.08.014

Kular, J. K., Basu, S., and Sharma, R. I. (2014). The extracellular matrix: structure, composition, age-related differences, tools for analysis and applications for tissue engineering. *J. Tissue Eng*. 5:2041731414557112. doi: 10.1177/2041731414557112

Latella, G., and Rieder, F. (2017). Intestinal fibrosis: ready to be reversed. *Curr. Opin. Gastroenterol*. 33, 239–245. doi: 10.1097/MOG.0000000000000363

Le Digabel, J., Ghibaudo, M., Trichet, L., Richert, A., and Ladoux, B. (2010). Microfabricated substrates as a tool to study cell mechanotransduction. *Med. Biol. Eng. Comput*. 48, 965–976. doi: 10.1007/s11517-010-0619-9

Leijten, J., Seo, J., Yue, K., Trujillo-de Santiago, G., Tamayol, A., Ruiz-Esparza, G. U., et al. (2017). Spatially and temporally controlled hydrogels for tissue engineering. *Mater. Sci. Eng.* 119, 1–35. doi: 10.1016/j.mser.2017.07.001

Leivo, I., Tani, T., Laitinen, L., Bruns, R., Kivilaakso, E., Lehto, V. P., et al. (1996). Anchoring complex components laminin-5 and type VII collagen in intestine: association with migrating and differentiating enterocytes. *J. Histochem. Cytochem*. 44, 1267–1277. doi: 10.1177/44.11.8918902

Lemma, E. D., Spagnolo, B., De Vittorio, M., and Pisanello, F. (2019). Studying cell mechanobiology in 3D: the two-photon lithography approach. *Trends Biotechnol*. 37, 358–372. doi: 10.1016/j.tibtech.2018.09.008

Lloyd-Price, J., Abu-Ali, G., and Huttenhower, C. (2016). The healthy human microbiome. *Genome Med*. 8:51. doi: 10.1186/s13073-016-0307-y

Lutolf, M. P., and Hubbell, J. A. (2005). Synthetic biomaterials as instructive extracellular microenvironments for morphogenesis in tissue engineering. *Nat. Biotechnol*. 23, 47–55. doi: 10.1038/nbt1055

Maghsoudlou, P., Totonelli, G., Loukogeorgakis, S. P., Eaton, S., and De Coppi, P. (2013). A decellularization methodology for the production of a natural acellular intestinal matrix. *J. Visualiz. Exp*. 50658. doi: 10.3791/50658

Martignoni, M., Groothuis, G. M. M., and de Kanter, R. (2006). Species differences between mouse, rat, dog, monkey and human CYP-mediated drug metabolism, inhibition and induction. *Exp. Opin. Drug Metabol. Toxicol*. 2, 875–894. doi: 10.1517/17425255.2.6.875

Martin, C. R., Osadchiy, V., Kalani, A., and Mayer, E. A. (2018). The Brain-Gut-Microbiome Axis. *Cell. Mol. Gastroenterol. Hepatol*. 6, 133–148. doi: 10.1016/j.jcmgh.2018.04.003

Matano, M., Date, S., Shimokawa, M., Takano, A., Fujii, M., Ohta, Y., et al. (2015). Modeling colorectal cancer using CRISPR-Cas9-mediated engineering of human intestinal organoids. *Nat. Med*. 21, 256–262. doi: 10.1038/nm.3802

Maurer, M., Gresnigt, M. S., Last, A., Wollny, T., Berlinghof, F., Pospich, R., et al. (2019). A three-dimensional immunocompetent intestine-on-chip model as in vitro platform for functional and microbial interaction studies. *Biomaterials* 220:119396. doi: 10.1016/j.biomaterials.2019.119396

Mayer, E. A., Tillisch, K., and Gupta, A. (2015). Gut/brain axis and the microbiota. *J. Clin. Investig*. 28, 203–209. doi: 10.1172/JCI76304

Merenda, A., Andersson-Rolf, A., Mustata, R. C., Li, T., Kim, H., and Koo, B. K. (2017). A protocol for multiple gene knockout in mouse small intestinal organoids using a CRISPR-concatemer. *J. Visualiz. Exp*. V125:55916. doi: 10.3791/55916

Millet, M., Messaoud, R., Ben, Luthold, C., and Bordeleau, F. (2019). Coupling microfluidic platforms, microfabrication, and tissue engineered scaffolds to

investigate tumor cells mechanobiology. *Micromachines* 10:418. doi: 10.3390/mi10060418

Miyoshi, H., and Stappenbeck, T. S. (2013). In vitro expansion and genetic modification of gastrointestinal stem cells in spheroid culture. *Nat. Protoc.* 8, 2471–2482. doi: 10.1038/nprot.2013.153

Mosa, M. H., Nicolle, O., Maschalidi, S., Sepulveda, F. E., Bidaud-Meynard, A., Menche, C., et al. (2018). Dynamic formation of microvillus inclusions during enterocyte differentiation in munc18-2–deficient intestinal organoids. *Cell. Mol. Gastroenterol. Hepatol.* 6, 477–493.e1. doi: 10.1016/j.jcmgh.2018.08.001

Nataro, J. P., Hicks, S., Phillips, A. D., Vial, P. A., and Sears, C. L. (1996). T84 cells in culture as a model for enteroaggregative *Escherichia coli* pathogenesis. *Infect. Immun.* 64, 4761–4768. doi: 10.1128/iai.64.11.4761-4768.1996

Nelson, C. M., Jean, R. P., Tan, J. L., Liu, W. F., Sniadecki, N. J., Spector, A. A., et al. (2005). Emergent patterns of growth controlled by multicellular form and mechanics. *Proc. Natl. Acad. Sci. U.S.A.* 102, 11594–11599. doi: 10.1073/pnas.0502575102

Nelson, C. M., Vanduijn M. M., Inman, J. L., Fletcher, D. A., and Bissell, M. J. (2006). Tissue geometry determines sites of mammary branching morphogenesis in organotypic cultures. *Science* 314, 298–300. doi: 10.1126/science.1131000

O'Brien, L. E., Zegers, M. M. P., and Mostov, K. E. (2002). Building epithelial architecture: insights from three-dimensional culture models. *Nat. Rev. Mol. Cell Biol.* 102, 11594–11599. doi: 10.1038/nrm859

Odijk, M., Van Der Meer, A. D., Levner, D., Kim, H. J., Van Der Helm, M. W., Segerink, L. I., et al. (2015). Measuring direct current trans-epithelial electrical resistance in organ-on-a-chip microsystems. *Lab Chip* 15, 745–752. doi: 10.1039/c4lc01219d

Okumura, R., and Takeda, K. (2018). Maintenance of intestinal homeostasis by mucosal barriers. *Inflamm. Regener.* 8:5. doi: 10.1186/s41232-018-0063-z

Orkin, R. W., Gehron, P., McGoodwin, E. B., Martin, G. R., Valentine, T., and Swarm, R. (1977). A murine tumor producing a matrix of basement membrane. *J. Exp. Med.* 145, 204–220. doi: 10.1084/jem.145.1.204

Paine, M. F., Hart, H. L., Ludington, S. S., Haining, R. L., Rettie, A. E., and Zeldin, D. C. (2006). The human intestinal cytochrome P450 "pie." *Drug Metabol. Disposit.* 34, 880–886. doi: 10.1124/dmd.105.008672

Petrey, A. C., and De La Motte, C. A. (2017). The extracellular matrix in IBD: a dynamic mediator of inflammation. *Curr. Opin. Gastroenterol.* 33, 234–238. doi: 10.1097/MOG.0000000000000368

Pinho, S. S., and Reis, C. A. (2015). Glycosylation in cancer: mechanisms and clinical implications. *Nat. Rev. Cancer* 15, 540–555. doi: 10.1038/nrc3982

Poceviciute, R., and Ismagilov, R. F. (2019). Human-gut-microbiome on a chip. *Nat. Biomed. Eng.* 3, 520–531. doi: 10.1038/s41551-019-0425-0

Pocock, K., Delon, L., Bala, V., Rao, S., Priest, C., Prestidge, C., et al. (2017). Intestine-on-a-chip microfluidic model for efficient in vitro screening of oral chemotherapeutic uptake. *ACS Biomater. Sci. Eng.* 3, 951–959. doi: 10.1021/acsbiomaterials.7b00023

Qiao, Y., Shiue, C. N., Zhu, J., Zhuang, T., Jonsson, P., Wright, A. P. H., et al. (2015). AP-1-mediated chromatin looping regulates ZEB2 transcription: new insights into TNFα-induced epithelial-mesenchymal transition in triple-negative breast cancer. *Oncotargetics* 6, 7804–7814. doi: 10.18632/oncotarget.3158

Qin, D., Xia, Y., and Whitesides, G. M. (2010). Soft lithography for micro- and nanoscale patterning. *Nat. Protoc.* 5, 491–502. doi: 10.1038/nprot.2009.234

Quigley, E. M. M. (2011). Microflora modulation of motility. *J. Neurogastroenterol. Motil.* 17, 140–147. doi: 10.5056/jnm.2011.17.2.140

Raimondi, M. T., Albani, D., and Giordano, C. (2019). An organ-on-a-chip engineered platform to study the microbiota–gut–brain axis in neurodegeneration. *Trends Mol. Med.* 25, 737–740. doi: 10.1016/j.molmed.2019.07.006

Rekdal, V. M., Bess, E. N., Bisanz, J. E., Turnbaugh, P. J., and Balskus, E. P. (2019). Discovery and inhibition of an interspecies gut bacterial pathway for Levodopa metabolism. *Science* 364:eaau6323. doi: 10.1126/science.aau6323

Righini-Grunder, F., Soglio, D. D., Faure, C., and Patey, N. (2017). Adequate determination of the transition zone in hirschsprung disease and the role of calretinin staining in clinical practice. *Gastroenterology* 152, S708–S709. doi: 10.1016/s0016-5085(17)32471-x

Round, J. L., and Mazmanian, S. K. (2009). The gut microbiota shapes intestinal immune responses during health and disease. *Nat. Rev. Immunol.* 9, 313–323. doi: 10.1038/nri2515

Rozario, T., and DeSimone, D. W. (2010). The extracellular matrix in development and morphogenesis: a dynamic view. *Dev. Biol.* 341, 126–140. doi: 10.1016/j.ydbio.2009.10.026

Salomon, J., Gaston, C., Magescas, J., Duvauchelle, B., Canioni, D., Sengmanivong, L., et al. (2017). Contractile forces at tricellular contacts modulate epithelial organization and monolayer integrity. *Nat. Commun.* 8:13998. doi: 10.1038/ncomms13998

Sancho, E., Batlle, E., and Clevers, H. (2004). Signaling pathways in intestinal development and cancer. *Annu. Rev. Cell Dev. Biol.* 20, 695–723. doi: 10.1146/annurev.cellbio.20.010403.092805

Sano, E., Mori, C., Matsuoka, N., Ozaki, Y., Yagi, K., Wada, A., et al. (2019). Tetrafluoroethylene-propylene elastomer for fabrication of microfluidic organs-on-chips resistant to drug absorption. *Micromachines* 10:E793. doi: 10.3390/mi10110793

Sansonetti, P. J., Arondel, J., Cantey, J. R., Prévost, M. C., and Huerre, M. (1996). Infection of rabbit Peyer's patches by *Shigella* flexneri: effect of adhesive or invasive bacterial phenotypes on follicle-associated epithelium. *Infect. Immun.* 64, 2752–2764. doi: 10.1128/iai.64.7.2752-2764.1996

Sato, T., Stange, D. E., Ferrante, M., Vries, R. G. J., Van Es, J. H., Van Den Brink, S., et al. (2011a). Long-term expansion of epithelial organoids from human colon, adenoma, adenocarcinoma, and Barrett's epithelium. *Gastroenterology* 141, 1762–1772. doi: 10.1053/j.gastro.2011.07.050

Sato, T., Van Es, J. H., Snippert, H. J., Stange, D. E., Vries, R. G., Van Den Born, M., et al. (2011b). Paneth cells constitute the niche for Lgr5 stem cells in intestinal crypts. *Nature* 469, 415–418. doi: 10.1038/nature09637

Sato, T., Vries, R. G., Snippert, H. J., Van De Wetering, M., Barker, N., Stange, D. E., et al. (2009). Single Lgr5 stem cells build crypt-villus structures in vitro without a mesenchymal niche. *Nature* 459, 262–265. doi: 10.1038/nature07935

Schwank, G., Andersson-Rolf, A., Koo, B. K., Sasaki, N., and Clevers, H. (2013a). Generation of BAC transgenic epithelial organoids. *PLoS ONE* 8:e76871. doi: 10.1371/journal.pone.0076871

Schwank, G., Koo, B. K., Sasselli, V., Dekkers, J. F., Heo, I., Demircan, T., et al. (2013b). Functional repair of CFTR by CRISPR/Cas9 in intestinal stem cell organoids of cystic fibrosis patients. *Cell Stem Cell* 13, 653–658. doi: 10.1016/j.stem.2013.11.002

Scudellari, M. (2016). How iPS cells changed the world. *Nature* 534, 310–312. doi: 10.1038/534310a

Shah, P., Fritz, J. V., Glaab, E., Desai, M. S., Greenhalgh, K., Frachet, A., et al. (2016). A microfluidics-based in vitro model of the gastrointestinal human-microbe interface. *Nat. Commun.* 7:11535. doi: 10.1038/ncomms11535

Sharkey, K. A., Beck, P. L., and McKay, D. M. (2018). Neuroimmunophysiology of the gut: advances and emerging concepts focusing on the epithelium. *Nat. Rev. Gastroenterol. Hepatol.* 15, 765–784. doi: 10.1038/s41575-018-0051-4

Shim, K. Y., Lee, D., Han, J., Nguyen, N. T., Park, S., and Sung, J. H. (2017). Microfluidic gut-on-a-chip with three-dimensional villi structure. *Biomed. Microdev.* 19: 37. doi: 10.1007/s10544-017-0179-y

Shin, W., Hinojosa, C. D., Ingber, D. E., and Kim, H. J. (2019). Human intestinal morphogenesis controlled by transepithelial morphogen gradient and flow-dependent physical cues in a microengineered gut-on-a-chip. *IScience* 15, 391–406. doi: 10.1016/j.isci.2019.04.037

Shin, W., and Kim, H. J. (2018). Intestinal barrier dysfunction orchestrates the onset of inflammatory host-microbiome cross-talk in a human gut inflammation-on-a-chip. *Proc. Natl. Acad. Sci. U.S.A.* 115, E10539–E10547. doi: 10.1073/pnas.1810819115

Shyer, A. E., Tallinen, T., Nerurkar, N. L., Wei, Z., Gil, E. S., Kaplan, D. L., et al. (2013). Villification: how the gut gets its villi. *Science* 342, 212–218. doi: 10.1126/science.1238842

Sicard, J. F., Bihan, G., Le, Vogeleer, P., Jacques, M., and Harel, J. (2017). Interactions of intestinal bacteria with components of the intestinal mucus. *Front. Cell. Infect. Microbiol.* 7:387. doi: 10.3389/fcimb.2017.00387

Simon-Assmann, P., Kedinger, M., De Arcangelis, A., Rousseau, V., and Simo, P. (1995). Extracellular matrix components in intestinal development. *Experientia* 51, 883–900. doi: 10.1007/BF01921739

Simon-Assmann, P., Lefebvre, O., Bellissent-Waydelich, A., Olsen, J., Orian-Rousseau, V., and De Arcangelis, A. (1998). The laminins: role in intestinal morphogenesis and differentiation. *Ann. N. Y. Acad. Sci.* 859, 46–64. doi: 10.1111/j.1749-6632.1998.tb11110.x

Solé, X., Crous-Bou, M., Cordero, D., Olivares, D., Guinó, E., Sanz-Pamplona, R., et al. (2014). Discovery and validation of new potential biomarkers for early detection of colon cancer. *PLoS ONE* 9:e106748. doi: 10.1371/journal.pone.0106748

Solomon, L., Mansor, S., Mallon, P., Donnelly, E., Hoper, M., Loughrey, M., et al. (2010). The dextran sulphate sodium (DSS) model of colitis: an overview. *Compar. Clin. Pathol.* 19, 235–239. doi: 10.1007/s00580-010-0979-4

Sontheimer-Phelps, A., Chou, D. B., Tovaglieri, A., Ferrante, T. C., Duckworth, T., Fadel, C., et al. (2020). Human colon-on-a-chip enables continuous in vitro analysis of colon mucus layer accumulation and physiology. *Cell. Mol. Gastroenterol. Hepatol.* 9, 507–526. doi: 10.1016/j.jcmgh.2019.11.008

Spence, J. R., Mayhew, C. N., Rankin, S. A., Kuhar, M. F., Vallance, J. E., Tolle, K., et al. (2011). Directed differentiation of human pluripotent stem cells into intestinal tissue in vitro. *Nature* 470, 105–109. doi: 10.1038/nature09691

Stewart, D. C., Berrie, D., Li, J., Liu, X., Rickerson, C., Mkoji, D., et al. (2018). Quantitative assessment of intestinal stiffness and associations with fibrosis in human inflammatory bowel disease. *PLoS ONE* 13:e0200377. doi: 10.1371/journal.pone.0200377

Sumigray, K. D., Terwilliger, M., and Lechler, T. (2018). Morphogenesis and compartmentalization of the intestinal crypt. *Dev. Cell.* 45, 183–197.e5. doi: 10.1016/j.devcel.2018.03.024

Sun, H., Chow, E. C. Y., Liu, S., Du, Y., and Pang, K. S. (2008). The Caco-2 cell monolayer: usefulness and limitations. *Exp. Opin. Drug Metabol. Toxicol.* 4, 395–411. doi: 10.1517/17425255.4.4.395

Sung, J. H., Yu, J., Luo, D., Shuler, M. L., and March, J. C. (2011). Microscale 3-D hydrogel scaffold for biomimetic gastrointestinal (GI) tract model. *Lab Chip* 11, 389–392. doi: 10.1039/c0lc00273a

Sunuwar, L., Yin, J., Kasendra, M., Karalis, K., Kaper, J., Fleckenstein, J., et al. (2020). Mechanical stimuli affect *Escherichia coli* heat-stable enterotoxin-cyclic GMP signaling in a human enteroid intestine-chip model. *Infect. Immun.* 88, e00866–e00719. doi: 10.1128/IAI.00866-19

Takahashi, K., Tanabe, K., Ohnuki, M., Narita, M., Ichisaka, T., Tomoda, K., et al. (2007). Induction of pluripotent stem cells from adult human fibroblasts by defined factors. *Cell* 131, 861–872. doi: 10.1016/j.cell.2007.11.019

Takahashi, K., and Yamanaka, S. (2006). Induction of pluripotent stem cells from mouse embryonic and adult fibroblast cultures by defined factors. *Cell* 126, 663–676. doi: 10.1016/j.cell.2006.07.024

Takahashi, K., and Yamanaka, S. (2013). Induced pluripotent stem cells in medicine and biology. *Development (Cambridge)* 140, 2457–2461. doi: 10.1242/dev.092551

Teller, I. C., Auclair, J., Herring, E., Gauthier, R., Ménard, D., and Beaulieu, J. F. (2007). Laminins in the developing and adult human small intestine: relation with the functional absorptive unit. *Dev. Dynam.* 236, 1980–1990. doi: 10.1002/dvdy.21186

Tezcan, D. S., De Munck, K., Pham, N., Luhn, O., Aarts, A., De Moor, P., et al. (2006). "Development of vertical and tapered via etch for 3D through wafer interconnect technology," in *Proceedings of the Electronic Packaging Technology Conference* (Singapore: IEEE), doi: 10.1109/EPTC.2006.342685

Thelen, K., and Dressman, J. B. (2009). Cytochrome P450-mediated metabolism in the human gut wall. *J. Pharm. Pharmacol.* 61, 541–558. doi: 10.1211/jpp.61.05.0002

Thorne, C. A., Chen, I. W., Sanman, L. E., Cobb, M. H., Wu, L. F., and Altschuler, S. J. (2018). Enteroid monolayers reveal an autonomous WNT and BMP circuit controlling intestinal epithelial growth and organization. *Dev. Cell.* 44, 624–633.e4. doi: 10.1016/j.devcel.2018.01.024

Thummel, K. E. (2007). Gut instincts: CYP3A4 and intestinal drug metabolism. *J. Clin. Investig.* 117, 3173–3176. doi: 10.1172/JCI34007

Tomasek, J. J., Gabbiani, G., Hinz, B., Chaponnier, C., and Brown, R. A. (2002). Myofibroblasts and mechano: regulation of connective tissue remodelling. *Nat. Rev. Mol. Cell Biol.* 3, 349–363. doi: 10.1038/nrm809

Tong, Z., Martyn, K., Yang, A., Yin, X., Mead, B. E., Joshi, N., et al. (2018). Towards a defined ECM and small molecule based monolayer culture system for the expansion of mouse and human intestinal stem cells. *Biomaterials* 154, 60–73. doi: 10.1016/j.biomaterials.2017.10.038

Totonelli, G., Maghsoudlou, P., Garriboli, M., Riegler, J., Orlando, G., Burns, A. J., et al. (2012). A rat decellularized small bowel scaffold that preserves villus-crypt architecture for intestinal regeneration. *Biomaterials* 33, 3401–3410. doi: 10.1016/j.biomaterials.2012.01.012

Tovaglieri, A., Sontheimer-Phelps, A., Geirnaert, A., Prantil-Baun, R., Camacho, D. M., Chou, D. B., et al. (2019). Species-specific enhancement of enterohemorrhagic *E. coli* pathogenesis mediated by microbiome metabolites. *Microbiome* 7:43. doi: 10.1186/s40168-019-0650-5

Trowers, E., and Tischler, M. (2014). *Gastrointestinal Physiology: A Clinical Approach*. Berlin: Springer, doi: 10.1007/978-3-319-07164-0

Tsamandouras, N., Chen, W. L. K., Edington, C. D., Stokes, C. L., Griffith, L. G., and Cirit, M. (2017). Integrated Gut and liver microphysiological systems for quantitative in vitro pharmacokinetic studies. *AAPS J.* 19, 1499–1512. doi: 10.1208/s12248-017-0122-4

Van De Wetering, M., Francies, H. E., Francis, J. M., Bounova, G., Iorio, F., Pronk, A., et al. (2015). Prospective derivation of a living organoid biobank of colorectal cancer patients. *Cell* 161, 933–945. doi: 10.1016/j.cell.2015.03.053

Vernetti, L., Gough, A., Baetz, N., Blutt, S., Broughman, J. R., Brown, J. A., et al. (2017). Functional coupling of human microphysiology systems: intestine, liver, kidney proximal tubule, blood-brain barrier and skeletal muscle. *Sci. Res.* 7:42296. doi: 10.1038/srep42296

Vickerman, V., Blundo, J., Chung, S., and Kamm, R. (2008). Design, fabrication and implementation of a novel multi-parameter control microfluidic platform for three-dimensional cell culture and real-time imaging. *Lab Chip* 8, 1468–1477. doi: 10.1039/b802395f

Walton, K. D., Whidden, M., Kolterud, A., Shoffner, S. K., Czerwinski, M. J., Kushwaha, J., et al. (2016). Villification in the mouse: Bmp signals control intestinal villus patterning. *Development (Cambridge)* 143, 427–436. doi: 10.1242/dev.130112

Wang, Y., DiSalvo, M., Gunasekara, D. B., Dutton, J., Proctor, A., Lebhar, M. S., et al. (2017a). Self-renewing monolayer of primary colonic or rectal epithelial cells. *Cell. Mol. Gastroenterol. Hepatol.* 4, 165–182.e7. doi: 10.1016/j.jcmgh.2017.02.011

Wang, Y., Gunasekara, D. B., Reed, M. I., DiSalvo, M., Bultman, S. J., Sims, C. E., et al. (2017b). A microengineered collagen scaffold for generating a polarized crypt-villus architecture of human small intestinal epithelium. *Biomaterials* 128, 44–55. doi: 10.1016/j.biomaterials.2017.03.005

Wang, Y., Kim, R., Sims, C. E., and Allbritton, N. L. (2019a). Building a thick mucus hydrogel layer to improve the physiological relevance of in vitro primary colonic epithelial models. *Cell. Mol. Gastroenterol. Hepatol.* 8, 653–655.e5. doi: 10.1016/j.jcmgh.2019.07.009

Wang, Y., Song, W., Wang, J., Wang, T., Xiong, X., Qi, Z., et al. (2019b). Single-cell transcriptome analysis reveals differential nutrient absorption functions in human intestine. *J. Exp. Med.* 217:e20191130. doi: 10.1084/jem.20191130

Wells, J. M., and Spence, J. R. (2014). How to make an intestine. *Development (Cambridge)* 141, 752–760. doi: 10.1242/dev.097386

Williamson, I. A., Arnold, J. W., Samsa, L. A., Gaynor, L., DiSalvo, M., Cocchiaro, J. L., et al. (2018). A high-throughput organoid microinjection platform to study gastrointestinal microbiota and luminal physiology. *Cell. Mol. Gastroenterol. Hepatol.* 6, 301–319. doi: 10.1016/j.jcmgh.2018.05.004

Wilson, S. S., Tocchi, A., Holly, M. K., Parks, W. C., and Smith, J. G. (2015). A small intestinal organoid model of non-invasive enteric pathogen-epithelial cell interactions. *Mucosal Immunol.* 8, 352–361. doi: 10.1038/mi.2014.72

Xi, W., Saw, T. B., Delacour, D., Lim, C. T., and Ladoux, B. (2019). Material approaches to active tissue mechanics. *Nat. Rev. Mater.* 4, 23–44. doi: 10.1038/s41578-018-0066-z

Yin, X., Mead, B. E., Safaee, H., Langer, R., Karp, J. M., and Levy, O. (2016). Engineering stem cell organoids. *Cell Stem Cell* 18, 25–38. doi: 10.1016/j.stem.2015.12.005

Conflict of Interest: The authors declare that the research was conducted in the absence of any commercial or financial relationships that could be construed as a potential conflict of interest.

frontiers in Bioengineering and Biotechnology

ORIGINAL RESEARCH
published: 31 August 2020
doi: 10.3389/fbioe.2020.00992

Bioengineering Novel *in vitro* Co-culture Models That Represent the Human Intestinal Mucosa With Improved Caco-2 Structure and Barrier Function

*Nicole J. Darling[1], Claire L. Mobbs[1,2], Ariana L. González-Hau[1], Matthew Freer[1] and Stefan Przyborski[1,2]**

[1] Department of Biosciences, Durham University, Durham, United Kingdom, [2] Reprocell Europe Ltd, Sedgefield, United Kingdom

OPEN ACCESS

Edited by:
María García-Díaz, Institute for Bioengineering of Catalonia (IBEC), Spain

Reviewed by:
Marco Metzger, Fraunhofer Society (FHG), Germany
Bruno Sarmento, University of Porto, Portugal

***Correspondence:**
Stefan Przyborski
stefan.przyborski@durham.ac.uk

Specialty section:
This article was submitted to Tissue Engineering and Regenerative Medicine, a section of the journal Frontiers in Bioengineering and Biotechnology

Received: *28 February 2020*
Accepted: *29 July 2020*
Published: *31 August 2020*

Citation:
Darling NJ, Mobbs CL, González-Hau AL, Freer M and Przyborski S (2020) Bioengineering Novel in vitro Co-culture Models That Represent the Human Intestinal Mucosa With Improved Caco-2 Structure and Barrier Function. Front. Bioeng. Biotechnol. 8:992. doi: 10.3389/fbioe.2020.00992

The Caco-2 monolayer is the most widely used *in vitro* model of the human intestinal mucosa to study absorption. However, models lack communication from other cells present in the native intestine, such as signals from fibroblasts in the lamina propria. In this study, we have investigated the effects of fibroblasts upon the Caco-2 epithelium through two mechanisms: indirect signaling from fibroblasts and direct contact with fibroblasts. Culture of Caco-2 cells with paracrine signals from fibroblasts, through the use of conditioned media, did not induce a significant change in epithelial cell morphology or function. To examine the effects of direct contact between the epithelium and fibroblasts, we developed novel, humanized three-dimensional (3D) co-culture models whereby Caco-2 cells are grown on the surface of a subepithelial-like tissue construct containing intestinal or dermal fibroblasts. In our models, we observed endogenous extracellular matrix production from the fibroblasts that provides support to the above epithelium. The Caco-2 epithelium displayed morphological changes in 3D co-culture including enhanced polarization and the formation of a basement membrane-like attachment to the underlying stromal compartment. An important structural alteration was the significantly straightened lateral membrane that closely mimics the structure of the *in vivo* intestinal mucosa. This enhanced lateral membrane phenotype, in correlation with an reduction in TEER to levels more similar to the human intestine, is thought to be responsible for the increased paracellular permeability observed in 3D co-cultures. Our results demonstrate that direct contact between epithelial and mesenchymal cells results in an enhanced epithelial barrier. The *in vitro* models described herein have the potential to be used for studying intestinal epithelial-fibroblast interactions and could provide more accurate tools for drug permeability studies.

Keywords: Caco-2, fibroblast, 3D co-culture, epithelium, *in vitro*, intestinal, extracellular-matrix, human

INTRODUCTION

The study of intestinal function greatly relies on animal models. With an increasing demand to replace animal use in science, coupled with a lack of availability of *ex vivo* human tissue, *in vitro* intestinal alternatives are utilized to understand complex cellular processes such as drug-permeability and toxicity in a simplified format. The current gold-standard *in vitro* model used extensively throughout academia and industry for over 30 years is the Caco-2 monolayer. This Transwell® -based culture system is one of the most extensively studied *in vitro* cell models due to its ability to form well-differentiated and polarized cell monolayers as surrogates for the human intestinal epithelium (Hidalgo et al., 1989). Although simple in design, Caco-2 monolayers possess important structural and functional characteristics of intestinal enterocytes, making them an attractive cell-line for investigating drug absorption. However, the models have many limitations which emanate from its adenocarcinoma origin and the simplicity of a monolayer culture system that lacks the complexity found in human tissue. For example, Caco-2 monolayers exhibit poor paracellular permeability to hydrophilic compounds as well as altered expression of efflux transporters, resulting in inaccuracy extrapolating *in vitro* permeability data to human tissue. Other limitations of the monolayer include abnormal cuboidal cell morphology as well as significantly heightened TEER compared to that of the normal human intestine.

Throughout the gastrointestinal tract there is a consistent quadruple layered structure comprising of a serosa, a muscularis propria, a submucosa and the innermost mucosa layer. The mucosa is defined as a layer of epithelial cells resting on a basement membrane supported by stromal cells. In the intestinal mucosa, the epithelial monolayer is situated above an extracellular matrix (ECM)-rich lamina propria, consisting of stromal cells, collagens, glycoproteins, and proteoglycans, separated by a protein-rich basement membrane. The ECM provides not only a physical scaffold for the cells but also mechanical and chemical signals fundamental to cellular processes (Kim et al., 2016). Epithelial-mesenchymal and epithelial-ECM interactions are essential for normal epithelial proliferation, differentiation and function (Dignass et al., 1994). Subepithelial fibroblasts directly influence the epithelial barrier through secretion of growth factors and cytokines, as well as indirectly through deposition of the ECM. The composition of the ECM affects enterocyte growth and function both *in vivo* and *in vitro* (Basson, 2001; Halttunen et al., 1996; Sanderson et al., 1996). Although the exact fibroblast secretome requires further elucidation, factors including transforming growth factor, keratinocyte growth factor, and epidermal growth factor are understood to influence the intestinal epithelial cells (Halttunen et al., 1996; Kim et al., 2012).

The most significant drawback of monolayer culture systems thus stems from the lack of complex, multicellular microenvironments that exist within the *in vivo* tissue. Recent models have sought to advance on these monolayer cultures either through the introduction of additional cell types or by using more complex tissue culture substrates. Most co-culture models include mucous secreting cells, immune components or fibroblasts, all of which have resulted in an enhanced epithelial layer (Béduneau et al., 2014; Pereira et al., 2015). One of the most common cell types added into Transwell® co-cultures is the mucous-secreting cell line, HT29-MTX. Addition of these epithelial cells enables the influence of a mucous layer on the transport of compounds to be studied and it has been demonstrated that inclusion of these cells resulted in a higher correlation of passive permeability of hydrophilic compounds with the fraction absorbed in humans (Walter et al., 1996; Hilgendorf et al., 2000).

Stromal cells have also been included in co-culture models with Caco-2; mouse embryonic fibroblasts are frequently used to represent intestinal fibroblasts in these culture systems. Addition of fibroblasts in a collagen gel has been demonstrated to reduce TEER and alkaline phosphatase activity to more *in vivo*-like levels (Zhang et al., 2019). One of the most complex models has included Caco-2, HT29-MTX, mouse embryonic fibroblasts and immune components embedded within collagen gels and have shown an enhanced epithelial function with an increased absorptive permeability correlation to the human fraction absorbed (Li et al., 2013). However the fibroblasts used in these models are not of human origin and the stromal compartments lack in-depth characterization. Furthermore, these models lack the columnar and polarized epithelium like that of *in vivo* tissue. Although additional cell types enable a more accurate reconstitution of intestinal tissue, the use of animal-derived cells results in discrepancies when compared to the human intestine.

Further advances using the Transwell® system have sought to use alternative culture substrates to support the growth of cells. Enhanced culture substrates most commonly utilize hydrogels, collagen-coated surfaces or nanofiber scaffolds, recapitulating *in vivo*-like structures (Holland-Cunz et al., 2004; Jabaji et al., 2014; Yi et al., 2017; Patient et al., 2019). As the most abundant ECM component, collagen I containing substrates in particular, successfully enhance enterocyte layer formation (Li et al., 2013; Jabaji et al., 2014). Collagen gels have also been adapted to recreate the villi structure observed in the intestine, leading to varying degrees of Caco-2 cell differentiation along the villus and increased permeability to hydrophilic compounds (Yu et al., 2012). HT29-MTX cells have also been included in such models and have the potential to be adapted to study bacterial attachment and invasion within the epithelium (Costello et al., 2014). Nevertheless, many of these gels remain poorly defined; they are mostly animal-derived, and display high variability. An additional concern with collagen gels is degradation, Caco-2 cells frequently invaded into degraded collagen structures resulting in the formation of structural abnormalities such as multilayers. Furthermore, some of the proteinaceous substrates commonly used consist of one or more ECM components, but also neglect other major ECM constituents such as fibronectin, which is implicated in epithelial attachment and integrity and is therefore essential in simulating the formation of *in vivo*-like tissue constructs (Kolachala et al., 2007).

In this paper, we have investigated the effect of two human fibroblast lineages of different tissue origins on the Caco-2 monolayer and have sought to determine whether secreted paracrine factors or direct contact with fibroblasts

has greater effect on the epithelial structure and function. Herein, we present novel, three-dimensional human co-culture systems that more accurately simulate mucosal tissue layers representative of human intestine. These physiologically relevant, fully humanized mucosal constructs supplant previous models as they allow for abundant *in situ* ECM deposition by resident human fibroblasts, prominent basement membrane formation, as well as *in vivo* like epidermal lateral membrane morphology. Cell lines utilized for these models are routinely used and commercially available, making model reproducibility accessible in other laboratories. We hypothesize that the physical presence of fibroblasts co-cultured in 3D immediately adjacent to the epithelium will enhance enterocyte structure and function more than fibroblast conditioned media alone. Our intestinal models have been characterized structurally and functionally with direct comparison to human intestinal tissue. In doing so, we will investigate the effects of fibroblasts on enterocyte lateral membrane morphology: a phenomenon that until now, has not been previously reported in the literature. We propose that our humanized, robust and reproducible models will provide more accurate research tools for drug-permeability assays as well as the study of biological and biochemical processes in the intestinal mucosa. This relatively simple system overcomes the intricacies and expensive cell-culture expertise required by other *in vitro* models, such as organoid-based systems, whilst retaining the ability to closely reproduce features of the native human intestinal mucosa (Schweinlin et al., 2016).

MATERIALS AND METHODS

Cell Maintenance

Caco-2 cells (861010202, ECACC, Porton Down, United Kingdom), CCD-18co (CRL-1459, ATCC, Middlesex, United Kingdom) and neonatal human dermal fibroblasts (HDFn, C0045C, Life Technologies, Fisher, Loughborough, United Kingdom) were maintained in T175 flasks (Greiner Bio-One, Kremsmunseter, Austria) in complete DMEM (Fisher), containing 10% fetal bovine serum (Fisher), 2 mM L-glutamine (Fisher) and 1% penicillin/streptomycin (Fisher) at 37°C, 5% CO_2 and 95% humidity. Cells were passaged at 80% confluence using 0.25% Trypsin EDTA (Fisher).

Transwell® Cultures

Caco-2 cells were seeded at a density of 2.5×10^5 onto Transwell® polycarbonate filter supports (0.4 μm pore size, 12 mm diameter) (Fisher). Seeding density was optimized from previously published Caco-2 protocols that seeded 2.6×10^5 cells per insert (Hubatsch et al., 2007). Cells cultured for a minimum of 21 days before analysis. Media was replaced every 2 days of culture with either fresh DMEM or fibroblast conditioned DMEM.

Collection of Conditioned Media

Conditioned media was collected from both CCD-18co and HDFn fibroblasts. Once cells had grown to 80% confluence, fresh media was applied to the cells. After 48 h media samples were collected, centrifuged and sterile filtered through 0.2 μm filters to remove any cells or debris. Conditioned media was mixed 1:1 with fresh media before application to Transwell® models.

3D Co-culture of Fibroblasts and Caco-2 Cells

To develop a viable co-culture model, robust foundations were first developed onto which Caco-2 cells were then seeded. 12-well Alvetex® Scaffold inserts (Reprocell Europe, United Kingdom) were prepared according to manufacturer's instructions. Fibroblasts were counted by the Trypan Blue exclusion assay and 0.5×10^6 cells were seeded onto the inserts and were cultured in complete DMEM for 14 days with media changes every 3–4 days. HDFn cells were supplemented with 5 ng/mL TGF-β1 (Life Technologies) and 100 μg/mL ascorbic acid (Sigma-Aldrich, United Kingdom) to generate a sufficient cell population to allow the epithelial cells to be cultured on the surface. Additional supplements to the 3D culture of CCD-18co cells did not result in a confluent subepithelial compartment and instead, had an additional 0.5×10^6 cells seeded at days 7 and 9 of culture to ensure sufficient fibroblasts were present within the scaffold. Caco-2 cells were then seeded onto 3D fibroblast cultures at a density of 0.4×10^6 cells/insert and were maintained in complete DMEM without any supplements for a further 21 days.

Paraffin Embedding and H&E Staining

In vitro models were washed in PBS prior to fixation in 4% paraformaldehyde (Fisher) for 2 h. Samples were dehydrated through a series of ethanols, followed by incubation in Histoclear (National Diagnostics, United States) then in 1:1 Histoclear:wax. Models were further incubated in wax before embedding and sectioning.

Paraffin sections were deparaffinized in Histoclear and rehydrated to dH_2O before being stained in Mayer's Hematoxylin (Sigma-Aldrich) for 5 min. Slides were then washed in dH_2O and submerged in alkaline EtOH to blue the nuclei. Samples were dehydrated to 95% EtOH counter-stained in Eosin followed by dehydration to 100% EtOH. Slides were cleared twice in Histoclear and mounted in Omni-mount (National Diagnositcs) before imaging on a Leica microscope.

Transmission Electron Microscopy

Tissue models were examined by transmission electron microscopy (TEM) by following standard procedures. Briefly, samples were fixed in Karnovsky's fixative followed by post-fixation in 1% Osmium Tetroxide and ethanol dehydration and subsequently in Epon resin. Semi-thin (1 μm) sections were stained with toluidine blue and examined by light microscopy. Ultra-thin sections were stained with uranyl acetate and lead citrate and viewed under a Hitachi H7600 electron microscope.

Scanning Electron Microscopy

Samples were fixed in Karnovsky fixative and osmium tetroxide and dehydrated through ethanol series as described for TEM sample preparation above. Samples were then critical point dried,

attached onto silicon chips and sputter coated with platinum. Coated samples were imaged on a Hitachi S5200 field emission scanning electron microscope (SEM).

Immunofluorescent Staining

Paraffin embedded samples were deparaffinized in Histoclear and rehydrated through 100%, 95 and 70% ethanol and PBS. Antigen retrieval was performed by incubation in citrate buffer at 95°C for 20 min. Samples were blocked in 20% newborn calf serum (Fisher) in 0.4% triton-X-100 PBS for 1 h. Primary antibodies (occludin sc-13256 and vimentin sc-6260 Santa Cruz Biotechnology; *E*-Cadherin #610181 BD biosciences; fibronectin ab23750; collagen I ab34710 and III ab7778 Abcam), diluted 1:100 in blocking buffer were added at concentrations recommended by the manufacture and incubated at 4°C overnight. Slides were washed x3 in PBS, incubated in secondary antibodies (donkey anti-mouse 488 A21202, donkey anti-rabbit 594 A21207, Invitrogen) diluted 1:1000 in blocking buffer for 1 h, washed again x3 in PBS before mounting in Vectashield with DAPI (Vector Labs, Peterborough, United Kingdom) and imaging on the Zeiss 880 confocal microscope.

TEER Measurements

The integrity of the Caco-2 monolayer was determined by measuring the transepithelial electrical resistance (TEER) using an EVOM2 Voltohmeter with STX2 Chopstick probes. The final TEER value was determined by subtracting the TEER measurement from a blank Transwell® insert and multiplying by the cell culture surface area (Equation 1):

$$TEER(\Omega.cm^2) = (\Omega\, Cell\ Layer - \Omega\ Blank\, Insert) \times Insert\ Surface\ Area\ cm^2 \quad (1)$$

Permeability of Model Compounds Across the Epithelial Barriers

Transport studies were conducted in a standard Ussing chamber system (WPI, United Kingdom). Lucifer yellow (Sigma-Aldrich) was reconstituted in PBS (Sigma-Aldrich) and used at a final concentration of 100 μM. TEER was measured throughout the assay period to ensure continued model integrity throughout experimentation. Transport assays were conducted in HBSS, 2% Glucose *(v/v)* and maintained at 37°C by use of circulating water bath. Carbogen (95%, O_2, 5% CO_2,) (BOC, UK) was used to oxygenate assay solutions and circulate fluid across model epithelia. Drug compounds were added to the apical compartments (donor) at the beginning of the assay and samples were taken from the basolateral (receiver) compartment after 120 min. Apparent permeability of the models was calculated according to Equation 2:

$$Papp\ (cm/s) = \frac{V_R * dC_R}{dt * A * C_{D0}} \quad (2)$$

Where VR is the volume of the receiver compartment dC_R/dt is the change in the analyte concentration of the receiver compartment over time, A is the area of the transport interface and C_{D0} is the concentration of the donor compartment at time zero.

Human Tissue Acquisition and Use

Fixed human intestinal tissues were collected by Biopta (Glasgow, United Kingdom) under appropriate ethical protocols in compliance with local laws and regulations. Tissues were received at Durham University under a formal MTA agreement and were processed following relevant UK HTA rules and guidelines at the time of publication.

Statistical Analysis

All statistical analysis was done using Graphpad Prism 5 software by One-way ANOVA with Dunnetts post-test multiple comparison analysis using the Caco-2 monolayer on Transwell® as the control. All values reported are averages ± SEM. The number of independent experiments in each instance (n) is noted in the figure legend.

RESULTS

Construction of the Intestinal Models

Caco-2 cells are an extensively used cell line that can be differentiated into enterocyte-like cells of the small intestine when cultured for 21 days upon a porous Transwell® polycarbonate membrane (**Figure 1A**). To investigate the effects of stromal cells on the structure and function of the epithelial cells, we employed two culture methods: paracrine factors from fibroblast conditioned media derived from 2D cultured fibroblasts or direct co-culture with fibroblasts grown in 3D. Two different fibroblast cell types of human origin were selected for this study: CCD-18co intestinal myofibroblast cells or HDFn skin fibroblasts. CCD-18co cells are one of the few commercially available intestinal fibroblast lineages and are thus widely used in the literature in co-cultures with Caco-2 cells that mimic the small intestinal function. They were selected as they are derived from the human colon and as such are a close match for Caco-2 cells which are also colonic in origin. Dermal fibroblasts are often used as a comparison to intestinal fibroblasts and their non-intestinal origin was used to test the importance of tissue-specific fibroblasts.

To examine the effects of fibroblast derived signals on the epithelium, conditioned media collected from either CCD-18co intestinal myofibroblast cells or HDFn skin fibroblasts and was mixed 1:1 with fresh media and applied to Transwell® cultures every 2 days for 21 days. The second method was to allow the epithelial and stromal cells to have direct physical contact by developing a 3D co-culture model utilizing Alvetex® Scaffold, an inert, porous polystyrene polyHIPE (**Figure 1B**). Fibroblast cells (CCD-18co or HDFn) were seeded onto the scaffold and were allowed to infiltrate the membrane for 14 days creating a robust foundation for Caco-2 growth. To achieve this, sequential seeding of CCD-18co cells was required as previously described while HDFn cells required additional supplementation of TGF and ascorbic acid. The overall outcome was the formation of a densely populated fibroblast compartment that could support

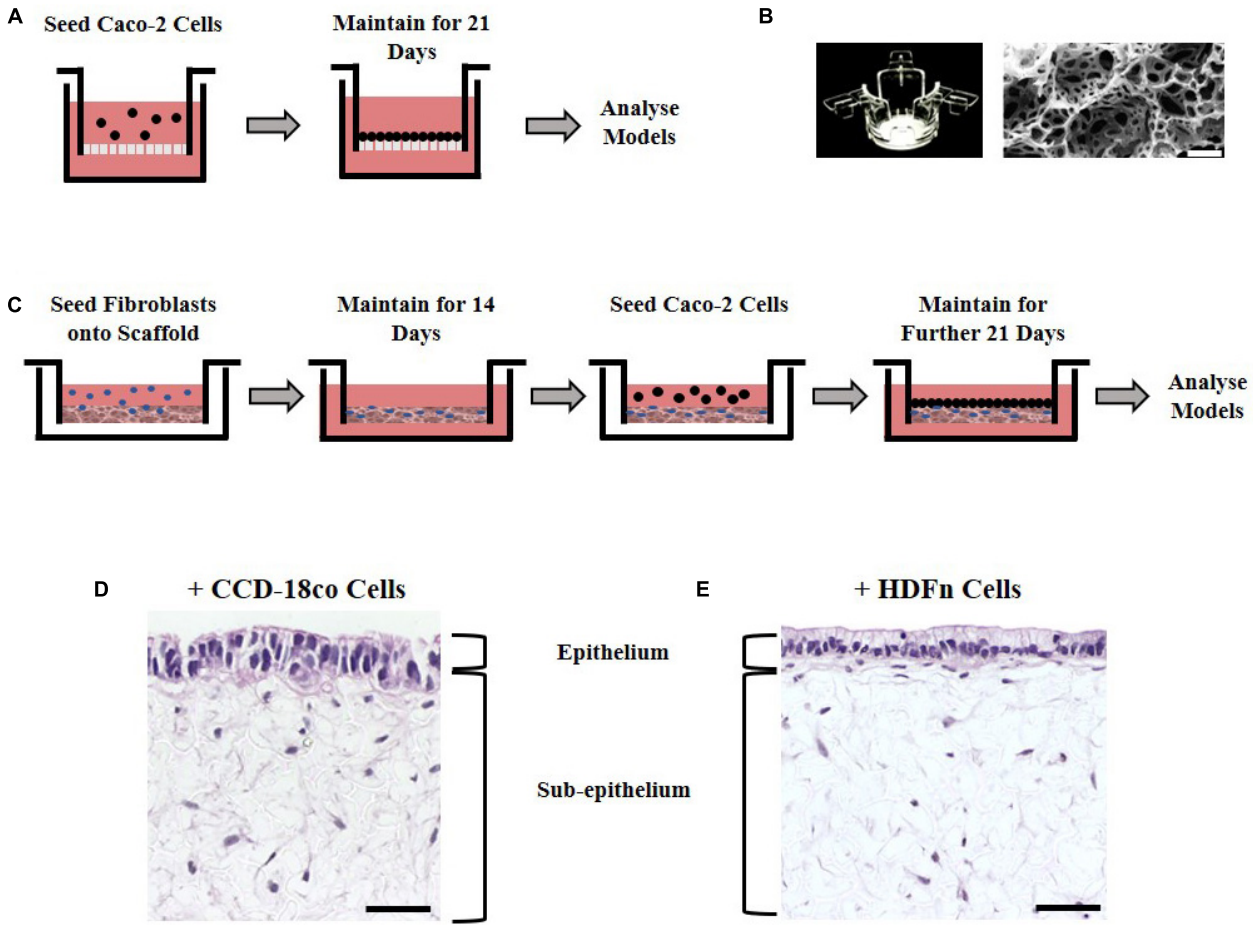

FIGURE 1 | Experimental set up in building models of the intestine. **(A)** Schematic representation of Caco-2 cell culture methodology on Transwell® inserts. **(B)** Alvetex® well insert and scanning electron micrographs showing the structure of the Alvetex® Scaffold membrane used in the co-culture models. **(C)** Schematic protocol depicting how fibroblast and epithelial cells were grown together in the 3D co-culture models. **(D)** H&E images of the resulting 3D co-culture models showing Caco-2 cells growing on top of Alvetex® Scaffold populated with either one of the two types of fibroblasts tested: **(D)** CCD-18co; **(E)** HDFn. Scale bars: 50 μm.

the growth and differentiation of Caco-2 cells. Following the establishment of a 3D stomal cell component, Caco-2 cells were seeded onto the surface and cultured for a further 21 days to allow enterocyte differentiation to occur (**Figure 1C**); the resulting co-culture models show the scaffold populated with fibroblasts and an epithelial monolayer of Caco-2 cells on the surface in contact with the fibroblasts (**Figures 1D,E**).

3D Co-culture Systems Provide a More Structurally Relevant *in vitro* Model When Compared to Human Tissues and Transwell® Controls

Histological analysis of the *in vitro* models showed that Caco-2 cells form a monolayer of cells when cultured on Transwell® membranes or on top of fibroblast cells (**Figure 2**). A brush-border can be observed through toluidine blue staining in all models indicating that the cells have differentiated into mature enterocytes with potential absorptive functions. Epithelial structural morphology did not significantly change with the addition of paracrine factors from fibroblast-conditioned media; however, cells show a significantly more elongated columnar phenotype when co-cultured with fibroblast cells in 3D culture. This enhanced polarization of the epithelium is more comparable to the *in vivo* intestine and is significantly altered compared to control Transwell® -based models.

Fibroblasts Provide Support to the Overlying Epithelium

Direct co-culture of stromal and epithelial cells initially required the formation of a robust support onto which Caco-2 cells can grow. Fibroblasts populate throughout the Alvetex® Scaffold membrane and build up on the surface of the scaffold (**Figure 3A**), generating the equivalent of a subepithelial compartment and acting as a foundation to provide structural support to the above enterocytes. Long-term differentiation of the fibroblasts in 3D (minimum of 14 days) is required to allow fibroblasts to layer on the surface of the membrane and to prevent epithelial cells infiltrating into the scaffold (**Figure 3B**).

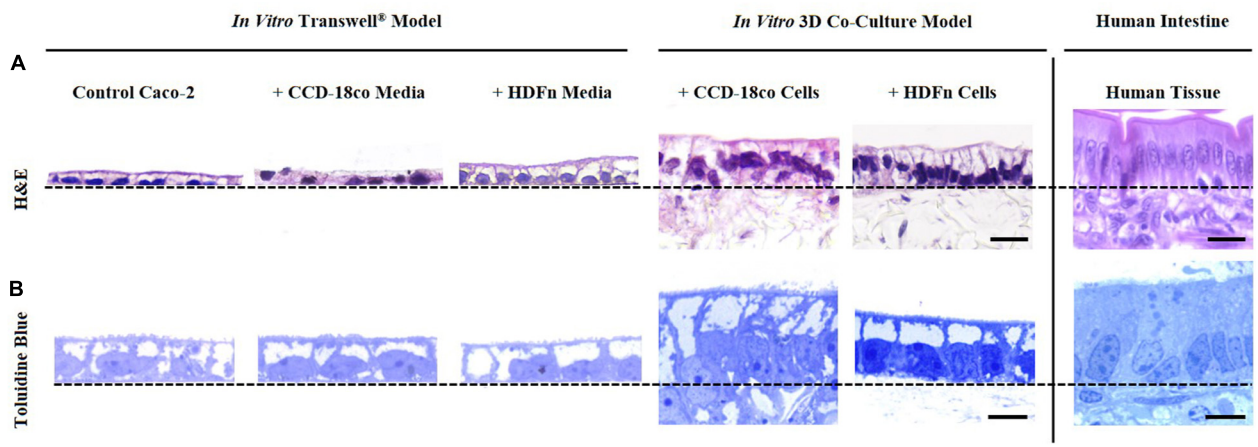

FIGURE 2 | Morphological assessment of Caco-2 epithelia under alternate growth conditions. **(A)** H&E and **(B)** toluidine blue staining of control models where Caco-2 cells were cultured on either Transwell® membranes alone; Transwell® models cultured in conditioned medium from CCD-18co or HDFn fibroblasts; or Caco-2 cells in direct co-culture with the two types of fibroblasts on Alvetex® Scaffold. Representative H&E and toluidine blue images of human small intestinal tissues are also shown for comparison. Note how the Caco-2 cell morphology changes and cells become more columnar, particularly in the 3D co-culture models. Scale bars: 20 μm **(A)** and 5 μm **(B)**.

Culture of Caco-2 cells on Alvetex® Scaffold without the support of the fibroblasts resulted in infiltration of the epithelium into the porous membrane and a loss of the monolayer structure (data not shown). Caco-2 cells formed a continuous monolayer when seeded on the surface of the 3D fibroblast culture. On the surface they exhibited a cobble stone morphology, typical of the apical pole of epithelial cells (**Figure 3C**), with clear evidence of microvilli associated with glycocalyx, a carbohydrate-rich coating over the surface of epithelial cells of the digestive tract (**Figure 3D**). TEM ultrastructural analysis highlights apical junctions in addition to electron dense layers at the base of the epithelial layer demonstrating the formation of a tri-lamina basement membrane between the epithelium and underlying fibroblasts and emphasizing the direct contact between the two cell populations (**Figures 3E,F**). No contact of Caco-2 enterocytes with the Alvetex® Scaffold was found through TEM analysis. Cellular interaction between the fibroblasts and enterocytes appears evident under closer analysis, with clear vesicle transfer between the two cell populations (**Figure 3F**, inset).

Fibroblasts Secrete Extracellular Matrix Proteins Within the Subepithelial Compartment

Immunofluorescent analysis (**Figure 4**) demonstrated that Caco-2 cells express the junctional markers occludin and *E*-cadherin, components of tight junctions and adherens junctions respectively. Occludin is present at the apical part of the cells while *E*-cadherin appears to be localized to the lateral membranes, in the same localization as in the intestine *in vivo*. Vimentin staining indicated the distribution of fibroblasts throughout the scaffold. Collagens I and III and fibronectin were found to be secreted by both intestinal and dermal fibroblasts, as well as being present in human intestinal tissue. Fibroblasts retain their metabolic activity throughout long term culture and continue to secrete ECM proteins (data not shown). The presence of both fibroblasts and ECM proteins is representative of a subepithelial tissue-like layer and results in the overall structure of the *in vitro* co-cultures being very similar to the *in vivo* intestine. Collectively, this acts as a foundation providing support for the intestinal epithelial cells.

During 3D Co-culture Signals From Fibroblasts Induce a More *in vivo*-Like Epithelial Morphology

Close examination of the ultra-structure through TEM analysis revealed that the height of Caco-2 cells increases when 3D co-cultured with fibroblasts. In contrast, this was not significantly altered by paracrine signals alone in conditioned media (**Figure 5A**). To determine whether the cells displayed a more cuboidal or columnar phenotype, we calculated the ratio of epithelial cell height:width; a ratio closer to 1 resembles a cuboidal phenotype while a number > 1 is indicative of a columnar cell, conversely a number < 1 suggests a flattened cell morphology. All Transwell® -based models displayed a cuboidal phenotype, while 3D co-culture of Caco-2 cells with fibroblasts resulted in the cells becoming columnar in structure and more similar to the morphology of human intestinal epithelial cells (**Figures 5B–D**).

Analysis of the lateral membrane between adjacent epithelial cells was performed by carefully tracing the membrane on TEM images to determine its length (**Figure 6A**). Transwell® Caco-2 models have a highly convoluted and interdigitated membrane, while Caco-2 cells co-cultured with fibroblasts in 3D and human tissue displayed a straightened membrane (**Figure 6A**). To directly compare lateral membrane length between cells in each of the *in vitro* models (**Figure 6B**), the length was normalized to epithelial cell height (**Figure 6C**). This demonstrated that conditioned media induces a slight change in the membrane structure that more closely resembles human tissue, and this

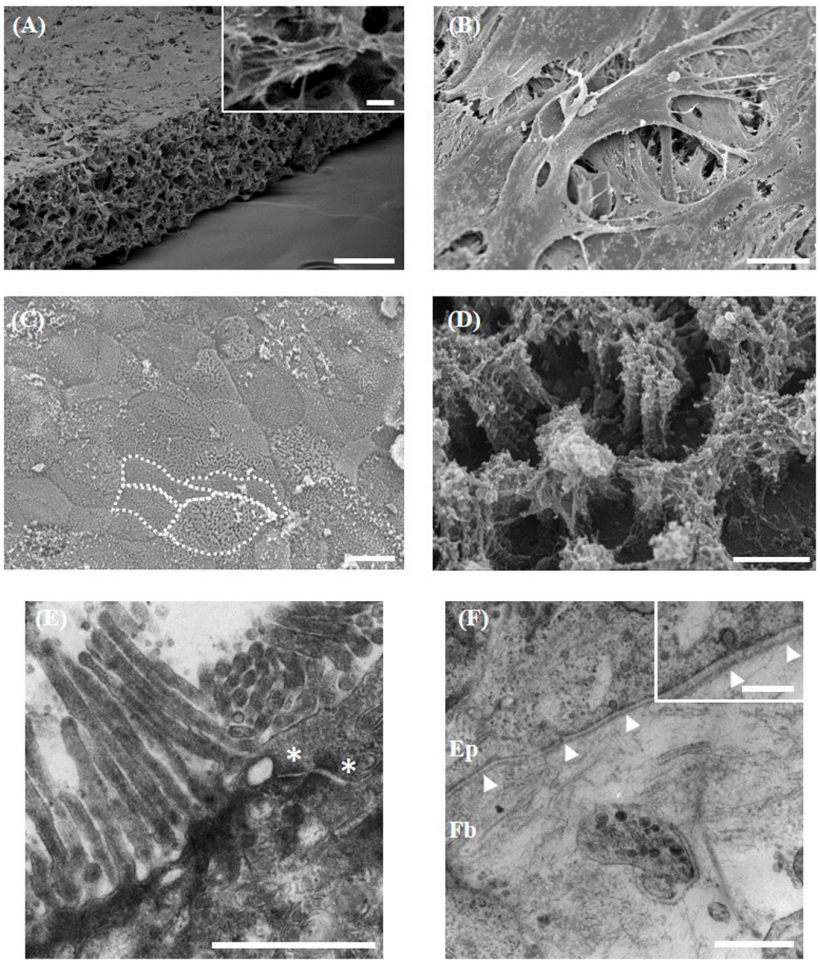

FIGURE 3 | Morphological analysis of the 3D co-culture intestinal model using electron microscopy. **(A,B)** Representative SEM micrographs of the surface of the fibroblast compartment of the co-culture prior to seeding epithelial cells. (**A**, inset) Higher power imaging showing evidence of ECM deposition. **(C,D)** Surface of the Caco-2 monolayer (examples of individual cells outlined in white). **(D)** Higher power micrograph showing microvilli and glycocalyx. TEM micrographs of the: **(E)** microvilli brush-border and electron dense apical tight junctions (*); **(F)** the basement membrane (arrowheads) forming between the epithelial (Ep) cells and underlying fibroblasts (Fb). (**F**, inset) Higher power imaging showing vesicle transfer between epithelial cells and fibroblasts across the basement membrane. Scale bars: 200 μm **(A)**, 10 μm (**A**, inset), 20 μm **(B,C)**, 1 μm **(D–F)**, 250 nm (**F**, inset).

change was significantly enhanced upon direct 3D co-culture of fibroblast and Caco-2 cells.

Quantitative assessment of the total number of electron dense junctional complexes per lateral membrane for each model type was determined (**Figure 6D**). Caco-2 control models on Transwell® membranes had the highest number of junctions observed between adjacent cells. Fibroblast paracrine conditions did not significantly alter the number of junctional complexes between cells, but 3D co-culture reduced the number of electron dense complexes observed.

Changes in Cell Structure Alter Epithelial Barrier Properties

TEER measurements were taken at day 21 of Caco-2 culture once the cells had fully differentiated (**Figure 7A**). Caco-2 Transwell® control models had a high TEER of over 2500 $\Omega.cm^2$, much higher than values reported for *in vivo* intestine (25–40 $\Omega.cm^2$) (Balimane and Chong, 2005). Conditioned media from fibroblasts, regardless of origin, reduced the TEER to 600–800 $\Omega.cm^2$ and this was further decreased below 200 $\Omega.cm^2$ when the Caco-2 epithelial layer was in direct 3D co-culture with the fibroblasts.

The concurrent decrease in TEER and straightened lateral membrane morphology was suggestive of a more permeable barrier formed by the epithelial cells. To investigate this further, we performed a simple transport assay with lucifer yellow, a marker that passes across the epithelium by passive paracellular transport, between the lateral membranes of adjacent cells (**Figure 7B**). Although TEER values were reduced when Caco-2 monolayers were treated with fibroblast paracrine factors, this was not reflected in the permeability of lucifer yellow, where no change in absorption was observed. However, in 3D co-culture, lucifer yellow permeability was increased

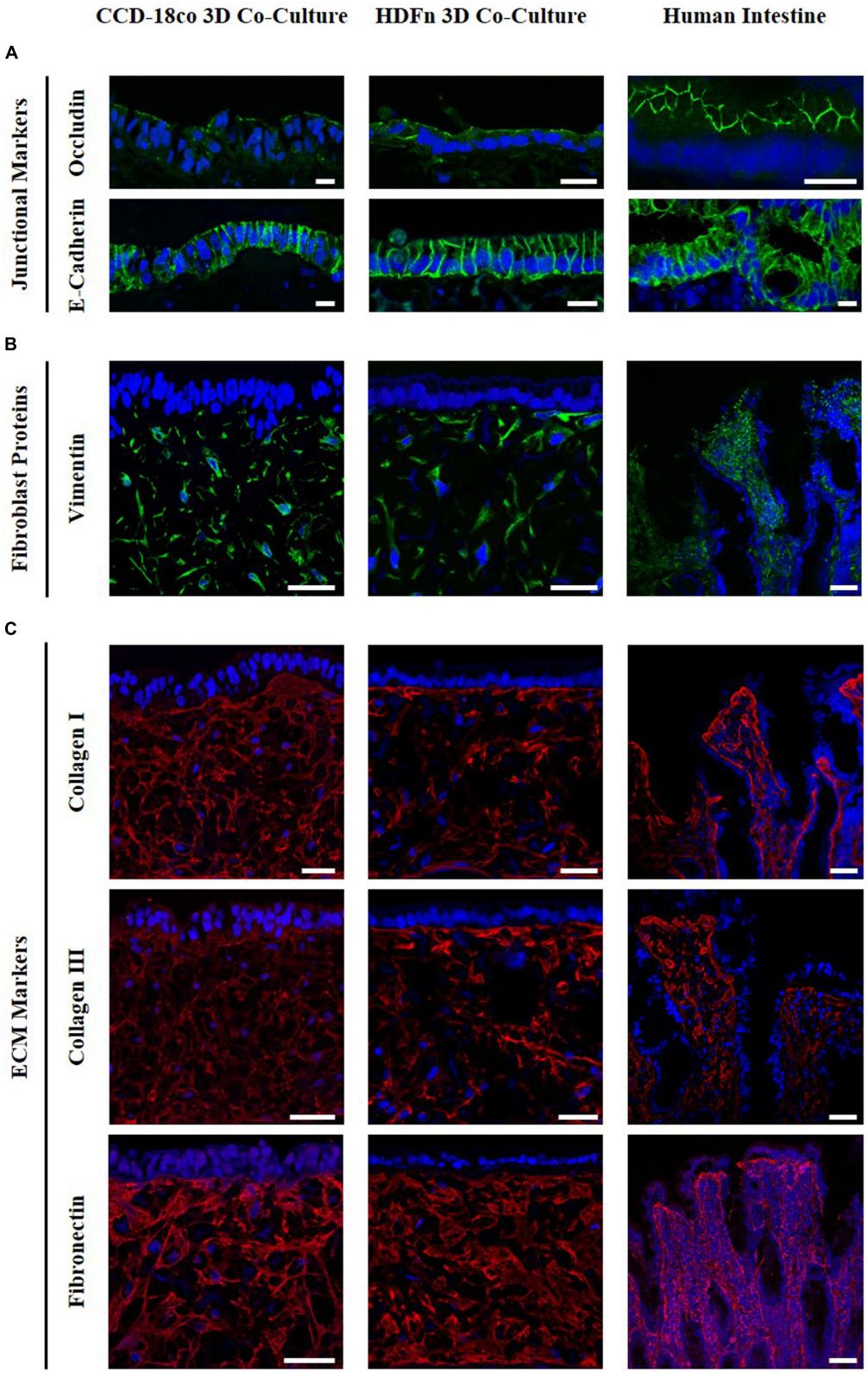

FIGURE 4 | Comparison of 3D co-culture models with human intestinal tissue. Immunofluorescent staining of **(A)** the junctional proteins; occludin, *E*-Cadherin, **(B)** the fibroblast marker vimentin, and **(C)** collagens I and III and fibronectin counterstained with DAPI. Images show protein expression in Caco-2 co-culture models with intestinal fibroblasts (left) and human dermal fibroblasts (middle) compared to human intestinal tissues (right). Scale bar: 20 μm **(A)** and 50 μm **(B,C)**.

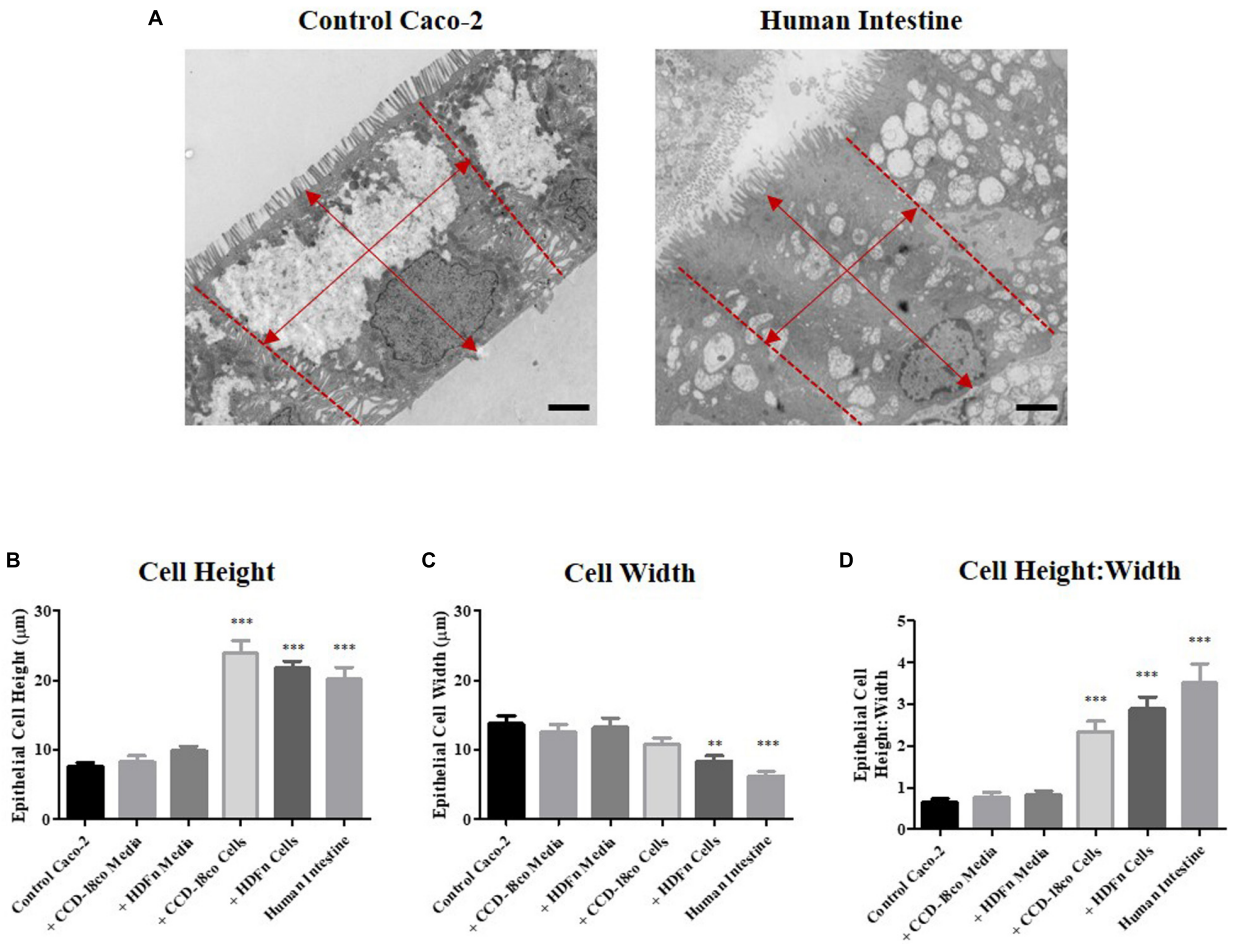

FIGURE 5 | Morphometric analysis of epithelial cells in *in vitro* models and intestinal tissue. **(A)** Example TEM micrographs of Caco-2 Transwell® control models and human tissue which were used to measure epithelial **(B)** cell height and **(C)** width [as indicated by arrows **(A)**], and **(D)** calculation of the ratio of epithelial cell height:width. Scale bars: 2 μm, $n = 15$ for *in vitro* models, $n = 10$ for human tissue, $^{**}P < 0.001$, $^{***}P < 0.0001$ compared to control Caco-2 monolayers.

almost 3-fold, correlating with the observed changes in TEER and the significantly straightened lateral membrane structure (**Figure 7B**).

DISCUSSION

The human adenocarcinoma cell line, Caco-2, forms the basis of many *in vitro* intestinal models as a result of their ease of culture and ability to form differentiated monolayers possessing enterocyte-like characteristics (Hidalgo et al., 1989). Despite these advantages, many limitations persist, in part preventing the replacement of animal and *ex vivo* human tissue models with Caco-2 cultures. The Caco-2 enterocyte layer exhibits structural and functional characteristics more like colonic tissue than small intestine, with higher TEER, lower permeability and lack of tissue complexity being the main differences (Balimane and Chong, 2005). In the present study, we propose novel, 3D models that overcome these limitations, whilst avoiding the many intricate and expensive steps associated with other *in vitro* intestinal models. Our intestinal tissue equivalents show enhanced epithelial structure and function more like that of native tissue, thus providing more suitable models for drug permeability studies as well as biological investigation of the mucosal layer.

In recent decades, scientists have endeavored to overcome the *in vitro* limitations of the Caco-2 Transwell® system by using alternative culture substrates or through increasing complexity of models. Several advances have been made resulting in more physiologically relevant enterocyte monolayers with more realistic TEER and permeability values (Antunes et al., 2013; Béduneau et al., 2014; Pereira et al., 2015). However, such systems still lack endogenous molecules and interactions required to mimic the *in vivo* tissue dynamics. Some of these improved models include primary enterocytes or intestinal fibroblasts, both of which present issues of variability and lack of reproducibility (Takenaka et al., 2014; Schweinlin et al., 2016). Many co-culture systems also utilize fibroblast layers as a subepithelial compartment, which fail to account for the spatial organization within the mucosal tissue (Li et al., 2013; Matsusaki et al., 2015).

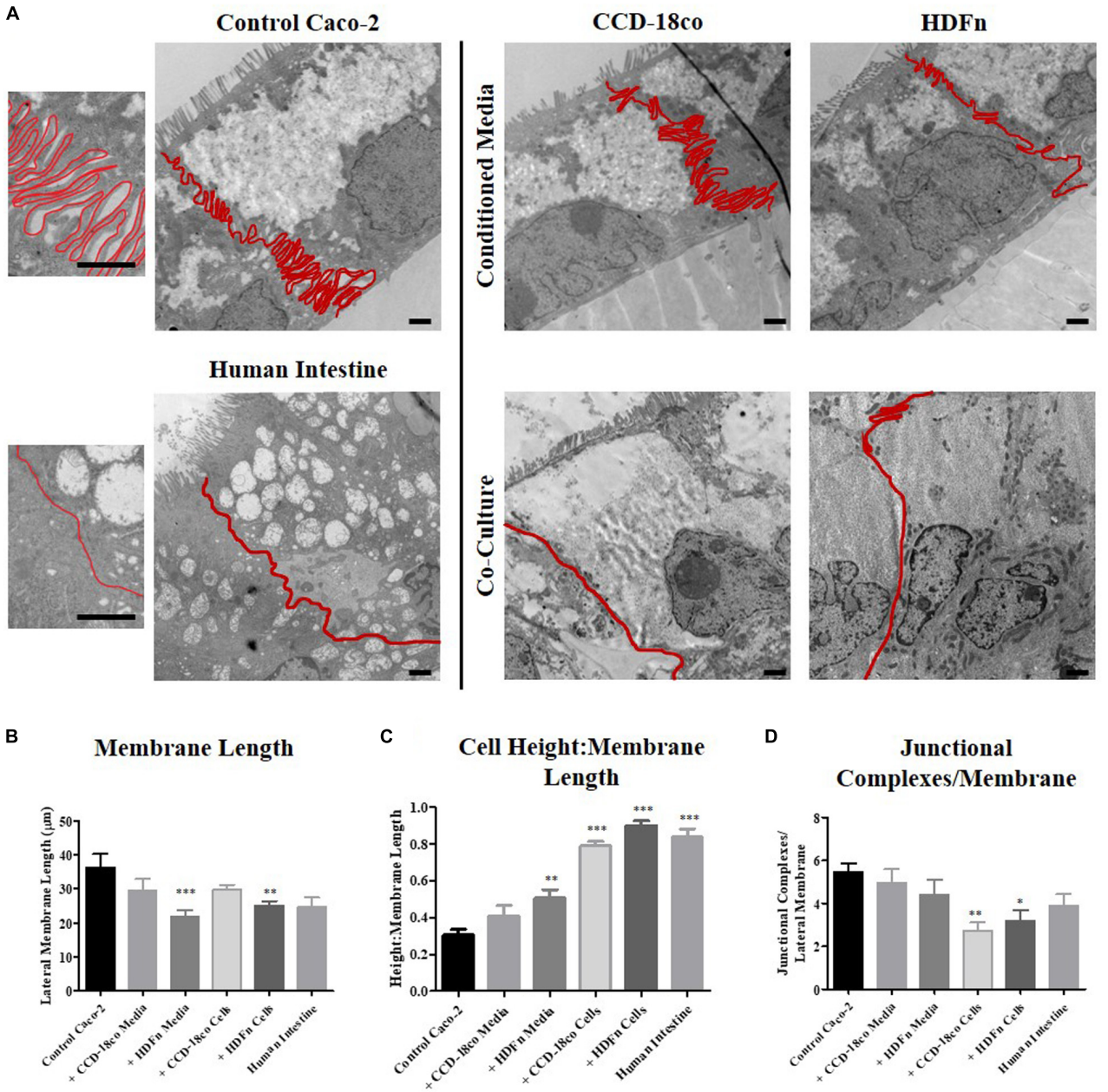

FIGURE 6 | The profile and length of the lateral membrane is decreased in 3D co-culture models. **(A)** TEM images of control Caco-2 Transwell® cultures; models cultured in fibroblast conditioned media; 3D co-cultured with fibroblasts; and human intestinal epithelial tissue. Lateral membranes of epithelial cells were traced and clearly outlined in red. Scale bars: 1 μm. **(B)** Lateral membrane length and **(C)** the ratio of cell height: membrane length of *in vitro* models compared to *in vivo* intestine. **(D)** Semi-quantitative analysis comparing the total number of electron dense junctions observed between adjacent epithelial cells. $n = 15$ for *in vitro* models, $n = 10$ for human tissue, $^{*}P < 0.01$, $^{**}P < 0.001$, $^{***}P < 0.0001$ compared to control Caco-2 monolayers.

Organoid-based systems have recently appeared as the most likely frontrunner as they provide multicellular systems containing accurate cell niches. These cell culture systems contain all key intestinal epithelial cell types including enterocytes, goblet cells, enteroendocrine cells and Paneth calls; and have the unique ability to self-organize into 3D structures that recapitulate the crypt-villi structure observed *in vivo*. Organoids have the potential to be used for many different studies regarding the intestinal development process and disease modeling; additionally, they have been successfully engrafted into mice and show promise for regenerative medicine experimentation (Liu et al., 2016; Baumann, 2017; Cortez et al., 2018). However, these systems usually require costly media supplementation, including Wnt signaling pathway ligands and essential intestinal morphogens (Sato et al., 2011; Leushacke and Barker, 2014). Moreover, such systems are primarily epithelial only, they are

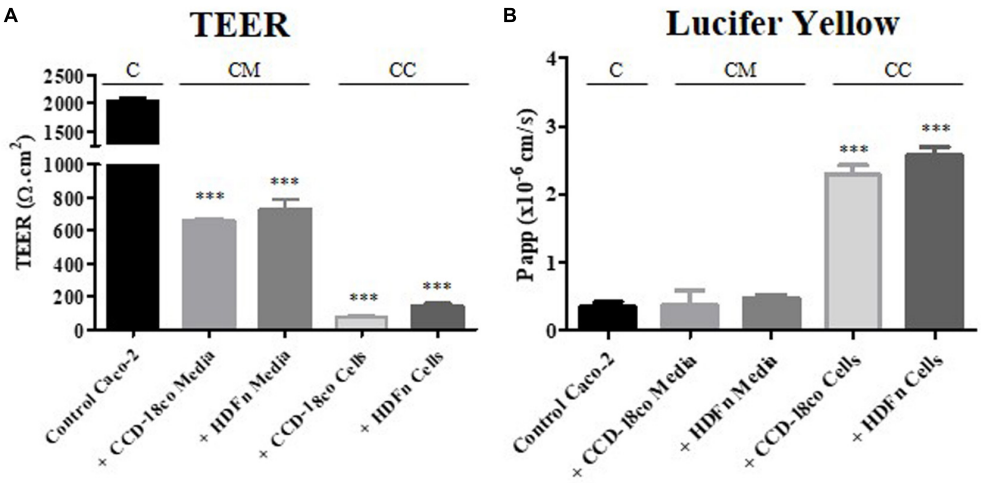

FIGURE 7 | Functional assessment of the epithelial barrier properties for each *in vitro* model. **(A)** TEER was measured at day 21 of Caco-2 cell growth. **(B)** The apparent permeability co-efficient of the passive paracellular maker was calculated by performing transport assays on the models between days 21 and 25 of Caco-2 cell culture. "C" denotes the control Caco-2 monolayer, "CM" represents the conditioned media samples, while "CC" indicates the co-culture models. $n = 3$, $^{***}P < 0.0001$ compared to control Caco-2 monolayers.

effectively inside-out with the apical surface of the cells being completely enclosed in a central hollow region. Thus, their spatial arrangement greatly inhibits the use of organoids in the drug screening process (Yin et al., 2016; Costa and Ahluwalia, 2019). More recent advances have sought to seed organoids onto decellularised small intestinal submucosa (SIS) scaffolds which can shorten the differentiation time of the different intestinal cell types in addition to recreating the appropriate epithelial-ECM interactions. Use of SIS scaffolds more accurately recreates the intestinal mucosa anatomy and enables transport studies to be performed on the *in vitro* models (Schweinlin et al., 2016). Such systems, however, are not yet fully humanized and the expense, variability, and technical expertise required to culture also makes large-scale studies unfeasible. The technology described herein is robust and reproducible, using a standardized epithelial cell line and commercially available fibroblasts, enabling the relatively simple production of a multi-layered *in vitro* mucosal equivalent.

Substantial evidence exists suggesting intestinal epithelial structure and function are heavily influenced by cell-cell and cell-ECM interactions that are important in the complex microenvironment within the human mucosa (Halttunen et al., 1996; Kedinger et al., 1998; Bernardo and Fibbe, 2013). Fibroblast secreted peptides and extracellular matrix components have been shown to enhance epithelial morphology and function in a variety of tissues (Dignass et al., 1994; Korpos et al., 2010; Hausmann et al., 2019). Although fibroblast secretomes remain largely unknown, many peptide growth factors have been investigated using both primary cells and established cell lines (Halttunen et al., 1996; Hausmann et al., 2019). Among these, transforming growth factor-beta is a well-studied multifunctional cytokine postulated to be involved in epithelial regulation, immune homeostasis and enterocyte differentiation (Kojima et al., 1998; Ray et al., 2002). Furthermore, studies using CCD-18co and dermal fibroblast conditioned medium highlighted that fibroblast production of hepatocyte growth factor was partially responsible for enhanced proliferation of Caco-2 cells (Göke et al., 1998). Keratinocyte growth factor produced by both fibroblast types has also been implicated in enhancing the proliferation and differentiation of a range of different intestinal epithelial cells, including Caco-2 cells (Visco et al., 2009). Supplementary to this, CCD-18co and Caco-2 co-cultures highlighted the importance keratinocyte growth factor in altering tight junction protein expression with a subsequent decrease in TEER of monolayers (Kim et al., 2012).

It is reasonable to expect that fibroblasts from alternative tissue origins secrete different peptide factors and further work is necessary to elucidate these factors and understand the effects on Caco-2 enterocytes. What remains unclear, however, is the importance of fibroblast tissue origin on epithelial structure and function *in vitro*. In this study, we used two different fibroblast cell types in all of our investigations: a primary dermal fibroblast (HDFn) and a colonic cell line (CCD-18co). Both fibroblast lineages have previously used in co-culture studies with Caco-2 cells and have induced changes in the epithelium to better resemble the *in vivo* intestine. For example, co-culture of dermal fibroblast and Caco-2 cells induced a switch in the predominantly expressed carboxylesterase (CE) expression in Caco-2 cells from CE1 to higher CE2 expression more accurately reflecting the human small intestine (Matsusaki et al., 2015). Co-cultures developed using CCD-18co cells embedded in Matrigel have been shown to reduce TEER and P-gp expression and more accurately predicted the permeability of insulin than Transwell® monolayers (Li et al., 2013; Pereira et al., 2015).

In our models, both fibroblast lineages tested supported the formation of a Caco-2 epithelium when co-cultured in 3D, with evidence of columnar cells. However, differences in epithelial morphology were obvious between Caco-2 cells grown in our 3D co-culture compared to models using fibroblast conditioned

media alone, where epithelia were more like controls and were significantly more cuboidal in comparison. This suggests that fibroblasts in physical contact are more influential than the fibroblast secretome alone on the morphology of Caco-2 epithelial layers. This is most likely a result of the abundant endogenous ECM present in our 3D systems, as well as the formation of a supportive basement membrane. Fibroblasts are known to influence basement membrane composition, enabling more accurate cellular adhesion (Marinkovich et al., 1993). Accordingly, this is a significant advance over previous existing systems that utilize synthetic basement membrane equivalents (Patient et al., 2019). Positive staining for ECM components including collagens and fibronectin revealed the stromal-like tissue layer formed throughout the inert Alvetex® Scaffold. Fibronectin in particular is an ECM component usually lacking in *in vitro* hydrogel and collagen coated models but is an extremely important protein in epithelial polarization (Kolachala et al., 2007). This *in situ* deposition of ECM by resident fibroblasts is a unique feature of our model that could prove invaluable in studies of epithelial-mucosal interactions and disease studies, particularly disorders involving ECM remodeling.

At present, our models only incorporate stromal cells and an absorptive epithelial cell line; inclusion of additional intestinal epithelial cell lineages, such as the HT29-MTX mucous secreting cell line could further enhance the structure and function of our models. HT29-MTX cells have been incorporated into Caco-2 co-cultures using scaffolds that recreate the hollow lumen structure of the intestine and the accumulation of mucous within these models induced a more physiologically relevant lower oxygen tension and allowed for the study of bacterial interactions (Chen et al., 2015). Reduced expression of the efflux transporter protein *P*-glycoprotein is also detected in these models resulting in more *in vivo*-like tissue constructs.

Lateral membrane interdigitation is a prominent characteristic of Caco-2 monolayers (Hidalgo et al., 1989). Previous studies have investigated the effect of fibroblast secreted factors and ECM components on enterocyte junctional complexes (Ichikawa-Tomikawa et al., 2011). However, to our knowledge, none have reported on the influence of fibroblasts on enterocyte lateral membrane morphology. Caco-2 cells cultured in the conventional Transwell® system result in monolayers exhibiting an extremely interdigitated lateral membrane, a characteristic that could explain abnormally high TEER values and low permeability. Paracrine factors from both fibroblast cell types did not significantly decrease lateral membrane folding. In contrast, Caco-2 monolayers in 3D culture systems displayed significantly less lateral membrane interdigitation and lateral membranes appeared straighter which is characteristic of *in vivo* tissue. Supplementary to this, we found total junctional complexes per lateral membrane decreased in the 3D models compared to the standard Transwell® model. These results suggest that epithelial-mesenchymal interactions are implicated in the structural connections between adjacent epithelial cells and lateral-membrane morphological dynamics. The lateral-basolateral membranes of enterocyte monolayers contain junctional complexes required for cellular adhesion and are implicated in paracellular transport.

Caco-2 cells are capable of spontaneous polarization. Varying degrees of polarization can be observed however, in different *in vitro* models (Gaillard and Finlay, 1996; Siccardi et al., 2004). Although all enterocyte monolayers exhibited polarization markers, such as brush border formation, those in our 3D co-culture models appeared more polarized than those grown in conditioned media and controls. Similarly, culture of Caco-2 cells on decellularised porcine jejunal segments induced an increase in cellular polarity, emphasizing the importance of epithelial-ECM interaction in *in vitro* models (Pusch et al., 2011). Decellularised small intestinal submucosa scaffolds are useful tools not only for recreating this crosstalk but also to induce the native intestinal architecture, which cannot currently be achieved in our 3D models. The decellularization process of such scaffolds, however, can result in ineffective ECM-remodeling subsequent to harsh decellularizing agents (Hussey et al., 2018). The establishment of polarity in enterocytes is important for barrier function and transport properties. Apical-basolateral polarity in many epithelial tissues can be enhanced through extracellular matrix components, particularly laminin (Hoffmann et al., 1996). This is a result of ECM interaction with enterocyte cell surface receptors such as integrins, which are known to affect polarity and junctional constituents such as *E*-cadherin in Caco-2 cells (Schreider et al., 2002). This is understood to be because cellular adhesions, both cell-cell and cell-ECM, connect to the cytoskeleton and thus influence the actin-dynamics involved in polarization. This could prove of particular interest in further experimentation, as integrin-mediated actin cytoskeletal changes may be the cause of the lateral membrane interdigitation reported herein. Further work is required to assess these interactions and actin cytoskeletons in our system. Whilst we might expect connections between cells to vary between different 3D co-culture models, interactions were considerably more *in vivo*-like compared to controls, most likely as a result of abundant ECM and basement membrane components.

We employed TEER to assess functional properties of the Caco-2 barriers in all of the culture systems. Conventional Caco-2 Transwell® models are known to have extremely high TEER, unlike human tissue, and are also known to be extremely variable between different laboratories (Hidalgo et al., 1989). Many different factors affect TEER of Caco-2 monolayers including medium composition, culture period and temperature (Sambuy et al., 2005). Inter-lab variability in TEER has been demonstrated in a number of different studies that examined the effect of passage number on TEER; some groups demonstrated a decrease in TEER as cells age while others found conflicting results (Ranaldi et al., 1992; Yu et al., 1997). In the present study, Caco-2 TEER values were moderately decreased by paracrine-mediated mechanisms when cultured with conditioned media from both fibroblast cell types. The most profound decreases in TEER were observed in our 3D co-culture models; with values being much more similar to human small intestine *in vivo* suggesting that epithelial integrity is also significantly influenced by the subepithelial stromal compartment. Similarly, Caco-2 co-cultures with mouse embryonic fibroblasts in collagen gels have demonstrated a significant decrease in TEER from

over 2000 $\Omega.cm^2$ in Caco-2 monocultures to levels below 1000 $\Omega.cm^2$ and demonstrated a concurrent increase in the apparent permeability of paracellularly transported compounds (Li et al., 2013; Zhang et al., 2019).

Examination of the permeability of lucifer yellow was performed to determine if there was any correlation between the level of lateral membrane interdigitation and paracellular permeability, as compounds may be retained for longer in the highly convoluted lateral membranes of Transwell® monolayers. Increased paracellular permeability was observed in the 3D co-cultures, reflecting the decreased TEER. However, this was not the case in the Transwell® -based paracrine systems which although demonstrated a reduction in TEER, retained abnormally low permeability values. It could therefore be implied that there is a correlation between degree of membrane interdigitation and paracellular permeability in enterocyte monolayers. Though beyond the scope of this study, further experiments are required to examine the effects of drug compound size on passive permeability and to determine of the effects of direct co-culture on the transcellular and efflux permeability.

CONCLUSION

To summarize, we have developed novel 3D co-cultures recapitulating the intestinal mucosa. We showed that when co-cultured in 3D immediately adjacent to fibroblasts, Caco-2 monolayers display enhanced morphological characteristics such as enhanced columnar shape polarization and altered lateral membrane morphology more similar to *in vivo* enterocytes We used TEER and paracellular permeability to provide preliminary evidence that our 3D co-cultures were functionally enhanced, however, further experiments are required to demonstrate how the improved structure impacts the function of the enterocytes and to determine whether the 3D tissue constructs have a more *in vivo*-like function compared to controls. Such morphological and functional characteristics were not observed in Caco-2 cells grown in fibroblast-conditioned media alone, emphasizing that direct co-culture in 3D is more influential on Caco-2 epithelial structure and function than the fibroblast secretome alone. In conclusion, the 3D co-culture models presented herein produce more tissue-like enterocyte lateral membranes, a physiologically relevant attribute that could prove beneficial for the use of Caco-2 cells in permeability studies.

DATA AVAILABILITY STATEMENT

All datasets generated for this study are included in the article/supplementary material.

ETHICS STATEMENT

The studies involving fixed human intestinal tissues were collected by REPROCELL Europe Limited (Glasgow, United Kingdom) under appropriate ethical protocols in compliance with local laws and regulations that were reviewed and approved by the West of Scotland Research Ethics Committee (REC Ref: 17/WS/0049). All tissue donors provided informed written consent. Tissues were received at Durham University under a formal MTA agreement and were processed following relevant UK HTA rules and guidelines at the time of publication.

AUTHOR CONTRIBUTIONS

AG-H, MF, CM, and ND performed the experiments. AG-H and MF conducted the data analysis. CM, ND, and SP wrote and revised the manuscript. SP had oversight of the project and approved the manuscript for submission. All authors contributed to the article and approved the submitted version.

FUNDING

This work was supported by funding from Biotechnology and Biosciences Research Council (BBSRC BB/M015645), NC3Rs (National Centre for the Replacement, Refinement and Reduction of Animals and Research (NC3Rs NC/N00289X/1), European Regional Development Fund Intensive Industrial Innovation and Reprocell Europe Ltd (25R07P01847), and Consejo Nacional de Ciencia y Tecnología (CONACYT).

ACKNOWLEDGMENTS

This work was supported by the technical staff the Department of Bioscience at Durham University: Christine Richardson and Helen Grindley (electron microscopy). We would like to thank Reprocell Europe for providing human tissue.

REFERENCES

Antunes, F., Andrade, F., Araújo, F., Ferreira, D., and Sarmento, B. (2013). Establishment of a triple co-culture in vitro cell models to study intestinal absorption of peptide drugs. *Eur. J. Pharm. Biopharm.* 83, 427–435.

Balimane, P. V., and Chong, S. (2005). Cell culture-based models for intestinal permeability: a critique. *Drug Discov. Today* 10, 335–343. doi: 10.1016/S1359-6446(04)03354-9

Basson, M. D. (2001). In vitro evidence for matrix regulation of intestinal epithelial biology during mucosal healing. *Life Sci.* 69, 3005–3018. doi: 10.1016/S0024-3205(01)01408-4

Baumann, K. (2017). Colonic organoids for drug testing and colorectal disease modelling. *Nat. Rev. Mol. Cell Biol.* 18, 467–467. doi: 10.1038/nrm.2017.70

Béduneau, A., Tempesta, C., Fimbel, S., Pellequer, Y., Jannin, V., Demarne, F., et al. (2014). A tunable Caco-2/HT29-MTX co-culture model mimicking variable permeabilities of the human intestine obtained by an original seeding procedure. *Eur. J. Pharm. Biopharm.* 87, 290–298. doi: 10.1016/j.ejpb.2014.03.017

Bernardo, M. E., and Fibbe, W. E. (2013). Mesenchymal stromal cells: sensors and switchers of inflammation. *Cell Stem Cell* 13, 392–402. doi: 10.1016/j.stem.2013.09.006

Chen, Y., Lin, Y., Davis, K. M., Wang, Q., Rnjak-Kovacina, J., Li, C., et al. (2015). Robust bioengineered 3D functional human intestinal epithelium. *Sci. Rep.* 5:13708. doi: 10.1038/srep13708

Cortez, A. R., Poling, H. M., Brown, N. E., Singh, A., Mahe, M. M., and Helmrath, M. A. (2018). Transplantation of human intestinal organoids into the mouse mesentery: a more physiologic and anatomic engraftment site. *Surgery* 164, 643–650. doi: 10.1016/j.surg.2018.04.048

Costa, J., and Ahluwalia, A. (2019). Advances and current challenges in intestinal in vitro model engineering: a digest. *Front. Bioeng. Biotechnol.* 7:144. doi: 10.3389/fbioe.2019.00144

Costello, C. M., Hongpeng, J., Shaffiey, S., Yu, J., Jain, N. K., Hackam, D., et al. (2014). Synthetic small intestinal scaffolds for improved studies of intestinal differentiation. *Biotechnol. Bioeng.* 111, 1222–1232. doi: 10.1002/bit.25180

Dignass, A. U., Tsunekawa, S., and Podolsky, D. K. (1994). Fibroblast growth factors modulate intestinal epithelial cell growth and migration. *Gastroenterology* 106, 1254–1262. doi: 10.1016/0016-5085(94)90017-5

Gaillard, J. L., and Finlay, B. B. (1996). Effect of cell polarization and differentiation on entry of Listeria monocytogenes into the enterocyte-like Caco-2 cell line. *Infect. Immun.* 64, 1299–1308. doi: 10.1128/IAI.64.4.1299-1308.1996

Göke, M., Kanai, M., and Podolsky, D. K. (1998). Intestinal fibroblasts regulate intestinal epithelial cell proliferation via hepatocyte growth factor. *Am. J. Physiol.-Gastrointest. Liver Physiol.* 274, G809–G818.

Halttunen, T., Marttinen, A., Rantala, I., Kainulainen, H., and Maki, M. (1996). Fibroblasts and transforming growth factor beta induce organization and differentiation of T84 human epithelial cells. *Gastroenterology* 111, 1252–1262. doi: 10.1053/gast.1996.v111.pm8898639

Hausmann, C., Zoschke, C., Wolff, C., Darvin, M. E., Sochorová, M., Kováčik, A., et al. (2019). Fibroblast origin shapes tissue homeostasis, epidermal differentiation, and drug uptake. *Sci. Rep.* 9:2913. doi: 10.1038/s41598-019-39770-6

Hidalgo, I. J., Raub, T. J., and Borchardt, R. T. (1989). Characterization of the human colon carcinoma cell line (Caco-2) as a model system for intestinal epithelial permeability. *Gastroenterology* 96, 736–749. doi: 10.1016/0016-5085(89)90897-4

Hilgendorf, C., Spahn-Langguth, H., Regaardh, C. G., Lipka, E., Amidon, G. L., and Langguth, P. (2000). Caco-2 versus Caco-2/HT29-MTX co-cultured cell lines: permeabilities via diffusion, inside-and outside-directed carrier-mediated transport. *J. Pharm. Sci.* 89, 63–75. doi: 10.1002/(sici)1520-6017(200001)89:1<63::aid-jps7>3.0.co;2-6

Hoffmann, M. P., Kibbey, M. C., Letterio, J. J., and Kleinman, H. K. (1996). Role of laminin-1 and TGF-beta 3 in acinar differentiation of a human submandibular gland cell line (HSG). *J. Cell Sci.* 109, 2013–2021.

Holland-Cunz, S., Bainczyk, S., Hagl, C., Wink, E., Wedel, T., Back, W., et al. (2004). Three-dimensional co-culture model of enterocytes and primary enteric neuronal tissue. *Pediatr. Surg. Int.* 20, 233–237. doi: 10.1007/s00383-003-1117-z

Hubatsch, I., Ragnarsson, E. G. E., and Artursson, P. (2007). Determination of drug permeability and prediction of drug absorption in Caco-2 monolayers. *Nat. Protoc.* 2, 2111–2119. doi: 10.1038/nprot.2007.303

Hussey, G. S., Cramer, M. C., and Badylak, S. F. (2018). Extracellular Matrix Bioscaffolds for Building Gastrointestinal Tissue. *Cell. Mol. Gastroenterol. Hepatol.* 5, 1–13. doi: 10.1016/j.jcmgh.2017.09.004

Ichikawa-Tomikawa, N., Sugimoto, K., Satohisa, S., Nishiura, K., and Chiba, H. (2011). Possible involvement of tight junctions, extracellular matrix and nuclear receptors in epithelial differentiation. *J. Biomed. Biotechnol.* 2011, 1–10. doi: 10.1155/2011/253048

Jabaji, Z., Brinkley, G. J., Khalil, H. A., Sears, C. M., Lei, N. Y., Lewis, M., et al. (2014). Type I collagen as an extracellular matrix for the in vitro growth of human small intestinal epithelium. *PLoS One* 9:e107814. doi: 10.1371/journal.pone.0107814

Kedinger, M., Duluc, I., Fritsch, C., Lorentz, O., Plateroti, M., and Freund, J. N. (1998). Intestinal Epithelial-Mesenchymal Cell Interactions. *Ann. N. Y. Acad. Sci.* 859, 1–17. doi: 10.1111/j.1749-6632.1998.tb11107.x

Kim, T. I., Poulin, E. J., Blask, E., Bukhalid, R., Whitehead, R. H., Franklin, J. L., et al. (2012). Myofibroblast keratinocyte growth factor reduces tight junctional integrity and increases claudin-2 levels in polarized Caco-2 cells. *Growth Factors* 30, 320–332. doi: 10.3109/08977194.2012.717076

Kim, Y., Ko, H., Kwon, I. K., and Shin, K. (2016). Extracellular matrix revisited: roles in tissue engineering. *Int. Neurourol. J.* 20, S23–S29. doi: 10.5213/inj.1632600.318

Kojima, H., Hidaka, H., Matsumura, K., Fujita, Y., and Nishio, H. (1998). Concerted regulation of early enterocyte differentiation by insulin-like growth factor I, insulin, and transforming growth factor-beta1. *Proc. Assoc. Am. Physicians* 110, 197–206.

Kolachala, V. L., Bajaj, R., Wang, L., Yan, Y., Ritzenthaler, J. D., Gewirtz, A. T., et al. (2007). Epithelial-derived fibronectin expression, signaling, and function in intestinal inflammation. *J. Biol. Chem.* 282, 32965–32973. doi: 10.1074/jbc.M704388200

Korpos, E., Wu, C., Song, J., Hallmann, R., and Sorokin, L. (2010). Role of the extracellular matrix in lymphocyte migration. *Cell Tissue Res.* 339, 47–57. doi: 10.1007/s00441-009-0853-3

Leushacke, M., and Barker, N. (2014). Ex vivo culture of the intestinal epithelium: strategies and applications. *Gut* 63:1345. doi: 10.1136/gutjnl-2014-307204

Li, N., Wang, D., Sui, Z., Qi, X., Ji, L., Wang, X., et al. (2013). Development of an improved three-dimensional in vitro intestinal mucosa model for drug absorption evaluation. *Tissue Eng. Part C Methods* 19, 708–719. doi: 10.1089/ten.tec.2012.0463

Liu, F., Huang, J., Ning, B., Liu, Z., Chen, S., and Zhao, W. (2016). Drug discovery via human-derived stem cell organoids. *Front. Pharmacol.* 7:334. doi: 10.3389/fphar.2016.00334

Marinkovich, M. P., Keene, D. R., Rimberg, C. S., and Burgeson, R. E. (1993). Cellular origin of the dermal-epidermal basement membrane. *Dev. Dyn.* 197, 255–267. doi: 10.1002/aja.1001970404

Matsusaki, M., Hikimoto, D., Nishiguchi, A., Kadowaki, K., Ohura, K., Imai, T., et al. (2015). 3D-fibroblast tissues constructed by a cell-coat technology enhance tight-junction formation of human colon epithelial cells. *Biochem. Biophys. Res. Commun.* 457, 363–369. doi: 10.1016/j.bbrc.2014.12.118

Patient, J. D., Hajiali, H., Harris, K., Abrahamsson, B., Tannergren, C., White, L. J., et al. (2019). Nanofibrous scaffolds support a 3D in vitro permeability model of the human intestinal epithelium. *Front. Pharmacol.* 10:456. doi: 10.3389/fphar.2019.00456

Pereira, C., Araujo, F., Barrias, C. C., Granja, P. L., and Sarmento, B. (2015). Dissecting stromal-epithelial interactions in a 3D in vitro cellularized intestinal model for permeability studies. *Biomaterials* 56, 36–45. doi: 10.1016/j.biomaterials.2015.03.054

Pusch, J., Votteler, M., Göhler, S., Engl, J., Hampel, M., Walles, H., et al. (2011). The physiological performance of a three-dimensional model that mimics the microenvironment of the small intestine. *Biomaterials* 32, 7469–7478. doi: 10.1016/j.biomaterials.2011.06.035

Ranaldi, G., Islam, K., and Sambuy, Y. (1992). Epithelial cells in culture as a model for the intestinal transport of antimicrobial agents. *Antimicrob. Agents Chemother.* 36, 1374–1381. doi: 10.1128/aac.36.7.1374

Ray, E. C., Avissar, N. E., and Sax, H. C. (2002). Growth factor regulation of enterocyte nutrient transport during intestinal adaptation. *Am. J. Surg.* 183, 361–371. doi: 10.1016/S0002-9610(02)00805-X

Sambuy, Y., De Angelis, I., Ranaldi, G., Scarino, M. L., Stammati, A., and Zucco, F. (2005). The Caco-2 cell line as a model of the intestinal barrier: influence of cell and culture-related factors on Caco-2 cell functional characteristics. *Cell Biol. Toxicol.* 21, 1–26. doi: 10.1007/s10565-005-0085-6

Sanderson, I. R., Ezzell, R. M., Kedinger, M., Erlanger, M., Xu, Z. X., Pringault, E., et al. (1996). Human fetal enterocytes in vitro: modulation of the phenotype by extracellular matrix. *Proc. Natl. Acad. Sci. U.S.A.* 93, 7717–7722. doi: 10.1073/pnas.93.15.7717

Sato, T., Stange, D. E., Ferrante, M., Vries, R. G. J., van Es, J. H., van den Brink, S., et al. (2011). Long-term expansion of epithelial organoids from human colon. Adenoma, adenocarcinoma, and barrett's epithelium. *Gastroenterology* 141, 1762–1772. doi: 10.1053/j.gastro.2011.07.050

Schreider, C., Peignon, G., Thenet, S., Chambaz, J., and Pinçon-Raymond, M. (2002). Integrin-mediated functional polarization of Caco-2 cells through E-cadherin—actin complexes. *J. Cell Sci.* 115, 543–552.

Schweinlin, M., Wilhelm, S., Schwedhelm, I., Hansmann, J., Rietscher, R., Jurowich, C., et al. (2016). Development of an Advanced Primary Human In Vitro Model of the Small Intestine. *Tissue Eng. Part C Methods* 22, 873–883. doi: 10.1089/ten.tec.2016.0101

Siccardi, D., Gumbleton, M., Omidi, Y., and McGuigan, C. (2004). Stereospecific chemical and enzymatic stability of phosphoramidate triester prodrugs of d4T in vitro. *Eur. J. Pharm. Sci.* 22, 25–31. doi: 10.1016/j.ejps.2004.02.006

Takenaka, T., Harada, N., Kuze, J., Chiba, M., Iwao, T., and Matsunaga, T. (2014). Human small intestinal epithelial cells differentiated from adult intestinal stem cells as a novel system for predicting oral drug absorption in humans. *Drug Metab. Dispos.* 42, 1947–1954. doi: 10.1124/dmd.114.059493

Visco, V., Bava, F. A., d'Alessandro, F., Cavallini, M., Ziparo, V., and Torrisi, M. R. (2009). Human colon fibroblasts induce differentiation and proliferation of intestinal epithelial cells through the direct paracrine action of keratinocyte growth factor. *J. Cell. Physiol.* 220, 204–213. doi: 10.1002/jcp.21752

Walter, E., Janich, S., Roessler, B. J., Hilfinger, J. M., and Amidon, G. L. (1996). HT29-MTX/Caco-2 cocultures as an in vitro model for the intestinal epithelium: In vitro–in vivo correlation with permeability data from rats and humans. *J. Pharm. Sci.* 85, 1070–1076. doi: 10.1021/js960110x

Yi, B., Shim, K. Y., Ha, S. K., Han, J., Hoang, H.-H., Choi, I., et al. (2017). Three-dimensional in vitro gut model on a villi-shaped collagen scaffold. *BioChip J.* 11, 219–231. doi: 10.1007/s13206-017-1307-8

Yin, X., Mead, B. E., Safaee, H., Langer, R., Karp, J. M., and Levy, O. (2016). Engineering Stem Cell Organoids. *Cell Stem Cell* 18, 25–38. doi: 10.1016/j.stem.2015.12.005

Yu, H., Cook, T. J., and Sinko, P. J. (1997). Evidence for diminished functional expression of intestinal transporters in Caco-2 cell monolayers at high passages. *Pharm. Res.* 14, 757–762. doi: 10.1023/a:1012150405949

Yu, J., Peng, S., Luo, D., and March, J. C. (2012). In vitro 3D human small intestinal villous model for drug permeability determination. *Biotechnol. Bioeng.* 109, 2173–2178. doi: 10.1002/bit.24518

Zhang, J., Penny, J., and Lu, J. R. (2019). Development of a novel in vitro 3D intestinal model for permeability evaluations. *Int. J. Food Sci. Nutr.* 2019:1700940. doi: 10.1080/09637486.2019.1700940

Conflict of Interest: SP is the original inventor of Alvetex® technology now commercialized by Reprocell Europe Ltd. SP currently acts as a scientific consultant for Reprocell via a research collaboration with Durham University. CM is part of an ERDF sponsored studentship in collaboration with Reprocell Europe.

The remaining authors declare that the research was conducted in the absence of any commercial or financial relationships that could be construed as a potential conflict of interest.

frontiers in Bioengineering and Biotechnology

ORIGINAL RESEARCH
published: 17 September 2020
doi: 10.3389/fbioe.2020.524018

Development of an Improved 3D *in vitro* Intestinal Model to Perform Permeability Studies of Paracellular Compounds

Maria Helena Macedo[1,2], *Elena Martínez*[3,4,5], *Cristina C. Barrias*[1,2] *and Bruno Sarmento*[1,6]*

[1] *Instituto de Investigação e Inovação em Saúde, Universidade do Porto, Porto, Portugal,* [2] *Instituto de Ciências Biomédicas Abel Salazar, Universidade do Porto, Porto, Portugal,* [3] *Institute for Bioengineering of Catalonia, Barcelona, Spain,* [4] *Consorcio Centro de Investigación Biomédica en Red de Bioingeniería, Biomateriales y Nanomedicina, Madrid, Spain,* [5] *Department of Electronics and Biomedical Engineering, Universitat de Barcelona, Barcelona, Spain,* [6] *CESPU–Instituto de Investigação e Formação Avançada em Ciências e Tecnologias da Saúde, Gandra, Portugal*

OPEN ACCESS

Edited by:
Abhay Pandit, National University of Ireland Galway, Ireland

Reviewed by:
Abhigyan Satyam, Harvard Medical School, United States
Elena Donetti, University of Milan, Italy
Amirali Popat, The University of Queensland, Australia
Juan Aparicio Blanco, Complutense University of Madrid, Spain

***Correspondence:**
Bruno Sarmento
bruno.sarmento@ineb.up.pt

Specialty section:
This article was submitted to Tissue Engineering and Regenerative Medicine, a section of the journal Frontiers in Bioengineering and Biotechnology

Received: *01 January 2020*
Accepted: *21 August 2020*
Published: *17 September 2020*

Citation:
Macedo MH, Martínez E, Barrias CC and Sarmento B (2020) Development of an Improved 3D in vitro Intestinal Model to Perform Permeability Studies of Paracellular Compounds. Front. Bioeng. Biotechnol. 8:524018. doi: 10.3389/fbioe.2020.524018

The small intestine is the primary site of drug absorption following oral administration, making paramount the proper monitoring of the absorption process. *In vitro* tools to predict intestinal absorption are particularly important in preclinical drug development since they are less laborious and cost-intensive and raise less ethical considerations compared to *in vivo* studies. The Caco-2 model is considered the gold standard of *in vitro* intestinal models regarding the prediction of absorption of orally delivered compounds. However, this model presents several drawbacks, such as the expression of tighter tight junctions, not being suitable to perform permeability of paracellular compounds. Besides, cells are representative of only one intestinal cell type, without considering the role of non-absorptive cells on the absorption pathway of drugs. In the present study, we developed a new three-dimensional (3D) intestinal model that aims to bridge the gap between *in vitro* tools and animal studies. Our 3D model comprises a collagen layer with human intestinal fibroblasts (HIFs) embedded, mimicking the intestinal lamina propria and providing 3D support for the epithelium, composed of Caco-2 cells and mucus-producing HT29-MTX cells, creating a model that can better resemble, both in terms of composition and regarding the outcomes of drug permeability when testing paracellular compounds, the human small intestine. The optimization of the collagen layer with HIFs was performed, testing different collagen concentrations and HIF seeding densities in order to avoid collagen contraction before day 14, maintaining HIF metabolically active inside the collagen disks during time in culture. HIF morphology and extracellular matrix (ECM) deposition were assessed, confirming that fibroblasts presented a normal and healthy elongated shape and secreted fibronectin and laminin, remodeling the collagen matrix. Regarding the epithelial layer, transepithelial electrical resistance (TEER) values decreased when cells were in the 3D configuration, comparing with the 2D analogs (Caco-2 and coculture of Caco-2+HT29-MTX models), becoming

more similar with *in vivo* values. The permeability assay with fluorescein isothiocyanate (FITC)–Dextran 4 kDa showed that absorption in the 3D models is significantly higher than that in the 2D models, confirming the importance of using a more biorelevant model when testing the paracellular permeability of compounds.

Keywords: three-dimensional (3D), intestinal model, permeability, paracellular, collagen, drug development, hydrogel, drug absorption

INTRODUCTION

The drug development field is increasingly requesting for reliable tools that can speed up the initial phases of drug development. Indeed, evaluating the absorption of compounds at an early stage of drug discovery is extremely important. Ineffective intestinal absorption allied with undesirable metabolic stability accounts for about 50% of drug failure in clinical studies (Kennedy, 1997; Li, 2001; Dahlgren and Lennernas, 2019). Understanding the absorption potential of a molecule in the beginning will allow the reduction of animal testing, besides saving time and resources.

Considering that the oral route is the most common and practical non-invasive way to administer a drug, the need for an intestinal model that can properly mimic what happens *in vivo* is unquestionable. In fact, although being the most practical route, not all drugs are suitable to be administered orally due to either toxicity or poor absorption, and this should be determined as early as possible (Billat et al., 2017).

In vitro cell-based intestinal models have the advantage of being simple to obtain and produce consistent results, and this is why they have been around since the 1980s (Pereira et al., 2016). Although there have been new developments and improvements to the intestinal *in vitro* models, trying to mimic as closer as possible the human intestine, the Caco-2 model is still considered the gold standard. Caco-2 cells are cultured on Transwell® inserts for 21 days in order to differentiate into enterocyte-like cells, forming a polarized monolayer with a brush border membrane, microvilli, and tight junctions (TJs) (Artursson and Karlsson, 1991). Besides, these cells express some relevant influx and efflux transporters, as well as enzymes (Maubon et al., 2007). Nevertheless, this model presents several drawbacks. The fact that these cells present tighter TJs than what is observed *in vivo* makes the permeability of paracellular compounds to be underestimated (Artursson et al., 2001; Sun et al., 2008). This happens because paracellular transport refers to the transfer of substances across the epithelium through the intercellular space between the cells forming it (Edelblum and Turner, 2015). It is a transport that is unmediated and passive down a concentration gradient. This route normally allows the permeation of hydrophilic molecules (e.g., nadolol, atenolol, terbutaline), which normally are not able to permeate through the lipid membrane and may not have affinity for membrane-bound transporters being, therefore, excluded from transcellular pathway. The TJs gating the entrance to this route restrict the paracellular pathway of transport, and this is enhanced in the Caco-2 model, where the presence of TJs is higher than in the human small intestine, forming a very tight monolayer and impeding the passage of paracellular compounds (Lennernäs et al., 1996; Artursson et al., 2001). Besides the tightness of the monolayer, the lower permeability of paracellular compounds in the Caco-2 model may also be attributed to the lower number of pores per cm^2 that is observed in this model comparing to that of the human jejunum (Linnankoski et al., 2010).

In fact, the Caco-2 model is better at predicting the permeability of transcellular compounds than paracellular, where, normally, values of permeability are much lower than what is observed *in vivo* (Tavelin et al., 2003). To overcome these issues, other cell lines have been proposed to be used in *in vitro* intestinal models, such as Madin-Darby canine kidney (MDCK), Lewis lung carcinoma–porcine kidney 1 (LLC-PK1), 2/4/A1, TC-7 (a Caco-2 subclone), and IEC-18 (Gres et al., 1998; Marano et al., 2001; Balimane and Chong, 2005; Lazorova et al., 2011; Turco et al., 2011). Besides presenting some advantages, they all possess their own limitations, making the Caco-2 *in vitro* model the most widely accepted until today. An enhancement of the Caco-2 model has been achieved, coculturing these cells with HT29-MTX cells. These cells are known to be mucus producers, mimicking the goblet cells of the small intestine. Besides, these cells present looser TJs, decreasing the tightness of the monolayer and making it more similar to what is observed *in vivo* (Antunes et al., 2013). More recently, a triple coculture model has been developed with the addition of Raji B monocytes that are capable of secreting factors that make a fraction of Caco-2 cells differentiate into M-cells that have a role in transepithelial transport (Antunes et al., 2013). Although this model is more similar to the human small intestine and provides better results regarding the permeability of compounds, it still continues to represent only one layer of the intestine—the epithelium. Besides, cells are seeded on top of the Transwell® insert membranes that do not provide biological cues to the epithelial cells and do not replicate the architecture and mechanisms occurring in the living organ. In fact, cells that are grown in two-dimensional (2D) lack the interactions that occur in *in vivo* 3D matrixes, which are crucial for maintaining cell functions and polarity (Darnell et al., 2011; Desrochers et al., 2014). The presence of a 3D matrix that can resemble the *in vivo* extracellular matrix (ECM) is of paramount importance regarding cell behavior and differentiation (Pampaloni et al., 2007; Justice et al., 2009; Chitcholtan et al., 2013). Besides, regarding intestinal absorption, the epithelium represents an important role in the absorption process, but it is not the unique anatomic barrier that conditions the permeability of drugs. The small intestine is divided into four main layers, mucosa, submucosa, muscularis propria, and serosa, although in most of the duodenum, the outer layer is the adventitia (Seeley et al., 2004; Pereira et al., 2016). The absorption process occurs in the mucosa, the most complex layer,

which comprises the epithelium, lamina propria, and muscularis mucosae (Pampaloni et al., 2007). The lamina propria, which provides vascular support for the epithelium and often contains mucosal glands, like Brunner's glands in the duodenum, which are spiral tubes that form a network in the submucosa and open through the lamina propria into the crypts between the villi, secreting a thin and alkaline mucus that helps protect the duodenum, aiding in acid neutralization (Cullen, 2008), can have a role in the absorption process and influence the behavior of the epithelial cells (Shaker and Rubin, 2010). The lamina propria is composed of connective tissue, like collagen and elastin, fibroblasts, blood, and lymphatic vessels. Nevertheless, a distinctive characteristic of this layer is that it contains a great number of immunologically competent cells, like mononuclear cells, plasma cells and lymphocytes, and nerve endings (Boudry et al., 2004). Trying to replicate the 3D intestinal environment and develop models that can better replicate the *in vivo* situation to better predict permeability outcomes is of extreme importance. Although being a relatively new topic, 3D models have been explored in the past years, and different models have been developed by different groups (Sung et al., 2011; Yu et al., 2012; Li et al., 2013; Pereira et al., 2015; Dosh et al., 2017; Yi et al., 2017; Madden et al., 2018). Each model has its own peculiarities, and there is a variety of models—from the ones that are based on scaffolds, to decellularized tissue models, to more complex gut-on-a-chip models or even organoids. Within the models that are based on scaffolds that serve as the 3D support for the cells, some are built in order to mimic the architecture of the human small intestine, namely, the villi, and authors observe that the architecture can give important cues for cells and alter their behavior *in vitro*, making cells respond to the shape and have a more physiological behavior, which can be important for several studies (Sung et al., 2011; Yu et al., 2012, 2014; Kim and Kim, 2018; Castano et al., 2019). However, it is important to consider that other aspects, besides the 3D structure and architecture, can influence the behavior of intestinal cells. For example, it has been shown that nutrients can modulate intestinal cell function and morphology, being that an excess of nutrients can lead to an increased number of epithelial cells, an increased proliferation rate, villi length and crypt depth, and even redistribution of TJ proteins (Altmann and Leblond, 1970; Brun et al., 2007; Verdam et al., 2011; Mao et al., 2013; Mah et al., 2014). These alterations were proven to occur in a Caco-2/HT29 model, where excess nutrients led to an increase in follicle-like structures and mucus production and a decrease in TJs, associated with an increase of paracellular permeability (Bottani et al., 2019). The activity of intestinal markers such as alkaline phosphatase, aminopeptidase N, and dipeptidyl peptidase-IV was raised. Besides nutrient exposure, it is also possible to modulate Caco-2 cell differentiation using different cell passages. Ferraretto et al. (2007) showed that early passages of Caco-2 cells are representative of an undifferentiated phenotype, with low enzyme activity, whether at intermediate passages (18–25) a differentiated phenotype is observed and is characterized by the presence of a mature brush border with microvilli and high enzymatic activity. From passage 26 on, the presence of microvilli is accompanied by the appearance of a junctional apparatus, which confirms the polarity and the transport functions of the monolayer.

Regarding the 3D models, not only the architecture may play an important role. The truth is that the 3D support itself, which is normally composed of ECM components, can serve as a more physiological support than the plastic membranes that are normally used and have in impact in cell behavior. In fact, not all laboratories and researchers are equipped and have the know-how to produce 3D complex structures using different techniques. So, if the aim is to develop a 3D model that can better represent the human small intestine but, at the same time, be simple enough so others can replicate it to test their compounds, maybe the complex 3D structures need to be left out. Since our aim was to develop a new model to be used for permeability testing, we opted by building a model that, although complex, could be simple enough so others could reproduce it. In this study, we propose a model that comprises a layer composed of collagen with fibroblasts embedded, which mimics the intestinal lamina propria, giving support to the epithelium and having a role in the behavior of epithelial cells and in the permeability outcomes (**Figure 1**). In this study, the aim was to obtain a model that could better resemble the human small intestine, making cells feel a more physiological environment and behaving in a way that could resemble more what is observed *in vivo*. Regarding the permeability of paracellular compounds, underestimated in the Caco-2 models, our hypothesis laid on the possibility of this model providing closer biomimetic conditions, considering the aforementioned reasons.

MATERIALS AND METHODS

Cell Culture Conditions

Human colon adenocarcinoma Caco-2 cells (passage 26) were purchased from American Type Culture Collection (ATCC, United States). Mucus-producing HT29-MTX (passage 41) cells were kindly provided by Dr. T. Lesuffleur (INSERM U178, Villejuif, France). Caco-2 and HT29-MTX cell lines were grown in Dulbecco's modified Eagle's medium (DMEM) with 4.5 g/L glucose and Ultraglutamine^{TM} (Gibco), supplemented with 1% non-essential amino acids (NEAA) 100X (Gibco), 1% penicillin/streptomycin 100X (Biowest), and 10% fetal bovine serum (FBS) (Biochrom). Human intestinal fibroblast (HIF) primary cells (passage 6) were obtained from ScienCell and were cultured in Fibroblast Medium (FM) supplemented with 2% FBS, 1% of Fibroblast Growth Supplement (FGS), and 1% penicillin/streptomycin solution (all from ScienCell). Cells were grown separately in tissue culture flasks (SPL) and maintained in an incubator (Binder) at 37°C and 5% CO_2 in a water-saturated atmosphere.

Collagen Hydrogel With Human Intestinal Fibroblasts Embedded

Different initial seeding densities of HIFs were used in order to understand the appropriate cell concentration without compromising their viability. To obtain the collagen layer with HIF, 10X phosphate buffered saline (PBS), 1N sodium

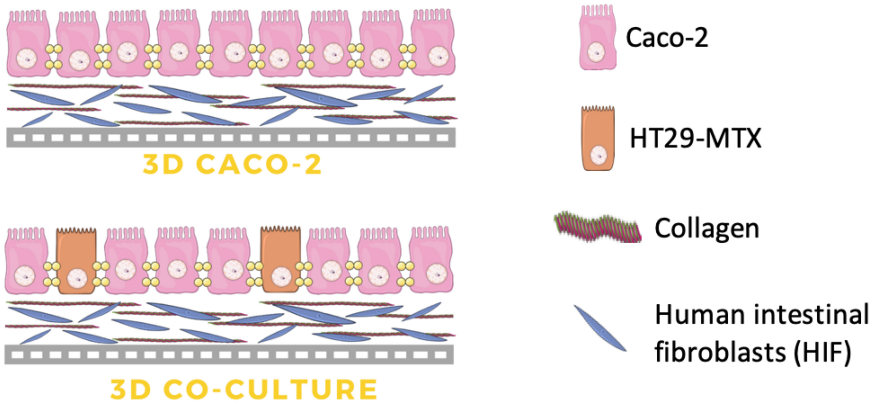

FIGURE 1 | Scheme of the configuration of the three-dimensional (3D) intestinal model (3D Caco-2 and 3D Coculture). The 3D model is composed of a collagen layer with human intestinal fibroblasts embedded, and on top, Caco-2 and HT29-MTX epithelial cells are added in order to mimic the intestinal enterocytes and goblet cells, respectively.

hydroxide (NaOH), and FM with HIF in different concentrations ranging from 1×10^5 to 2×10^6 cells/ml were added to the high concentrated rat tail collagen solution (Corning), following supplier recommendations, in order to obtain a final concentration of 5 mg/ml of collagen. The solution was placed on the 12-well Transwell® inserts (Millicell) using 110 μl to obtain a layer with approximately 1 mm of thickness. The solution was dispersed carefully in order to cover the entire surface of the insert and was incubated at 37°C, 5% CO_2 in a water-saturated atmosphere for 30 min to allow gelation. Disks were monitored for 21 days. Since with these conditions, contraction of the disks was observed, an increase in collagen concentration was tested. New disks with a collagen concentration of 6 mg/ml were obtained, using the same method, and HIFs were embedded using the lower density previously tested (1×10^5 cells/ml). This setup was used for further experiments.

Determination of Collagen Hydrogels Rheological Properties

To determine the rheological properties of the collagen hydrogels, the rotational rheometer Kinexus Pro (Malvern Instruments) with an 8-mm parallel disk geometry was used. Frequency sweep experiments were performed at 1% strain and a frequency ranging from 0.1 to 10 Hz within the linear viscoelastic region to determine the shear elastic and viscous moduli of the samples. The experiments were performed on collagen disks obtained as previously mentioned, without fibroblasts embedded, with approximately 1-mm thickness and cut into 8-mm diameter disks.

Visualization of Collagen Hydrogels

Collagen disks with a concentration of 6 mg/ml, without HIFs embedded, were obtained, as mentioned previously, to visualize the fibers through atomic force microscopy (AFM) and scanning electron cryomicroscopy (CryoSEM).

Atomic force microscopy images in collagen were obtained using a PicoPlus 5500 controller (Keysight Technologies, United States). The images were performed in Contact mode, in liquid (PBS), using a V-shaped MLCT-BIO-DC-D cantilever with a spring constant (k) in the range of 0.03 N/m (Bruker Corporation, United States).

The scan speed was set at 0.5 l/s. The scan size was 30 $\mu m^2 \times 30$ μm^2. The software used to obtain the images was the PicoView 1.2 (Keysight Technologies, United States).

The CryoSEM examination was performed using the high-resolution scanning electron microscope JSM 6301F (JEOL), X-ray microanalysis using INCA Energy 350 (Oxford), and the low-temperature sample observation system Alto-2500 (Gatan). The sample was rapidly cooled through immersion in slush nitrogen and transferred, in vacuum, to the sample preparation chamber with cooled platinum. The sample was fractured, sublimated for 120 s at −90°C and coated with Au/Pd by ionic pulverization for 50 s. The sample was then transferred to the SEM chamber, and visualization of the sample was performed at −150°C.

Metabolic Activity of the Human Intestinal Fibroblasts Inside the Collagen Hydrogels

The metabolic activity of the HIFs inside the collagen disks was determined at different time points using the resazurin assay. Collagen hydrogels with a final concentration of 6 mg/ml and 1×10^5 HIF/ml embedded were obtained, dispersed in 48-well plates, and allowed to gel for 30 min inside the incubator at 37°C, 5% CO_2 in a water-saturated atmosphere. After complete gelation, 2 ml of DMEM was added to each well, the plate was placed again in the incubator, and the medium was changed every 2–3 days. The resazurin solution was obtained dissolving 50 mg of resazurin sodium salt (Sigma) into 25 ml of PBS 20X and 475 ml of dH_2O overnight, at room temperature with agitation in the dark, and then filtered. At each time point (collagen disks with 1, 7, 14, and 21 days in culture), a solution containing 20% resazurin in DMEM complete was prepared. The solution was pre-warmed to 37°C, and 600 μl was added to each well. The

plate was incubated for 2 h at 37°C, 5% CO_2 in a water-saturated atmosphere in order to allow viable cells with active metabolism to reduce resazurin into the resorufin product, which is pink and fluorescent. After the incubation period, samples were quantified by measuring the relative fluorescence units (RFUs) using a microplate reader Synergy^{TM} Mx HM550 (Biotek) set at 530/590 (excitation/emission wavelength, respectively), and results were normalized by subtracting the blank (collagen gel without cells).

Three-Dimensional *in vitro* Model

Collagen hydrogels with a concentration of 6 mg/ml and 1×10^5 HIF/ml were obtained as previously described. After the 30-min gelation process, Caco-2 cells (1×10^5 cells/cm^2) (3D Caco-2) or a mixture of Caco-2 and HT29-MTX (1×10^5 cells/cm^2 at a 9:1 ratio, respectively) (3D Co-culture) in 0.5 ml of DMEM were added on top of the fibroblast-embedded collagen layer. Then, 1.5 ml of DMEM was added to the basolateral side, and plates were incubated at 37°C, 5% CO_2 in a water-saturated atmosphere. Same cell numbers of Caco-2 (2D Caco-2) and Caco-2+HT29-MTX (2D Coculture) were added directly on top of inserts without collagen, with the same DMEM volume to use as 2D controls. The cultures were maintained during 14 or 21 days, and the medium of the models was changed every 2–3 days. Transepithelial electrical resistance (TEER) was periodically measured using an EVOM^2 equipment (World Precision Instruments).

Assessment of Human Intestinal Fibroblast Morphology and Extracellular Matrix Secretion

The morphology of the HIFs seeded inside the collagen hydrogels after 14 days was assessed using an antibody against vimentin, which is a filament protein present in mesenchymal cells (Danielsson et al., 2018). The expression of fibronectin and laminin, which are components of the ECM, was also assessed.

Samples were washed once with PBS and fixed using 2% paraformaldehyde (PFA) in PBS for 30 min at room temperature (RT). After the fixation step, samples were washed three times for 5 min with PBS. This step was followed by permeabilization with a solution of 0.2% (v/v) Triton X-100 in PBS for 10 min at RT, and samples were washed thrice with PBS for 5 min. Afterward, a blocking step was performed using a blocking solution (BS) containing 1.5% bovine serum albumin (BSA) and 5% FBS in PBS for 1 h at RT. Samples were then transferred to a humidified chamber and were incubated either with mouse anti-human vimentin primary antibody (1:50) (sc-6260, Santa Cruz Biotechnology) + rabbit anti-human fibronectin primary antibody (1:50) (F3648, Sigma Aldrich) or with mouse anti-human vimentin primary antibody (1:50) + rabbit anti-human laminin primary antibody (1:30) (L9393, Sigma Aldrich) overnight at 4°C. After incubation with the primary antibodies, samples were washed three times for 5 min with a solution of 0.05% Tween-20 in PBS (PBST). This was followed by incubation with the secondary antibodies F(ab')2-Goat anti-Mouse IgG (H+L) Cross-Adsorbed, Alexa Fluor 594 (A-11020, Thermo Fisher Scientific) (1:500) + Goat anti-Rabbit IgG (H+L) Cross-Adsorbed, Alexa Fluor 488 (A-11008, Thermo Fisher Scientific) (1:500), and cell nuclei were counterstained with 4',6-diamidino-2-phenylindole (DAPI) (Sigma Aldrich) (500 ng/ml). Finally, cells were washed twice with PBST and once with PBS for 5 min and kept in PBS until visualization by a spectral confocal laser scanning microscope TCS-SP5 AOBS (Leica).

Assessment of Cell Layer Formation by Hematoxylin and Eosin Staining

To assess cell layer formation in both 2D models at days 14 and 21 and 3D models at day 14, hematoxylin and eosin (H&E) staining was performed. For this, inserts with the cells were washed once with PBS for 5 min and fixed using 2.5% glutaraldehyde and 2% PFA in 0.1 M phosphate buffer (PB) for 1 h at RT. Then, inserts were washed thrice with PBS for 5 min and kept in PBS at 4°C until further processing for paraffin embedding. Sections of 3 μm were obtained using an RM2255 microtome (Leica). Sections were then stained for H&E. Briefly, sections were deparaffinized and rehydrated, stained for 3 min in Gil's Hematoxylin (Thermo Scientific), 6 min in running water, dehydrated, stained for 1 min in Eosin Y (Thermo Scientific), cleared, and mounted in Entellan (Merck).

Assessment of Cell Layer Formation, Tight Junction, and MUC2 Expression by Immunocytochemistry

The formation of an intact layer was confirmed using an antibody against EpCAM, and the presence of TJs was assessed using claudin-1 and zona occludens 1 (ZO-1), which are integral transmembrane and peripheral TJ proteins, respectively. The presence of adherens junctions was evaluated using an antibody against *E*-chaderin. MUC2 was chosen to evaluate mucin expression because it is the mostly expressed mucin in the small intestinte (Schneider et al., 2018).

The models were washed with PBS and fixed with 2% PFA for 30 min. Then, cells were washed three times with PBS. The models were submerged in a solution of sucrose 15% (in PBS) for 3 h, and after that, they were left overnight in a solution of 30% sucrose. Then, models were embedded in Optimal Cutting Temperature (OCT) compound (Kaltek) and frozen at −20°C. Sections with 7 μm were obtained using an HM550 cryostat (Microm).

To stain with different antibodies, the slides with the cuts were dipped into PBS to dissolve the OCT. A permeabilization step using a solution of 0.2% (v/v) Triton X-100 in PBS for 5 min at RT was performed. Afterward, slides were washed thrice with PBS for 5 min. A blocking step was performed using a solution containing 1.5% BSA and 5% FBS in PBS for 1 h at RT. Slides were incubated with the primary antibodies' solutions [rabbit anti-human EpCAM primary antibody (1:250) (10694-R028, Sino Biological) + mouse anti-human vimentin primary antibody (1:100) (sc-6260, Santa Cruz Biotechnology) or rabbit anti-human ZO-1 primary antibody (1:50) (sc-10804, Santa Cruz Biotechnology) + mouse anti-human MUC2 primary antibody (1:50) (ab118964, Abcam) or rabbit anti-human claudin-1 primary antibody (1:200) (MA5-16351, Thermo Fisher) or mouse

anti-human *E*-cadherin primary antibody conjugated with Alexa Fluor 488 (1:100) (324110, Biolegend)] overnight at 4°C. Slides where washed three times for 5 min with PBST and incubated with the secondary antibodies and DAPI to counterstain the nuclei (500 ng/ml) (Sigma). For the first two combinations, F(ab')2-Goat anti-Mouse IgG (H+L) Cross-Adsorbed, Alexa Fluor 594 (A-11020, Thermo Fisher Scientific) (1:500) and Goat anti-Rabbit IgG (H+L) Cross-Adsorbed, Alexa Fluor 488 (A-11008, Thermo Fisher Scientific) (1:500) were used, and for claudin-1, the secondary antibody against rabbit (Alexa Fluor 488) was used. Secondary antibodies were added to samples for 3 h at 4°C. For *E*-cadherin, no secondary antibody was needed, since the primary antibody was already conjugated to a fluorochrome. Slides were then washed twice with PBST and once with PBS, all for 5 min. Slides were mounted using fluorescent mounting medium (Dako). Samples were left to dry overnight protected from light at 4°C and were maintained in these conditions until visualization by a spectral confocal laser scanning microscope TCS-SP5 AOBS (Leica). Since the aim was to compare the amount and localization of tight and adherens junctions between samples, laser power and gain of each laser were maintained for all samples regarding each antibody.

Permeability Assay With Fluorescein Isothiocyanate–Dextran

Permeability of fluorescein isothiocyanate (FITC)–Dextran 4 kDa (Sigma) was performed through the 3D and 2D intestinal models to assess the robustness of each model regarding paracellular transport. FITC-Dextran with a molecular weight of 4 kDa was chosen because it represents a measure for paracellular permeability of the intestinal epithelium (Woting and Blaut, 2018). The permeability assays were performed at the 14th and 21st day of culture.

Culture medium was removed from both sides of the Transwell® inserts and washed twice with pre-warmed Hank's balanced salt solution (HBSS). After the washes, 1.5 and 0.5 ml of HBSS were placed on the basolateral and apical sides of the inserts, respectively, and they were allowed to equilibrate for 30 min at 37°C and 100 rpm in a KS 4000 ic control orbital shaker (IKA). After 30 min, HBSS on the apical side was replaced by 0.5 ml of 200 μg/ml FITC-Dextran dissolved in HBSS. At predetermined time points (15, 30, 45, 60, 90, 180, 240, and 300 min), TEER was measured in order to assess the monolayer integrity, and a sample of 200 μl was taken from the basolateral side and replaced by the same amount of HBSS. At the end of the assay, a sample from the apical side was taken. The amount of FITC-Dextran was measured using a Synergy microplate reader (Biotek) at excitation/emission wavelengths of 490/520. The permeability results were expressed in percentage of release and apparent permeability (P_{app}) that was calculated using the following equation:

$$P_{app} = \frac{\Delta Q}{A \times C_0 \times \Delta t} \S \quad (1)$$

where ΔQ is the amount of compound detected in the basolateral side (mg), A is the surface area of the insert (cm^2), C_0 is the initial concentration in the apical compartment (mg/ml), and Δt is the time of the experiment (s).

Statistical Analysis

To perform statistical analysis, the software GraphPad Prism 7.0 (GraphPad Software Inc.) was used. All results are represented as mean ± standard error deviation (SEM). Differences between groups in percentage of permeability were compared using one-way analysis of variance (ANOVA) Tukey's *post hoc* test. Differences in resazurin and Papp results were compared using *T*-student test. The level of significance was set at probabilities of $^{*}p < 0.05$, $^{**}p < 0.01$, $^{***}p < 0.001$, and $^{****}p < 0.0001$.

RESULTS

Contraction of the Collagen Matrix by Fibroblasts

Using the initial collagen concentration of 5 mg/ml, contraction of the disks by the fibroblasts was observed in all conditions, being that contraction was proportional to the density of cells inside the disk (**Supplementary Material**).

It was observed that an increase in collagen concentration to 6 mg/ml was enough to prevent collagen contraction, at least until day 14 in culture. In fact, when fibroblasts were seeded inside the collagen disks and no epithelial cells were seeded on top, disks would not contract for 20–21 days. However, when only Caco-2 cells were seeded on top of the gels, contraction of the disks occurred around day 16. Although contraction did not occur for the 3D coculture, in order to be coherent, both 3D models were used after 14 days.

Collagen Hydrogels Properties

Rheological assays allowed the determination of the elastic and viscous components of the shear modulus (**Figure 2A**) under test conditions. The average value of the elastic component of the shear modulus was 483 ± 106 Pa, while the viscous component was 198 ± 18 Pa.

AFM (**Figure 2B**) and CryoSEM (**Figures 2C,D**) techniques showed that hydrogels have a porous mesh, with random porous size, ranging from less than 1–10 μm, and random distribution.

Metabolic Activity of Human Intestinal Fibroblasts Inside the Disks

The metabolic activity of the fibroblasts inside the collagen disks was assessed, presenting a stairway profile along the time in culture and showing a significant increase from week to week (**Figure 3**). This means that fibroblasts are active inside the gels, which indicates that they are healthy and proliferating.

Human Intestinal Fibroblast Morphology and Fibronectin and Laminin Secretion Inside the Collagen Disks

To observe the morphology of the HIFs inside the collagen hydrogels and understand if they present a normal morphology, as well as to assess the secretion of fibronectin and laminin,

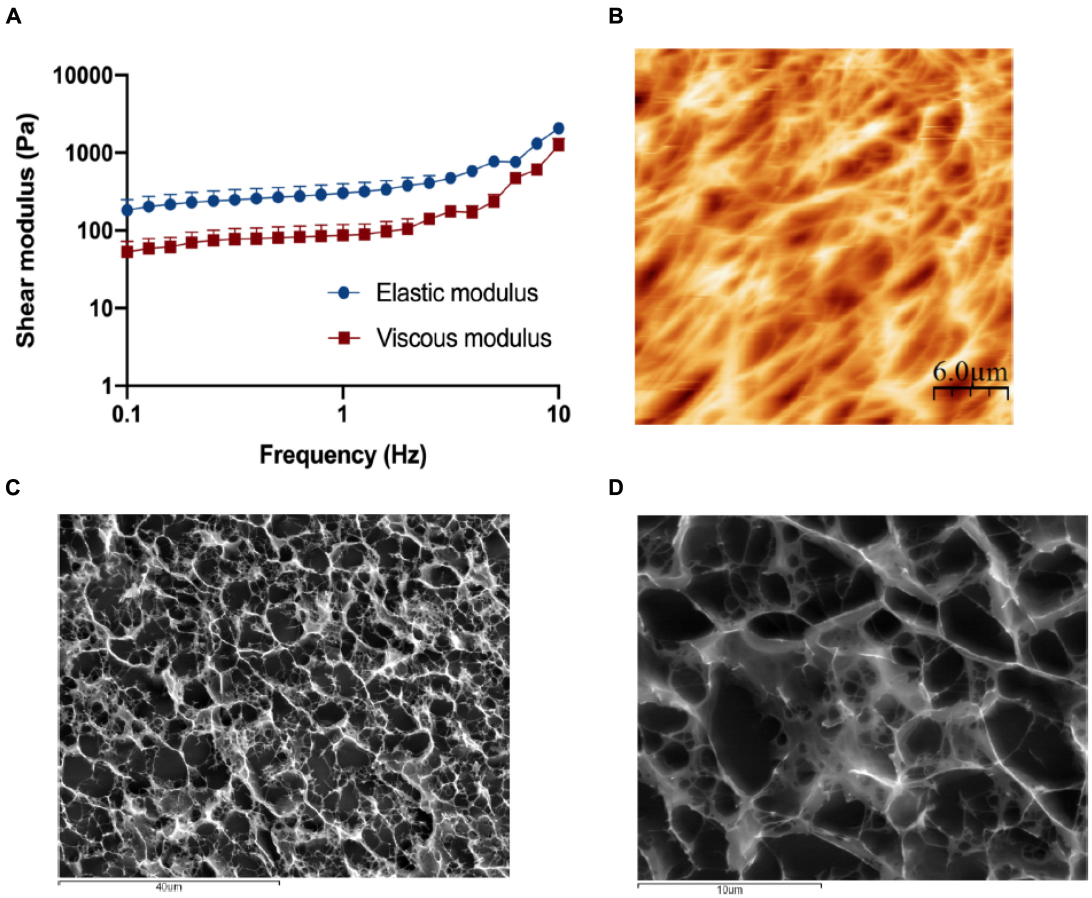

FIGURE 2 | Characterization of the collagen matrix. **(A)** Rheological behavior of the 6 mg/ml collagen hydrogels when subjected to frequency sweep tests (0.1–10 Hz) with a strain of 1% show that the elastic modulus of the disks is around 500 Pa, which is considered within normal lamina propria values. Results are the average of triplicates, and bars represent the standard error deviation (SEM). **(B)** Visualization of the 6 mg/ml collagen hydrogel surface by atomic force microscopy (AFM). Collagen gels present a highly porous surface, with porous sizes ranging from 1 to 10 μm. **(C,D)** Visualization of the 6 mg/ml collagen hydrogel inner structure by CryoSEM. Like its surface, the inner structure of the disks is highly porous, with random distribution and a size ranging from 1 to 10 μm.

immunocytochemistry technique was used. **Figure 4** depicts the elongated shape of fibroblasts in each condition. Besides, a higher cellular density and a higher amount of fibronectin and laminin (**Figures 4A,B**) are observed when Caco-2 or Caco-2+HT29-MTX cells are seeded on top of the gels when comparing to the disks embedded with HIFs without epithelial cells on top. Comparing the 3D Caco-2 with the 3D Coculture model, it was possible to observe that there is a higher number of fibroblasts and fibronectin deposition inside the disks when only Caco-2 cells are on top comparing to the Coculture.

Cell Layer Formation and Expression of Proteins of the Junctions

The cell layer formation was assessed through H&E staining and immunocytochemistry on the different time points to understand if there were differences regarding the epithelial layer in different days. It was observed that, in all models, the cellular layer is already formed at day 14 (**Figures 5**, **6A**). It is also possible to observe some multilayer formation in the Caco-2 models, both in 2D and 3D, and these multilayers seem to be decreased in the Coculture models.

Regarding the expression of tight and adherens junctions and the secretion of mucins by HT29-MTX cells, it is possible to see that claudin-1 and *E*-cadherin are expressed in all the models at the different time points (**Figures 6B,C**). Comparing the 2D Caco-2 model at different days, there is a higher expression of the proteins on day 21 comparing to day 14. Nevertheless, when comparing the 2D Coculture models, although the expression of *E*-cadherin seems higher at day 21, the same does not happen with the expression of claudin-1, which seems lower. Regarding the 3D models, the expression of *E*-cadherin is in the middle of the expression of the 2D models, whether for claudin-1, expression seems to be similar to the 2D models at 21 days.

Regarding the expression of the TJ protein ZO-1 (**Figure 7**), it is possible to observe that all the models have a high expression of this protein, and there are no visible differences between the models. Regarding the expression of MUC2 (**Figure 7**), as it was expected, this mucin is only secreted when HT29-MTX cells

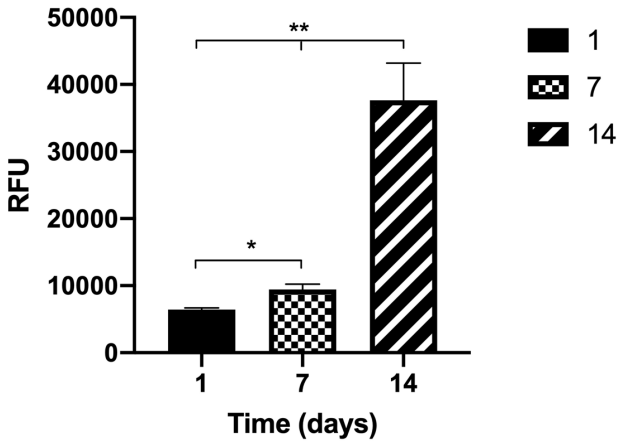

FIGURE 3 | The metabolic activity of the human intestinal fibroblasts (HIFs) inside the collagen hydrogels for 14 days shows that cells have an increase in metabolic activity from week to week. Results are the average of triplicates, and bars represent the standard error deviation (SEM). Statistical differences $p < 0.05$ are denoted by * and $p < 0.01$ are denoted by **.

are present in the model, since these are mucus-secreting cells, unlike Caco-2 cells.

Permeability Assay With Fluorescein Isothiocyanate–Dextran 4 kDa

The barrier integrity of the intestinal models was accessed by TEER measurements along the time in culture (**Figure 8A**). As expected, the 2D Caco-2 model was the one with higher TEER values, around 800 $\Omega.cm^2$. The addition of HT29-MTX cells to the model renders a decrease in TEER to approximately 350 $\Omega.cm^2$. Regarding the 3D models, both models present lower TEER values than their 2D analogs. As it happens in the 2D models, in 3D, the Caco-2 model presents higher TEER values than those in the 3D Coculture.

Regarding the permeability outcomes, it was observed that all models show a similar tendency of increased permeability with time. It can be observed in **Figures 8B,D** that regarding the 2D Caco-2 model, there are significant differences between permeability values at days 14 and 21, being that permeability is higher at day 14 than 21. Regarding the 2D Coculture model, the opposite occurs. When comparing the permeability of the 2D models at day 21, that is what is described in the literature as the proper time for the cells to be in culture and form a confluent and polarized monolayer, with the 3D models at day 14 (**Figures 8C,E**), it is possible to observe that 3D models present higher permeability, when comparing to their 2D analogs, being that the 3D Coculture model is the model that presents the greatest permeability.

DISCUSSION

In the present study, a new 3D *in vitro* intestinal model was developed. The main purpose of the study was to obtain a more physiologically relevant intestinal *in vitro* model that could render more accurate results when testing the absorption of paracellular compounds in the gut and in a faster way. To obtain this model, a collagen layer with HIFs embedded was optimized in order to mimic the intestinal lamina propria, which is the substrate where the epithelial cells sit in the small intestine (Powell et al., 2011). Any active compound to reach the systemic circulation must cross the epithelium, but also the lamina propria, which is, mostly, neglected in the *in vitro* screening of drug absorption. Besides, the lamina propria provides 3D support to the epithelium and gives important cues to the cells, influencing their behavior (Griffith and Swartz, 2006; Castano et al., 2019). Since it is well established that fibroblasts have the ability to degrade and contract collagen (Zhu et al., 2001; Branco da Cunha et al., 2014), a high collagen concentration of 5 mg/ml was used and different HIF seeding densities were embedded in the hydrogels to access their behavior. This high concentration of collagen was also based on the concentration in native tissues, which is normally above 5 mg/ml, despite most 3D models that are developed use lower concentrations, not mimicking the native tissue (Antoine et al., 2014). It was observed that even with this high concentration of collagen, fibroblasts were able to contract the gel and that higher initial amounts of fibroblasts led to higher contraction and degradation of the collagen disks. Since an intact disk covering the entire area of the Transwell® insert is needed, otherwise it would not be possible to perform reliable permeability assays, an optimization of the layer had to be performed. With an optimized collagen concentration of 6 mg/ml and an HIF seeding density of 1×10^5 cells/ml, the disks' rheological properties were evaluated, indicating the disks are soft matrices and rheological values are within normal values for the intestinal lamina propria, whose elastic modulus is around 0.5 and 1 kPa (Stidham et al., 2011; Stewart et al., 2018; Costa and Ahluwalia, 2019). Nevertheless, comparisons with human values or values found in the literature are not straightforward. Using different equipment, e.g., a rheometer or a nanoindentation tester, or even using the same equipment but changing the geometry, introduces variability to the results, making it hard to compare with the existing literature. Regarding the hydrogels' inner structure, it was possible to observe highly porous structures, as it was expected, since hydrogels are composed mainly of water, enabling the survival and proliferation of fibroblasts (Ahmed, 2015).

The metabolic activity of the cells inside the gels along the time in culture was assessed. Although it is important that fibroblasts do not contract the gel, it is also very important that they are healthy and metabolically active inside the gels, obtaining a compromise between fibroblast proliferation and disk integrity. During the time in culture, the metabolic activity of fibroblasts inside the gels significantly increased every week. Besides metabolic activity, it is also important to understand if cells present their physiological elongated shape. When fibroblasts are surrounded by stiff matrices, they are not able to spread, staying in a round shape, which is not representative of what happens in the human body (Branco da Cunha et al., 2014). Regarding the morphology and ECM component secretion of fibroblasts, it was possible to observe that fibroblasts presented an elongated shape when entrapped in the collagen matrix and were

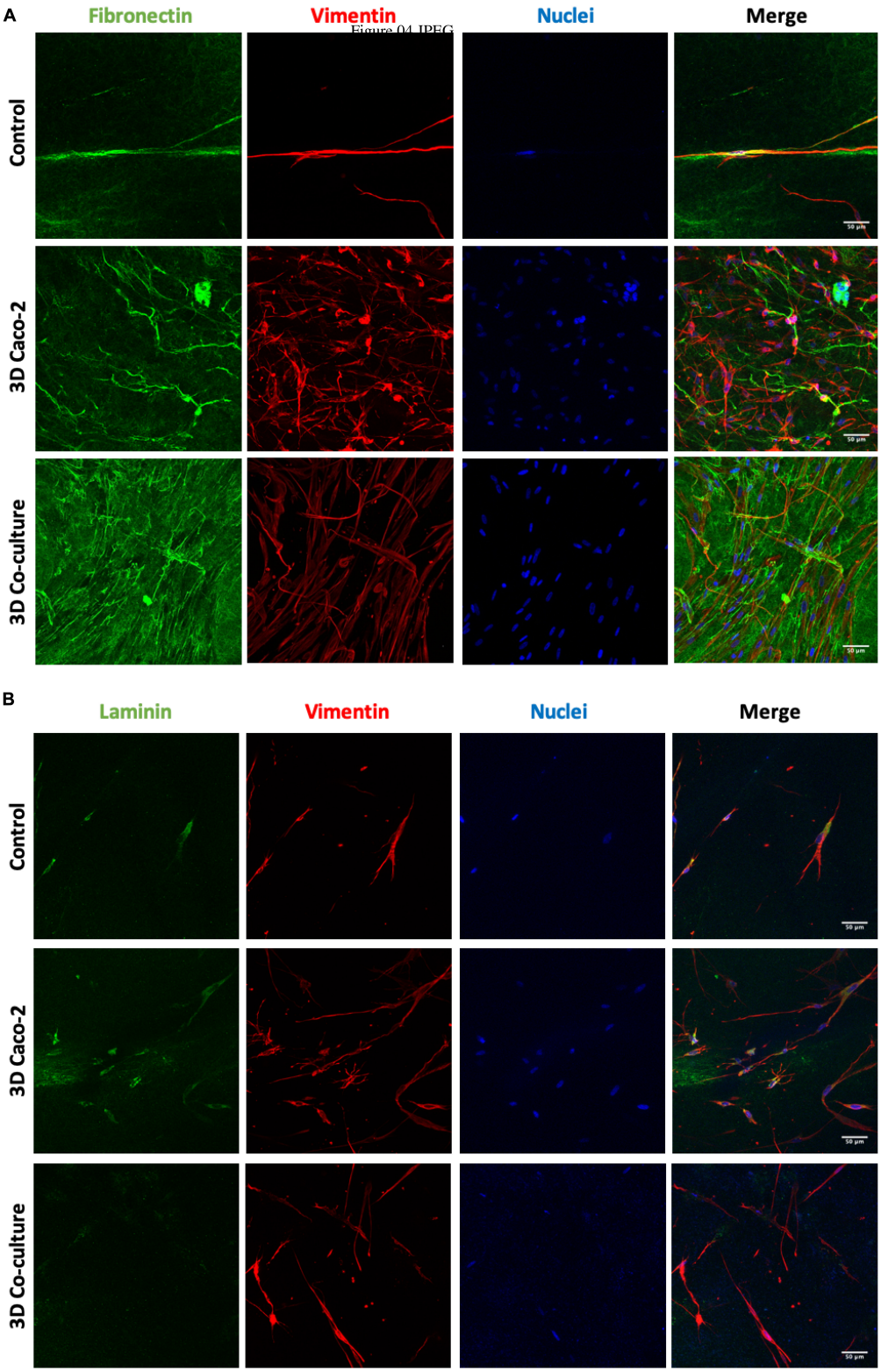

FIGURE 4 | Human intestinal fibroblast (HIF) morphology and **(A)** fibronectin and **(B)** laminin deposition by HIFs in collagen hydrogels, during the time in culture, with and without epithelial cells on top. The control refers to HIF embedded in the collagen layer alone, and the 3D Caco-2 and 3D Coculture refer to the addition of Caco-2 and Caco-2 + HT29-MTX on top of this layer, respectively. Pictures show maximal projections of several stacks of the gels. Fibronectin and laminin were labeled with Alexa-Fluor 488 (green), and vimentin was labeled with Alexa-Fluor 594 (red). The nucleus was counterstained with 4′,6-diamidino-2-phenylindole (DAPI) (blue).

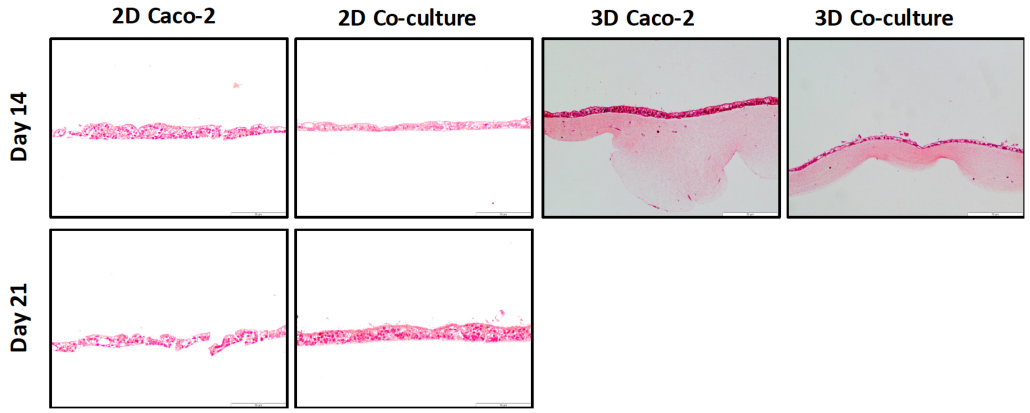

FIGURE 5 | H&E staining of the different models at 14 and 21 days shows that at day 14, a cell layer is already formed in all the models.

able to secrete fibronectin and laminin, shown to be key players in the remodeling of the matrix. After 14 days in culture, the disks are no longer comprised of only type I collagen from rat tail, but human fibronectin and laminin, secreted by the fibroblasts. This indicates that fibroblasts are able to degrade the collagen and proliferate, secreting their own matrix, remodeling their surrounding environment, which is important for cell survival (Roulis and Flavell, 2016).

It is well known that cells have the ability to communicate with each other, this phenomenon being regarded as cellular crosstalk (Geiger et al., 2001). It was, then, investigated whether epithelial cells on top of the collagen gels could exert some effect on the fibroblasts inside the collagen gels. When epithelial cells were added to the cultures, a higher number of fibroblasts inside the disks were observed, which seem to indicate that epithelial cells enhance the proliferation of stromal cells inside the collagen matrix. The secretion of ECM components, such as fibronectin and laminin, was also increased when this crosstalk occurred, which can be explained by the fact that epithelial adhesions with the ECM are most commonly mediated by integrins, and the extracellular ligands that anchor these adhesions include fibronectin (Geiger et al., 2001). There was also a higher number of fibroblasts when only Caco-2 cells were seeded on top, being that the addition of HT29-MTX seemed to have an inhibitory effect on the crosstalk between Caco-2 and the fibroblasts. Besides being visible by the higher number of fibroblasts and fibronectin deposition, this is also supported by the fact that 3D Caco-2 models contracted after 16 days in culture, whether 3D Coculture models maintained their integrity for 21 days, meaning that fibroblasts of the 3D Caco-2 models were more contractile than the ones of the 3D Coculture model.

Before performing the permeability assays with the 3D models at day 14, the establishment of an intact monolayer was confirmed, since an intact barrier is crucial to perform reliable permeability experiments. Since TEER values of the models were lower in the 3D comparing to the 2D models, H&E and EpCAM stainings were performed to observe the cellular barrier. It was observed by both methods that at 14 days, the monolayer of the 3D models is already completely formed, as well as the monolayer of the 2D models, and no visible differences in the 2D models are observed between days 14 and 21. Indeed, it is described that when cells are seeded on top of biological matrices, instead of artificial ones like the Transwell® membrane, the TEER decreases (Li et al., 2013). This decrease in TEER is usually not associated with barrier integrity, but with the tightness of the TJs (Li et al., 2013; Yi et al., 2017). When cells are seeded on top of 3D biological matrices, they tend to show a more *in vivo* behavior, not forming such tight TJs and becoming more similar to what is observed in the intestinal epithelium, where TEER values are around 30 Ω (Legen et al., 2005). The decrease in the TEER values is likely related to the TJs and not barrier integrity. Claudins are able to bind to ZO, through a PDZ-binding motif. Claudins are the major determinant of barrier junction. Intestinal claudins form two different classes: sealing and pore forming. Claudin-1 belongs to the sealing class, and if its expression is increased, this results in a tighter barrier, which restricts the movement of luminal contents through the paracellular route (Hamazaki et al., 2002; Shen et al., 2011). Regarding ZO-1, besides binding to claudins and other transmembrane proteins, is also able to interact with actin cytoskeleton and its associated proteins through the C-terminal region, which is very important to maintain TJ formation and function (Hamazaki et al., 2002; Lee, 2015; Lee et al., 2018). The presence of cadherins, which are responsible for cellular adhesion, was also assessed. It was possible to observe that for the 2D models, the expression of claudin-1 and *E*-cadherin seems to be higher at day 21 than at day 14, which is in accordance to TEER values. Nevertheless, the expression of ZO-1 seems to be similar in the 2D Caco-2 models at days 14 and 21, whether for the Caco-2/HT29-MTX 2D Coculture, expression is higher at day 14, which could be explained by the higher presence of HT29-MTX cells at day 21, since they have 1 more week to proliferate and increase their number in the model, and since these cells do not possess so many TJ proteins as the Caco-2 cells, its expression is lower. Regarding the expression of TJ proteins by the 3D models, it was observed that both claudin-1 and ZO-1 were expressed to the same extent as observed on the 2D models, leading to the conclusion that TJs are present

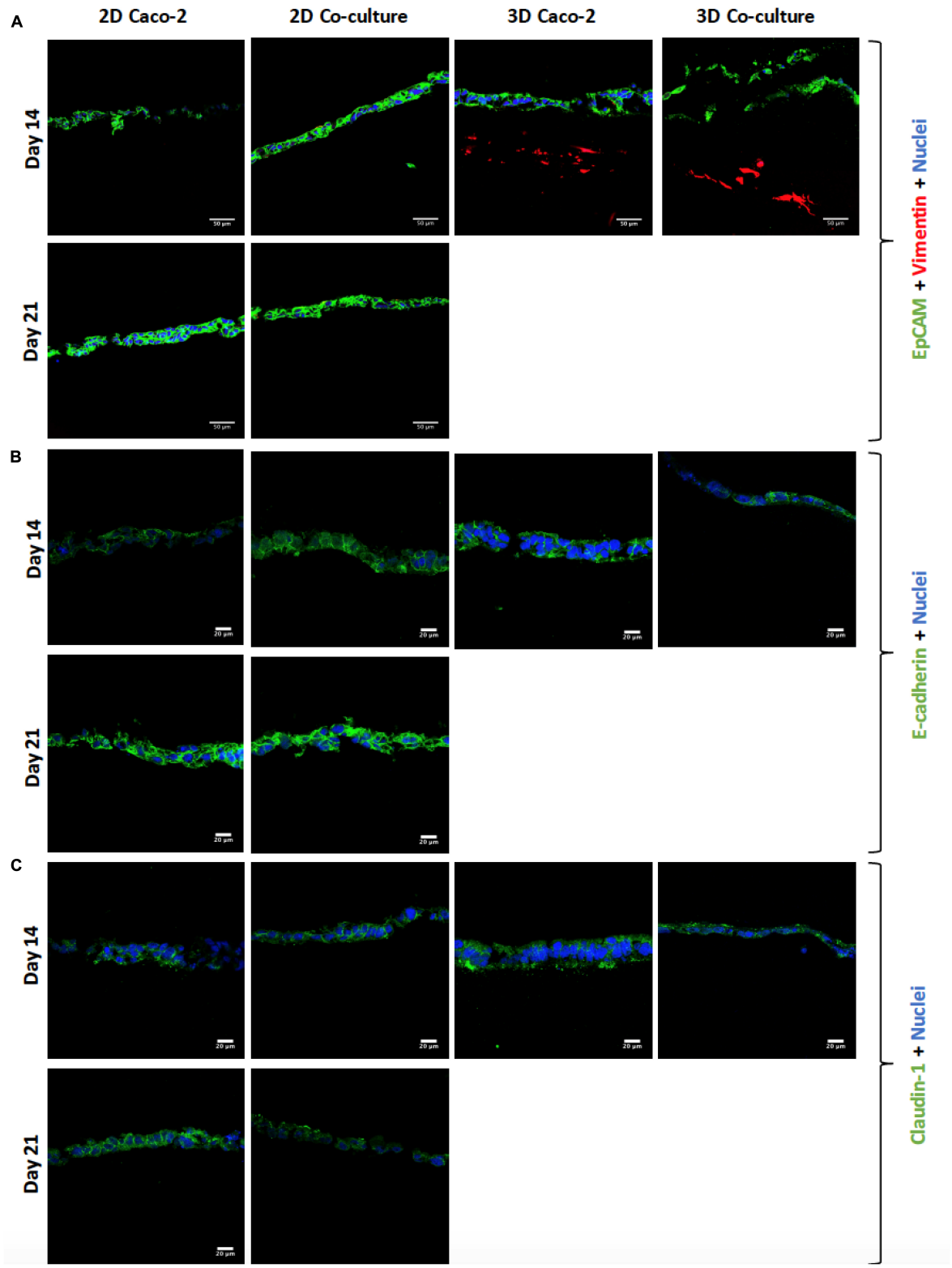

FIGURE 6 | (A) Visualization of cell layer formation by EpCAM, confirming the presence of a cell layer in all models. **(B)** Assessment and comparison of cellular adherens junctions in different models at different time points using *E*-cadherin. **(C)** Assessment and comparison of the tight junctions' protein claudin-1 in the different models at different time points. EpCAM, *E*-cadherin, and claudin-1 were labeled with Alexa-Fluor 488 (green), and nuclei were stained with 4′,6-diamidino-2-phenylindole (DAPI) (blue).

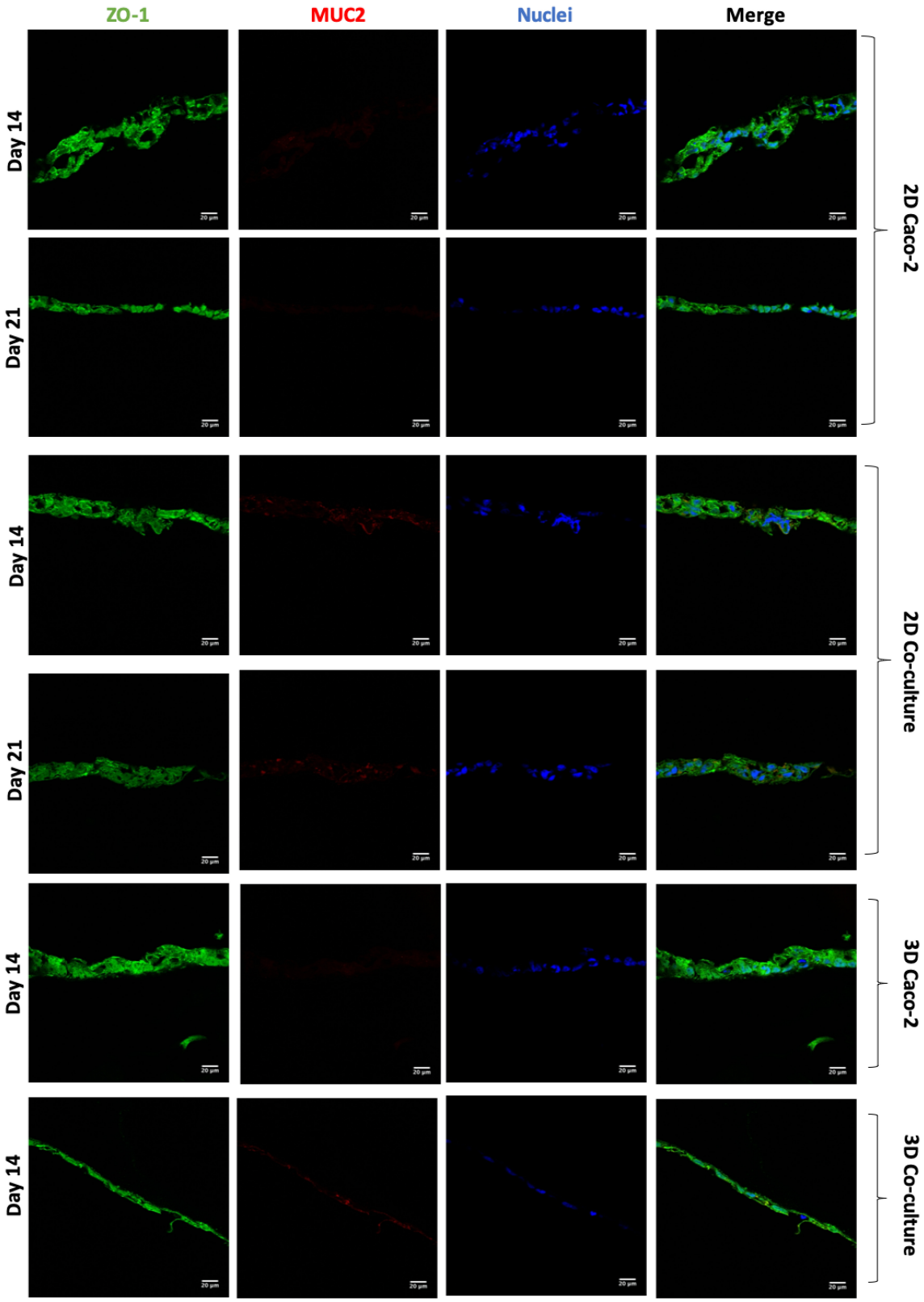

FIGURE 7 | Assessment and comparison of the tight junctions' protein ZO-1 and the mucin MUC2 in the different models at different time points. ZO-1 was labeled with Alexa-Fluor 488 (green), and MUC2 was labeled with Alexa Fluor 594 (red). The nucleus was counterstained with 4′,6-diamidino-2-phenylindole (DAPI) (blue).

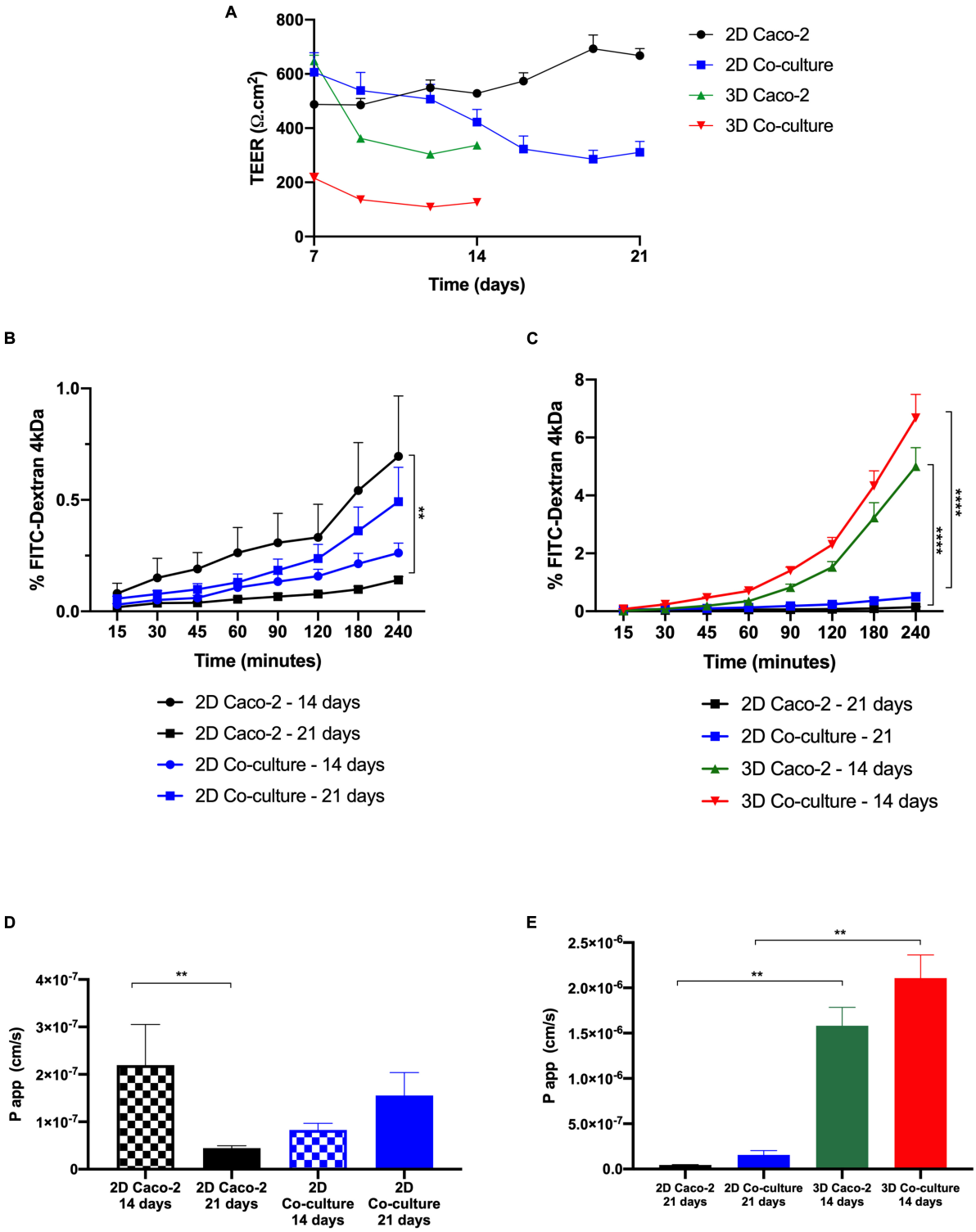

FIGURE 8 | Comparison between two-dimensional (2D) and 3D models regarding transepithelial electrical resistance (TEER) values and permeability. **(A)** TEER values of the models over time. Comparison of the cumulative transport of fluorescein isothiocyanate (FITC)–Dextran across the **(B)** 2D models after 14 vs. 21 days in culture and **(C)** 3D models after 14 days in culture vs. 2D models after 21 days in culture. Comparison of Papp values of **(D)** 2D models after 14 vs. 21 days in culture and **(E)** 3D models after 14 days in culture vs. 2D models after 21 days in culture. Results are the average of triplicates (except for permeability of 3D Caco-2, which is $n = 2$), and bars represent the standard error deviation (SEM). Statistical differences $p < 0.05$ are denoted by *, $p < 0.01$ are denoted by **, and $p < 0.0001$ are denoted by ****.

and are not downregulated in the models. The presence of the MUC2 mucin was also evaluated and confirmed the ability of the HT29-MTX as mucus-producing cells, resembling the intestinal goblet cells.

After it was confirmed that 3D models at 14 days of culture presented an intact barrier, permeability studies were performed. First, as control, permeability assays with FITC-Dextran 4 kDa in 2D models at days 14 and 21 were performed. A significant difference was observed between the 2D Caco-2 model at day 14 and day 21, with permeability being higher at day 14. This can be explained by the fact that at day 14, the Caco-2 monolayer in the 2D model does not possess such tight TJs, which makes the compound pass more easily. This is actually sustained by the expression of claudin-1, with higher expression at day 21, comparing to day 14. Since it is described that the Caco-2 model is not a suitable model to study the permeability of paracellular compounds because of the tightness of the barrier, making permeability underestimated, maybe it would be better to perform permeability assays at day 14 when using the Caco-2 model to study paracellular transport (Tavelin et al., 2003). Nevertheless, it is important to say that permeability was still low on the 2D Caco-2 model at day 14, and that even with the addition of HT29-MTX cells, which are able to decrease the TEER of the barrier, values of absorption of dextran remained very low (Antunes et al., 2013). Regarding the 2D coculture, the opposite occurs, and it is possible to observe that permeability is higher at day 21 than at day 14. We hypothesize that this is related to the number of HT29-MTX cells that increases with time in culture. Since these cells do not possess such tight TJs, a higher number of these cells in the model may improve the passage of compounds paracellularly.

Considering the widely established protocols for 2D Caco-2 and Coculture models for 21 days in culture, the permeability of these models with the values obtained for the 3D models after 14 days was compared (Hidalgo et al., 1989; Delie and Rubas, 1997). When relating the 2D with the 3D models, it was possible to see that the permeability of FITC-Dextran was significantly higher in the 3D models. These results are in accordance with the TEER values, since the 3D models present lower TEER values than the 2D models, which means the compound can pass more easily between the cells. Nevertheless, when comparing the TEER values of the 3D Caco-2 model at day 14 with the values of the 2D Coculture model at day 21, values are similar and around 300 $\Omega.cm^2$. However, when it comes to permeability, the values are completely different, being that permeability on the 3D Caco-2 model is five times higher than in the 2D Coculture model. This discrepancy indicates that permeability is not just merely related to the TEER values but most likely to the cells themselves and the fact that a 3D layer that mimics the *in vivo* environment is present that can have a huge impact on cellular behavior, as already stated. In fact, permeability phenomenon may be regulated not only by the fact that cells are seeded on top of the collagen layer but also by the crosstalk between the epithelial and stromal cells that we have seen have an important role in the remodeling of the matrix (Geiger et al., 2001). It is likely that this crosstalk also influences the behavior of cells regarding the permeability of compounds. This correlates with the expression of TJs. When comparing the expression of claudin-1 and ZO-1, which are TJ proteins, it seems that the expression in the 3D models at day 14 is similar to the expression of the 2D models at day 21. It is expected that the TEER values are not only regulated by the TJ expression, but other mechanisms may have a role. Besides, it is also a proof that the absorption of the paracellular compounds does not depend merely on TJ expression and barrier tightness but that the cells are in a more *in vivo* state may influence their behavior at other levels, and this may affect the permeability of the compounds. Besides, although it was not tested in the present work, we believe that this model can be suitable to test the permeability of not only paracellular compounds but also compounds that cross the intestinal barrier transcellularly. In fact, it has been reported that cells in 3D models may present a more relevant expression of drug transporters, like P-glycoprotein (P-gp), an efflux transporter that can limit the absorption of several compounds, which can have a great impact on permeability (Li et al., 2013; Yi et al., 2017). So, this model should be further studied and its potential to be used as a model to evaluate the permeability of transcellular compounds should be assessed, since it would bring enormous added value to the model.

CONCLUSION

In the present work, a novel 3D intestinal model was established, reproducing, in a more physiological way, the architecture and composition of the human small intestine. It was observed that fibroblasts embedded in collagen, mimicking the intestinal lamina propria, had the capability of producing ECM components, remodeling the surrounding environment and had a pivotal role in the behavior of epithelial cells. The 3D models were used for permeability assays after 14 days of culture, since it was observed that the epithelial layer was already formed and the expression of claudin-1 was similar to that of the 2D models at day 21. Besides, although TEER values presented differences between the 2D and 3D models, the expression of TJs (claudin-1 and ZO-1) and adherens junctions was similar between them. The permeability of FITC-Dextran 4 kDa, a hydrophilic compound that is known to cross the epithelium by the paracellular route, was significantly higher in the 3D models. We believe that these results are important, since it is known that paracellular permeability in the Caco-2 model is underestimated, since these cells resemble more the colonic epithelium. These results show that when cells are in a more physiological configuration and sensing a biological 3D matrix, instead of the Transell insert membrane, there is an effect on the cells, making them behave more similarly to what is observed *in vivo*. In fact, we believe that a crosstalk between epithelial and stromal cells occurs during the maturation of the model, since there is an enhancement on HIF contraction capability when Caco-2 cells are seeded on top of the collagen gels with fibroblasts that is likely regulated by the secretion of cytokines and growth factors by the cells. In conclusion, a new *in vitro* intestinal model is herein proposed to better and faster predict the

permeability of paracellular compounds, helping in bridging the gap between *in vitro* models and animal testing and contributing to the 3Rs policy.

DATA AVAILABILITY STATEMENT

The raw data supporting the conclusions of this article will be made available by the authors, without undue reservation, to any qualified researcher.

AUTHOR CONTRIBUTIONS

MM performed the experimental work. BS, CB, and EM provided the scientific guidance. All authors contributed to the writing of the manuscript.

FUNDING

This work was financed by Portuguese funds through FCT – Fundação para a Ciência e a Tecnologia/Ministério da Ciência, Tecnologia e Ensino Superior in the framework of the project "Institute for Research and Innovation in Health Sciences" UID/BIM/04293/2019. MM would like to thank FCT for financial support (SFRH/BD/131587/2017).

ACKNOWLEDGMENTS

The authors acknowledge the support of the i3S Scientific Platform Bioimaging, member of the national infrastructure PPBI–Portuguese Platform of Bioimaging (PPBI-POCI-01-0145-FEDER-022122). The authors would also like to thank Cláudia Machado for help regarding histology and Flávia Sousa for the help with statistical analysis.

SUPPLEMENTARY MATERIAL

The Supplementary Material for this article can be found online at: https://www.frontiersin.org/articles/10.3389/fbioe.2020.524018/full#supplementary-material

REFERENCES

Ahmed, E. M. (2015). Hydrogel: Preparation, characterization, and applications: A review. *J. Adv. Res.* 6, 105–121. doi: 10.1016/j.jare.2013.07.006

Altmann, G. G., and Leblond, C. P. (1970). Factors influencing villus size in the small intestine of adult rats as revealed by transposition of intestinal segments. *Am. J. Anatomy.* 127, 15–36. doi: 10.1002/aja.1001270104

Antoine, E. E., Vlachos, P. P., and Rylander, M. N. (2014). Review of collagen I hydrogels for bioengineered tissue microenvironments: characterization of mechanics, structure, and transport. *Tissue Eng. Part B Rev.* 20, 683–696. doi: 10.1089/ten.TEB.2014.0086

Antunes, F., Andrade, F., Araújo, F., Ferreira, D., and Sarmento, B. (2013). Establishment of a triple co-culture in vitro cell models to study intestinal absorption of peptide drugs. *Eur. J. Pharm. Biopharm.* 83, 427–435. doi: 10.1016/j.ejpb.2012.10.003

Artursson, P., and Karlsson, J. (1991). Correlation between oral drug absorption in humans and apparent drug permeability coefficients in human intestinal epithelial (Caco-2) cells. *Biochem. Biophys. Res. Commun.* 175, 880–885. doi: 10.1016/0006-291X(91)91647-U

Artursson, P., Palm, K., and Luthman, K. (2001). Caco-2 monolayers in experimental and theoretical predictions of drug transport. *Adv. Drug Deliv. Rev* 46, 27–43. doi: 10.1016/s0169-409x(00)00128129

Balimane, P. V., and Chong, S. (2005). Cell culture-based models for intestinal permeability: a critique. *Drug Discov. Today* 10, 335–343. doi: 10.1016/S1359-6446(04)033543359

Billat, P. A., Roger, E., Faure, S., and Lagarce, F. (2017). Models for drug absorption from the small intestine: where are we and where are we going? *Drug Discov. Today* 22, 761–775. doi: 10.1016/j.drudis.2017.01.007

Bottani, M., Cornaghi, L., Donetti, E., and Ferraretto, A. (2019). Excess of nutrient-induced morphofunctional adaptation and inflammation degree in a Caco2/HT-29 in vitro intestinal co-culture. *Nutrition* 58, 156–166.

Boudry, G., Yang, P.-C., and Perdue, M. H. (2004). *Encyclopedia of Gastroenterology*. New York: Elsevier.

Branco da Cunha, C., Klumpers, D. D., Li, W. A., Koshy, S. T., Weaver, J. C., Chaudhuri, O., et al. (2014). Influence of the stiffness of three-dimensional alginate/collagen-I interpenetrating networks on fibroblast biology. *Biomaterials* 35, 8927–8936. doi: 10.1016/j.biomaterials.2014.06.047

Brun, P., Castagliuolo, I., Leo, V. D., Buda, A., Pinzani, M., Palù, G., et al. (2007). Increased intestinal permeability in obese mice: new evidence in the pathogenesis of nonalcoholic steatohepatitis. *Am. J. Physiol. Gastr. Liver Physiol.* 292, G518–G525. doi: 10.1152/ajpgi.00024.2006

Castano, A. G., Garcia-Diaz, M., Torras, N., Altay, G., Comelles, J., and Martinez, E. (2019). Dynamic photopolymerization produces complex microstructures on hydrogels in a moldless approach to generate a 3D intestinal tissue model. *Biofabrication* 11, 25007. doi: 10.1088/1758-5090/ab0478

Chitcholtan, K., Asselin, E., Parent, S., Sykes, P. H., and Evans, J. J. (2013). Differences in growth properties of endometrial cancer in three dimensional (3D) culture and 2D cell monolayer. *Exp. Cell Res.* 319, 75–87. doi: 10.1016/j.yexcr.2012.09.012

Costa, J., and Ahluwalia, A. (2019). Advances and Current Challenges in Intestinal in vitro Model Engineering: A Digest. *Front. Bioengin. Biotechnol.* 7:144. doi: 10.3389/fbioe.2019.00144

Cullen, J. J. (2008). Shackelford's Surgery of the Alimentary Tract 6th Edition. *J. Am. Coll. Surg.* 206, 1–174. doi: 10.1016/j.jamcollsurg.2007.07.007

Dahlgren, D., and Lennernas, H. (2019). Intestinal Permeability and Drug Absorption: Predictive Experimental, Computational and In Vivo Approaches. *Pharmaceutics* 11, 411. doi: 10.3390/pharmaceutics11080411

Danielsson, F., Peterson, M. K., Caldeira Araújo, H., Lautenschläger, F., and Gad, A. K. B. (2018). Vimentin Diversity in Health and Disease. *Cells* 7, 147. doi: 10.3390/cells7100147

Darnell, M., Schreiter, T., Zeilinger, K., Urbaniak, T., Soderdahl, T., Rossberg, I., et al. (2011). Cytochrome P450-dependent metabolism in HepaRG cells cultured in a dynamic three-dimensional bioreactor. *Drug Metab. Dispos.* 39, 1131–1138. doi: 10.1124/dmd.110.037721

Delie, F., and Rubas, W. (1997). A human colonic cell line sharing similarities with enterocytes as a model to examine oral absorption: advantages and limitations of the Caco-2 model. *Crit. Rev. Ther. Drug Carr. Syst.* 14, 221–286. doi: 10.1615/CritRevTherDrugCarrierSyst.v14.i3.20

Desrochers, T. M., Palma, E., and Kaplan, D. L. (2014). Tissue-engineered kidney disease models. *Adv. Drug Deliv. Rev* 6, 67–80.

Dosh, R. H., Essa, A., Jordan-Mahy, N., Sammon, C., and Le Maitre, C. L. (2017). Use of hydrogel scaffolds to develop an in vitro 3D culture model of human intestinal epithelium. *Acta Biomater.* 62, 128–143.

Edelblum, K. L., and Turner, J. R. (2015). "Chapter 12 - Epithelial Cells: Structure, Transport, and Barrier Function," in *Mucosal Immunology (Fourth Edition)*, eds J. Mestecky, W. Strober, and M. W. Russell (Boston: Academic Press).

Ferraretto, A., Gravaghi, C., Donetti, E., Cosentino, S., Donida, B. M., Bedoni, M., et al. (2007). New methodological approach to induce a differentiation phenotype in Caco-2 cells prior to post-confluence stage. *Anticancer. Res.* 27, 3919–3925.

Geiger, B., Bershadsky, A., Pankov, R., and Yamada, K. M. (2001). Transmembrane crosstalk between the extracellular matrix and the cytoskeleton. *Nat. Rev. Mol. Cell Biol.* 2, 793–805. doi: 10.1038/35099066

Gres, M. C., Julian, B., Bourrie, M., Meunier, V., Roques, C., Berger, M., et al. (1998). Correlation between oral drug absorption in humans, and apparent drug permeability in TC-7 cells, a human epithelial intestinal cell line: comparison with the parental Caco-2 cell line. *Pharm. Res.* 15, 726–733. doi: 10.1023/a:1011919003030

Griffith, L. G., and Swartz, M. A. (2006). Capturing complex 3D tissue physiology in vitro. *Nat. Rev. Mol. Cell Biol.* 7, 211–224. doi: 10.1038/nrm1858

Hamazaki, Y., Itoh, M., Sasaki, H., Furuse, M., and Tsukita, S. (2002). Multi-PDZ domain protein 1 (MUPP1) is concentrated at tight junctions through its possible interaction with claudin-1 and junctional adhesion molecule. *J. Biol. Chem.* 277, 455–461. doi: 10.1074/jbc.M109005200

Hidalgo, I. J., Raub, T. J., and Borchardt, R. T. (1989). Characterization of the human colon carcinoma cell line (Caco-2) as a model system for intestinal epithelial permeability. *Gastroenterology* 96, 736–749. doi: 10.1016/0016-5085(89)9089790894

Justice, B. A., Badr, N. A., and Felder, R. A. (2009). 3D cell culture opens new dimensions in cell-based assays. *Drug Discov. Today* 14, 102–107. doi: 10.1016/j.drudis.2008.11.006

Kennedy, T. (1997). Managing the drug discovery/development interface. *Drug Discov. Today* 2, 436–444. doi: 10.1016/S1359-6446(97)010991094

Kim, W., and Kim, G. (2018). Intestinal Villi Model with Blood Capillaries Fabricated Using Collagen-Based Bioink and Dual-Cell-Printing Process. *ACS Appl. Mater Interfaces.* 10, 41185–41196.

Lazorova, L., Hubatsch, I., Ekegren, J. K., Gising, J., Nakai, D., Zaki, N. M., et al. (2011). Structural features determining the intestinal epithelial permeability and efflux of novel HIV-1 protease inhibitors. *J. Pharm. Sci.* 100, 3763–3772. doi: 10.1002/jps.22570

Lee, B., Moon, K. M., and Kim, C. Y. (2018). Tight Junction in the Intestinal Epithelium: Its Association with Diseases and Regulation by Phytochemicals. *J. Immunol. Res.* 2018, 2645465.

Lee, S. H. (2015). Intestinal permeability regulation by tight junction: implication on inflammatory bowel diseases. *Intest. Res.* 13, 11–18. doi: 10.5217/ir.2015.13.1.11

Legen, I., Salobir, M., and Kerè, J. (2005). Comparison of different intestinal epithelia as models for absorption enhancement studies. *Int. J. Pharm.* 291, 183–188. doi: 10.1016/j.ijpharm.2004.07.055

Lennernäs, H., Palm, K., Fagerholm, U., and Artursson, P. (1996). Comparison between active and passive drug transport in human intestinal epithelial (caco-2) cells in vitro and human jejunum in vivo. *Int. J. Pharm.* 127, 103–107. doi: 10.1016/0378-5173(95)042044200

Li, A. P. (2001). Screening for human ADME/Tox drug properties in drug discovery. *Drug Discov. Today* 6, 357–366. doi: 10.1016/s1359-6446(01)017121713

Li, N., Wang, D., Sui, Z., Qi, X., Ji, L., Wang, X., et al. (2013). Development of an Improved Three-Dimensional In Vitro Intestinal Mucosa Model for Drug Absorption Evaluation. *Tissue Engin. Part C Methods.* 19, 708–719. doi: 10.1089/ten.tec.2012.0463

Linnankoski, J., Mäkelä, J., Palmgren, J., Mauriala, T., Vedin, C., Ungell, A. L., et al. (2010). Paracellular Porosity and Pore Size of the Human Intestinal Epithelium in Tissue and Cell Culture Models. *J. Pharm. Sci.* 99, 2166–2175. doi: 10.1002/jps.21961

Madden, L. R., Nguyen, T. V., Garcia-Mojica, S., Shah, V., Le, A. V., Peier, A., et al. (2018). Bioprinted 3D Primary Human Intestinal Tissues Model Aspects of Native Physiology and ADME/Tox Functions. *Science* 2, 156–166.

Mah, A. T., Van Landeghem, L., Gavin, H. E., Magness, S. T., and Lund, P. K. (2014). Impact of Diet-Induced Obesity on Intestinal Stem Cells: Hyperproliferation but Impaired Intrinsic Function That Requires Insulin/IGF1. *Endocrinology* 155, 3302–3314. doi: 10.1210/en.20141112

Mao, J., Hu, X., Xiao, Y., Yang, C., Ding, Y., Hou, N., et al. (2013). Overnutrition Stimulates Intestinal Epithelium Proliferation Through β-Catenin Signaling in Obese Mice. *Diabetes Metab. Res. Rev.* 62, 3736–3746. doi: 10.2337/db13-0035

Marano, C. W., Garulacan, L. A., Ginanni, N., and Mullin, J. M. (2001). Phorbol ester treatment increases paracellular permeability across IEC-18 gastrointestinal epithelium in vitro. *Dig. Dis. Sci.* 46, 1490–1499. doi: 10.1023/a:1010696005958

Maubon, N., Le Vee, M., Fossati, L., Audry, M., Le Ferrec, E., Bolze, S., et al. (2007). Analysis of drug transporter expression in human intestinal Caco-2 cells by real-time PCR. *Fundam. Clin. Pharmacol.* 21, 659–663. doi: 10.1111/j.1472-8206.2007.00550.x

Pampaloni, F., Reynaud, E. G., and Stelzer, E. H. (2007). The third dimension bridges the gap between cell culture and live tissue. *Nat. Rev. Mol. Cell Biol.* 8, 839–845. doi: 10.1038/nrm2236

Pereira, C., Araujo, F., Barrias, C. C., Granja, P. L., and Sarmento, B. (2015). Dissecting stromal-epithelial interactions in a 3D in vitro cellularized intestinal model for permeability studies. *Biomaterials* 56, 34–36.

Pereira, C., Costa, J., Sarmento, B., and Araújo, F. (2016). *Cell-based in vitro models for intestinal permeability studies. Concepts and Models for Drug Permeability Studies*. Cambridge: Woodhead Publishing.

Powell, D. W., Pinchuk, I. V., Saada, J. I., Chen, X., and Mifflin, R. C. (2011). Mesenchymal cells of the intestinal lamina propria. *Annu. Rev. Physiol.* 73, 213–213.

Roulis, M., and Flavell, R. A. (2016). Fibroblasts and myofibroblasts of the intestinal lamina propria in physiology and disease. *Differentiation* 92, 116–131. doi: 10.1016/j.diff.2016.05.002

Schneider, H., Pelaseyed, T., Svensson, F., and Johansson, M. E. V. (2018). Study of mucin turnover in the small intestine by in vivo labeling. *Sci. Rep.* 8, 5760. doi: 10.1038/s41598-018-24148-x

Seeley, R., Stephens, T., and Tate, P. (2004). *Anatomy and Phisiology 6th*. New York, NY: McGraw-Hill.

Shaker, A., and Rubin, D. C. (2010). Intestinal stem cells and epithelial-mesenchymal interactions in the crypt and stem cell niche. *Transl. Res.* 156, 180–187. doi: 10.1016/j.trsl.2010.06.003

Shen, L., Weber, C. R., Raleigh, D. R., Yu, D., and Turner, J. R. (2011). Tight junction pore and leak pathways: a dynamic duo. *Annu. Rev. Physiol.* 73, 283–309. doi: 10.1146/annurev-physiol-012110142150

Stewart, D. C., Berrie, D., Li, J., Liu, X., Rickerson, C., Mkoji, D., et al. (2018). Quantitative assessment of intestinal stiffness and associations with fibrosis in human inflammatory bowel disease. *PLoS One* 13:e0200377. doi: 10.1371/journal.pone.0200377

Stidham, R. W., Xu, J., Johnson, L. A., Kim, K., Moons, D. S., McKenna, B. J., et al. (2011). Ultrasound elasticity imaging for detecting intestinal fibrosis and inflammation in rats and humans with Crohn's disease. *Gastroenterology* 141, 819.e–826.e. doi: 10.1053/j.gastro.2011.07.027

Sun, H., Chow, E. C., Liu, S., Du, Y., and Pang, K. S. (2008). The Caco-2 cell monolayer: usefulness and limitations. *Exp. Opin. Drug Metabol. Toxicol.* 4, 395–411. doi: 10.1517/17425255.4.4.395

Sung, J. H., Yu, J., Luo, D., Shuler, M. L., and March, J. C. (2011). Microscale 3-D hydrogel scaffold for biomimetic gastrointestinal (GI) tract model. *Lab Chip.* 11, 389–392. doi: 10.1039/c0lc00273a

Tavelin, S., Taipalensuu, J., Soderberg, L., Morrison, R., Chong, S., and Artursson, P. (2003). Prediction of the oral absorption of low-permeability drugs using small intestine-like 2/4/A1 cell monolayers. *Pharm. Res.* 20, 397–405. doi: 10.1023/a:1022699920043

Turco, L., Catone, T., Caloni, F., Di Consiglio, E., Testai, E., and Stammati, A. (2011). Caco-2/TC7 cell line characterization for intestinal absorption: how reliable is this in vitro model for the prediction of the oral dose fraction absorbed in human? *Toxicol. Vitro.* 25, 13–20. doi: 10.1016/j.tiv.2010.08.009

Verdam, F. J., Greve, J. W. M., Roosta, S., van Eijk, H., Bouvy, N., Buurman, W. A., et al. (2011). Small Intestinal Alterations in Severely Obese Hyperglycemic Subjects. *J. Clin. Endocrinol. Metabol.* 96, E379–E383. doi: 10.1210/jc.2010-1333

Woting, A., and Blaut, M. (2018). Small Intestinal Permeability and Gut-Transit Time Determined with Low and High Molecular Weight Fluorescein Isothiocyanate-Dextrans in C3H Mice. *Nutrients* 10:685. doi: 10.3390/nu10060685

Yi, B., Shim, K. Y., Ha, S. K., Han, J., Hoang, H.-H., Choi, I., et al. (2017). Three-dimensional in vitro gut model on a villi-shaped collagen scaffold. *BioChip. J.* 11, 219–231. doi: 10.1007/s13206-017-13071308

Yu, J., Carrier, R. L., March, J. C., and Griffith, L. G. (2014). Three dimensional human small intestine models for ADME-Tox studies. *Drug Discov. Today* 19, 1587–1594. doi: 10.1016/j.drudis.2014.05.003

Yu, J., Peng, S., Luo, D., and March, J. C. (2012). In vitro 3D human small intestinal villous model for drug permeability determination. *Biotechnol. Bioeng.* 109, 2173–2178. doi: 10.1002/bit.24518

Zhu, Y. K., Umino, T., Liu, X. D., Wang, H. J., Romberger, D. J., Spurzem, J. R., et al. (2001). Contraction of fibroblast-containing collagen gels: initial collagen concentration regulates the degree of contraction and cell survival. *Vitro Cell. Dev. Biol. Anim.* 37, 10–16. doi: 10.1290/1071-26902001037<0010:COFCCG<2.0.CO;2

Conflict of Interest: The authors declare that the research was conducted in the absence of any commercial or financial relationships that could be construed as a potential conflict of interest.

Advantages of publishing in Frontiers

OPEN ACCESS
Articles are free to read for greatest visibility and readership

FAST PUBLICATION
Around 90 days from submission to decision

HIGH QUALITY PEER-REVIEW
Rigorous, collaborative, and constructive peer-review

TRANSPARENT PEER-REVIEW
Editors and reviewers acknowledged by name on published articles

Frontiers
Avenue du Tribunal-Fédéral 34
1005 Lausanne | Switzerland

Visit us: www.frontiersin.org
Contact us: info@frontiersin.org | +41 21 510 17 00

REPRODUCIBILITY OF RESEARCH
Support open data and methods to enhance research reproducibility

DIGITAL PUBLISHING
Articles designed for optimal readership across devices

FOLLOW US
@frontiersin

IMPACT METRICS
Advanced article metrics track visibility across digital media

EXTENSIVE PROMOTION
Marketing and promotion of impactful research

LOOP RESEARCH NETWORK
Our network increases your article's readership